Usinage cryogénique de l'alliage aéronautique : Inconel 718

Sana Chaabani

ÉCOLE DOCTORALE SCIENCES DES MÉTIERS DE L'INGÉNIEUR
[LAMPA– Campus d'Angers]

THÈSE

présentée par : **Sana Chaabani**

soutenue le : **18 juin 2021**

pour obtenir le grade de : **Docteur**

préparée à : **École Nationale Supérieure d'Arts et Métiers**

et Mondragon Unibertsitatea

Spécialité : **Mécanique-Procédés de fabrication "**

Cryogenic machining of the aeronautic alloy: Inconel 718

THÈSE dirigée par :
M. GERMAIN Guénael et M. ARRAZOLA Pedro

et co-encadrée par :
M. AYED Yessine

Jury

M. Lorenzo SEVILLA, Professeur, Université de Malaga, Espagne	Président
M. Oscar MARTIN, Maître de conférences, Université de Valladolid, Espagne	Rapporteur
M. Aitor MADARIAGA, Maître de conférences, Université de Mondragon, Espagne	Rapporteur
M. Mohammed NOUARI, Professeur des universités, InSIC, France	Examinateur
M. José OUTEIRO, Maître de conférences, LaBoMaP, ENSAM Cluny, France	Examinateur
M. Pedro ARRAZOLA, Professeur, Université de Mondragon, Espagne	Examinateur
M. Yessine AYED, Maître de conférences, LAMPA, ENSAM Angers, France	Examinateur

THÈSE

Dedication

”Dedicated to the memory of my grandmother, who always believed in my ability to be successful. You are gone but your belief in me has made this journey possible.”

Statement of originality

I hereby declare that this PhD thesis is the result of my personal work, and that it has not been previously presented to obtain another degree or professional qualification. The ideas, formulations, images and illustrations taken from outside sources have been duly cited and referenced.

Creative Commons

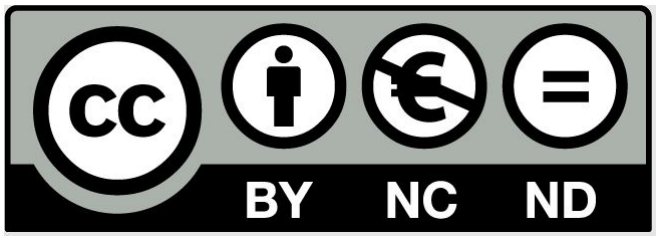

Acknowledgments

I would like to express my deep appreciation and grace to my supervisors Pedro Arrazola from Mondragon University in Spain and Guénael Germain from LAMPA at ENSAM-Angers in France. You have been special mentors for me. I would like to thank you for encouraging my research and for allowing me to grow as a research scientist. Your advice on both research as well as on my career have been priceless.

My appreciation goes to my advisor Yessine Ayed, for all the special guide, discussions and conversations we had to make this work successfull and worth to defend.

Very special thanks addressed to Professor Albert Tidu for his collaboration and continuous support to my Phd work from LEM3, "Laboratoire d'étude des Microstructures et de Mécanique des Matériaux" at Metz, France. I would like also to thank all the members of LEM3 who helped me to fulfill my work.

And, I address my thanks to everyone in all the laboratories Machining Laboratory, LAMPA and LEM3. It was tremendous sharing and working with all of you my first year of the Phd.

I would also like to thank the jury members for serving as my committee members. I also want to thank you for letting my defense be an enjoyable moment, and for your brilliant comments and suggestions.

Very special gratitude addressed to all my family members : My mother, my father, my sisters and my brothers in law.
To my best friend Houssam, I am so thankful for your unconditional support and help ! !

Thanks for all your contributions !

Résumé

Les alliages à base de nickel sont largement utilisés dans le secteur aéronautique vu leurs excellentes propriétés mécaniques à haute température et leur résistance à la corrosion. Cependant, l'usinage de ces matériaux est particulièrement difficile. Ceci est dû principalement à leur grandes propriétés mécaniques, leur très haute réactivité chimique avec la plupart des matériaux coupants et à un dégagement de chaleur important au niveau de la zone de coupe. Dans ce cadre, s'inscrivent les procédés d'usinage avec assistance visant à améliorer la productivité de certains matériaux qui sont difficiles à couper. Dans notre cas, on s'intéresse à l'assistance cryogénique. Elle consiste à injecter l'azote liquide (LN_2) ou le dioxide de carbone liquide (LCO_2) dans la zone de coupe permettant de faire chuter la température. Par conséquent, certains mécanismes d'usure sont décélérés et la durée de vie de l'outil est augmentée. En revanche, l'application de cette approche lors de l'usinage de l'Inconel 718 a démontré certaines limites en termes de durée de vie de l'outil et l'intégrité de surface de la pièce usinée contrairement à l'alliage de titane Ti64. C'est pourquoi, il s'avère très intéressant de discerner les mécanismes de dégradation de la productivité de l'Inconel 718 sous assistance cryogénique et d'améliorer au mieux les conditions opératoires. En plus, le comportement dynamique de l'Inconel 718 à des températures cryogéniques a été établi dans le but de caractériser les changements métallurgiques de l'Inconel 718 qui peuvent avoir lieu. Finalement, la prédiction de la tenue en fatigue est réalisée pour des éprouvettes percées sous conditions cryogéniques.

Mots clés : Comportement dynamique, Inconel 718, Usinage cryogénique, Tenue en fatigue.

Abstract

Nickel-based alloys are widely used in the manufacture of aerospace engine components due to their excellent high-temperature thermo-mechanical properties and good corrosion resistance. However, machining these materials poses a number of challenges, mainly because they maintain their properties at high temperatures. Additional difficulties result from their high chemical reactivity with most cutting tool materials and their low thermal conductivity, which leads to wear due to the high temperatures reached at the cutting edge. In this context, the use of cooling/lubrication systems are very relevant in order to improve productivity in machining. Thus, this research work focuses on cryogenic machining, which consists of projecting liquid nitrogen (LN_2) or liquid carbon dioxide (LCO_2) into the cutting zone to reduce the temperature. The aim is to reduce some wear mechanisms and increase tool life. However, the application of this lubrication system machining Inconel 718 has to date shown limitations in terms of tool life and surface integrity of the machined part, as opposed to Ti64 titanium alloy. It is therefore considered of great interest to discern the mechanisms responsible for the poor machinability of Inconel 718 in cryogenic machining in order to propose a suitable process window. To this end, the dynamic behavior of Inconel 718 at cryogenic temperatures is characterized to determine the metallurgical alterations that may occur in the machined part. The surface integrity condition obtained is also analyzed and a study is made of the fatigue behavior of drilled specimens under cryogenic conditions.

Keywords : Cryogenic machining, Dynamic behavior, Fatigue resistance, Inconel 718.

RESUMEN

Las aleaciones base níquel se utilizan ampliamente en la fabricación de componentes de motores de industria aeroespacial debido a sus excelentes propiedades termomecánicas a altas temperaturas y buena resistencia a la corrosión. Sin embargo, el mecanizado de estos materiales es particularmente difícil debido, principalmente, a que mantienen sus propiedades a altas temperaturas, pero también a su elevada reactividad química con la mayoría de los materiales de herramientas de corte y su baja conductividad térmica, lo que conlleva valores de desgaste elevados debidos a las altas temperaturas alcanzadas en el filo de corte. En este contexto, el empleo de sistemas de refrigeración/lubrificación son muy relevantes de cara a mejorar la productividad en su mecanizado. Así, este trabajo de investigación, se centra en el mecanizado criogénico, que consiste en proyectar nitrógeno liquido (LN_2) o dióxido de carbono liquido (LCO_2) en la zona de corte para reducir la temperatura. Se busca que algunos mecanismos de desgaste disminuyan y la vida útil de la herramienta aumente. Sin embargo, la aplicación de este sistema de lubrificación mecanizando Inconel 718 ha mostrado hasta la fecha limitaciones en cuanto a la vida útil de la herramienta y la integridad superficial de la pieza mecanizada, a diferencia de lo que sucede con la aleación de titanio Ti64. Por ello, se considera que es muy interesante discernir los mecanismos responsables de la mala maquinabilidad del Inconel 718 en el mecanizado criogénico para poder proponer una ventana de procesos adecuada. Para ello, se caracterizará el comportamiento mecánico-dinámico del Inconel 718 a temperaturas criogénicas de cara a determinar las alteraciones metalúrgicas que puedan ocurrir en la pieza mecanizada. Asimismo, se analizará la condición de integridad superficial obtenida y se hará un estudio del comportamiento de fatiga en probetas taladradas bajo asistencia criogénica.

Palabras clave : Comportamiento dinámico, Comportamiento de fatiga, Inconel 718, Mecanizado criogénico.

Résumé étendu en français

1 Introduction générale II
1.1 Contexte et motivation II
1.2 Les objectifs du travail de la thèse IV
2 Synopsis de l'état de l'art : Effet de l'usinage cryogénique V
2.1 Effet de l'usinage cryogénique sur les températures de coupe . . V
2.2 Effet de l'usinage cryogénique sur les efforts de coupe VI
2.3 Effet de l'usinage cryogénique sur le coefficient de frottement . VII
2.4 Effet de l'usinage cryogénique sur l'usure de l'outil IX
2.5 Intégrité de surface XIII
2.5.1 État de surface - La rugosité R_a XIV
2.5.2 Les contraintes résiduelles XV
2.5.3 Couche fortement écrouite XVI
2.6 Conclusion XVIII
3 Essais de caractérisation XIX
3.1 Procédure expérimentale XIX
3.2 Résultats et discussions XX
4 Essais de tournage avec assistance cryogénique XXIII
4.1 Procédure expérimentale XXIII
4.2 Résultats et discussions XXIV
4.2.1 Essais d'usure XXIV
4.2.2 État de surface : La rugosité XXVI
5 Essais de fatigue XXVII
5.1 Procédure expérimentale XXVII
5.2 Résultats et discussions XXVIII
5.2.1 Contraintes-cycles : S-N curves XXVIII
5.2.2 Fractographies d'éprouvettes rompues XXX
6 Conclusions et perspectives XXXIV
6.1 Conclusions XXXIV
6.1.1 Caractérisation mécanique à température cryogénique XXXIV
6.1.2 Essais d'usinage avec assistance cryogénique XXXIV
6.1.3 Résistance à la fatigue XXXV
6.1.4 Conclusion générale XXXV
6.2 Perspectives XXXV

1 Introduction générale

1.1 Contexte et motivation

L'innovation dans l'industrie aéronautique est motivée par la nécessité d'atteindre l'amélioration des performances des pièces mécaniques et la réduction de la masse de tous les composants de l'avion. Pour répondre à ces enjeux croissants, certains matériaux ayant des propriétés spécifiques sont l'objet d'une recherche et d'un développement continus. Depuis plusieurs décennies, un grand nombre des alliages à base de nickel ont été incorporés dans les moteurs de l'avion (Ulutan and Ozel, 2011). Ces matériaux se prêtent bien à l'industrie aéronautique, car ils présentent d'excellentes propriétés mécaniques à haute température, des résistances élevées à la corrosion et au fluage (Kumar et al., 2019; Hongbo and Gaochao, 2015). En particulier, les superalliages à base de nickel sont largement exploités dans les turboréacteurs qui sont soumis aux sollicitations thermiques et mécaniques intenses en service.

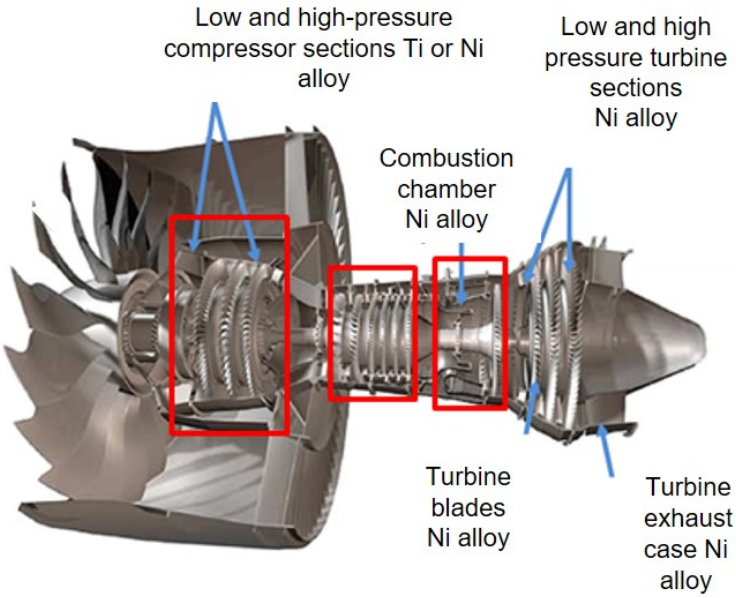

FIGURE 1 – Illustration d'une coupe transversale d'un moteur à réaction (Ulutan and Ozel, 2011).

Cependant, l'utilisation intensive de ces matériaux a mis en évidence un problème lié au procédé d'usinage. Appréciés pour leur capacité à conserver leurs propriétés mécaniques en service sur une large plage de températures, leurs performances lors de la coupe est défavorablement limité. Pour cette raison, les approches de refroidissement visent à améliorer la productivité de certains matériaux classés comme "difficiles à couper". Le problème majeur rencontré lors de l'usinage est l'augmentation significative de la température dans la zone de coupe qui conduit à la dégradation des outils de coupe. La durée de vie de l'outil est ainsi fortement réduite et l'état de surface des pièces usinées est alors détériorée. De nouvelles alternatives pour maintenir l'outil de coupe froid ont été investiguées dans des recherches antérieures. L'une de ces alternatives est appelée "usinage cryogénique", où l'azote liquide est utilisé comme lubrifiant pour réduire significativement la température de coupe, vu que sa température en phase liquide est de -196°C. Cette nouvelle approche d'usinage est considérée comme un processus prometteur pour l'industrie du futur. En dehors de son efficacité à réduire sensiblement la température dans la zone de coupe, l'usinage cryogénique présente plusieurs avantages écologiques, environnementaux et économiques. Pour cela, les procédés d'usinage cryogénique rendent inutile l'utilisation des lubrifiants conventionnels. Ces lubrifiants contiennent une quantité importante d'huile qui a un impact nocif sur l'environnement et peut provoquer des maladies de la peau et des poumons pour les opérateurs (Memmi et al., 2019). Un avantage supplémentaire d'éliminer les lubrifiants conventionnels est qu'il n'est pas nécessaire de dégraisser les pièces usinées et donc les copeaux ne sont pas contaminés avant recyclage.
Dans ce contexte, des études antérieures ont examiné l'efficacité de l'approche cryogénique lors de l'usinage de plusieurs matériaux (aciers, alliages de titane et alliages à base de nickel). Il a été démontré que la durée de vie de l'outil est améliorée dans le cas des alliages de titane (Ayed et al., 2017), contrairement aux alliages à base de nickel (Iturbe et al., 2016). D'après les résultats précédents, l'Inconel 718 s'est avéré induire une durée de vie de l'outil plus faible et une intégrité de surface plus détériorée (rugosité, contraintes résiduelles, micro-dureté) en condition cryogénique avec LN_2 que avec une lubrification conventionnelle. Récemment, des chercheurs se sont penchés sur un autre fluide cryogénique : le dioxyde de carbone LCO_2. Dans ce travail de thèse, de nombreux aspects sont traités pour étudier l'efficacité des approches cryogéniques. Tout d'abord, pour comprendre l'influence des stratégies de refroidissement cryogénique sur l'usure des outils et l'intégrité de surface, nous avons opté pour les opérations de tournage de l'Inconel 718. Ainsi, une étude comparative est menées en utilisant les deux fluides cryogéniques à savoir LN_2 et LCO_2 afin de déterminer la performance de l'approche cryogénique en comparant avec la lubrification conventionnelle.

Un autre aspect qui semble intéressant à étudier est lié au comportement mécanique de l'Inconel 718 à température cryogénique. Pendant l'usinage, le matériau est soumis à plusieurs sollicitations mécaniques et thermiques pouvant considérablement influencer sur le comportement du matériau pendant le processus de coupe. Il s'agit notamment de la température élevée résultante des mécanismes de frottement et de déformation plastique et de la très faible température de refroidissement de LN_2 (-196°C). La surface non usinée est particulièrement affectée par le fluide cryogénique, puisque ce dernier est livré avant le démarrage du procédé d'usinage pour obtenir l'état stabilisé.

Les disques de turbine de moteur d'avion sont principalement composés de composants critiques, par exemple la zone du moyeu (Witek, 2006) et les trous d'assemblage

(Fig. 2). De telles régions sont soumises aux chargements cycliques pendant leur service. En particulier, les trous percés sont les sources de concentration de contraintes et sont donc sensibles à l'amorçage de fissures de fatigue. En conséquence, les fabricants sont tenus de respecter des spécifications très strictes et des niveaux de précision élevés pour éviter toute défaillance brutale.

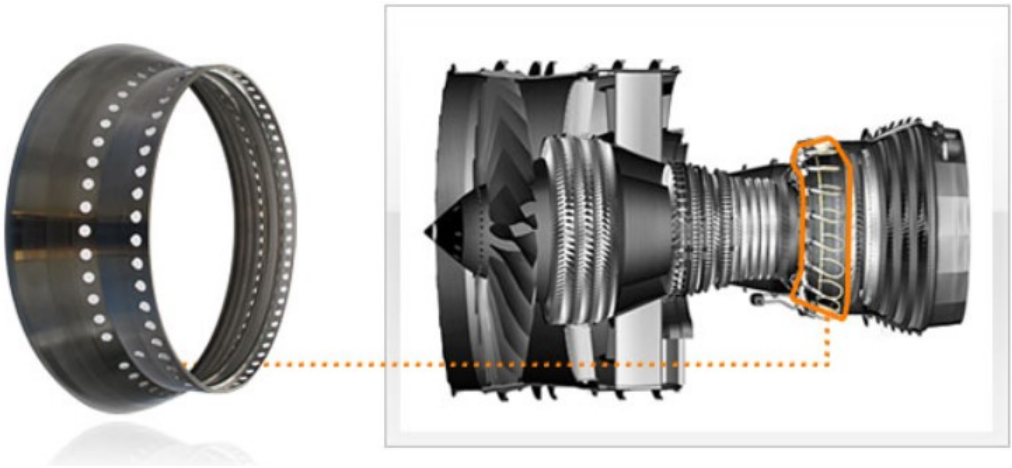

FIGURE 2 – Illustration d'une chambre de combustion d'assemblage de haute technologie fabriquée en Inconel et d'autres superalliages (Chaheng, 2020).

Le procédé d'usinage est souvent la dernière ou l'avant-dernière étape de fabrication. Les usineurs doivent optimiser le processus de coupe et améliorer l'intégrité de surface des pièces usinées. Pour cette raison, la présente étude adopte une approche originale du problème, en se concentrant sur l'adaptation de l'opération du perçage cryogénique pour examiner son impact sur la résistance à la fatigue. En effet, les éprouvettes percées révèlent une concentration de contraintes au niveau de la surface du trou. Par conséquent, l'influence de la surface est plus importante. Ainsi, l'effet du procédé d'usinage est mieux discriminé.

1.2 Les objectifs du travail de la thèse

L'objectif principal de ce travail de thèse est d'évaluer les performances de l'approche cryogénique. A cet effet, deux fluides cryogéniques différents : l'azote liquide (LN_2) et le dioxyde de carbone (LCO_2) sont analysés en termes de performances en usinage et de résistance à la fatigue considérant comme référence la lubrification conventionnelle (wet). Cet objectif se divise en objectifs spécifiques suivants :

— Étudier le comportement mécanique de l'Inconel 718 à température cryogénique et examiner les changements de la microstructure des échantillons déformés pour extraire des informations liées aux mécanismes qui pourraient se produire pendant l'usinage cryogénique ;

— Pour étudier les performances cryogéniques des deux fluides LN_2 et LCO_2 en termes de durée de vie de l'outil et intégrité de surface en tournage de l'Inconel 718 en comparaison avec la condition de lubrification conventionnelle ;

— Évaluer l'efficacité des nouvelles approches cryogéniques sur la résistance à la fatigue des éprouvettes percées.

2 Synopsis de l'état de l'art : Effet de l'usinage cryogénique

2.1 Effet de l'usinage cryogénique sur les températures de coupe

Hong et al. (2001a) ont menée une étude profonde dans le but d'estimer les températures de coupe par le biais de deux approches (experimentales et EF) dans plusieurs configurations de refroidissement : usinageà sec, lubrification conventionnelle, refroidissement cryogénique anticipé de la pièce à usiner, refroidissement de la face de dépouille de l'outil, refroidissement de la face de coupe de l'outil, refroidissement de la face de dépouille et de la face de coupe de l'outil simultanément. Ils ont prouvé que les températures de coupe diminuent significativement en utilisant la méthode de l'assistance cryogénique. En contre partie, les valeurs les plus élevées ont été identifiées dans le cas de l'usinage à sec.

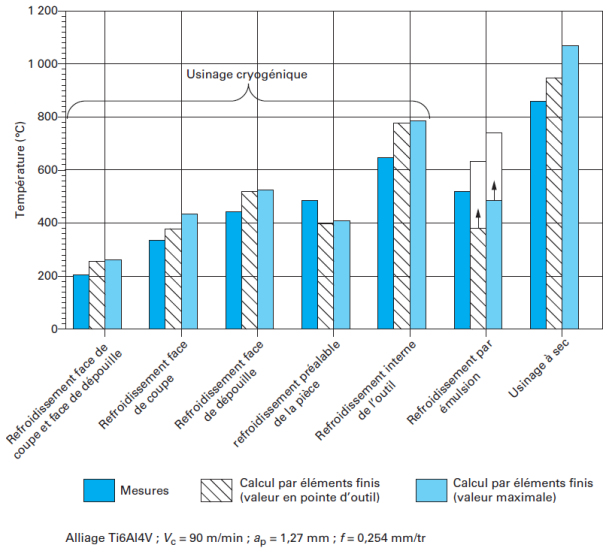

FIGURE 3 – L'évolution des températures de coupe pour différentes approches de refroidissement (Hong et al., 2001a)

.

Il est à noter que la manière de refroidir en utilisant l'azote liquide influe, elle aussi, sur les températures générées dans la zone de coupe. La méthode la plus efficace est de refroidir les deux faces de l'outil de coupe (la face de dépouille et la face de coupe) permettant de diminuer les températures de coupe jusqu'à 500°C pour une vitesse de coupe égale à 150 m/min (Figure 4).

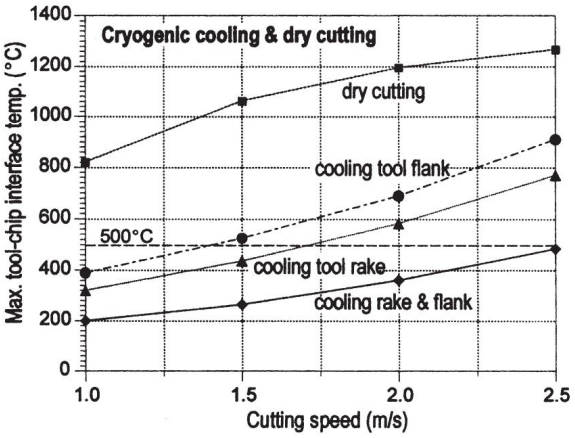

FIGURE 4 – Températures maximales de l'interface outil-pièce (prédites par FEM) en fonction de la vitesse de coupe pour différentes approches de refroidissement (Hong et al., 2001a)

.

2.2 Effet de l'usinage cryogénique sur les efforts de coupe

Hong et al. ont largement investigué l'effet de l'assitance cryogénique sur l'usinabilité de l'alliage TA6V menant plusieurs études (Hong and Yucheng, 2001; Hong et al., 2001b,a). Ces travaux ont montré que le refroidissement cryogénique lors de l'usinage (opération de tournage) du TA6V induit à l'élévation des efforts de coupe. En effet, l'utilisation de l'azote liquide (-196°C) conduit à réduire considérablement les températures de coupe. Ce qui rend le matériau de la pièce à usiner plus dur au niveau de la surface (Figure 5) générant des efforts de coupe plus élevés. Effectivement, toutes les composantes des efforts de coupe sont plus élevées dans le cas de l'assistance cryogénique en comparaison avec le cas de l'usinage à sec (Figure 5).

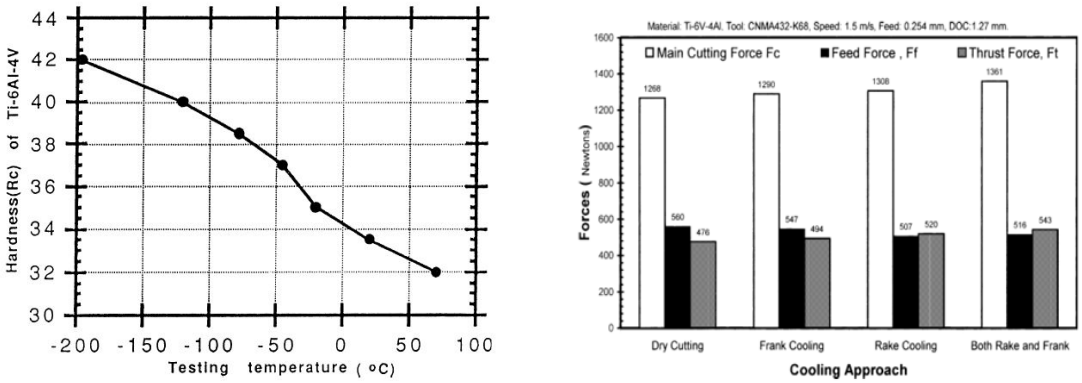

(a) (b)

FIGURE 5 – a) La dureté de l'alliage TA6V en fonction de la température (Hong et al., 2001a), b) Evolution des efforts de coupe pour différentes stratégies de refroidissement (TA6V) (Hong et al., 2001a).

Pusavec et al. (2014)ont mené une étude concernant l'influence des différentes stratégies de refroidissement sur l'usinabilité de l'Inconel 718 dont la démarche est basée essentiellement sur la variation des paramètres de coupe (a_p, f et V_c). Ils ont prouvé que l'assistance cryogénique génèrent des efforts de coupe moins élevés pour de faibles

valeurs de l'avance et de la profondeur de coupe. En revanche, quand a_p >1 mm et f >0.1 mm/tr, l'effort de coupe a tendance à avoir des valeurs plus élevées par rapport aux autres méthodes de refroidissement vu que l'usinage cryogénique augmente la dureté du matériau de la pièce à usiner (Figure 6).

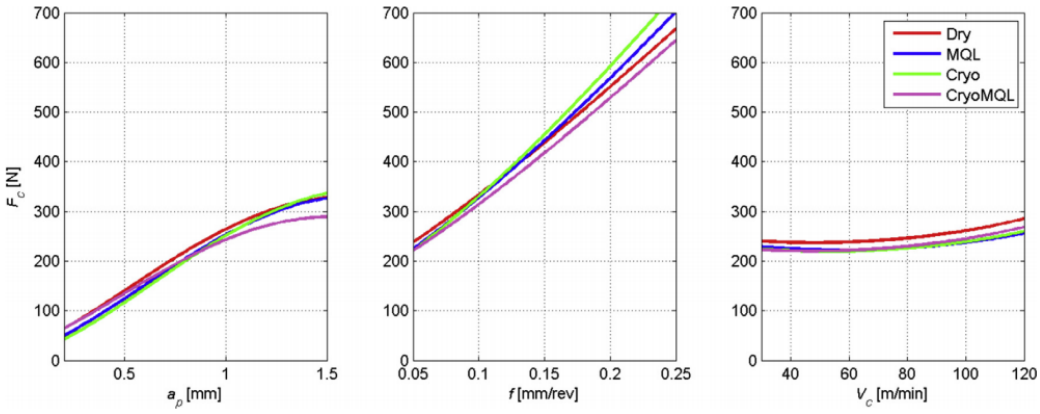

FIGURE 6 – Evolution des efforts de coupe en fonction des paramètres de coupe (a_p, f et V_c) pour différentes stratégies de refroidissement (Inconel 718) (Pusavec et al., 2014)

.

2.3 Effet de l'usinage cryogénique sur le coefficient de frottement

Hong et al. (2001b) ont testé l'effet de l'assistance cryogénique sur le coefficient de frottement lors de l'usinage du TA6V. En effet, pour évaluer le coefficient de frottement au niveau de la zone de contact outil-copeau (cf. equation 1), les efforts (N : Normal et F : Tangentiel), au niveau de la face de coupe de l'outil sont calculés à partir des efforts de coupe (F_c, F_f *et* F_p) mesurés à l'aide d'un dynamomètre (cf. equation 2).

$$\mu = \frac{F}{N} \tag{1}$$

$$\begin{aligned} N = Pe_n \,;\; F = Pe_f \\ P = \{-F_f,\, F_c,\, F_p\} \end{aligned} \tag{2}$$

Avec
e_n : c'est le vecteur unitaire normal à la face de coupe de l'outil
e_f : c'est le vecteur unitaire dans la direction de l'écoulement du copeau

Ils ont prouvé que le coefficient de frottement présente la plus faible valeur dans le cas du refroidissement cryogénique indépendamment de la méthode utilisée pour refroidir (face de dépouille de l'outil, face de coupe de l'outil ou les deux faces simultanément) en comparaison avec le cas de l'usinage à sec qui favorise une forte adhésion entre la face de coupe de l'outil et le copeau (μ=0.57). Ce qui permet de conclure que LN_2 joue un double rôle au cours de l'usinage : le *côté* refroidissement en contribuant à chuter les températures de coupe ainsi que le *côté* lubrifiant en servant à diminuer significativement le coefficient de frottement (μ=0.23).

Hong et al. (2001b) ont expliqué cette amélioration par le fait que les températures cryogéniques peuvent réduire l'affinité chimique du matériau étudié et notamment la création d'une mousse formée par l'évaporation de l'azote au niveau de l'interface outil-pièce jouant le rôle d'un lubrifiant.

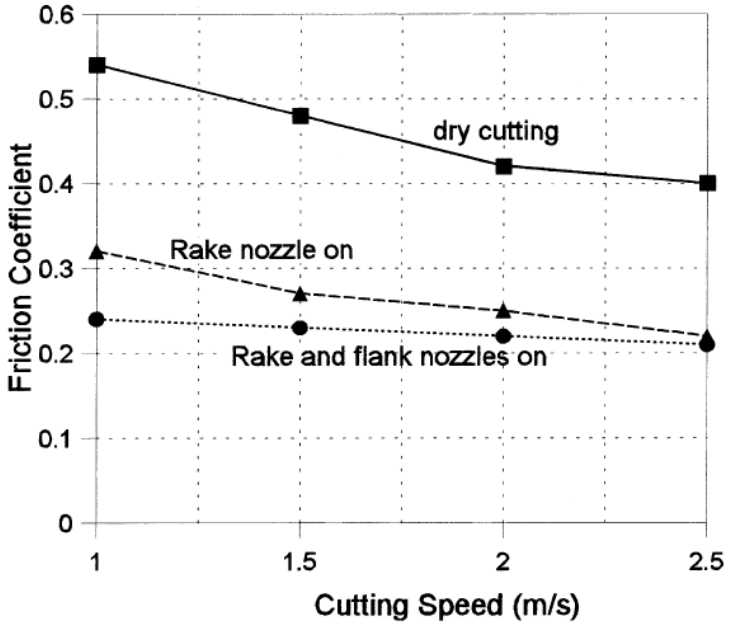

FIGURE 7 – Evolution du coefficient de frottement au niveau de l'interface outil-copeau en fonction de la vitesse de coupe (TA6V) Hong et al. (2001b).

Ultérieurement, Courbon et al. (2013) ont investigué l'efficacité du fluide cryogénique (LN_2) en termes de refroidissement et lubrification par rapport à l'usinage de l'Inconel 718 et TA6V. Pour ce faire, Courbon et al. (2013) a étudié le comportement tribologique d'une plaquette en carbure en contact avec les deux matériaux précédents. Ils ont utilisé un tribomètre ouvert équipé d'un outil en carbure revêtu TiN frottant d'un *côté* sur un lingot d'Inconel 718 et de l'autre *côté* sur un lingot de TA6V. Suite aux tests effectués pour mesurer le coefficient de frottement, ils ont constaté, contrairement à Hong et al. (2001b) dans le cas du TA6V, le coefficient de frottement ne change pratiquement pas. Cependant, une bonne amélioration a été détecté dans le cas de l'Inconel 718. En d'autres termes, le coefficient de frottement décroit dans les conditions cryogéniques. Ceci pourrait être expliqué par le fait que le comportement tribo-chimique des deux matériaux est différent, entre autre, le titane présente une affinité tribo-chimique plus élevée avec l'azote que l'Inconel 718 (Courbon et al., 2013) (Figure 8 et Figure 9).

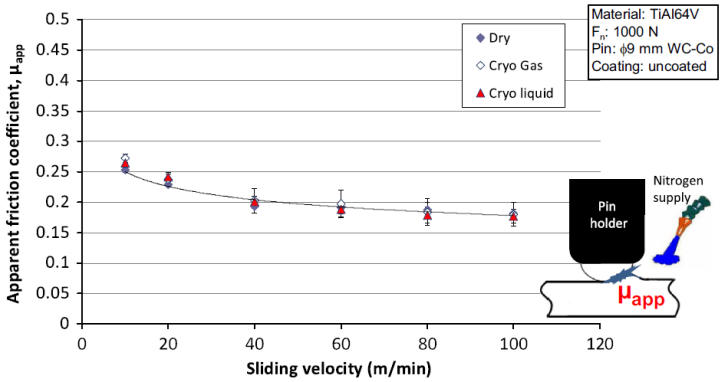

FIGURE 8 – Evolution du coefficient de frottement au niveau de l'interface outil-copeau en fonction de la vitesse de glissement (TA6V) (Courbon et al., 2013).

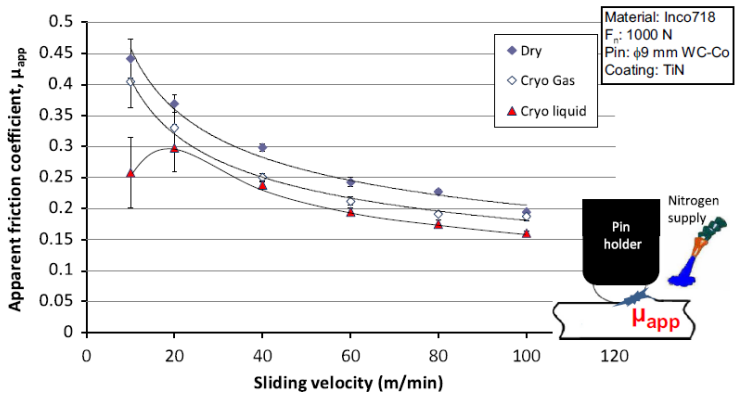

FIGURE 9 – Evolution du coefficient de frottement au niveau de l'interface outil-copeau en fonction de la vitesse de glissement (Inconel 718) (Courbon et al., 2013).

2.4 Effet de l'usinage cryogénique sur l'usure de l'outil

En usinage, les interactions entre le matériau usinant et la matière usinée génèrent des phénomènes physiques très complexes. En effet, ce procédé de fabrication est un processus thermomécanique fortement couplé dans lequel la chaleur, les phénomènes de frottement et les déformations plastiques, jouent un rôle crucial en terme d'usure (List, 2004). Dans cette section, on s'intéresse à investiguer l'influence de l'assistance cryogénique par rapport à l'usure des plaquettes en usinage du TA6V et de l'Inconel 718 respectivement.
Dans ce cadre, Dhananchezian and Kumar (2011) ont reporté l'effet du refroidissement cryogénique sur l'usure de la plaquette, en particulier l'usure en dépouille. Suite aux essais réalisés lors de l'usinage du TA6V, ils ont révélé que l'évolution de l'usure en dépouille, après 5 min d'usinage, est moins importante dans les conditions cryogéniques (Figure 10).

A titre d'exemple, pour une vitesse de coupe $V_c = 63$ m/min et une avance f =0.159 mm/tr, l'usure en dépouille est égale à 536 μm and 370 μm dans le cas de refroidissement conventionnel et cryogénique respectivement. En fait, une diminution de l'usure en dépouille a été relevée avec un gain de 31% dans le cas cryogénique par comparaison avec la lubrification conventionnelle. Ceci revient au fait que le jet d'azote contribue à baisser la température de coupe et par la suite contrôler relativement les mécanismes d'usure (Figure 11).

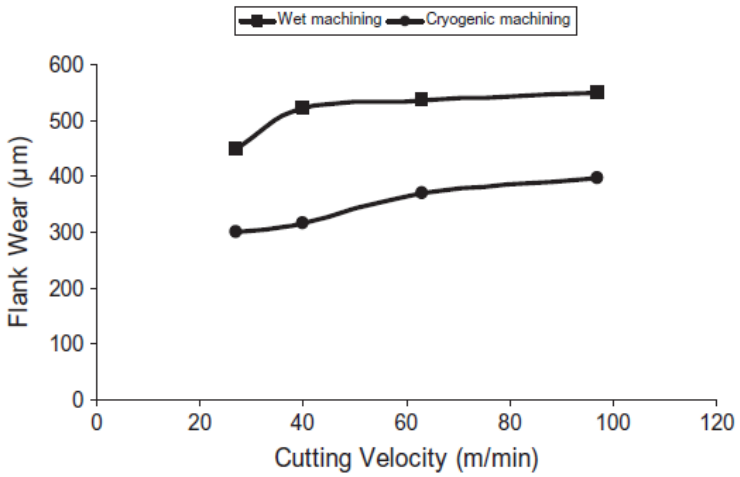

FIGURE 10 – Comparaison de l'usure en dépouille de l'outil lors de l'usinage du TA6V pour différentes approches de refroidissement (Dhananchezian and Kumar, 2011).

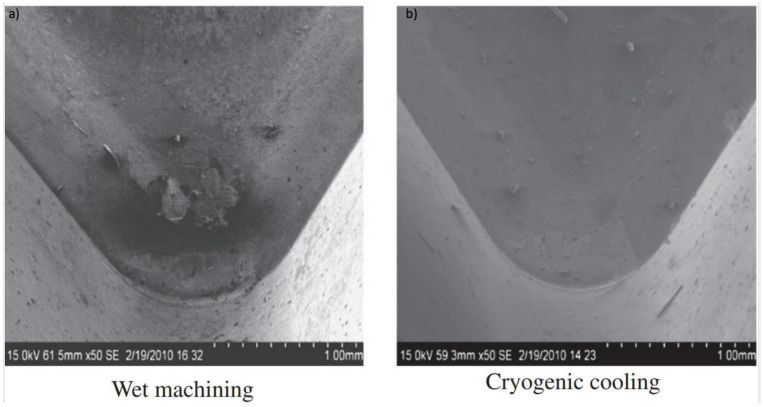

FIGURE 11 – Illustration des outils usés observés sous le MEB après 5 min d'usinage à $V_c = 27m/min$: a) refroidissement conventionnel b) refroidissement cryogénique (Hong et al., 2001a).

Hong et al. (2001a) ont constaté un effet identique par rapport à l'impact du fluide cryogénique sur la durée de vie de la plaquette lors de l'usinage du TA6V. Effectivement, les résultats obtenus pendant les essais réalisés prouvent une amélioration notable en termes de durée de vie d'outil dans le cas de l'usinage avec assistance cryogénique du TA6V. Ils ont aussi déterminé l'ordre de l'efficacité de la méthode de refroidissement (du plus faible au meilleur) comme suit : à sec, refroidissement conventionnel, refroidissement cryogénique de la face de dépouille de l'outil, refroidissement cryogénique de la face de coupe de l'outil et le refroidissement cryogénique des deux faces de l'outil simultanément (Figure 12).

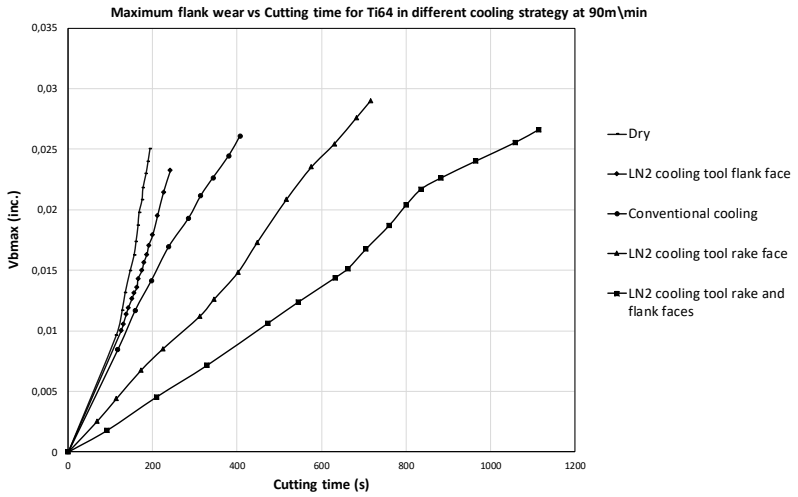

FIGURE 12 – Comparaison de la durée de vie de l'outil lors de l'usinage du TA6V pour différentes approches de refroidissement (Hong et al., 2001a).

Ultérieurement, Kaynak (2014) a investigué les performances de l'usinage avec assistance cryogénique de l'Inconel 718 en menant une comparaison avec l'usinage à sec et MQL. En effet, au cours des essais réalisés, il a opté deux buses pour injecter l'azote liquide au niveau de la face de coupe et la face de dépouille de l'outil . Les résultats obtenus indiquent un bon accord avec les résultats cités précédemment par rapport à la diminution de l'usure en dépouille de l'outil en comparant les autres modes d'usinage (à sec et MQL)(Figure 13). En fait, la plus grande mesure a été identifiée dans le cas de l'usinage à sec. Cependant, l'approche MQL a fourni des valeurs légèrement proche de celles obtenues en usinage cryogénique jusqu'au 150 s. Et puis, l'usure en dépouille croit rapidement pour montrer la même tendance que la courbe obtenue à sec.

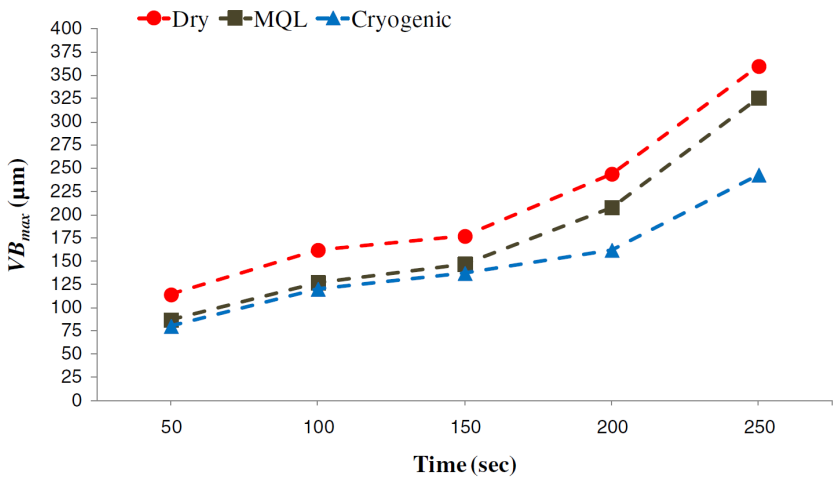

FIGURE 13 – Évolution de l'usure en dépouille lors de l'usinage de l'Inconel 718 : à sec, MQL et cryogénique (Kaynak, 2014).

Bien que l'usure en dépouille est un paramètre fondamental permettant de déterminer la durée de vie de l'outil coupant et affectant l'intégrité de surface de la pièce usinée, le facteur crucial générant la défaillance de la plaquette dans le cas de l'usi-

nage de l'Inconel 718 en assistance cryogénique est l'usure en entaille (Kaynak, 2014; Musfirah et al., 2017). En effet, sous les conditions cryogéniques, on constate un effet inverse après 100s en usinage. En d'autres termes, pendant un temps d'usinage très court (inférieur à 100s), la courbe de l'usure en entaille présente la pente la plus faible par comparaison avec celles de l'usinage à sec et en MQL. Toutefois, l'évolution de cette courbe montre une augmentation très rapide après 100s (Figure 14). Ce qui induit à la fin de la durée de vie de l'outil.

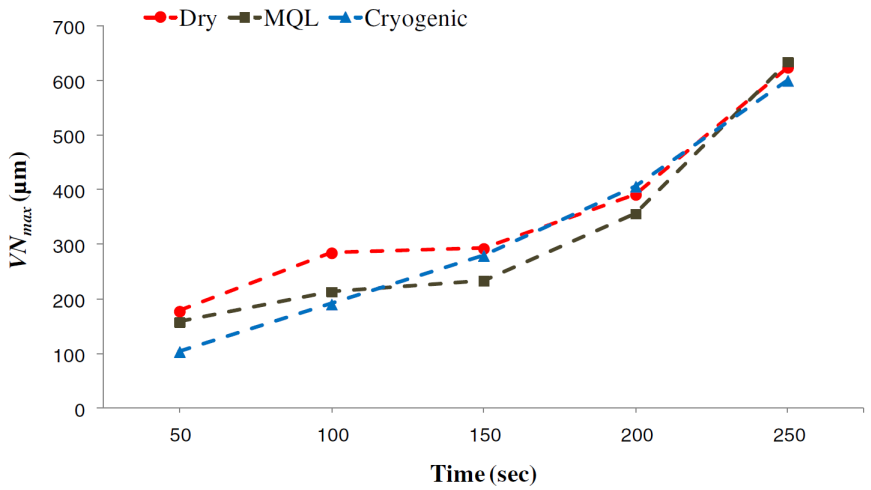

FIGURE 14 – Évolution de l'usure en entaille lors de l'usinage de l'Inconel 718 : à sec, MQL et cryogénique (Kaynak, 2014).

Selon Musfirah et al. (2017), l'évolution de l'entaille au niveau de la face de dépouille de l'outil revient essentiellement aux mécanismes d'abrasion et d'adhésion qui dégradent fortement la résistance de l'outil. En plus, la coupe interrompue engendrent des chocs thermiques et mécaniques pouvant favoriser l'évolution de l'entaille.

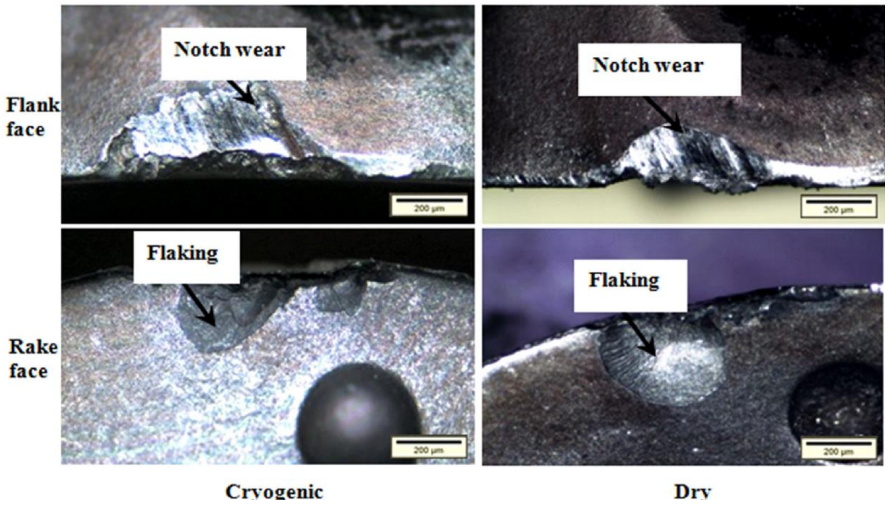

FIGURE 15 – Illustration d'une comparaison de l'usure de l'outil dans deux conditions : à sec et cryogénique Musfirah et al. (2017).

Par la suite, Iturbe et al. (2016) a mené des recherches approfondies dans le but d'estimer dans quels mesures la lubrification classique pourrait être remplacée par le fluide cryogénique. Pour ce faire, elle a repris la même configuration exploitée par

(Kaynak, 2014) (les paramètres de coupe, la géométrie de l'outil). En effet, les essais ont été réalisés sous deux conditions à savoir usinage conventionnel et usinage associant MQL et la cryogénie. En conséquence, les constations révèlent que la durée de vie de l'outil présente un écart significatif entre les conditions de lubrification classique et les conditions cryogéniques. Dans le cas de l'usinage classique, la durée de vie de l'outil dépassent les 20 min et montre une évolution homogène. Cependant, l'autre cas (MQL+cryogénie), l'évolution de l'usure de l'outil se produit rapidement et le critère standard de la durée de vie de l'outil est atteint pour des temps moins longs (moins de 7 min)(Figure 16). Certains auteurs expliquent cette différence de performance par le fait que le matériau usiné l'Inconel 718 a tendance à s'écrouir excessivement sous l'effet des températures cryogéniques. Ce qui génère la dégradation de l'outil et par conséquent la réduction de sa durée de vie.

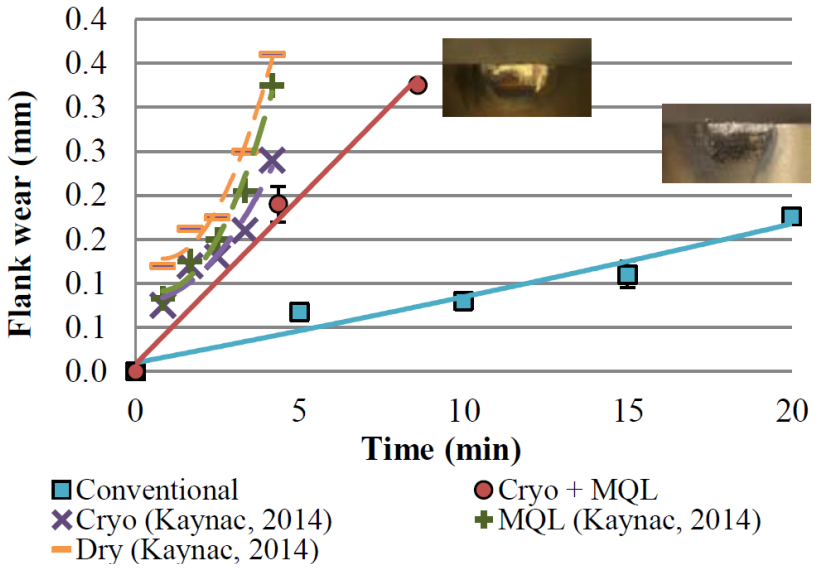

FIGURE 16 – Évolution de l'usure en dépouille lors de l'usinage de l'Inconel 718 en : cryogénique (Kaynak, 2014), MQL (Kaynak, 2014), cryogénique + MQL et conventionnel (Iturbe et al., 2016).

2.5 Intégrité de surface

En usinage, l'intégrité de surface est un paramètre très important puisqu'elle affecte la tenue en service des pièces soumises à des chargements mécaniques et thermiques pendant leur emploi. A titre d'exemple, dans le secteur aéronautique, les différents composants de l'avion sont sévèrement sollicitées (températures très élevées, chargements mécaniques importants et environnement hostile). En effet, plusieurs analyses de rupture des pièces dynamiques démontrent que ces dernières cassent par fatigue, fluage et corrosion à cause des fissurations qui s'initient et se propagent à partir de la surface. La raison pour laquelle, il faut accorder une grande attention à l'intégrité de surface des pièces usinées. Dans ce qui suit, on abordera l'effet de l'usinage avec assistance cryogénique sur l'intégrité de surface des composants fabriqués.

2.5.1 État de surface - La rugosité R_a

La rugosité R_a est un paramètre majeur permettant de caractériser l'état de surface de la pièce usinée. Il s'avère très intéressant de quantifier cette variable. Dans ce contexte, Rotella et al. (2014) ont étudié l'effet des différentes stratégies de refroidissement lors de l'usinage du TA6V. Ils ont constaté que les valeurs mesurées dans le cas de l'usinage avec assistance cryogénique sont les plus faibles quelques soient les vitesses de coupe et les avances testées au cours des essais (Figure 17). Ces résultats sont conformes avec ceux trouvés par (Bordin et al., 2015) qui ont mené une étude expérimentale pour tester la faisabilité de l'usinage cryogénique par rapport à l'usinage à sec de l'alliage de titane TA6V.

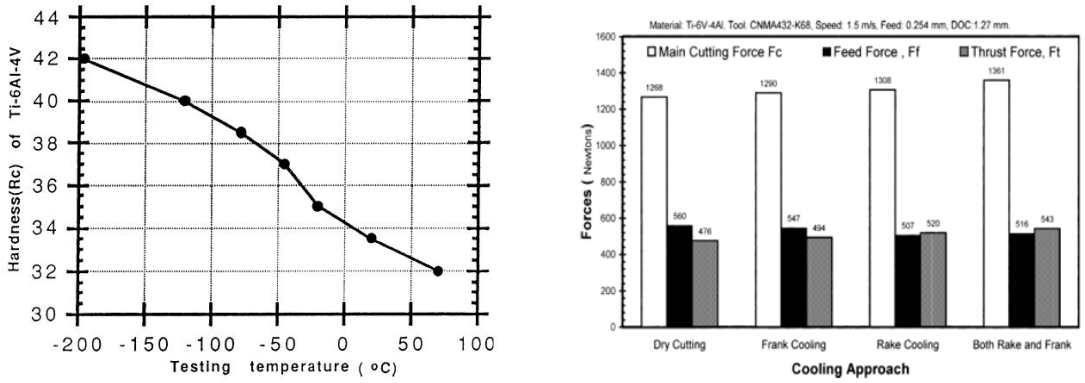

(a) (b)

FIGURE 17 – a) Illustration de l'effet des différentes stratégies de refroidissement sur la rugosité moyenne Ra après 8 min d'usinage en tournage du TA6V Rotella et al. (2014), b) Illustration de l'effet des différentes stratégies de refroidissement sur la rugosité moyenne Ra du TA6V Bordin et al. (2015)..

Cependant, Iturbe et al. (2016) ont constaté l'effet contraire quant à l'usinage de l'Inconel 718 dans le cas de Cryo et MQL combinées. En effet, les rugosités mesurées (R_a *et* R_t) présentent des valeurs moins importantes dans le cas de l'usinage en lubrification classique pour des temps de coupe plus élevés (20 min). En effet, cette conséquence est étroitement liée à l'usure de l'outil relevée au cours de l'opération de coupe qui affecte significativement l'état de surface de la pièce usinée (Figure 18).

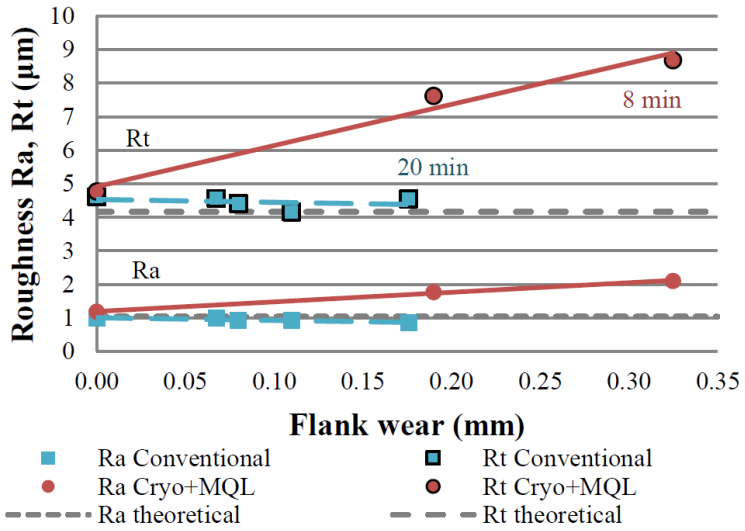

FIGURE 18 – Illustration de l'évolution de la rugosité en fonction de l'usure en dépouille de l'outil lors de l'usinage en tournage de l'Inconel 718 en conventionnel et Cryo+MQL (Iturbe et al., 2016).

2.5.2 Les contraintes résiduelles

Les contraintes résiduelles jouent un rôle crucial par rapport à la tenue des pièces usinées en service. En fait, chaque composant est soumis à des sollicitations mécanique et/ou thermique pendant son utilisation. Il est donc urgent d'atténuer au maximum les contraintes résiduelles lors du procédé de fabrication afin d'éviter les ruptures anticipées des composants voire obtenir des contraintes résiduelles en compression.
Plusieurs travaux ont reporté l'effet des procédés d'usinage sur l'intégrité de surface des pièces coupées, en particulier les contraintes résiduelles. Ayed et al. (2017) ont divulgué l'impact des conditions d'usinage, notamment en assistance cryogénique de l'alliage de titane TA6V. Il a révélé que les contraintes résiduelles sont extrêmement influencées par les méthodes de refroidissement en usinage. Le résultat le plus performant est obtenu dans le cas du refroidissement avec le fluide cryogénique. Ceci peut être justifié par le fait que refroidir à des températures cryogéniques induit à décroitre significativement les températures dans la zone de coupe. Par la suite, diminuer la tendance à générer des chargements thermiques engendrant des contraintes résiduelles en traction. D'ailleurs, puisque l'usinage cryogénique produit des efforts de coupe importants, donc des chargements mécaniques en plus. Par conséquent, les contraintes résiduelles résultantes de cette évolution de chargement mécanique et thermique sont en compression (Figure 19).

Pusavec et al. (2011) ont investigué largement l'usinage avec assistance cryogénique de l'Inconel 718 en termes de l'efficacité de cette technique par rapport à la durée de vie des outils coupants et l'intégrité de surface des composants coupés. En effet, dans un travail antérieur, Pusavec et al. (2010) ont déterminé une configuration optimale entre autres, les paramètres de coupe ($V_c = 60m/min$, $f = 0.05mm/tr$ et $a_p = 0.63mm$) permettant de relever des efforts de coupe, et des températures de coupe et des durées de vie des outils optimaux.
En ce qui concerne les contraintes résiduelles, les profils mesurées en surface et en sous-surface de la pièce usinée prouvent qu'en surface les contraintes résiduelles sont en traction jusqu'à une profondeur proche de 12 μm et deviennent relativement compres-

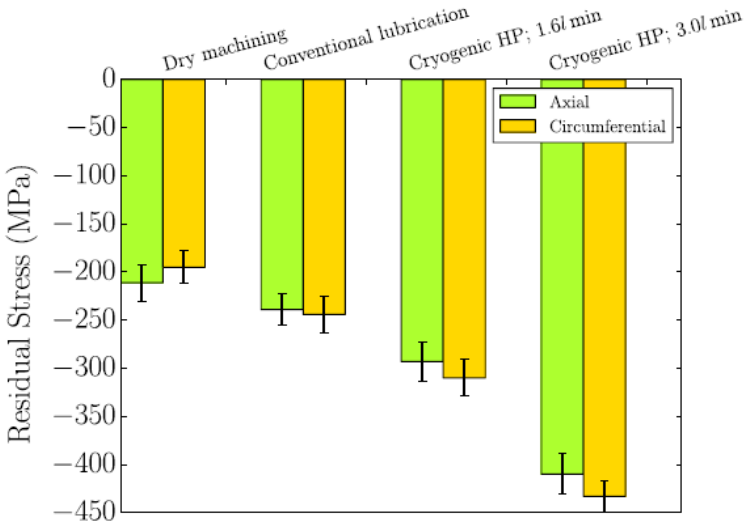

FIGURE 19 – Illustration de l'effet des différentes stratégies de refroidissement sur les contraintes résiduelles lors de l'usinage en tournage du TA6V (Ayed et al., 2017).

sives jusqu'au le cœur du matériau (Figure 20). D'ailleurs, les valeurs les plus optimales sont obtenues dans le cas de l'usinage cryogénique. La même explication énoncé précédemment a été annoncé pour justifier ces résultats.

2.5.3 Couche fortement écrouite

Lors du procédé d'usinage, le matériau usinée est soumis à des chargements à la fois mécanique et thermique. De ce fait, plusieurs altérations au niveau de la surface usinée et la sous-surface peuvent avoir lieu (Rotella et al., 2014; Pusavec et al., 2011; Touazine et al., 2017). Ces effets consiste à des changements microstructuraux (recristallisation), des grains distordus, une déformation plastique sévère, écrouissage induisant un durcissement localisé, des réactions chimiques (oxydation) (Figure 21). Ces changements sont étroitement liés aux paramètres de coupe, les conditions de refroidissement et le matériau à usiner. Dans le cas de l'Inconel 718, sous les conditions cryogéniques, la surface usinée est fortement écrouie générant une augmentation notable de sa dureté par rapport à celle du matériau d'origine (de 500 à 700 HV).

Il est à noter que lors de l'usinage de l'Inconel 718, d'autres aspects peuvent se déclencher en plus de la couche fortement déformée. En effet, plusieurs chercheurs ont reporté qu'une déformation plastique a lieu dans des zones plus profondes que la couche affectée notamment près des carbures ou encore au niveau des joints de macles (Figure 22). Telles localisations ont tendance à accumuler la déformation pour donner naissance à des fissures potentielles par fatigue (Touazine et al., 2017).

D'autres auteurs ont associé l'initiation et la propagation des fissures à l'oxydation des carbures (Dosbaeva et al., 2010). En effet, l'oxydation des carbures de niobium NbC s'initie à partir de sa surface externe, se propage jusqu'à sa surface intérieure causant une rupture. Toutefois, dans le cas du carbure de titane TiC, l'oxydation et la rupture se produisent uniquement au niveau de sa surface externe et ne se propage pas au cours de l'usinage (Figure 23).

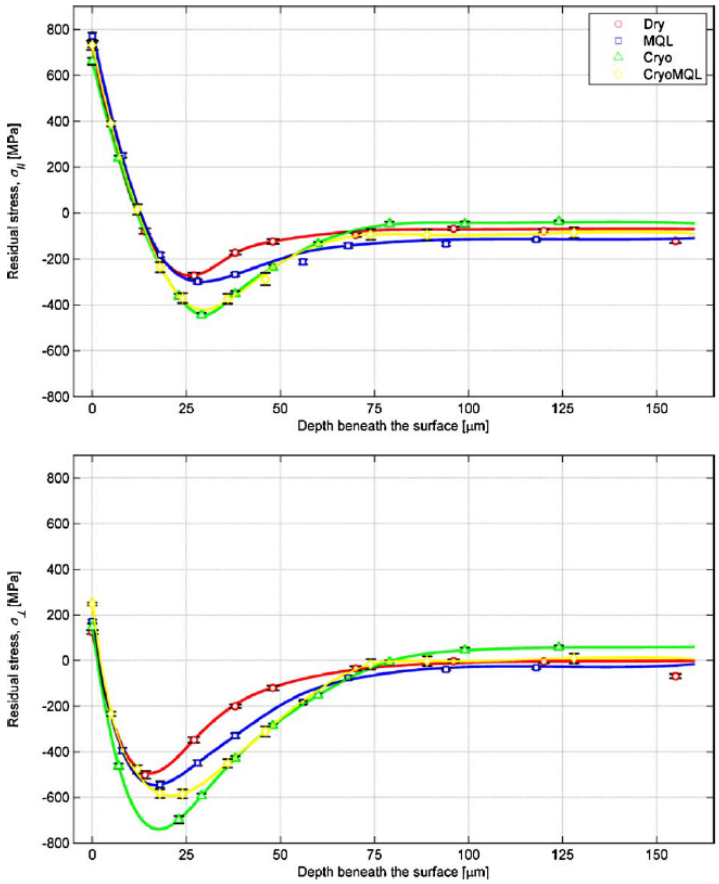

FIGURE 20 – Illustration des contraintes résiduelles en surface et en profondeur de surface usinée lors de l'usinage en tournage de l'Inconel 718 sous plusieurs stratégies de refroidissement ($V_c = 60m/min$, $f = 0.05mm/tr$ et $a_p = 0.63mm$) (Pusavec et al., 2011).

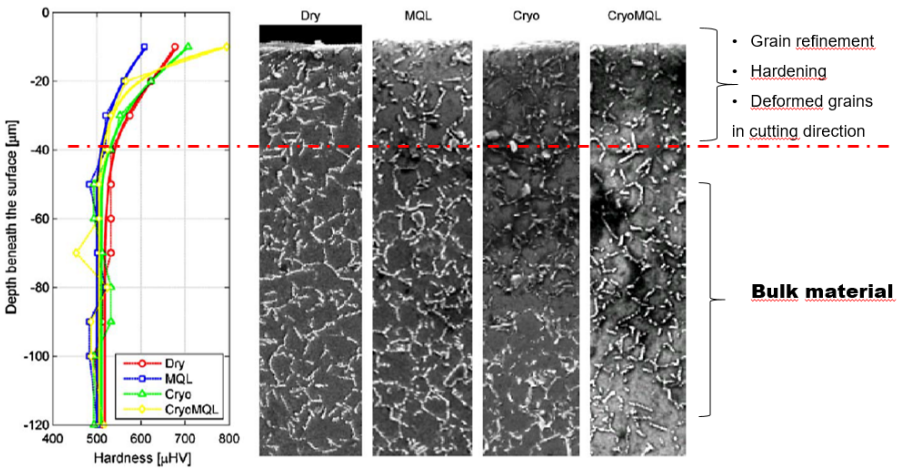

FIGURE 21 – Illustration du profil de la dureté mesurée le long de la profondeur de la sous-surface, et corrélation avec les changements métallographiques en dessous de la surface usinée pour différentes conditions de lubrification (Pusavec et al., 2011).

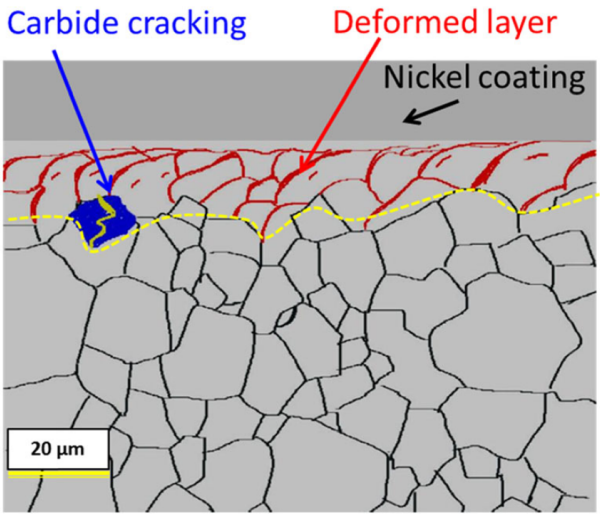

FIGURE 22 – Illustration d'une fracture déclenchée à partir d'un carbure pour l'Inconel 718 (Touazine et al., 2017).

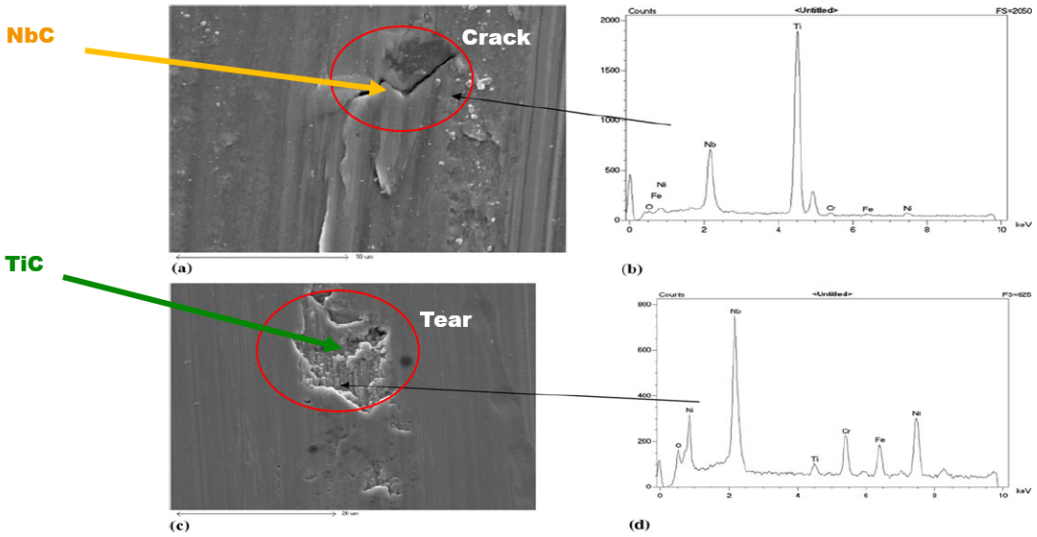

FIGURE 23 – MEB-EDS au niveau de la surface usinée illustrant la morphologie et les défauts formés pour l'Inconel 718 : (a,b) fissurations et (c,d) déchirure. (Dosbaeva et al., 2010).

2.6 Conclusion

Dans cette partie, un résumé de l'état d'art a été développé concernant l'influence de l'usinage cryogénique sur les performances des matériaux au cours de la coupe. Un résultat très intéressant a été identifié qui consiste à montrer un gain notable quant à l'usinage avec assistance cryogénique de l'alliage de titane TA6V. Par contre, l'alliage à base de nickel Inconel 718 génère des problèmes multiples au niveau de la durée de vie de l'outil coupant et l'intégrité de surface du composant usiné.

3 Essais de caractérisation

3.1 Procédure expérimentale

Afin d'étudier le comportement mécanique de l'Inconel 718 ainsi que les changements au niveau de la microstructure déformée, des essais de compression uniaxiale ont été menés sur un large intervalle de température allant de -188°C jusqu'à 900°C, variant la vitesse de 10^{-2} s^{-1} jusqu'à 10 s^{-1}. Le système expérimental utilisé lors des essais est le simulateur thermomécanique Gleeble 3500. La capacité de chargement de cette machine est de 100 kN. Le processus de chauffage est induit suivant l'e et Joule par le chauffage par résistance réalisant une vitesse de chauffe jusqu'à 10 000 C/s. Grâce à la méthode de chauffage, le simulateur permet d'effectuer des cycles thermiques beaucoup plus rapides (5 à 10 fois) que la machine conventionnelle utilisant des fours traditionnels.

Pendant les essais de compression, les éprouvettes ont été placées entre deux enclumes en carbure de tungstènes pour assurer le transfert du courant électrique ainsi que pour préserver une uniformité de température dans l'éprouvette lors de la réalisation de l'essai de compression. Des feuilles de graphite ont été placées entre les enclumes et l'échantillon pour éviter les frottements aux interfaces correspondantes (enclume-éprouvette-enclume).

A haute température, afin d'éviter l'oxydation, les expériences ont été réalisées sur une chambre à vide primaire. De plus, pour les observations métallographiques, la microstructure a été trempée après essai grâce à un système de refroidissement (par un jet d'air comprimé) permettant d'atteindre des vitesses de refroidissement supérieures à 230°C/s. Des thermocouples de type K ont été utilisés pour mesurer la température pendant les tests. Les thermocouples ont été soudés en position centrée sur la surface de l'éprouvette. La charge thermique appliquée consiste à chauffer l'éprouvette à une vitesse de chauffe constante de 10°C/s jusqu'à la température d'essai. Par la suite, la température est maintenue constante pendant 20 s pour homogénéiser la température le long de l'échantillon sans dessouder les thermocouples. L'éprouvette est immédiatement déformée à une vitesse de déformation constante. Une fois l'essai terminé, le chauffage est arrêté et l'échantillon est trempé instantanément sous vide afin d'éviter tout changement de microstructure. Il est à noter que pour éviter la transformation microstructurale au cours du chargement thermique, on s'intéresse à se reporter au schéma TTT et à identifier le temps de maintien du chauffage des éprouvettes comme indiqué dans la figure ci-contre :

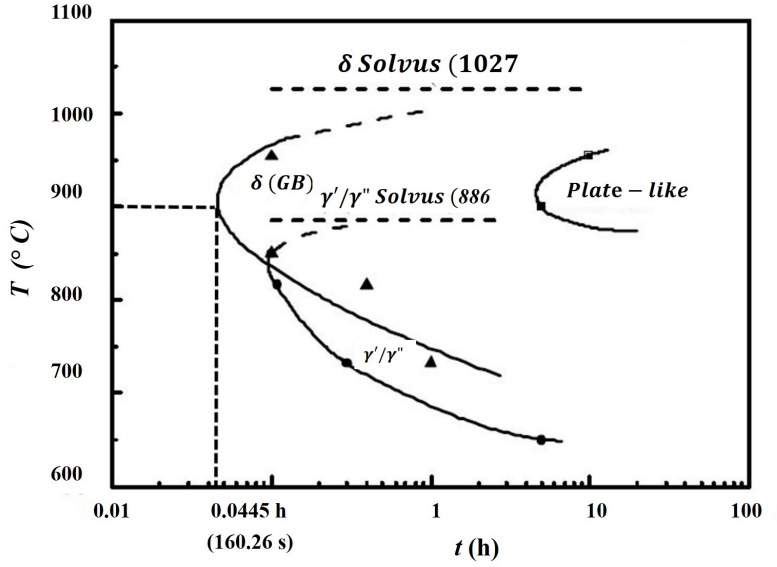

FIGURE 24 – Illustration du TTT-diagramme de l'Inconel 718 (Xie et al., 2005).

Quant à la condition thermique cryogénique, il était pertinent de maintenir le refroidissement des échantillons durant 10 min avant essai afin d'assurer une température stable et homogène.
Dans cette étude, un système cryogénique a été développé au sein du laboratoire LAMPA afin de réaliser des essais de compression à température cryogénique. La tâche la plus difficile pendant la conception du système cryogénique est de maintenir la température cryogénique avant et pendant les essais de compression. L'installation cryogénique est essentiellement composée d'entonnoir d'où le fluide cryogénique (LN_2) est fourni pour être acheminé à travers un tuyau afin de tremper l'échantillon. Ce dernier est fixé dans un contenant positionné entre les deux enclumes lors de la trempe ainsi que les essais de compression. Il est intéressant de souligner que le contenant a été fabriqué à l'aide d'une imprimante 3D. Pour chaque essai cryogénique, un contenant a été produit.

3.2 Résultats et discussions

Les courbes contrainte-déformation du superalliage Inconel 718 obtenues sur une large gamme de températures de -188°C à 900°C et de vitesses de déformation allant de 0.01 s^{-1} to 10 s^{-1} ont été identifiées. D'après les résultats obtenus, l'Inconel 718 a présenté un comportement thermoplastique quel que soit la vitesse de déformation : à mesure que la température augmente, la contrainte diminue relativement. Évidemment, ce fait a permis de dégager une tendance typique de la dominance des effets de température. Ces effets sont classiquement justifiés par l'impact de l'augmentation de la mobilité des dislocations proportionnellement à l'augmentation de la température induisant une diminution de la contrainte.
De plus, lors de l'examen des courbes contrainte-déformation, il est remarquable que les pentes de la plupart des courbes sont positives indiquant que le phénomène d'écrouissage est plutôt dominant. Le phénomène d'écrouissage est étroitement lié à l'augmentation de la densité de dislocation. À un intervalle de basse température (de -188°C à 500°C), les pentes de la majorité des courbes de contrainte-déformation sont positives. Cependant, à niveau de température élevé (900°C), l'Inconel 718 a révélé un équilibre

entre l'écrouissage et l'adoucissement thermique. Ce phénomène pourrait être favorisé par la restauration dynamique (DRV). En effet, la compétition entre l'annihilation des dislocations (DRV) et la recristallisation dynamique (DRX) en plus de la multiplication des dislocations régit le comportement thermo-mécanique de l'Inconel 718 à cette plage de température.

Concernant le coefficient de sensibilité à la vitesse de déformation, "m" a présenté une valeur très faible à la plage de température de -188°C à 500°C (Figure. 25). Cependant, à haute température (900°C), ce paramètre a augmenté de façon remarquable pour confirmer que l'Inconel 718 présente un comportement visqueux à très haute température. En effet, la sensibilité à la vitesse de déformation est presque négligeable dans le domaine des basses températures jusqu'à 500°C. Néanmoins, quand la température est devenue plus élevée, l'influence de la vitesse de déformation est beaucoup plus importante. Des observations similaires ont été rapportées par des études antérieures confirmant que l'Inconel 718 est plus sensible à la vitesse de déformation quand la temperature dépasse à 700°C. En effet, la sensibilité à la vitesse de déformation est associée au mouvement de la dislocation (Cheng et al., 2013). Au fur et à mesure que la température augmente, la mobilité des dislocations augmente également. Cette affirmation confirme la valeur élevée de m à 900°C.

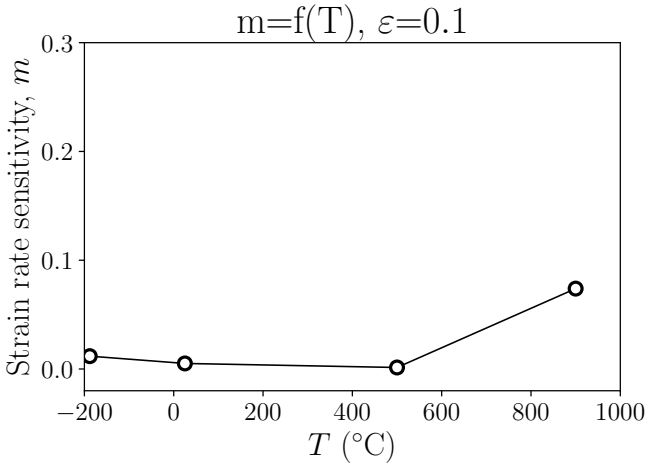

FIGURE 25 – Illustration du coefficient de sensibilité à la vitesse de déformation "m" calculé à un niveau de déformation égal à 0.1.

Quant au coefficient d'écrouissage, "n" a été évalué à un niveau de déformation de 0.1 à partir des courbes de contrainte-déformation. Les résultats ont montré que toutes les valeurs de ce paramètre, à toutes les vitesses de déformations et pour tous les domaines de température, ont révélé des valeurs positives confirmant la dominance de l'écrouissage lors des essais de compression comme mentionné précédemment (Figure. 26).

Afin de vérifier les résultats précédents concernant le coefficient d'écrouissage "n", des mesures de micro-dureté ont été réalisées selon la méthode Vickers avec un 200 gf de charge. Dans cette étude, l'objectif principal est d'examiner l'effet de la température cryogénique sur le comportement mécanique de l'Inconel ainsi que l'évolution de la microstructure suite aux tests de compression. Par conséquent, les mesures longitudinales et transversales ont été réalisées au centre des éprouvettes après déformation

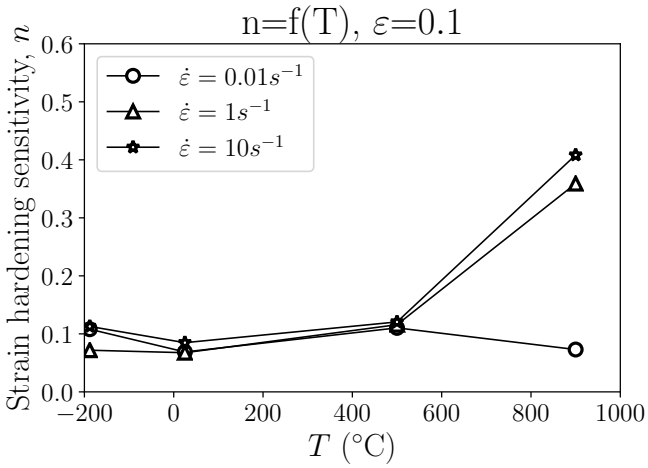

FIGURE 26 – Illustration du coefficient d'écrouissage "n".

du matériau d'étude à température ambiante ainsi qu'à température cryogénique sous chargement statique et chargement dynamique.
Les mesures dans les deux directions (longitudinale et transversale) ont présenté approximativement les mêmes valeurs. C'est pourquoi, pour chaque configuration, une moyenne des mesures était considérée. Les résultats sont présentés à Figure 27.

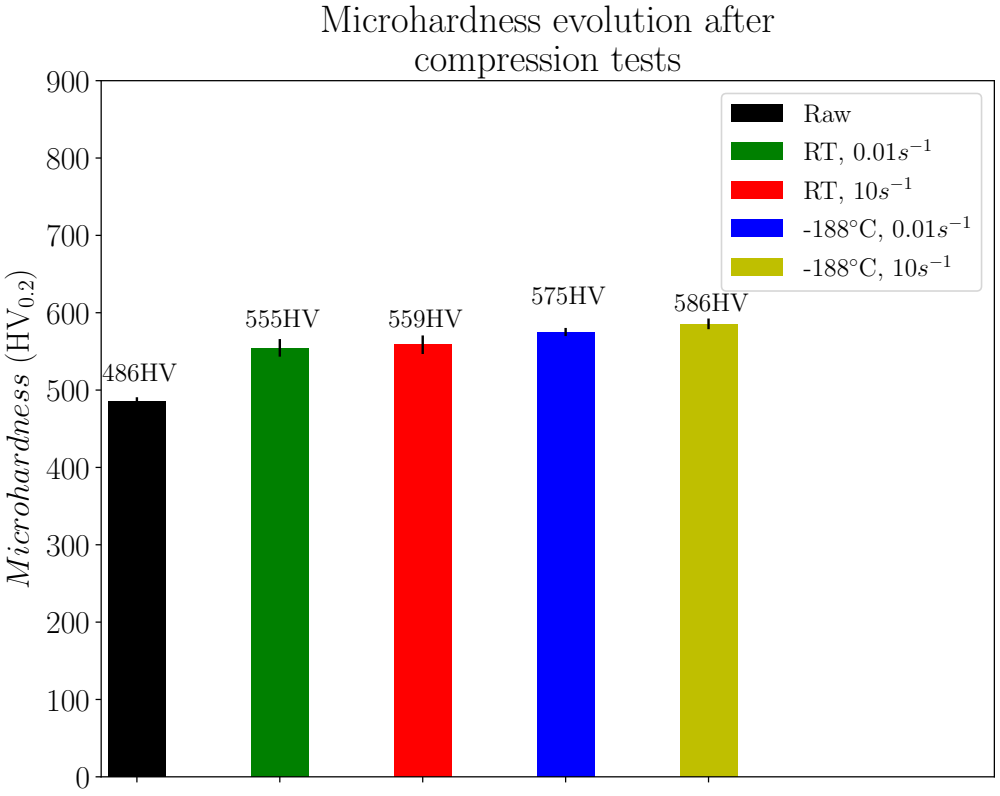

FIGURE 27 – Illustration des profiles de micro-dureté obtenus après déformation.

4 Essais de tournage avec assistance cryogénique

Selon la revue de la littérature, les études sur l'usinage cryogénique de l'Inconel 718 soulèvent un certain désaccord concernant l'amélioration de la durée de vie de l'outil. Par rapport à l'intégrité de surface (les contraintes résiduelles, la rugosité de surface), des lacunes ont été identifiées. De plus, jusqu'à présent, il n'y a pas de travail qui a étudié une comparaison entre les performances de l'usinage cryogénique en utilisant deux fluides cryogéniques (LN_2 et LCO_2) lors du tournage de l'Inconel 718 en termes de durée de vie de l'outil ainsi que l'intégrité de la surface de la pièce usinée.

4.1 Procédure expérimentale

Des essais de chariotage en finition ont été réalisés sur un lingot d'Inconel 718 en utilisant les mêmes paramètres de coupe et le même outil de coupe que (Iturbe et al., 2016). Dans cette étude, ces paramètres ont été fixés alors que le montage LN_2 a été modifié. Outre les fluides cryogéniques (LN_2 et LCO_2), le lubrifiant conventionnel a été utilisé comme référence afin d'évaluer les performances cryogéniques lors de l'usinage de l'Inconel 718. Des plaquettes en carbure de tungstène revêtues (DNMG 150612-MS US905) ont été exploitées dans les essais fournies par Mitsubishi (Mitsubishi, 2006).

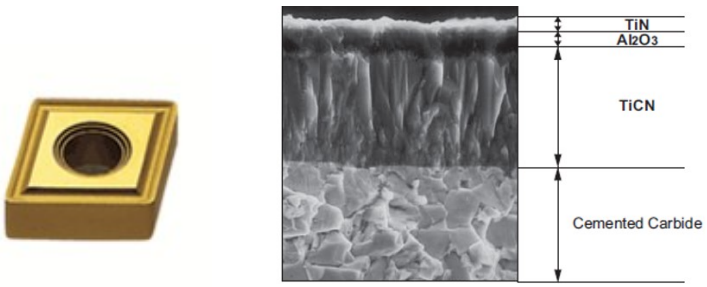

(a) (b)

FIGURE 28 – (a) La géométrie de la plaquette ; (b) Le revêtement de la plaquette (Mitsubishi, 2006).

Tableau 1 présente les conditions d'usinage.

TABLE 1 – Les conditions d'usinage

La pièce à usiner	Géométrie	un lopin cylindrique
	Matériau	Inconel 718
Les paramètres de coupe	La vitesse de coupe (m/min)	70
	L'avance (mm/tr)	0.2
	La profondeur de coupe (mm)	0.2
L'outil	L'angle de coupe (°)	9
	L'angle de dépouille (°)	6
	Le rayon du bec de l'outil (mm)	1.2
Les fluides de refroidissement	Conventionnel	Wet
	Cryogénique	LN_2
	Cryogénique	LCO_2

Les essais ont été effectués jusqu'à atteindre le temps de coupe cible de 15 min ou lorsque l'usure en dépouille maximale définie par $V_{BMAX} = 0.3$ mm a été obtenue.

4.2 Résultats et discussions

4.2.1 Essais d'usure

L'usure en dépouille de l'outil a été mesurée tout au long des opérations de tournage pour toutes les stratégies de refroidissement (conditions conventionnelles et cryogéniques). Les essais ont été arrêtés lorsqu'ils ont atteint 15 min d'usinage en lubrification classique même si le critère d'usure à savoir V_{BMAX}= 0.3 mm n'a pas été atteint. Concernant la condition LCO_2, les deux tests ont été arrêtés à 15 min alors que les niveaux d'usure des outils de coupe étaient notablement différents. Cependant, en condition cryogénique avec LN_2, les essais ont été arrêtés lorsque le critère de V_{BMAX} a été atteint. En se basant sur la Figure 29, les résultats ont indiqué que la condition conventionnelle a révélé la plus longue durée de vie de l'outil. En effet, l'usure de l'outil n'a pas dépassé 0.12 mm après 15 min de coupe en lubrification conventionnelle. Les

deux répétitions ont induit la même tendance pendant le processus de coupe montrant une bonne répétabilité.

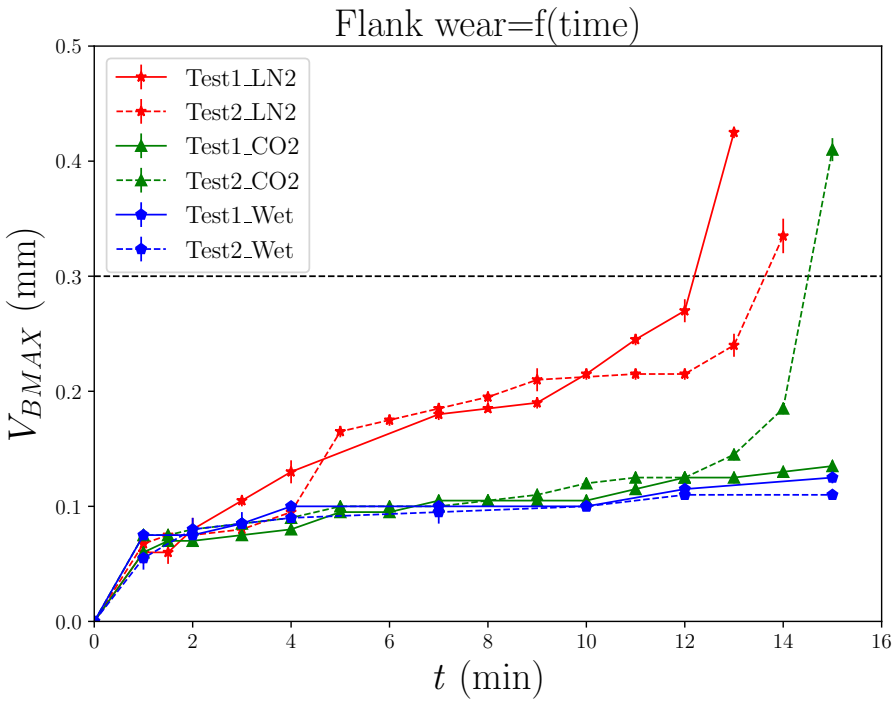

FIGURE 29 – Évolution de l'usure en dépouille de l'outil en conditions de refroidissement Wet, LN_2 et LCO_2 lors des essais d'usinage.

Quant à la stratégie de refroidissement LCO_2, une évolution similaire a été perçue jusqu'à 13 min du temps de coupe. Néanmoins, au-delà de cette durée, l'usure de l'outil a progressé pour dépasser drastiquement le critère à 15 min lors de la deuxième répétition de l'essai LCO_2. En ce qui concerne la condition cryogénique en utilisant LN_2, l'usure de l'outil a augmenté rapidement dès les premières 2 et 6 minutes d'usinage au cours du Test 1 et du Test 2 respectivement provoquant des durées de vie réduites. De plus, l'usure en dépouille de l'outil dans les deux conditions cryogéniques est approximativement similaire au début de l'usinage. Néanmoins, une importante variabilité a été observée à 11 min et 13 min respectivement en LN_2 et LCO_2 où l'usure en dépouille de l'outil a augmenté notablement. En lubrification conventionnelle, l'évolution de l'usure a été constatée comme homogène même après plus de temps d'usinage. En revanche, lors de l'usinage cryogénique avec LN_2, des pics d'usure se sont produits dès le début du procédé de tournage, indiquant que le processus de coupe n'est pas effectué de manière homogène alors que ce paramètre a montré une évolution régulière et lente au cours de la condition cryogénique LCO_2 sauf les dernières minutes d'usinage.

4.2.2 État de surface : La rugosité

L'état de surface est un paramètre crucial qui fournit de bonnes performances d'usinage de pièces usinées. La figure 30 illustre l'évolution de la rugosité de surface obtenue en conditions de lubrification conventionnelle et cryogéniques.

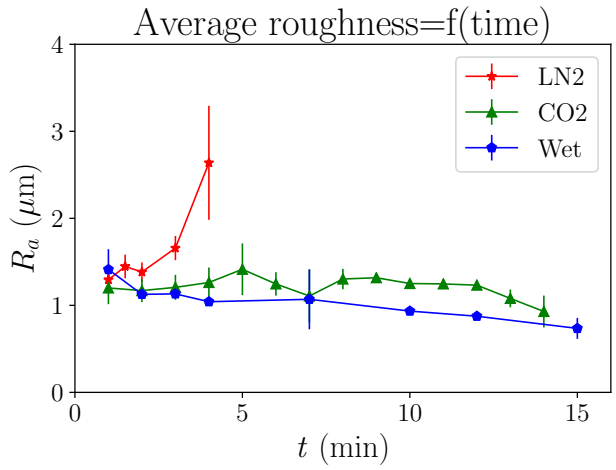

(a)

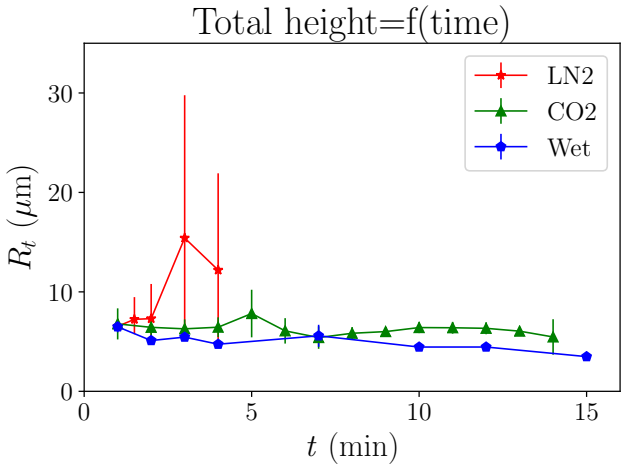

(b)

FIGURE 30 – L'évolution de la rugosité dans les trois conditions de refroidissement Wet, LN_2 and LCO_2 : (a) R_a ; (b) R_t.

Les résultats ont montré que la lubrification conventionnelle fournit les valeurs les plus faibles en termes de la rugosité moyenne R_a ainsi que la hauteur totale du profile R_t. Concernant la condition en utilisant le LCO_2, elle induit approximativement la même tendance que la stratégie conventionnelle. Néanmoins, en condition cryogénique LN_2, la qualité de surface présentait un état médiocre par rapport aux conditions Wet et LCO_2. En effet, en condition cryogénique LN_2, la rugosité de surface a atteint des valeurs très élevées arrivait à plus de 3 μm de R_a et 20 μm de R_t.
En comparaison avec la lubrification conventionnelle, la condition cryogénique LN_2, produit une détérioration de plus de 30%. Cela dénote que le choix du refroidissement et de la lubrification affecte drastiquement les résultats en ce qui concerne les exigences de rugosité de surface établies par les industriels de fabrication. De plus, comme le montre la figure 30, les mesures de la rugosité ne sont pas enregistrées jusqu'à la fin du processus de coupe dans le cas de la stratégie de refroidissement LN_2 en raison des limites de l'équipement car l'état de surface était trop rugueuse. Pour cette raison, il a été recouru à l'utilisation du profilomètre pour caractériser la surface obtenue dans le cas de LN_2 mesurant la rugosité surfacique moyenne S_a.

5 Essais de fatigue

5.1 Procédure expérimentale

L'objectif principal de cette étude est d'évaluer l'effet de l'usinage cryogénique sur la durée de vie en fatigue, en particulier les opérations de perçage. Par conséquent, les éprouvettes de fatigue ont été percées dans des conditions de refroidissement conventionnelle et cryogéniques. Les deux fluides cryogéniques qui ont été employés sont l'azote liquide LN_2 et le dioxyde de carbone LCO_2. Les essais de perçage ont été réalisés en utilisant la même configuration (paramètres de coupe, géométrie du foret, montage) en variant les conditions de refroidissement. Les conditions de coupe sont résumées dans le tableau 2.

Table 2 – Working conditions

La pièce	Matériau	Inconel 718
Les paramètres de coupe	La vitesse de coupe (m/min)	30
	L'avance (mm/tr)	0.1
	La profondeur du trou (mm)	2 (trou débouchant)
L'outil de coupe	Le foret	Carbure revêtu (TiAlN)
	L'angle de pointe (SIG) (°)	140
	Le diamètre du foret (mm)	14
	La référence du foret	SD103-14.00/14.99-50-16R7
	Référence de pointe échangeable	SD100-14.00-M
Les fluides de refroidissement	Conventionnel	Wet
	Cryogénique	LN_2
	Cryogénique	LCO_2
Les fluides de refroidissement	Wet	Interne
	LN_2	Interne
	LCO_2	Interne

Les campagnes d'essais en fatigue sont gourmandes en pièces et il faut donc beaucoup de temps pour effectuer ces tests. Il était donc pertinent d'optimiser les plans

d'essais expérimentaux. Dans ce travail, l'objectif principal des expériences de fatigue est de déterminer la limite d'endurance à la fatigue cyclique élevée (HCF) pour trois lots d'éprouvettes puisque HCF est très sensible aux effets du procédé. Par conséquent, la méthode de l'escalier a été choisie car elle permet de déterminer de manière appropriée la limite d'endurance à la fatigue et d'estimer la dispersion des données correspondantes.
Les essais de fatigue ont été réalisés à température ambiante avec un rapport de charge R=0.1 et à une fréquence égale à 20 Hz. Chaque éprouvette est soumise à des charges cycliques à une amplitude prédéterminée de la contrainte appliquée (σ_a). Une durée de vie maximale en fatigue de 2.10^6 cycles a été imposée. Le critère d'arrêt a été choisi pour être la rupture de l'éprouvette ou l'atteinte de l'imposé durée de vie en fatigue (2.10^6). Comme souligné précédemment, la stratégie des essais de fatigue était d'employer la méthode d'escalier . A ce niveau, les trois types de lots sont détaillés ci-dessous :

— Staircase de 15 éprouvettes percées en condition de lubrification conventionnelle Wet ;
— Staircase de 15 éprouvettes percées en condition cryogénique avec LCO_2 ;
— Staircase de 15 éprouvettes percées en condition cryogénique avec LN_2.

5.2 Résultats et discussions

5.2.1 Contraintes-cycles : S-N curves

Afin d'estimer la limite d'endurance à 2.10^6 cycles du matériau étudié, la méthode de l'escalier a été employée. Les résultats correspondants sont présents dans le tableau 3, le tableau 4 et le tableau 5 établis respectivement pour les trois lots (Wet, LCO_2 et LN_2).
O : éprouvette non-rompue, X : éprouvette rompue

TABLE 3 – Les résultats de la staircase pour le lot "Wet"

Éprouvette n°	2	3	4	5	6	7	8	9	10	12	13	14	15	16	17
σ_a=160 MPa				X		X						X			
σ_a=150 MPa			O		O		X		X		O		X		
σ_a=140 MPa		O						O		O				X	
σ_a=130 MPa	O														O

TABLE 4 – Les résultats de la staircase pour le lot "LCO_2"

Éprouvette n°	3	4	5	6	7	8	9	10	11	12	13	14	15	1	16	17
σ_a=150 MPa	X		X													
σ_a=140 MPa		O		X		X								X		X
σ_a=130 MPa					O		X				X		O		O	
σ_a=120 MPa								X		O		O				
σ_a=110 MPa									O							

Une différence attendue liée à la résistance à la fatigue pourrait être remarquée lors de l'examen des résultats obtenus pour les trois lots. En général, le lot Wet présentait un niveau plus élevé de la contrainte appliquée σ_a. Quant au lot LCO_2, cette condition

TABLE 5 – Les résultats de la staircase pour le lot "LN_2"

Éprouvette n°	6	2	7	8	10	11	12	1	13	14	15	16	17	18
σ_a=120 MPa		X						X						
σ_a=110 MPa	O		X				O		X					
σ_a=100 MPa				X		O				X				O
σ_a=90 MPa					O						X		O	
σ_a=80 MPa												O		

induit une contrainte appliquée σ_a relativement plus faible ainsi que plus d'éprouvettes cassées. Néanmoins, la conditions de refroidissement LN_2 a considérablement réduit l'intervalle de la contrainte appliquée σ_a.

Les résultats de la méthode d'escalier sont rassemblés dans les courbes Contraintes-Cycles (S-N) illustrées dans la figure 31. Les graphes présentent les performances en fatigue de l'Inconel 718 en fonction de la stratégie du refroidissement des éprouvettes percées.

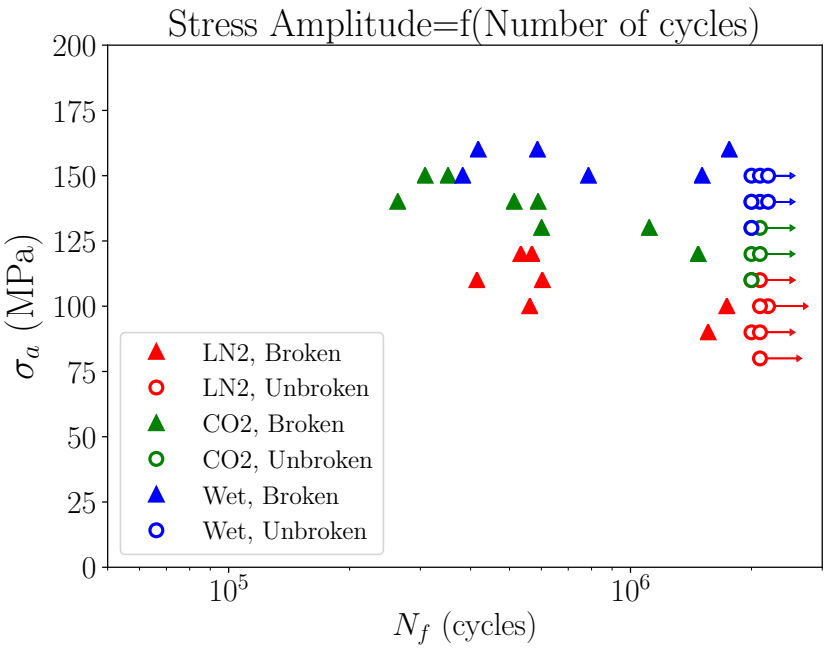

FIGURE 31 – Illustration des courbes de Contraintes-Cycles (S-N) présentant les performances en fatigue de l'Inconel 718 en fonction de la stratégie du refroidissement des éprouvettes percées.

Les résultats ont montré que la condition Wet présentait la résistance à la fatigue la plus élevée par rapport aux deux lots cryogéniques. En revanche, la condition LN_2 a révélé la plus faible résistance à la fatigue par rapport aux éprouvettes percées LCO_2. De plus, la condition Wet montrait une dispersion plus faible par rapport à la résistance à la fatigue du lot LCO_2. La condition LN_2 indiquait la plus grande dispersion en termes d'amplitude de la contrainte appliqué. Éventuellement, la durée de vie en fatigue augmente avec la diminution de l'amplitude de contrainte relativement aux cas étudiés.

La limite d'endurance σ_d est donc calculée pour mieux évaluer les performances des éprouvettes percées. La figure 32 illustre la limite d'endurance à la fatigue des éprouvettes percées en fonction de la stratégie de refroidissement.

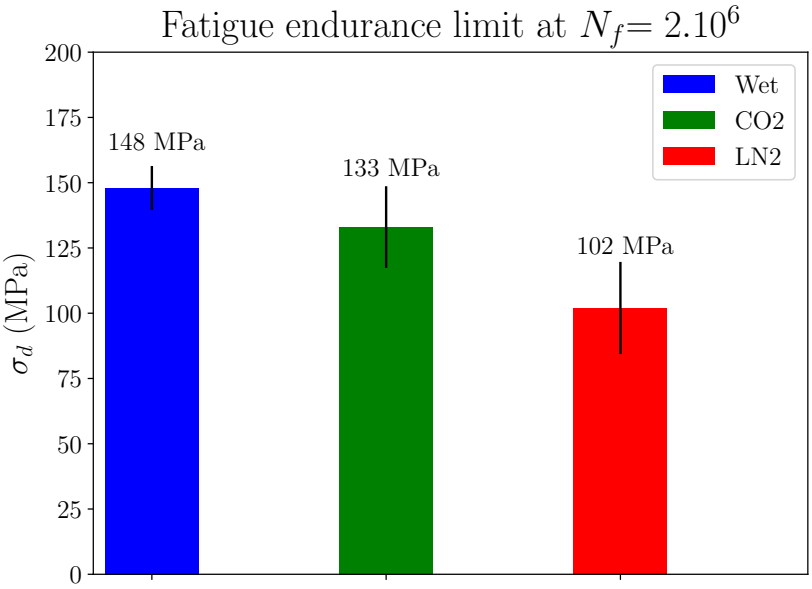

FIGURE 32 – Illustration la limite d'endurance à la fatigue des éprouvettes percées en fonction de la stratégie de refroidissement.

Les limites d'endurance σ_d (à 2.10^6 cycles) étaient de 148 MPa, 133 MPa et 102 MPa respectivement en conditions Wet, LCO_2 et LN_2 révélant un écart type de 8.4 MPa, 15.65 MPa et 17.66 MPa respectivement. Ainsi, les éprouvettes percées en conditions cryogéniques présentaient une limite d'endurance inférieure à celle obtenue en lubrification conventionnelle, révélant plus de 10 % de détérioration dans le cas du LCO_2 et de l'ordre de 30 % dans le cas du LN_2. Bien que le postulat selon lequel la dispersion continue à se produire et nécessite beaucoup d'échantillons pour être statistiquement précis au mieux, il pourrait être souligné que la dispersion des résultats, dans notre cas d'étude, pourrait être fortement liée au processus de perçage, en particulier les conditions de refroidissement.

5.2.2 Fractographies d'éprouvettes rompues

Afin d'exporter des informations complémentaires permettant d'identifier l'origine de la différence de la limite d'endurance révélée dans les courbes S-N, il convient d'examiner les faciès de rupture des éprouvettes de fatigue rompues. Il est important de souligner que la cible principale de cette enquête consistait à identifier les sites d'amorçage des fissures pour les trois types de lots et essayer d'expliquer la différence de la limite de fatigue observée.

La figure 33 montre le faciès de rupture de l'éprouvette rompue (n°7) obtenue dans la condition Wet. L'éprouvette a été soumise à σ_a =160 MPa induisant une durée de vie en fatigue de N_f=586 775.

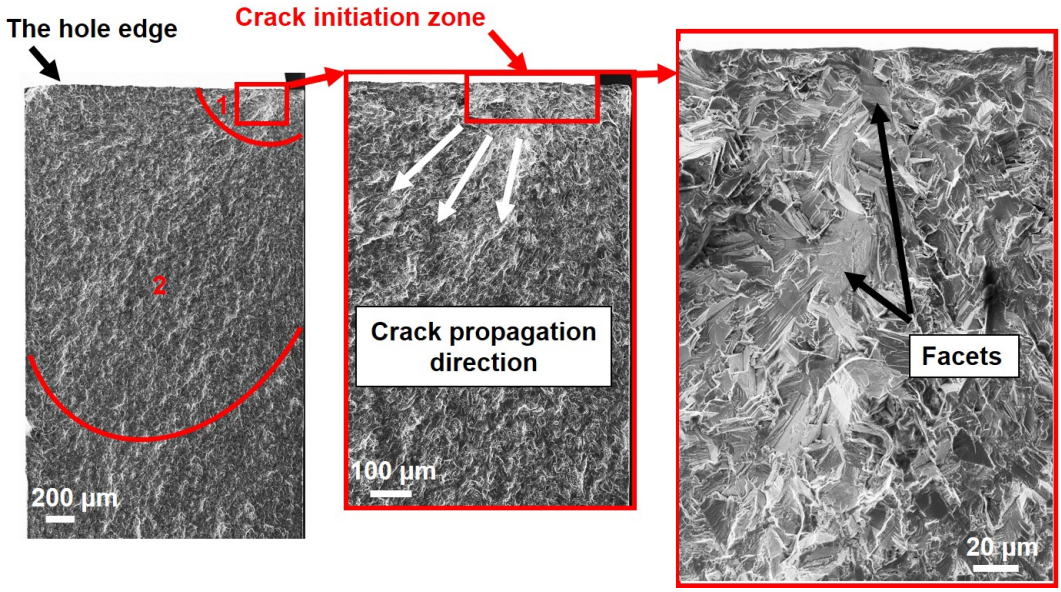

FIGURE 33 – Illustration du faciès de rupture de l'éprouvette rompue (n°7) percée dans la condition Wet (N_f= 586 775, σ_a=160 MPa).

On peut observer que les fissures de fatigue sont amorcées proche de la surface de l'éprouvette où des facettes ont été observées autour du site d'amorçage des fissures. La facette pourrait être induite soit par la décohésion des joints de grains (intergranulaire), soit par l'accumulation de la déformation plastique à l'intérieur du grain (intragranulaire) conduisant à l'amorçage des fissure en fatigue.

Dans ce contexte, Price and Kunc (1986) ont profondément étudié l'occurrence de facettes dans les faciès de rupture de dans le cas des superalliages de nickel. Ils ont signalé que les principales causes de la présence des facettes ne sont pas seulement la taille des grains mais aussi de faibles niveaux de contraintes par rapport à la limite d'élasticité. Cette dernière condition semble convenir à ce cas d'étude puisque les niveaux de chargement en contrainte sont très faibles par rapport à la limite d'élasticité du matériau d'étude. Actuellement, la majorité des procédés de fabrication induisent des défauts qui favorisent la l'amorçage des fissures de fatigue à savoir les porosités et les inclusions. En effet, de telles caractéristiques génèrent des concentrations de contraintes induisant l'amorçage de la fissure et donc la propagation provoquant la défaillance comme rapportée dans (Qian et al., 2020). Par conséquent, les analyses EDS ont été effectué afin d'identifier si ces caractéristiques existent dans le site d'initiation à proximité de la surface.
La figure 34 illustre l'analyse EDS qui a été menée sur la surface de rupture de l'éprouvette n°7 au voisinage de la surface car il a été supposé que les sites d'amorçage de la fissure ont eu lieu très proche de la surface (autour des structures à facettes). Ça peut être observé que les différentes zones analysées ont prouvé que ni les inclusions ni les des particules telles que des particules d'oxyde ont été détectées. Cette conclusion pourrait confirmer que les facettes jouent un rôle majeur pour l'amorçage des fissures.

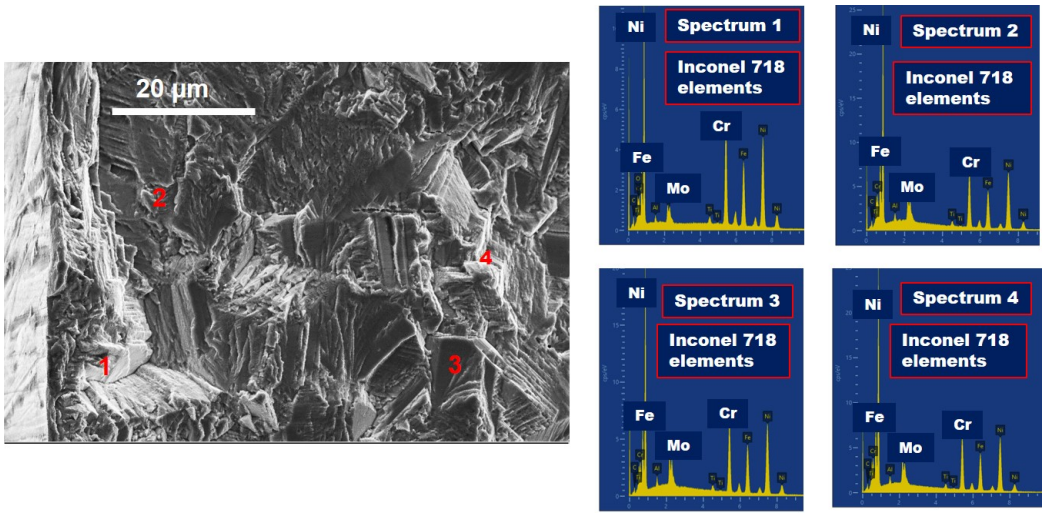

FIGURE 34 – Illustration des analyse EDS réalisées sur la surface de rupture de l'éprouvette n°7 percée en condition "Wet" (N_f= 586 775, σ_a=160 MPa).

Pour les éprouvettes LCO_2 rompues, la figure 35 illustre le faciès de rupture de l'éprouvette n°13 qui a été soumise à 130 MPa induisant N_f= 600 883.

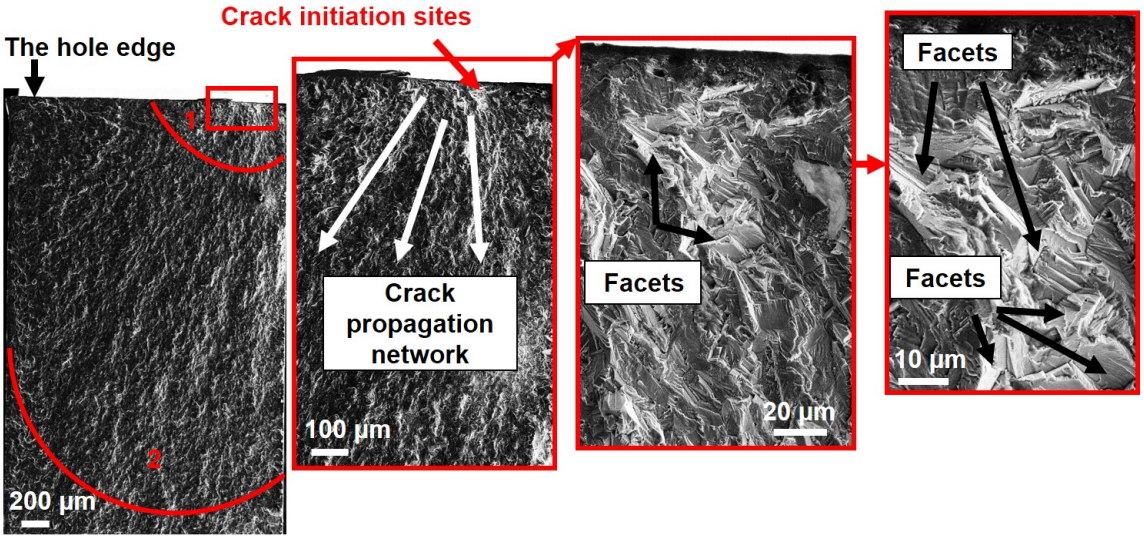

FIGURE 35 – Illustration du faciès de rupture de l'éprouvette rompue n°13 percée dans la condition LCO_2 (N_f= 600 883, σ_a=130 MPa).

On peut en déduire que le cas de l'éprouvette rompue LCO_2 semble être très similaire à la fractographie décrite précédemment révélée dans la condition Wet. En s'appuyant sur la figure 35, on peut juger que les sites d'amorçage des fissures sont localisés dans la structure facettaire. En effet, les sites d'initiation de fissures ont été supposés être dominés par des initiations facettaires en raison de certaines petites déformations locales se produisant lors de chaque charge. En gros, la rupture par fatigue pourrait avoir lieu à des très faibles amplitudes de contraintes où la réponse du matériau sous les charges appliquées est supposée élastique. De manière macroscopique, cette hypothèse est tout à fait vraie, mais localement une petite déformation doit se produire pendant chaque cycle de charge. Ces déformations, même petites, s'ajoutent encore tant que plus de cycles sont appliqués jusqu'à provoquer la rupture.

Concernant le troisième lot à savoir les éprouvettes percées en condition LN_2, les analyses fractographiques ont révélé une différence notable par rapport aux sites d'amorçage de fissure observés dans les cas précédents. La figure 36 montre le faciès de rupture de l'éprouvette rompue n°2 percée en condition LN_2 induisant N_f= 533534 lorsque le niveau de contrainte appliqué était égal à 120 MPa.

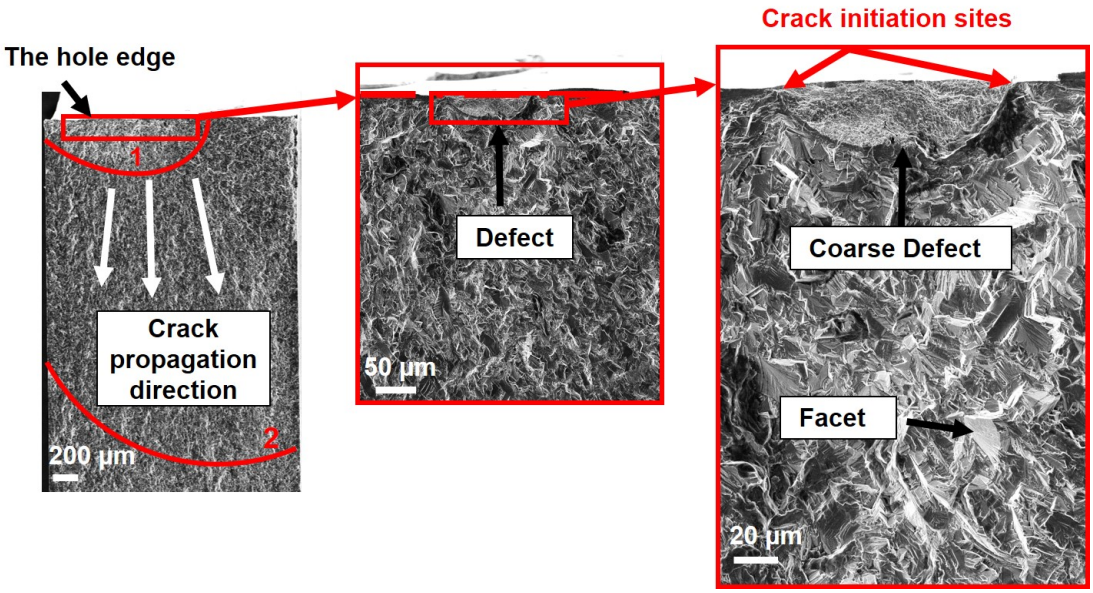

FIGURE 36 – Illustration du faciès de rupture de l'éprouvette rompue n°2 percée in LN_2 condition (N_f= 533 534, σ_a=120 MPa).

Évidemment, on peut observer que des fissures de fatigue ont été amorcées proche de la surface de l'éprouvette. Comme illustré à la figure 36, on peut estimer que les sites d'amorçage de fissure sont localisés au niveau des défauts grossiers. De tels défauts sont vraisemblablement générés lors du perçage dans la condition de refroidissement LN_2. Le défaut existant proche de la surface observé dans l'éprouvette a réduit considérablement sa durée de vie. Il a été largement reconnu que la résistance à la fatigue est sensible à la position du défaut ainsi qu'à la taille du défaut. Ces deux paramètres agissent de manière compétitive. Bonneric et al. (2020) ont affirmé que la position de défaut est la gagnante d'un point de vue que la cause principale de rupture par fatigue est la surface en supposant que la cause essentielle des fissures de surface est l'interaction avec l'environnement extérieur qui pourrait avoir un impact important sur l'amorçage de la fissure.

6 Conclusions et perspectives

6.1 Conclusions

L'objectif principal de ce travail de thèse était d'évaluer les performances de l'approche cryogénique en utilisant deux fluides cryogéniques différents à savoir l'azote liquide "LN_2" et le dioxyde de carbone "LCO_2". En effet, des essais en usinage avec assistance cryogénique et des essais de fatigue effectués sur des éprouvettes percées avec assistance cryogénique ont été réalisés en considérant comme référence la lubrification conventionnelle "wet". D'après les résultats des travaux de thèse, les principales conclusions qui pourraient être tirées en fonction de chaque tache sont listées ci-dessous :

6.1.1 Caractérisation mécanique à température cryogénique

— Un nouveau système cryogénique a été conçu permettant de fournir des niveaux de températures cryogéniques stables et homogènes (-185°C) durant des essais de compression mécaniques ;

— Les températures cryogéniques ont induit la plus élevée résistance mécanique pour toutes les vitesses de déformation testées. En particulier, la limite élastique et la résistance maximale sont plus élevées à température cryogénique en comparaison avec la température ambiante ;

— Concernant les changements de la microstructure, la température cryogénique n'a probablement pas montré tout changement par rapport à la condition de test de température ambiante indépendamment de la valeur de la vitesse de déformation selon les analyses menées dans cette étude.

6.1.2 Essais d'usinage avec assistance cryogénique

— La lubrification conventionnelle a fourni la plus basse valeur d'usure de l'outil durant 15 min d'usinage et les efforts de coupe les plus faibles. Cependant, les deux fluides cryogéniques ont induit des efforts de coupe plus élevés. Concernant l'usure de l'outil, le LCO_2 a montré des résultats similaires par rapport à la condition conventionnelle révélant une durée de vie de 15 min. En revanche, la condition cryogénique en utilisant LN_2 a conduit à une usure de l'outil la plus élevée et une durée de vie la plus courte (13 min) ;

— Les composantes des efforts de coupe (F_c, F_f et F_p) ont indiqué des valeurs plus élevées sous les deux conditions cryogéniques par rapport à la lubrification conventionnelle révélant que la contrainte d'écoulement du matériau de travail a augmenté en raison de la température cryogénique. En outre, il a été remarqué que les efforts radiaux F_p sont la composante la plus sensible à l'augmentation de l'usure en dépouille de l'outil ;

— Concernant la répartition des contraintes résiduelles, les résultats ont montré que lors de la coupe en utilisant de nouveaux outils, la lubrification conventionnelle a révélé la valeur de traction la plus élevée près de la surface (483 MPa) et a produit le pic de compression le plus bas (-200 MPa) selon la direction

de coupe. Dans les deux conditions cryogéniques, près de la surface, selon la direction de coupe, les contraintes résiduelles ont montré des valeurs approximativement similaires (180 MPa et 102 MPa obtenus respectivement en LCO_2 et LN_2). Néanmoins, la condition LCO_2 a induit la valeur de compression maximale la plus élevée se tenant autour de -300 MPa lors de l'usinage avec de nouveaux outils.

— Globalement, en comparant les trois conditions de refroidissement testées, la stratégie de refroidissement en utilisant le LCO_2 est la plus appropriée puisqu'elle procure une durée de vie de 15 min avec une usure d'outil acceptable et une meilleure intégrité de surface par comparaison avec la lubrification conventionnelle et la condition de refroidissement avec LN_2. On pourrait conclure que la stratégie de refroidissement LCO_2 est une bonne alternative pour remplacer la lubrification conventionnelle en raison de l'avantage écologie aussi.

6.1.3 Résistance à la fatigue

— Les éprouvettes percées avec assistance cryogénique en utilisant LN_2 ont montré une limite de fatigue la plus basse par rapport au LCO_2 et la lubrification conventionnelle tenant respectivement 102 MPa, 133 MPa et 148 MPa sous régime de fatigue à cycle élevé (2.10^6) ;

— Les analyses des faciès de rupture ont montré que les fissures de fatigue ont amorcé à partir de structure à facettes dans la majorité des cas étudiés pour les éprouvettes percées dans les conditions de refroidissement conventionnel et LCO_2. Cependant, la plupart des faciès de rupture des éprouvettes percées avec LN_2 présentaient des défauts grossiers au voisinage de la surface, quelle que soit la contrainte appliquée et le nombre de cycle abouti à rupture. Ces défauts sont probablement les principales sources de l'amorçage de fissure.

6.1.4 Conclusion générale

En guise de conclusion, le LCO_2 a révélé une démarche prometteuse puisqu'il a montré une très bonne performance non seulement pendant les essais d'usinage en tournage mais aussi en ce qui concerne la limite de fatigue par rapport à la condition cryogénique en utilisant LN_2. De ce fait, des enquêtes approfondies pourraient être menées afin d'optimiser l'efficacité de cette méthode cryogénique.

6.2 Perspectives

La présente thèse a proposé une étude comparative en termes d'efficacité entre deux fluides cryogéniques que ce soit par rapport aux performances d'usinage, ou par rapport à la limite de fatigue en considérant la condition de lubrification conventionnelle comme référence. Cependant, d'autres travaux peuvent encore être réalisés à l'avenir visant à améliorer nos résultats actuels et à essayer d'autres techniques. Par conséquent, les perspectives estimées comme une continuité pour le présent travail sont énumérées ci-contre :

— Récemment, les chercheurs se sont concentrés sur des stratégies de refroidissement plus efficaces lors de l'usinage des aciers et des alliages de titane. Ils ont prouvé que la combinaison entre la quantité minimale de lubrifiant (MQL) et le LCO_2 a amélioré la performances d'usinage de ces matériaux en termes de durée de vie ainsi que d'intégrité de la surface. Pour cette raison, la combinaison MQL+LCO_2 pourrait être examinée dans le cas de l'Inconel 718 ;

— Par ailleurs, il pourrait être intéressant de réaliser des campagnes d'essais de perçage cryogénique sous les trois stratégies de refroidissement employées dans le travail de doctorat actuel afin d'estimer les exigences industrielles liées à la durée de vie de l'outil et à l'intégrité de surface ;

— Enfin, il est bien connu que l'accès à une zone très locale est difficilement possible par des approches ou des techniques expérimentales telles que les déformations locales, les contraintes locales et les températures de coupe. La méthode complémentaire parfaite consiste à la modélisation numérique permettant de mieux comprendre les phénomènes locaux et les mécanismes d'endommagement se produisant pendant le procédé d'usinage dans les conditions cryogéniques.

Bibliographie

Ayed, Y., Germain, G., Melsio, A.M., Kowalewski, P., Locufier, D., 2017. Impact of supply conditions of liquid nitrogen on tool wear and surface integrity when machining the ti-6al-4v titanium alloy. International Journal of Advanced Manufacturing Technology 93. doi :10.1007/s00170-017-0604-7.

Ayed, Y., G, G., Pubill, M.A., P, K., D, L., 2017. Impact of supply conditions of liquid nitrogen on tool wear and surface integrity when machining the ti-6al-4v titanium alloy. The International Journal of Advanced Manufacturing Technology 93, 1199–1206. doi :10.1007/s00170-017-0604-7.

Behera, B.C., Alemayehu, H., Ghosh, S., Rao, P.V., 2017. A comparative study of recent lubricoolant strategies for turning of ni based superalloy. Journal of Manufacturing Processes 30, 541–552.

Bonneric, M., Brugger, C., Saintier, N., 2020. Investigation of the sensitivity of the fatigue resistance to defect position in aluminium alloys obtained by selective laser melting using artificial defects. International Journal of Fatigue 134, 105505. URL : doi :https://doi.org/10.1016/j.ijfatigue.2020.105505.

Bordin, A., Bruschi, S., Ghiotti, A., Bariani, P., 2015. Analysis of tool wear in cryogenic machining of additive manufactured ti6al4v alloy. Wear 328-329, 89–99. doi :https://doi.org/10.1016/j.wear.2015.01.030.

Chaheng, P., 2020. Chaheng precision Chaheng precision co., LTD.

Cheng, G., Jian, W., Xu, W., Yuan, H., Millett, P., Zhu, Y., 2013. Grain size effect on deformation mechanisms of nanocrystalline bcc metals. Materials Research Letters 1, 26–31. URL : https://doi.org/10.1080/21663831.2012.739580, doi :10.1080/21663831.2012.739580,

Courbon, C., Pusavec, F., Dumont, F., Rech, J., Kopac, J., 2013. Tribological behaviour of ti-6al-4v and inconel 718 under dry and cryogenic conditions : Application to the context of machining with carbide tools. Tribology International 66, 72 – 82. doi :https://doi.org/10.1016/j.triboint.2013.04.010.

Dhananchezian, M., Kumar, M.P., 2011. Cryogenic turning of the ti–6al–4v alloy with modified cutting tool inserts. Cryogenics 51, 34 – 40. doi :https://doi.org/10.1016/j.cryogenics.2010.10.011.

Dosbaeva, G.K., Veldhuis, S.C., Elfizy, A., Fox-Rabinovich, G., Wagg, T., 2010. Microscopic observations on the origin of defects during machining of direct aged (da) inconel 718 superalloy. Journal of Materials Engineering and Performance 19, 1193–1198. doi :10.1007/s11665-009-9587-3.

Hong, S., Irel, M., Woo-cheol, J., 2001a. New cooling approach and tool life improvement in cryogenic machining of titanium alloy ti-6al-4v. International Journal of Machine Tools and Manufacture 41, 2245 – 2260. doi :https://doi.org/10.1016/S0890-6955(01)00041-4.

Hong, S., Yucheng, D., 2001. Cooling approaches and cutting temperatures in cryogenic machining of ti-6al-4v. International Journal of Machine Tools and Manufacture 41, 1417 – 1437. doi :https://doi.org/10.1016/S0890-6955(01)00026-8.

Hong, S., Yucheng, D., Woo-cheol, J., 2001b. Friction and cutting forces in cryogenic machining of ti–6al–4v. International Journal of Machine Tools and Manufacture 41, 2271 – 2285. doi :https://doi.org/10.1016/S0890-6955(01)00029-3.

Hongbo, D., Gaochao, W., 2015. Effect of deformation process on superplasticity of inconel 718 alloy. Rare Metal Materials and Engineering 44, 298–302.

Iturbe, A., Hormaetxe, E., Garay, A., Arrazola, P.J., 2016. Surface integrity analysis when machining inconel 718 with conventional and cryogenic cooling. Procedia CIRP 45, 67 – 70. 3rd CIRP Conference on Surface Integrity.

Kaynak, Y., 2014. Evaluation of machining performance in cryogenic machining of inconel 718 and comparison with dry and mql machining. The International Journal of Advanced Manufacturing Technology 72, 919–933. doi :10.1007/s00170-014-5683-0.

Kumar, S., Satapathy, B., Pradhan, D., Mahobia, G., 2019. Effect of surface modification on the hot corrosion resistance of inconel 718 at 700 c. Materials Research Express 6. doi :10.1088/2053-1591/ab1dc7.

List, G., 2004. Etude des mécanismes d'endommagement des outils carbure WC-Co par la caractérisation de l'interface outil copeau : application à l'usinage à sec de l'alliage d'aluminium aéronautique AA2024 T351. Ph.D. thesis. URL : http://www.theses.fr/2004ENAM0041. thèse de doctorat dirigée par Girot, Franck Sciences de l'ingénieur. Mécanique Paris, ENSAM 2004.

Memmi, S., Rosankis, E., Sandret, N., Duprat, P., Leonard, M., Morand, S., Tassy, V., 2019. Premiers résultats de l'enquête sumer 2017 : comment ont évolué les expositions des salariés aux risques professionnels sur les vingt dernières années. Références en santé au travail.

Musfirah, A., Ghani, J., Haron, C.C., 2017. Tool wear and surface integrity of inconel 718 in dry and cryogenic coolant at high cutting speed. Wear 376-377, 125 – 133. doi :https://doi.org/10.1016/j.wear.2017.01.031. 21st International Conference on Wear of Materials.

Mitsubishi, 2006. Highly rigid and light-weight heads prevent vibration and achieve good surface finish Tool news,2006.7.Update B047A.

Price, C., Kunc, R., 1986. Occurrence of faceted fatigue fractures in nickel. Metallography 19, 317 – 326. URL : doi :https://doi.org/10.1016/0026-0800(86)90019-4.

Pusavec, F., Hamdi, H., Kopac, J., Jawahir, I., 2011. Surface integrity in cryogenic machining of nickel based alloy—inconel 718. Journal of Materials Processing Technology 211, 773 – 783. doi :https://doi.org/10.1016/j.jmatprotec.2010.12.013.

Pusavec, F., Krajnik, P., Kopac, J., 2010. Transitioning to sustainable production – part i : application on machining technologies. Journal of Cleaner Production 18, 174 – 184. doi :https://doi.org/10.1016/j.jclepro.2009.08.010.

Pusavec, F., Ashish, D., Shu, Y., Rachid, M., Janez, K., Oscar, W.D., IS, J., 2014. Sustainable machining of high temperature nickel alloy inconel 718, part 1 predictive performance models. Journal of Cleaner Production 81, 255 – 269.

Qian, G., Li, Y., Paolino, D., Tridello, A., Berto, F., Hong, Y., 2020. Very-high-cycle fatigue behavior of ti-6al-4v manufactured by selective laser melting : Effect of build orientation. International Journal of Fatigue 136, 105628. URL : doi :https://doi.org/10.1016/j.ijfatigue.2020.105628.

Rotella, G., W., D.O., D., U., L., S., S., J.I., 2014. The effects of cooling conditions on surface integrity in machining of ti6al4v alloy. The International Journal of Advanced Manufacturing Technology 71, 47–55. doi :10.1007/s00170-013-5477-9.

Touazine, H., Jahazi, M., Bocher, P., 2017. Accurate determination of damaged sub-surface layers in machined inconel 718. The International Journal of Advanced Manufacturing Technology 88, 3419–3427. doi :10.1007/s00170-016-9039-9.

Ulutan, D., Ozel, T., 2011. Machining induced surface integrity in titanium and nickel alloys a review. International Journal of Machine Tools and Manufacture 51, 250 – 280.

Witek, L., 2006. Failure analysis of turbine disc of an aero engine. Engineering Failure Analysis 13, 9 – 17.

Xie, X., Xu, C., Wang, G., Dong, J., Cao, W., Kennedy, R., 2005. Ttt diagram of a newly developed nickel-base superalloy- allvac ® 718plusa". Superalloys , 193–202.

Contents

I General introduction **61**

1 Background and motivation 62
2 Objectives of the PhD work 64
3 Structure of the manuscript 64

II Literature review **67**

1 Introduction 68
2 General information about nickel based superalloy: Inconel 718 68
2.1 Inconel 718 nickel based alloy 68
2.2 Machinability of Inconel 718 70
3 Cooling and machining approaches 72
3.1 Machining process 72
3.1.1 Chip formation 73
3.1.2 Tool wear mechanisms 74
3.1.2.a Tool wear assessment 74
3.1.2.b Adhesion wear 75
3.1.2.c Abrasion wear 75
3.1.2.d Diffusion wear 76
3.1.2.e Oxidation wear 77
3.2 Machining cooling/lubrication approaches 79
3.2.1 Laser machining approach 79
3.2.2 High pressure machining approach 79
3.2.3 Vibration machining approach 80
3.2.4 Cryogenic machining approach 81
3.3 Cryogenic fluids characteristics: LCO_2 and LN_2 81
3.3.1 Liquid carbon dioxide: LCO_2 82
3.3.2 Liquid nitrogen: LN_2 82
4 The effect of cryogenic machining 83
4.1 Effect on tool wear 83
4.2 Effect on cutting forces 91
4.3 Effect on the cutting temperature 93
4.4 Effect on friction coefficient 95
4.5 Effect on surface integrity 97
4.5.1 Surface roughness 97
4.5.2 Residual stresses 99
4.6 Summary of the literature review 103
5 Conclusion 106

III Mechanical characterization of Inconel 718 at cryogenic temperature 113
1 Introduction . . . 114
2 Description of the work material . . . 116
2.1 Heat treatment and chemical composition . . . 116
2.2 Microstructure observations . . . 118
2.2.1 Optical Microscope(OM) . . . 118
2.2.2 Scanning Electron microscopy (SEM) . . . 119
2.2.3 Electron Back Scatter Diffraction (EBSD) . . . 120
2.3 Samples preparation . . . 121
3 Mechanical characterization of Inconel 718 at low temperature . . . 122
3.1 Experimental procedure . . . 122
3.1.1 Experimental equipment . . . 122
3.1.2 Experimental methodology . . . 129
3.2 Results and discussions . . . 131
3.2.1 Stress-strain curves . . . 131
3.2.2 Mirco-hardness measurements . . . 134
3.2.3 Metallographic analysis . . . 137
3.2.3.a Microstructure observations . . . 137
3.2.3.b EBSD analysis . . . 140
4 Conclusion . . . 144

Bibliography 147

IV Cylindrical turning operations of Inconel 718 under cryogenic conditions 148
1 Introduction . . . 149
2 Experimental work . . . 152
2.1 Workpiece Material . . . 152
2.2 Experimental equipment . . . 152
2.3 Experimental Methodology . . . 154
3 Results and discussions . . . 156
3.1 Tool wear mechanisms . . . 156
3.2 Cutting forces . . . 162
3.3 Surface Integrity . . . 166
3.3.1 Surface roughness . . . 166
3.3.2 Microhardness Profiles . . . 172
3.3.3 Surface and subsurface damage . . . 173
3.3.4 Residual stresses . . . 178
3.4 Discussions: correlation between the outcome of the study . . . 181
4 Conclusion . . . 183

Bibliography 189

V Fatigue tests of cryogenic drilled samples 190
1 Introduction . . . 191
2 Experimental work . . . 195
2.1 Work material . . . 195
2.2 Experimental equipment . . . 196
2.3 Description of the drilled batches . . . 197
2.4 Description of the fatigue specimen . . . 198

2.5 Experimental Methodology . . . 199
2.5.1 Staircase method . . . 199
2.5.2 Loading conditions . . . 200
2.5.3 Estimation of the fatigue limit . . . 200
3 Results analysis and discussions . . . 201
3.1 Stress-cycles: S-N curves . . . 201
3.2 Hole topology . . . 207
3.2.1 Surface topology : SEM observations . . . 207
3.2.2 Areal parameters . . . 209
3.3 Microhardness profiles . . . 212
3.4 Surface and subsurface damage . . . 213
3.5 Fractography of broken fatigue specimens . . . 215
3.6 Discussions: summary of the outcome of the study . . . 227
4 Conclusion . . . 229

Bibliography **234**

VI Conclusions and perspectives **235**
1 Main conclusions . . . 236
2 Perspectives . . . 237

Scientific Contributions **239**

List of Figures

I.1 Illustration of a cross section of a jet engine (Ulutan and Ozel, 2011). . 62
I.2 Illustration of a high-tech assembly combustor which is made by Inconel and other superalloys (Chaheng, 2020). 63
I.3 Illustration of a summarized structure of the outline of the manuscript. 65

II.1 Illustration of the microstructure of Inconel 718: (a) δ phase (Ni_3Nb) and the carbide NbC; (b) γ'' phase (Ni_3Nb) evenly distributed in the matrix γ (Bushlya et al., 2011). 69
II.2 Illustration of the crystallographic cells of the matrix γ, the phases γ' and γ'' (Farhat, 2007). 70
II.3 Illustration of the relationship between the material properties and the machining problems of Inconel 718 (Yin et al., 2020). 71
II.4 Illustration of the influence factors of the unmachined material (initial microstructure, mechanical and thermal properties) on the machinability of Inconel 718 and thereby the generated surface integrity (Yin et al., 2020). 72
II.5 Illustration of the shear zones involved during the cutting operation. . 73
II.6 Illustration of types of wear on turning tools according to ANSI/ASME B94.55M-1985 standard. 74
II.7 Illustration of the wear mechanisms in metal cutting (Li, 2012). 75
II.8 Illustration of adhesion mechanism on the tool rake face followed by EDS analysis obtained during the end milling of Inconel 718 at V_c =160 m/min, f_z= 0.15 mm/tooth, a_p=0.30 mm, a_e=0.20 mm (Musfirah et al., 2017). 75
II.9 Illustration of abrasion mechanism on the tool flank face in orthogonal cutting of Inconel 718 using PCBN inserts at V_c =300 m/min, f= 0.05 mm/rev (Khan et al., 2012). 76
II.10 Illustration of diffusion profiles conducted on the cutting tool when machining Ti–6Al–4V at V_c = 20 m/min (Nouari and Makich, 2013). . . . 76
II.11 Illustration of an EDS analysis illustrated oxidation obtained at the flank wear when the coating exposed (V_c= 180 m/min, feed rate = 0.15 mm/tooth and axial depth=1 mm) (Kadirgama et al., 2011). . . 77
II.12 An overview of the causes, mechanisms, types and consequences of the tool wear in cutting of nickel based superalloys (Zhu et al., 2013). . . . 78
II.13 Illustration of Laser turning principle (Ayed et al., 2014). 79
II.14 Illustration of the High Pressure machining approach (Braham Bouchnak, 2010) 80
II.15 Illustration of the ultrasonically turning system (Ahmed et al., 2007) . 80

II.16 Illustration of LN_2 Cryogenic system: (a) Experimental setup; (b) High-speed camera acquisition (Ayed et al., 2017). 81
II.17 Illustration of schematic phase diagrams for: (a) Carbon dioxide; (b) Nitrogen (Stoll et al., 2014). 82
II.18 Comparison of tool flank wear when machining Ti64 under wet and LN_2 cryogenic conditions after 5 min of cutting (Dhananchezian and Kumar, 2011). 84
II.19 Illustration of tool wear damage when turning Ti64 after 8 min of machining under dry and cryogenic conditions (V_c= 80m/min and f =0.2 mm/rev) (Bordin et al., 2015). 85
II.20 Comparison of tool life obtained during machining Ti64 under miscellaneous cooling approaches (Hong et al., 2001). 86
II.21 Tool flank wear evolution during machining Inconel 718 under : dry, MQL and LN_2 cryogenic conditions (Kaynak, 2014). 86
II.22 Notch wear evolution during machining Inconel 718 under: dry, MQL and LN_2 cryogenic conditions (Kaynak, 2014). 87
II.23 Illustration of a comparison of tool wear under two conditions: dry and cryogenic coolant (Musfirah et al., 2017). 88
II.24 Illustration of tool flank wear when machining Inconel 718 under: HPJ, cryogenic, MQL, nMQL and dry machining environments (V_c=80 m/min, f= 0.2 mm/rev, γ =1 °) (Behera et al., 2017). 89
II.25 Tool flank wear progress as a function of cutting length when machining Ti64 under: CO_2, CO_2+MQL, CMQL and CO_2 (modified nozzle): (a) Maximum flank wear; (b) Average flank wear (V_c=150 m/min, f=0.2 mm/rev, a_p=1 mm, uncoated carbide inserts TPGN160308) (Bagherzadeh and Budak, 2018). 90
II.26 Tool flank wear progress as a function of cutting length when machining Inconel 718 under: CO_2, CO_2+MQL, CMQL and CO_2 (modified nozzle): (a) Maximum flank wear; (b) Average flank wear (V_c=100 m/min, f=0.2 mm/rev, a_p=1mm, Uncoated carbide inserts TPGN160308) (Bagherzadeh and Budak, 2018). 90
II.27 Thrust forces evolution when drilling Inconel 718 in dry, wet and LN_2 conditions (Ucak and Cicek, 2018). 91
II.28 Cutting forces evolution under various machining environment: (a) feed force F_x; (b) normal force F_y and (c) axial force F_z (Ross and Manimaran, 2020). 92
II.29 Main cutting forces evolution when varying feed rate at different cutting speed in different machining conditions (Jerold and Kumar, 2012). . . . 93
II.30 Illustration of cutting temperature measured by means of an infrared camera during milling operation of Inconel 718: (a) dry; (b) cryogenic given in Kelvin (Aramcharoen and Chuan, 2014). 94
II.31 SEM images of the cross section of the workpiece showing positions and dimensions of thermocouple holes (Ucak and Cicek, 2018) 94
II.32 Cutting temperature values under different machining conditions (Ucak and Cicek, 2018). 95
II.33 Friction coefficient evolution at the interface between tool-chip versus the sliding velocity (Ti64) (Courbon et al., 2013). 96
II.34 Friction coefficient evolution at the interface between tool-chip versus the sliding velocity (Inconel 718) (Courbon et al., 2013). 96

II.35 Illustration of the surface roughness evolution during machining time under dry, wet and LN_2 cryogenic conditions at V_c=264 m/min and f= 0.13 mm/rev (Dhar and Kamruzzaman, 2007). 97
II.36 Illustration of surface roughness evolution versus tool flank wear during the machining of Inconel 718 in turning operations under conventional and Cryo+MQL cooling strategies (Iturbe et al., 2016). 98
II.37 Illustration of surface roughness obtained under dry, MQL, LN_2 and CO_2 cooling conditions showing the effect of milling parameters and cooling modes (Jamil et al., 2021). 99
II.38 Illustration of the residual stresses profiles measured along : (a) Axial direction; (b) Cutting direction (Leadebal Jr et al., 2018). 100
II.39 Illustration of the effect of several cooling strategies on residual stresses when machining Ti64 in turning operations (Ayed et al., 2017). 101
II.40 Illustration of residual stresses on the surface and along the depth of the machined surface in turning operations of Inconel 718 under different cooling strategies (V_c = 60 m/min, f=0.05 mm/tr and a_p =0.63 mm) (Pusavec et al., 2011). 102
II.41 Illustration of residual stress on the machined surface under different environmental conditions at V_c = 75 m/min and f_z = 0.08 mm/rev (Ross and Manimaran, 2020). 103

III.1 Engineering stress vs the plastic strain curves for the three materials (Camilo et al., 2017). 115
III.2 Stress-strain curves at sub zero temperatures (Sharath Chandra et al., 2020). 115
III.3 EDS analysis carried out at a grain of the austenitic matrix γ in order to identify its chemical composition. 117
III.4 EDS analysis carried out at a NbC carbide in order to identify its chemical composition. 117
III.5 Illustration of the microstructure of the raw material at the as-received state. 118
III.6 Illustration of Inconel 718 microstructure in the as-received state observed by SEM technique using the SE beam. 119
III.7 Experimental device of scanning electron microscope in EBSD mode (Barbier, 2010). 120
III.8 Illustration of Inverse Pole Figure (IPF) obtained from EBSD analysis of in the as-received state (Projection axis [001]). 121
III.9 Illustration of the experimental set-up of the compression trials using the Gleeble 3500 machine (Iturbe et al., 2017). 123
III.10 Illustration of the two configurations used for the compression tests on Glebble 3500 machine: A-Configuration used for tests performed at high strain rates ($\dot{\varepsilon} > 1\ s^{-1}$); B-Configuration used for tests performed at low and medium strain rates ($\dot{\varepsilon} \leq 1\ s^{-1}$) (Hor et al., 2013). 124
III.11 Illustration of the thermal cycle applied at high temperature. 125
III.12 Illustration of TTT-diagram of Inconel 718 (Xie et al., 2005). 125
III.13 Illustration of the thermal cycle applied at cryogenic temperature. . . 126

III.14 Illustration of the cryogenic set-up of the compression trials conducted at cryogenic temperature using the Gleeble 3500 machine: The front view of the Gleeble machine (on the left); The back view of the Gleeble machine (on the right) 127
III.15 Illustration of temperature evolution during the compression test at $T = -188$ °C and $\dot{\varepsilon} = 0.01$ s^{-1}. 128
III.16 Illustration of the experimental plan presenting the working temperature T (°C) and the strain rate $\dot{\varepsilon}$ (s^{-1}) used during the compression tests. 129
III.17 Illustration of the evolution of the Young Modulus versus temperature (Fabre, 2013). 130
III.18 Illustration of stress-strain curves obtained at a fixed strain rate $\dot{\varepsilon}$=0.01 s^{-1} over different temperature range. 131
III.19 Illustration of stress-strain curves obtained at a fixed strain rate $\dot{\varepsilon}$ =1 s^{-1} over different temperature range. 131
III.20 Illustration of stress-strain curves obtained at a fixed strain rate $\dot{\varepsilon}$ =10 s^{-1} over different temperature range. 132
III.21 Illustration of the sensitivity coefficient to strain rate "m" calculating at a strain level equal to 0.1. 133
III.22 Illustration of the strain hardening coefficient "n" over a wide range of strain rate (from 0.01 s^{-1}to 10 s^{-1}). 134
III.23 Illustration of the micro-hardness profiles obtained after compression tests at low and room temperatures. 135
III.24 Illustration of the mechanical properties evolution of Inconel 718 along temperature at two strain rates : a) Yield stress "R_e"; b) Peak stress "R_m". 136
III.25 Illustration of metallographic observations of the deformed microstructure at strain rate equal to 0.01 s^{-1} : (a) at room temperature (RT); (b) cryogenic temperature (T=-188°C). 138
III.26 Illustration of metallographic observations of the deformed microstructure at strain rate equal to 10 s^{-1} : (a) at room temperature (RT); (b) cryogenic temperature (T=-188 °C). 139
III.27 Inverse Pole Figure (IPF) obtained from EBSD analyses of the deformed specimens (Projection axis [001]) established at 0.01 s^{-1} in room temperature (a) and cryogenic temperature (b); Misorientation gradients measured inside deformed grains in the case of: (c) Room temperature; (d) Cryogenic temperature; (e) Undeformed grains of a raw specimen. . 141
III.28 Inverse Pole Figure (IPF) obtained from EBSD analyses of the deformed specimens (Projection axis [001]) established at 10 s^{-1} in room temperature (a) and cryogenic temperature (b); Misorientation gradients measured inside deformed grains in the case of: (c) Room temperature; (d) Cryogenic temperature. 143

IV.1 Illustration of tool wear results obtained under MQL, LN_2 and MQL+LN_2 cooling conditions when machining Inconel 718 (Yildirim et al., 2020). . 150
IV.2 Illustration of Inconel 718 microstructure in the as-received state observed by SEM technique. 152
IV.3 Experimental set-up for the cryogenic tests: (a) LN_2 set-up; (b) Illustration of the different parts constituting the LN_2 set-up; (c) LCO_2 set-up. 153
IV.4 (a) Tool geometry; (b) Tool coating (Mitsubishi, 2006). 154

IV.5 Tool flank wear evolution under Wet, LN_2 and LCO_2 cooling conditions during the tests. 156
IV.6 SEM observations of the tool wear after 15 min of machining in wet condition: (a) Rake face/EDS analysis; (b) Flank face. 157
IV.7 SEM observations of the tool wear after 15 min of machining in LCO_2 condition during Test 1: (a) Rake face/EDS analysis; (b) Flank face. . 158
IV.8 SEM observations of the tool wear after 15 min of machining in LCO_2 condition during Test 2. 158
IV.9 SEM observations of the tool wear after 13 min of machining in LN_2 condition during Test 1: (a) Rake face/EDS analysis; (b) Flank face. . 159
IV.10 SEM observations of the tool wear after 14 min of machining in LN_2 condition during Test 2: (a) Rake face/EDS analysis; (b) Flank face. . 159
IV.11 Assessment of the adhered material volume and the material loss volume using the Alicona- Profilometer measurements: (a) Volume of adhered material; (b) Volume of material loss. 160
IV.12 Chip morphology obtained in the three cooling strategies: (a) Wet; (b) LCO_2; (c) LN_2. 161
IV.13 Illustration of the evolution of cutting forces components under all cooling strategies: (a) Cutting forces; (b) Feed forces; (c) Passive forces. . . 163
IV.14 Correlation between cutting forces components evolution and tool flank wear under Wet, LN_2 and LCO_2 conditions: (a) Cutting forces; (b) Passive forces. 165
IV.15 Surface roughness evolution under Wet, LN_2 and LCO_2 cooling conditions: (a) Average roughness; (b) Total height of the profile. 166
IV.16 Surface topography scanned using the Bruker profilometer after machining under LN_2 condition: (a) t=0.5 min; (b) t=5.5 min and(c) t=11 min. 168
IV.17 SEM observations of the surface topography after 11 min of machining under LN_2 condition. 169
IV.18 EDS analysis carried out on the machined surface after 11 min of machining under LN_2 condition. 169
IV.19 Surface roughness versus tool wear evolution under Wet, LN_2 and LCO_2 cooling conditions: (a) Average roughness; (b) Total height of the profile. 171
IV.20 Illustration of the evolution of the microhardness below the machined surfaces using semi−worn tools under conventional and LCO_2 cooling conditions and worn tool under LN_2 condition. 172
IV.21 SEM observations of the machined surfaces in wet condition using new and semi−worn tools: (a) New tool; (b) Semi−worn tool (V_{BMAX}=0.12mm, t=15min). 173
IV.22 SEM observations of the machined surfaces in LCO_2 condition using new and semi−worn tools: (a) New tool; (b) Semi-worn tool (V_{BMAX}=0.14 mm, t=15min). 173
IV.23 SEM observations of the machined surfaces in LN_2 condition using new and worn tools: (a) New tool; (b) Worn tool (V_{BMAX}=0.35mm, t=14min). 174
IV.24 Inverse Pole Figure (IPF) obtained from EBSD analyses of the machined surfaces (Projection axis [001]) established in LCO_2 condition using new tool (a) and semi−worn tool (b); Misorientation gradients measured inside deformed grains (in the direction as indicated by lines) in the case of: (c) New tool; (d) Semi-worn tool. 175

IV.25 Inverse Pole Figure (IPF) obtained from EBSD analyses of the machined surfaces (Projection axis [001]) established in wet condition using a semi−worn tool (a) and in LN_2 condition using worn tool (b); Misorientation gradients measured inside deformed grains in the case of: (c) Wet, Semi-worn tool; (d) LN_2, Worn tool. 177
IV.26 Residual stress profiles near and beneath the machined surface using a new tool under Wet, LCO_2 and LN_2 cooling conditions measured along: (a) Hoop direction (cutting direction); (b) Axial direction (feed direction). 178
IV.27 Residual stresses profiles near and beneath the machined surface using semi−worn tools under conventional and LCO_2 cooling conditions and worn tool under LN_2 condition measured along: (a) Hoop direction; (b) Axial direction. 180
IV.28 Schematic of the plastic deformation mechanisms considering tool flank wear effect and the impact on the surface integrity (residual stresses, microstructure damage and microhardness). 182

V.1 Illustration of fatigue results compared to S_a for tested technologies (Suárez et al., 2019). 191
V.2 Illustration of average values (four replications) of surface roughness, residual stresses, and average fatigue lives (three RBF tests) for the selected turning conditions and the polished specimens (Javadi et al., 2018). 192
V.3 Illustration of S-N diagrams at 4 K, 77 K and 293 K for Inconel 718 alloy (Ono et al., 2004). 193
V.4 Illustration of SEM secondary electron images showing the fatigue crack initiation sites (a), (c), and niobium mapping by EDS (b), (d) respectively. These specimens were fatigue-tested at 4 K. (Ono et al., 2004). . 194
V.5 Illustration of the tensile specimen. 195
V.6 Illustration of Inverse pole figures of as-received material for (a) normal direction; (b) rolling direction and (c) transverse direction. 196
V.7 (a) Illustration of the drill geometry; (b) Illustration of the drill bit (Seco, 2020). 197
V.8 Illustration of the experimental set-up of fatigue specimen drilling operation: LN_2 configuration. 197
V.9 Illustration of Fatigue specimen geometry. 198
V.10 Illustration of the fatigue machine INSTRON 3-axes. 199
V.11 Illustration of a schema highlighting the areas where the hole topology analyses were conducted (SEM analyses and areal roughness measurements), the cross sections along the cutting direction (surface and subsurface damage observations and the micro-hardness measurements). . 201
V.12 Illustration of Stress-cycle (S-N) curves showing the fatigue performances of Inconel 718 as a function of cooling strategy of the drilled specimens. 202
V.13 Illustration of tool wear state after drilling the first 6 specimens under wet condition. 203
V.14 Illustration of Stress-cycle (S-N) curves showing the fatigue performances obtained for each cooling condition as a function of the chronology of drilling the fatigue specimens : (a) Wet; (b) LCO_2 and (c) LN_2. 204
V.15 Illustration of the fatigue endurance limit as a function of cooling strategy of the drilled specimens. 205

V.16 Illustration of the machining process effect on fatigue endurance limit reported in literature review (R=0.1). 206
V.17 Topology of the drilled specimen under wet condition using SEM. . . . 207
V.18 Topology of the drilled specimen under LCO_2 condition using SEM. . 207
V.19 Topology of the drilled specimen under LN_2 condition using SEM. . . 208
V.20 Surface topgraphy scanned using the Brucker profilometer of the drilled specimens under all cooling strategies : (a) Wet; (b) LCO_2 and (c) LN_2. 210
V.21 (a) Illustration of micro-hardness profiles of drilled specimens under all cooling machining strategies; (b) Illustration of the correspondent indentations of the micro-hardness profiles. 212
V.22 Surface and subsurface damage of cross section of the drilled fatigue specimens under wet condition. 213
V.23 Surface and subsurface damage of cross section of the drilled fatigue specimens under LCO_2 condition. 213
V.24 Surface and subsurface damage of cross section of the drilled fatigue specimens under LN_2 condition. 214
V.25 Illustration of the fatigue steps site at the macroscopic scale : (a) in the plane (xy); (b) in the plane (xz). 216
V.26 Illustration of the fractured surfaces of the broken specimen n°7 drilled in wet condition (N_f= 586 775, σ_a=160 MPa). 217
V.27 Illustration of the EDS analysis conducted on fractured surfaces of the broken specimen n°7 drilled in wet condition (N_f= 586 775, σ_a=160 MPa). 218
V.28 Illustration of the fractured surfaces of the broken specimen n°14 drilled in wet condition (N_f= 1.76 10^6, σ_a=160 MPa). 218
V.29 Illustration of the fractured surfaces of the broken specimen n°13 drilled in LCO_2 condition (N_f= 600 883, σ_a=130 MPa). 219
V.30 Illustration of the fractured surfaces of the broken specimen n°9 drilled in LCO_2 condition (N_f= 1.11 10^6, σ_a=130 MPa). 220
V.31 Illustration of the EDS analyses conducted in the fractured surfaces of the broken specimen n°8 drilled in LCO_2 condition (N_f= 588 758, σ_a=140 MPa). 221
V.32 Illustration of the fractured surfaces of the broken specimen n°2 drilled in LN_2 condition (N_f= 533 534, σ_a=120 MPa). 222
V.33 Illustration of the EDS analyses conducted in the fractured surfaces of the broken specimen n°2 drilled in LN_2 condition (N_f= 533 534, σ_a=120 MPa). 223
V.34 Illustration of the fractured surfaces of the broken specimen n°8 drilled in LN_2 condition (N_f= 1.73 10^6, σ_a=100 MPa). 223
V.35 Illustration of the probable crack initiation sites experienced from the defects close to the surface of the LN_2 failed specimens : a) Specimen n°2: N_f=533534; b) Specimen n°7 : N_f=414 773; c) Specimen n°8: N_f= 1.73 10^6; d) Specimen n°15 : N_f= 1.56 10^6. 225
V.36 Illustration of applied stresses versus fatigue lifetime of the LN_2 failed specimens taking into account the square root of the defect area. 225
V.37 Illustration of the fatigue endurance limit obtained for the three fatigue batches linked with the fatigue failure mechanisms observed in the surface fracture. 226

V.38 Illustration of the fatigue endurance limit obtained for the three fatigue batches linked with the fatigue failure mechanisms observed in the surface fracture. 227

List of Tables

II.1 Mechanical properties of Inconel 718 at room temperature (Ezugwu et al., 2005) . . . 68
II.2 Chemical composition of Inconel 718 (% wt) (Zixing et al., 2012) . . . 69
II.3 Characteristics of LN_2 and LCO_2 employed during the machining process (Blau et al., 2015). . . . 83
II.4 Summary of the previous studies showing the effect of the cryogenic coolants LN_2 and LCO_2 performances compared to different cooling methods. . . . 104

III.1 Mechanical properties of Inconel 718 at room temperature . . . 117
III.2 Chemical composition of Inconel 718 (% wt) . . . 117

IV.1 LN_2 and LCO_2 flow parameters . . . 154
IV.2 Working conditions . . . 155

V.1 Mechanical properties of the work material . . . 195
V.2 The dimensions of the tensile specimens . . . 195
V.3 Working conditions . . . 196
V.4 The chronology of the fatigue specimens drilling. . . . 198
V.5 The dimensions of the fatigue specimens . . . 198
V.6 Staircase results of fatigue specimens drilled in wet condition . . . 201
V.7 Staircase results of fatigue specimens drilled in LCO_2 condition . . . 202
V.8 Staircase results of fatigue specimens drilled in LN_2 condition . . . 202
V.9 Areal parameters evaluated from the profilometer analyses . . . 211
V.10 Summary of the broken specimens outputs for the three kinds of batches whose failure surface will be presented in this section . . . 215
V.11 Summary of the output of the study . . . 228

Abreviations

LN_2	Liquid Nitrogen
LCO_2	Liquid Carbon Dioxide
MQL	Minimum Quantity Lubrication
HPJW	High Pressure Jet Water
V_c	Cutting speed (m/min)
a_p	Depth of cut (mm)
f	Feed (mm/rev)
F_c	Cutting force(N)
F_f	Feed force(N)
F_p	Passive force(N)
VB	Tool flank wear)
VB_N	Notch wear (mm)
VB_B	Average tool flank wear (mm)
V_{BMAX}	Maximum tool flank wear (mm)
KB	Width of crater wear (mm)
KT	Depth of crater wear (mm)
KM	Distance to middle of crater wear (mm)
R_a	Average roughness (μm)
R_t	Total height of the profile (μm)
OM	Optical Microscope
SEM	Scanning Electron microscope
EDS	Energy Dispersive spectroscopy
EBSD	Electron Back Scatter Diffraction
XRD	X-Ray Diffraction

Chapter I

General introduction

1 Background and motivation 62
2 Objectives of the PhD work 64
3 Structure of the manuscript 64

1 Background and motivation

Manufacturing innovation in the aviation industry is driven by the need to achieve performance improvements in mechanical parts, and reduce mass in all aircraft components. To meet these growing challenges, certain materials with specific properties are the subject of continuous investigation and development. For several decades, a growing number of nickel-based superalloys have been incorporated into the engines of the airplane (Ulutan and Ozel, 2011). These materials lend themselves well to aerospace manufacturing, as they exhibit excellent mechanical properties at high temperatures, high corrosion and creep resistances (Kumar et al., 2019; Hongbo and Gaochao, 2015). In particular, nickel-based superalloys are widely exploited in turbojets which are subjected to intense thermal and mechanical loads in service.

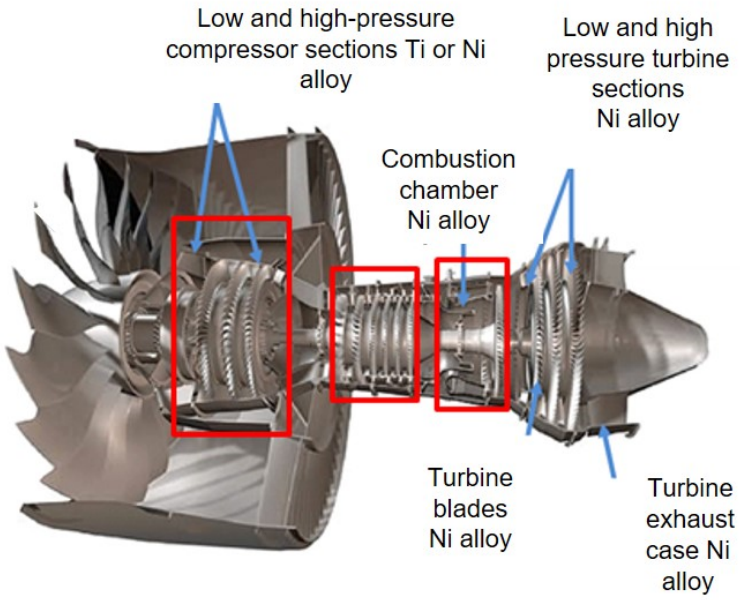

Figure I.1 – Illustration of a cross section of a jet engine (Ulutan and Ozel, 2011).

However, the extensive use of these materials has highlighted a problem related to machining process. Valued for their capacity to retain their in-service mechanical properties over a wide range of temperatures, their performance during the cutting process is unfavourably limited. For this reason, cooling approaches aim to improve the productivity of certain materials classified as " difficult to cut". The major problem encountered during machining is the significant increase in temperature in the cutting zone which leads degradation of the cutting tools. Tool life is thus greatly reduced and the surface finish of the machined parts is then deteriorated.
New alternatives to keeping the cutting tool cold, are therefore being investigated in the literature. One such alternative is called "cryogenic machining", in which liquid nitrogen is used as a lubricant for effectively reducing the cutting temperature, since its temperature at the liquid phase is -196°C. This novel machining approach is gaining recognition as a promising process for the industry of the future. Aside from its effectiveness in substantially reducing the temperature in the cutting zone, cryogenic machining presents several ecological, environmental, and economic advantages. Cryogenic processes render the use of the conventional lubricants unnecessary. These lubricants contain a significant amount of oil that has a harmful environmental impact and can cause skin and lung diseases for the operators (Memmi et al., 2019). An additional

advantage of eliminating conventional lubricant is that there is no need to degrease the machined parts and hence the chips are not contaminated before recycling.
In this context, previous researches have examined the efficiency of cryogenic approach when machining several materials (steels, titanium alloys and nickel based alloys). It has been shown that the tool life is improved in the case of titanium alloys (Ayed et al., 2017), unlike nickel based alloys (Iturbe et al., 2016). According to the previous results, Inconel 718 was found to induce lower tool life and poorer surface integrity (surface roughness, residual stresses, micro-hardness, etc..) under LN_2 cryogenic condition than with conventional lubrication. Recently, researchers are turning their attention to another cryogenic coolant: the carbon dioxide LCO_2. In this Phd work, many aspects are treated to study the effect of the cryogenic approaches. First, to understand the influence of the cryogenic cooling strategies on the tool wear and the surface integrity, we have opted for the turning operations of Inconel 718. So that, a comparative study is conducted including both cryogenic fluids namely LN_2 and LCO_2 in order to determine the efficiency of the cryogenic approach using the two cryogenic coolants compared to conventional lubrication.

Another aspect that seems to be interesting to study is related to the mechanical behavior of Inconel 718 at cryogenic temperature. During machining, the workpiece material is subjected to several mechanical and thermal loads that may significantly affect the material behavior during the cutting process. These include the high temperature resulting from friction and plastic deformation mechanisms and the very low temperature of cooling with LN_2 (-196°C). The unmachined surface is particularly affected by the cryogenic fluid, since the latter is delivered before starting the machining process to obtain the stabilized state.

Aeroengine turbine discs are mainly composed of critical components for instance the hub zone (Witek, 2006) and the assembly holes (Fig. I.2). Such regions are subjected to cyclic loads during their service. In particular, the drilled holes are the important sources of stress concentration and are therefore susceptible to nucleating fatigue cracks. As a consequence, manufactures are required to adhere to very strict specifications and high levels of accuracy to prevent any brutal failure.

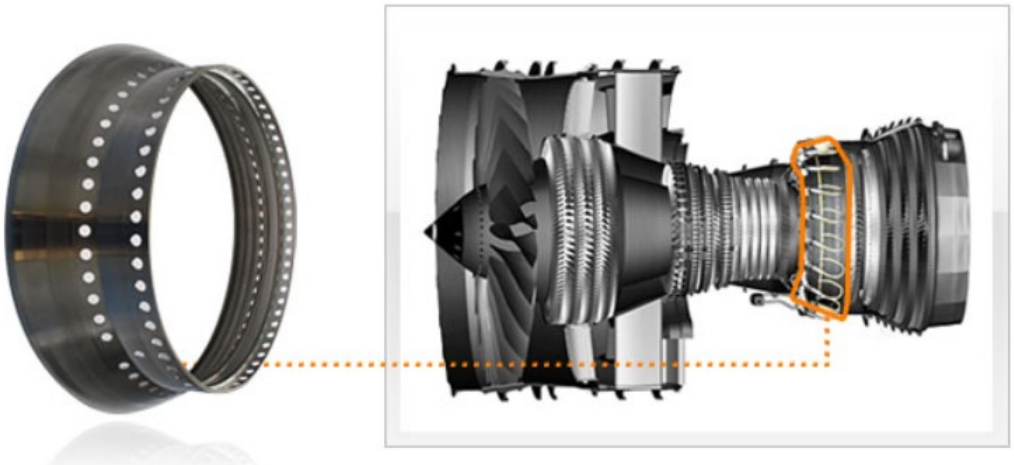

Figure I.2 – Illustration of a high-tech assembly combustor which is made by Inconel and other superalloys (Chaheng, 2020).

Machining process is often the last or second to last manufacturing stage. The machinists must optimize the cutting process and enhance the surface integrity of the machined parts. For this reason, the present study takes an original approach to the problem, focusing on adapting the cryogenic drilling process to examine its impact on fatigue resistance. Indeed, drilled specimens reveal stress concentration at the hole surface. Therefore, the influence of the surface is more significant. Thus, the effect of the process is better discriminated.

2 Objectives of the PhD work

The main objective of this PhD work is to evaluate the performance of cryogenic approach. To this end, two different cryogenic fluids: liquid nitrogen (LN_2) and carbon dioxide (LCO_2) are analyzed in terms of machining performance and fatigue limit taking as a reference the conventional lubrication (wet). This objective is divided in the following specific goals :

— To study the mechanical behavior of Inconel 718 at cryogenic temperature and to examine the microstructure alterations of the deformed samples to export information related to the mechanisms that could occur during the cryogenic machining process;

— To investigate the cryogenic performance of LN_2 and LCO_2 coolants in terms of tool life and surface integrity in finishing turning of Inconel 718 in comparison with the wet condition;

— To evaluate the effectiveness of the new cryogenic approaches on the fatigue limits of drilled samples.

3 Structure of the manuscript

The outline of the present manuscript is illustrated in Fig. I.3.
In chapter I, the PhD work is briefly introduced explaining the motivation of this thesis as well as the main objectives. The review of the literature is then set out in chapter II. In this chapter, general information about nickel based alloys is presented focusing on the metallurgic aspects and the machinability of this alloy. Next, cooling approaches are described, followed by an extensive analysis of the effect of cryogenic conditions when machining Inconel 718. Chapter III deals with the mechanical characterization at cryogenic temperature under static and dynamic loads. In addition, microstructural examination is conducted in order to reveal the influence of cryogenic conditions on the deformed microstructure. In chapter IV, turning operations under cryogenic conditions using liquid nitrogen (LN_2) and carbon dioxide (LCO_2) are reported. Tool wear mechanisms and surface integrity are investigated under cryogenic conditions and the conventional lubrication is considered as a reference. Chapter V focuses on the cryogenic effect on fatigue performance of Inconel 718. Particular attention is paid to the fatigue performance of cryogenic drilled specimens and the surface integrity of drilled specimens under both cryogenic cooling strategies and the wet condition is analyzed. Finally, the main conclusions are presented, together with implications for industry and future research lines.

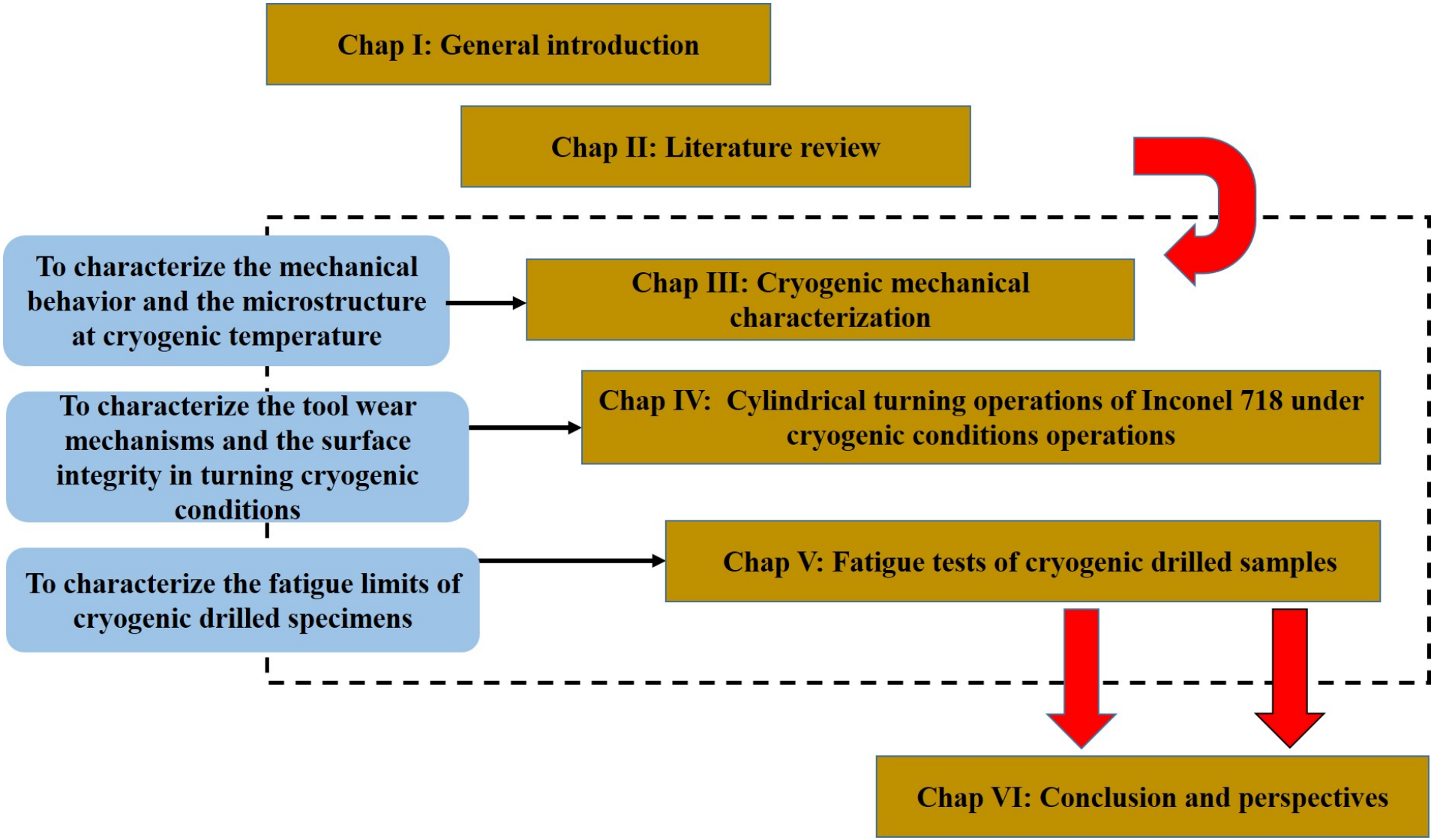

Figure I.3 – Illustration of a summarized structure of the outline of the manuscript.

Bibliography

Ayed, Y., Germain, G., Melsio, A.M., Kowalewski, P., Locufier, D., 2017. Impact of supply conditions of liquid nitrogen on tool wear and surface integrity when machining the ti-6al-4v titanium alloy. International Journal of Advanced Manufacturing Technology 93. doi:10.1007/s00170-017-0604-7.

Behera, B.C., Alemayehu, H., Ghosh, S., Rao, P.V., 2017. A comparative study of recent lubricoolant strategies for turning of ni based superalloy. Journal of Manufacturing Processes 30, 541–552.

Chaheng, P., 2020. Chaheng precision Chaheng precision co., LTD.

Hongbo, D., Gaochao, W., 2015. Effect of deformation process on superplasticity of inconel 718 alloy. Rare Metal Materials and Engineering 44, 298–302.

Iturbe, A., Hormaetxe, E., Garay, A., Arrazola, P.J., 2016. Surface integrity analysis when machining inconel 718 with conventional and cryogenic cooling. Procedia CIRP 45, 67 – 70. 3rd CIRP Conference on Surface Integrity.

Kumar, S., Satapathy, B., Pradhan, D., Mahobia, G., 2019. Effect of surface modification on the hot corrosion resistance of inconel 718 at 700 c. Materials Research Express 6. doi:10.1088/2053-1591/ab1dc7.

Memmi, S., Rosankis, E., Sandret, N., Duprat, P., Leonard, M., Morand, S., Tassy, V., 2019. Premiers résultats de l'enquête sumer 2017 : comment ont évolué les expositions des salariés aux risques professionnels sur les vingt dernières années. Références en santé au travail .

Ulutan, D., Ozel, T., 2011. Machining induced surface integrity in titanium and nickel alloys a review. International Journal of Machine Tools and Manufacture 51, 250 – 280.

Witek, L., 2006. Failure analysis of turbine disc of an aero engine. Engineering Failure Analysis 13, 9 – 17.

Chapter II

Literature review

1 Introduction . . . 68
2 General information about nickel based superalloy: Inconel 718 . . . 68
2.1 Inconel 718 nickel based alloy . . . 68
2.2 Machinability of Inconel 718 . . . 70
3 Cooling and machining approaches . . . 72
3.1 Machining process . . . 72
3.1.1 Chip formation . . . 73
3.1.2 Tool wear mechanisms . . . 74
3.1.2.a Tool wear assessment . . . 74
3.1.2.b Adhesion wear . . . 75
3.1.2.c Abrasion wear . . . 75
3.1.2.d Diffusion wear . . . 76
3.1.2.e Oxidation wear . . . 77
3.2 Machining cooling/lubrication approaches . . . 79
3.2.1 Laser machining approach . . . 79
3.2.2 High pressure machining approach . . . 79
3.2.3 Vibration machining approach . . . 80
3.2.4 Cryogenic machining approach . . . 81
3.3 Cryogenic fluids characteristics: LCO_2 and LN_2 . . . 81
3.3.1 Liquid carbon dioxide: LCO_2 . . . 82
3.3.2 Liquid nitrogen: LN_2 . . . 82
4 The effect of cryogenic machining . . . 83
4.1 Effect on tool wear . . . 83
4.2 Effect on cutting forces . . . 91
4.3 Effect on the cutting temperature . . . 93
4.4 Effect on friction coefficient . . . 95
4.5 Effect on surface integrity . . . 97
4.5.1 Surface roughness . . . 97
4.5.2 Residual stresses . . . 99
4.6 Summary of the literature review . . . 103
5 Conclusion . . . 106

1 Introduction

In order to discern well the framework and the motivations of this work, it is important to highlight the characteristics of the cryogenic machining approaches. This first chapter therefore reveals the main results of the literature review related to the cryogenic performance during the machining process when using two cryogenic fluids namely the liquid nitrogen (LN_2) and the carbon dioxide (LCO_2). At the beginning of the chapter, we will focus on the presentation of the Inconel 718, which is the subject of this study in terms of the metallurgical specificities in addition to the machinability properties. The second part of this chapter describes the several machining assistance approaches, in particular the cryogenic assisted strategy. Then, a specific focus is attributed to the description of both cryogenic coolants (LN_2 and LCO_2). The effect of the cryogenic approach on the tool wear as well as the surface integrity of the machined parts is also detailed. In the last part, an overview will be figured out in order to position the objectives of the present PhD work versus the previous studies reported in literature.

2 General information about nickel based superalloy: Inconel 718

2.1 Inconel 718 nickel based alloy

Nickel based alloys are superalloys that exhibit excellent mechanical properties in an extended temperature range up to 700°C (Iturbe et al., 2017) and good resistance to corrosion and oxidation (Hongbo and Gaochao, 2015), see Table II.1. These properties are closely related to the chemical composition of such alloys. In this work, the nickel based alloy Inconel 718 will be deeply studied.

Table II.1 – Mechanical properties of Inconel 718 at room temperature (Ezugwu et al., 2005)

Tensile stength (MPa)	1310
Yield strength (MPa)	1110
Young modulus (GPa)	206
Hardness (HV_{100})	427-454
Density ($g.cm^{-3}$)	8.19
Thermal conductivity coefficient (W/m.K)	11.2

Inconel 718 is an alloy containing several additive elements such as iron, chromium, aluminum, titanium and niobium (Table II.2). Each element contributes to the improvement of the characteristics of this alloy. For instance, chromium (18.84 %) inhibits the diffusion of oxygen in the depth of the part by reacting with oxygen to form chromium oxide Cr_2O_3 at the surface (Alexis, 2013). Molybdenum provides the mechanical strength of the matrix even at high temperature and niobium leads to the formation of the hardening phase of this alloy by precipitation (C. Slama and G. Cizeron, 1997).

Table II.2 – Chemical composition of Inconel 718 (% wt) (Zixing et al., 2012)

Ni	Cr	Fe	Mo	Nb	Ti	Al	Si	Mn	P	S	C
53.64	18.84	17.62	3.08	5.23	0.95	0.53	0.06	0.02	0.003	0.002	0.024

The metallurgical structure of Inconel 718 consists of several phases whose matrix is a disordered austenitic solid solution, called "γ" (Sundararaman et al., 1988). Fig. II.1 illustrates the microstructure of Inconel 718.

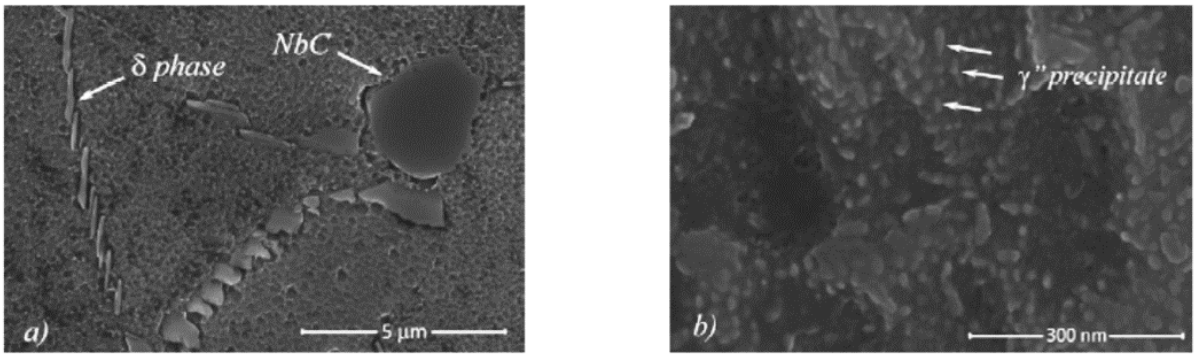

Figure II.1 – Illustration of the microstructure of Inconel 718: (a) δ phase (Ni_3Nb) and the carbide NbC; (b) γ'' phase (Ni_3Nb) evenly distributed in the matrix γ (Bushlya et al., 2011).

The correspondent crystallographic structure is face centered cubic (FCC) whose cell parameter is $a_y = 3.61$ Å that can vary depending on the addition elements (Alexis, 2013; Gael, 2012; Niang, 2010; Ter-Ovanessian, 2011). This matrix γ is hardened by the precipitation of two phases namely γ' and γ''.

The phase γ' is stable and coherent with the matrix whose crystallographic structure is cubic of type $L1_2$ (Mohan et al., 1992). The chemical composition is of the type A_3B where A is essentially nickel and the element B can be either aluminum or titanium.

Unlike the majority of nickel based alloys, which are hardened by precipitation of the γ' phase, the γ'' is the main hardening phase of Inconel 718 whose chemical formula is Ni_3Nb (C. Slama and G. Cizeron, 1997). It is a metastable and semi-coherent phase which crystallizes according to the quadratic centered structure of type DO_{22} (Sundararaman et al., 1988) (Fig. II.2).

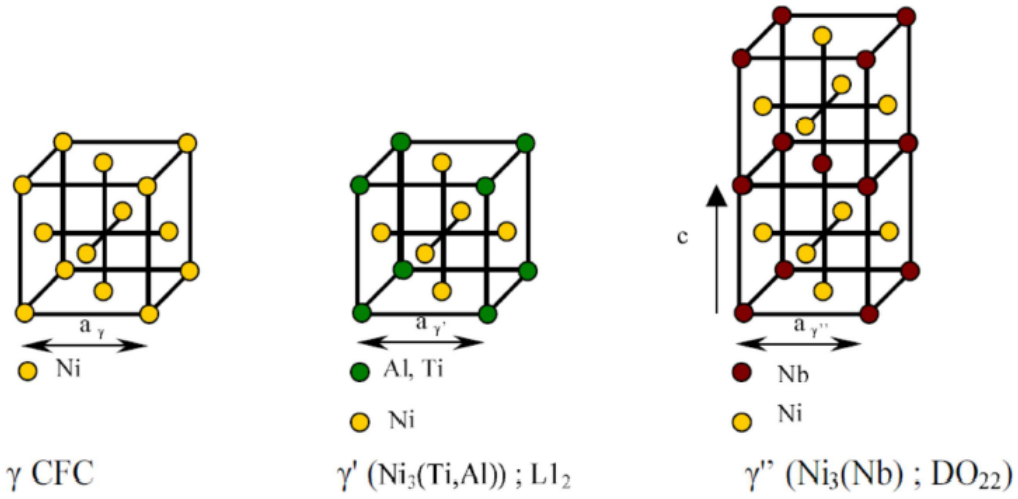

Figure II.2 – Illustration of the crystallographic cells of the matrix γ, the phases γ' and γ'' (Farhat, 2007).

Another phase that is formed by precipitation is the phase δ (also called β) that has an orthorhombic structure of type DO_a. Its chemical composition is the same as the phase γ'' (Ni_3 Nb) of which it is the stable form. The δ phase does not harden the Inconel 718 alloy but it contributes to increasing the creep resistance by decelerating the slippage of grain boundaries at high temperature.
There are also carbides, mainly MC type, whose crystallographic structure is face centered cubic having a heterogeneous distribution in the alloy located either at the grain boundaries or inside the grain of the austenitic matrix. The carbides are essentially formed by the presence of titanium (TiC) and niobium (NbC) since these two elements are very carburigen. The role of carbides consists of reinforcing the creep resistance by delaying the migration of grain boundaries at high temperatures. Nevertheless, their presence in large quantities may weaken the material.

2.2 Machinability of Inconel 718

The machinability of nickel alloys is poor in comparison with stainless steels and steels. Indeed, these alloys cause machining problems in terms of tool wear, cutting forces and surface integrity (residual stresses, surface roughness, affected layer) of the machined parts (Dudzinski and Molinari, 1997; Imran et al., 2014; Thellaputta et al., 2017).
Fig. II.3 summarizes the relationship between the Inconel 718 material properties and the machining problems.

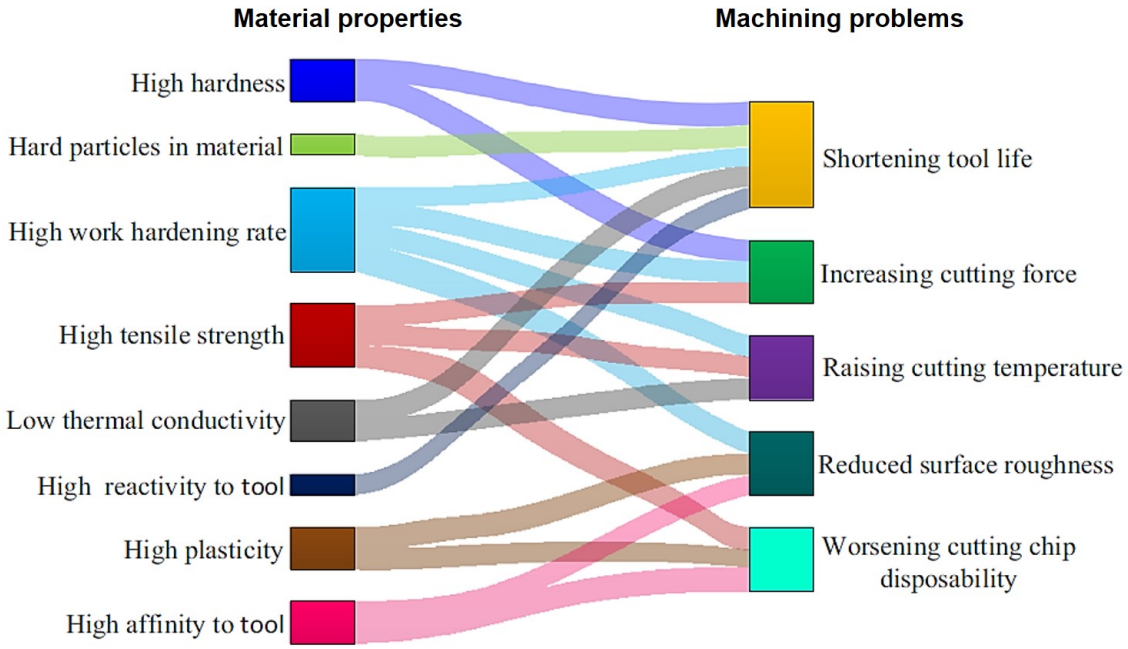

Figure II.3 – Illustration of the relationship between the material properties and the machining problems of Inconel 718 (Yin et al., 2020).

The main factors responsible for the poor machinability (tool wear and cutting forces) of Inconel 718 alloys are detailed below:

— Excellent mechanical properties at high temperature. Consequently, high cutting forces are generating which may lead to vibrations of the whole system (workpiece, tool and machine) affecting the quality of the machined surface;

— Low thermal conductivity preventing heat evacuation that remains mostly stored in the material of the machined part;

— High chemical affinity with several tool materials leading to tool wear by diffusion;

— Adhesion of microparticles from the machined material on the tool cutting edge during machining process. Thereby, high tool wear by adhesion is generated;

— Inconel 718 exhibit a very high hardening tendency when machining, inducing higher cutting forces (Iturbe et al., 2016);

— The carbides present in the Inconel 718 microstructure reveal abrasive behavior leading to abrasive wear of the tool.

In order to improve the poor productivity of these alloys, the following aspects should be selected carefully:

— The cutting tool with respect to important parameters (the tool material, the coating and the geometry);

— Cutting conditions (the cutting speed, the feed rate and the depth of cut);

— Cooling conditions (dry, MQL and conventional lubrication);

— Non-conventional cooling strategies (laser machining, High pressure machining, vibration machining and cryogenic machining).

3 Cooling and machining approaches

3.1 Machining process

Machining is a method of manufacturing parts by removing material. This process is in continuous development aiming to improve the machinability of the work materials of the machined parts. This is conditioned by the optimization of the cutting parameters, the understanding of the mechanisms of chip formation, the physical phenomena involved during the cutting, the tool wear mechanisms as well as the improvement of the machinability of certain alloys including materials that are difficult to cut (Fig. II.4).

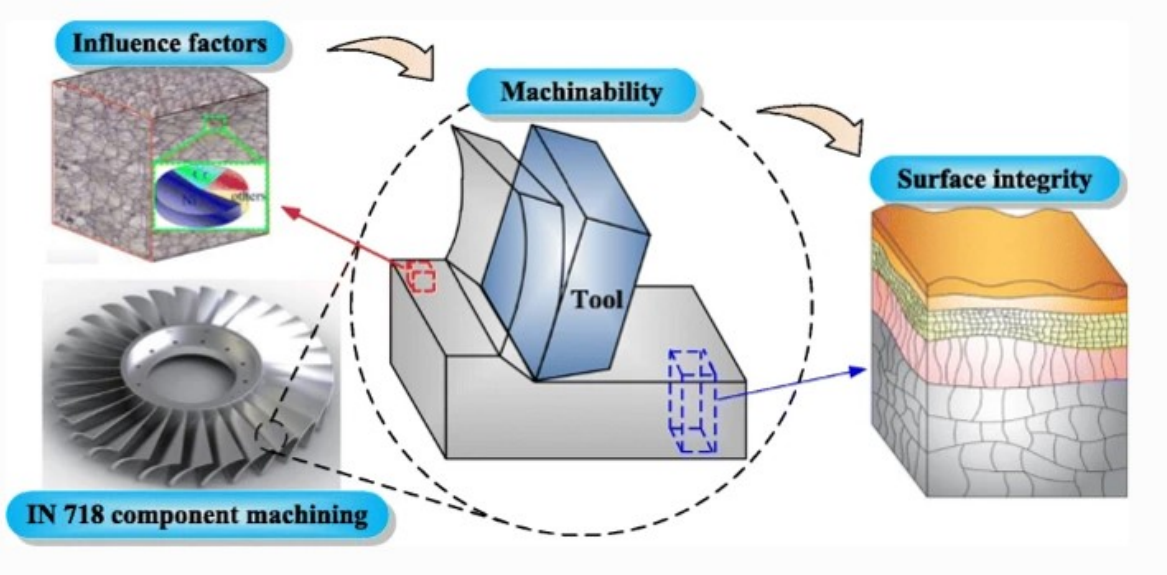

Figure II.4 – Illustration of the influence factors of the unmachined material (initial microstructure, mechanical and thermal properties) on the machinability of Inconel 718 and thereby the generated surface integrity (Yin et al., 2020).

In this context, the concept of machining assistance is revealed. Indeed, machining performance depends strongly on the choice of the cooling conditions that affect the friction between the tool-workpiece contact zone, the cutting temperatures, the cutting forces, etc. Thus, the tool life, the workpiece accuracy and the surface integrity of the components are significantly affected.
In the next paragraphs, we will present briefly the general information related to the cutting process namely the chip formation, the tool wear mechanisms and the different assisted machining strategies.

3.1.1 Chip formation

The study of the chip formation is carried out according to several scales from the macroscopic scale to the microscopic scale passing by the mesoscopic scale. The macroscopic scale corresponds to the machine-tool scale targeting to better control the problems of vibration and the dynamic rigidity of the cutting machine. The mesoscopic scale is the scale of chip formation, surface integrity and wear up to the microscopic scale aiming to identify the localization of the deformation phenomena and the microstructural changes.
Indeed, to be able to understand the physical mechanisms generated during the cutting operation, one is generally interested in the mesoscopic and microscopic scale. Therefore, it is possible to identify the shear zones related to the chip formation as displayed in Fig. II.5.

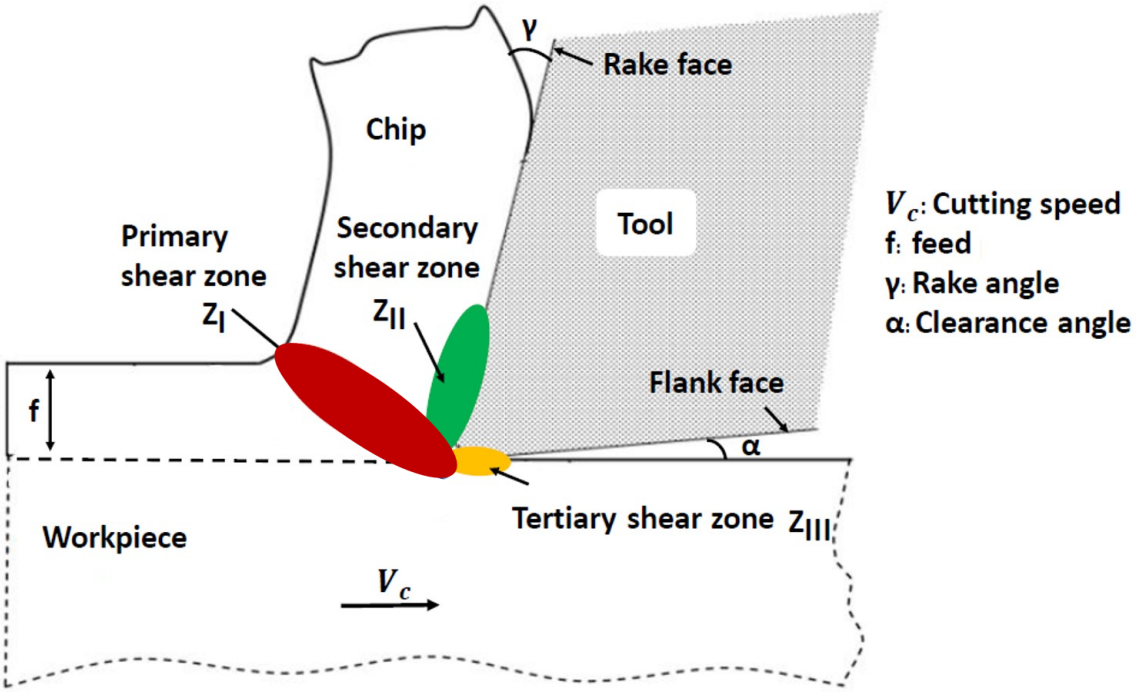

Figure II.5 – Illustration of the shear zones involved during the cutting operation.

As it can be seen, the shear zones consist mainly of :

— Primary shear zone(Z_I): It is a zone of intense shear between the tip of the tool and the rough surface of the workpiece during the passage of the tool ensuring the formation of the chip. This zone makes an angle of inclination with respect to the cutting direction. This zone is characterized by localized deformation and a significant rise in temperature;

— Secondary shear zone(Z_{II}): It is the contact zone between tool-chip inducing a high heat generation due to friction and sliding;

— Tertiary shear zone(Z_{III}): This zone corresponds to the friction between tool flank face and the machined part generating high heat energy that may cause

microstructural alterations of the workpiece material.

3.1.2 Tool wear mechanisms

In machining, the local pressures, temperatures and sliding velocity of the material against the cutting tool promote the wear of the cutting tools. It has been clearly shown in the literature that the tool flank wear affects the surface integrity of the machined components in addition to the frequency of changing the cutting tools for a given production.
In this section, we will present shortly the assessment of the cutting tool wear. Besides, we will highlight the tool wear mechanisms.

3.1.2.a Tool wear assessment

To guarantee the industrial requirements (tool life, geometric tolerances and the surface integrity of the machined component), it is compulsory to choose a tool wear criterion from then on the cutting tool must be replaced by a new one. At this line, one could cite the most used tool wear criteria that are considered as an indicator to define the maximum tool wear allowed. For instance, two geometric criteria that are used on the tool rake face and the tool flank face. The first is KB, KM and KT revealing the crater wear criteria. The second consists of VB_N and VB disclosing respectively the notch tool wear and the tool flank wear. It should be noted that the tool flank wear is not always uniform. For this reason, other criteria could be employed namely the VB_B and VB_Bmax. According to the ANSI/ASME B94.55M-1985 standard, tool flank wear criteria are commonly used to define the tool lives. Fig. II.6 shows the types of wear on turning tools.

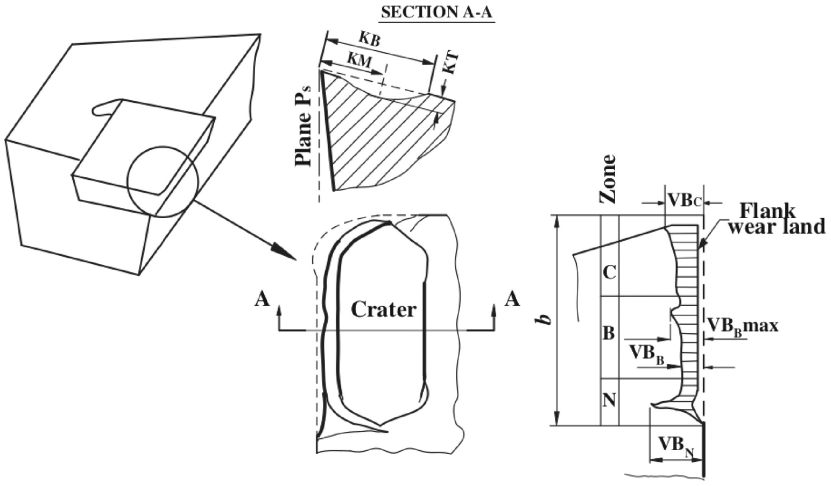

Figure II.6 – Illustration of types of wear on turning tools according to ANSI/ASME B94.55M-1985 standard.

The mechanisms of tool wear can be of mechanical origin (abrasion, mechanical fatigue, extrusion of burrs), thermo-mechanical (creep, thermal fatigue) and physico-chemical (diffusion, oxidation) (Éric and Pierre, 2016). Fig. II.7 summarizes the tool wear mech-

anisms depending on the cutting speed and the cutting temperature.

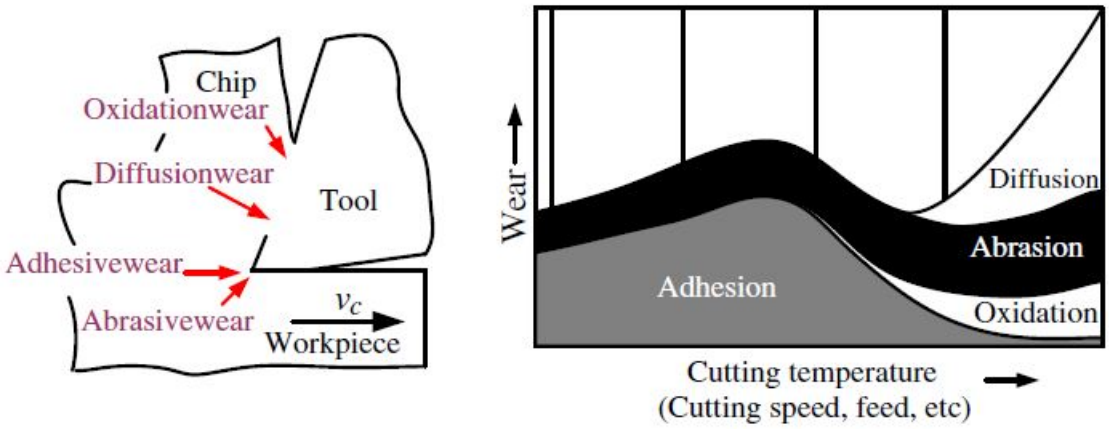

Figure II.7 – Illustration of the wear mechanisms in metal cutting (Li, 2012).

3.1.2.b Adhesion wear

Tool wear by adhesion is essentially related to the high temperature at the cutting zone, the chemical affinity of the machined material and the cutting pressure. These factors contribute to forming a layer stuck on the insert, called usually the built-up edge (BUE) (Fig. II.7). However, due to chip sliding on the tool rake face or the tool flank wear, the deposit formed is more and more important. From a certain size, the deposit becomes unstable and is carried away by the chip, it comes off therefore by tearing particles from the surface of the tool.

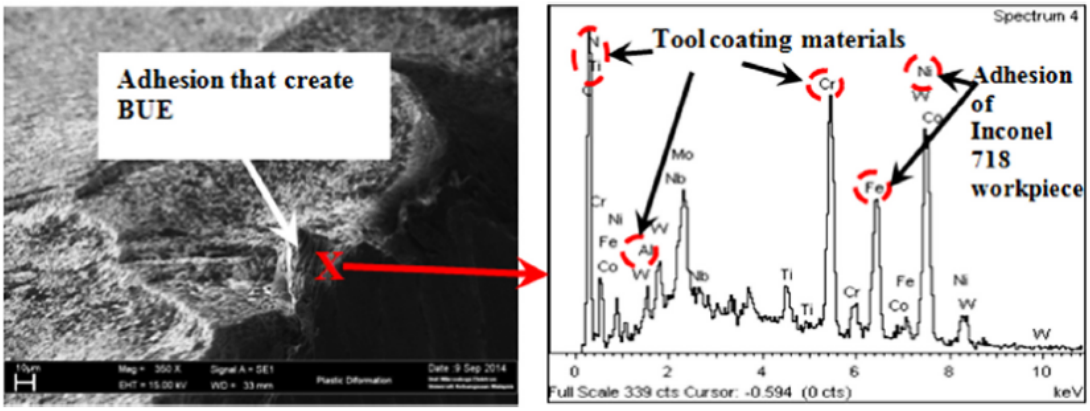

Figure II.8 – Illustration of adhesion mechanism on the tool rake face followed by EDS analysis obtained during the end milling of Inconel 718 at V_c =160 m/min, f_z= 0.15 mm/tooth, a_p=0.30 mm, a_e=0.20 mm (Musfirah et al., 2017).

3.1.2.c Abrasion wear

During the machining of certain alloys, an intruder interpenetrates between the insert and the chip. It consists of particles that stick to the insert from either the machined material or the cutting tool under the effect of contact pressure and the slip speed of

the chip. In the case of Inconel 718, carbides, having an abrasive character, can lead to this type of wear (Fig. II.9).

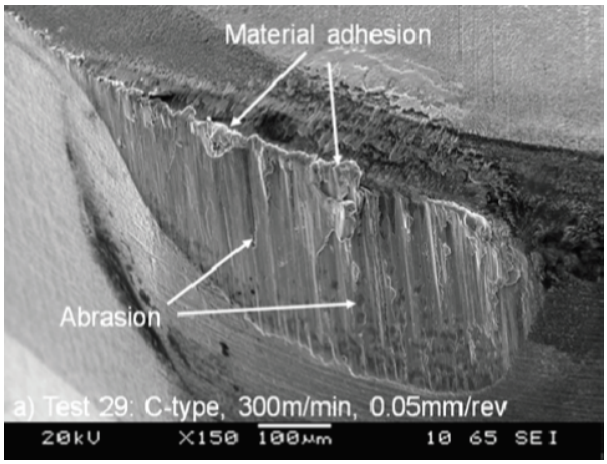

Figure II.9 – Illustration of abrasion mechanism on the tool flank face in orthogonal cutting of Inconel 718 using PCBN inserts at V_c =300 m/min, f= 0.05 mm/rev (Khan et al., 2012).

3.1.2.d Diffusion wear

The diffusion phenomenon is thermally activated inducing the displacements of the atoms of the tool material to the workpiece material. This phenomenon is more pronounced when the temperature reaches very high values that can affect about twenty micrometers from the machined surface or even the insert (Nouari and Makich, 2013). Fig. II.10 shows diffusion profiles performed on the adhesion zone and inside the worn tool revealing the diffusion of chemical elements from the machined material (Ti, Al, and V) to the cutting tool (W, Co, and C). This case study is obtained when machining Ti–6Al–4V at V_c = 20 m/min using coated (TiAlN) carbide inserts made of tungsten carbide (WC–Co).

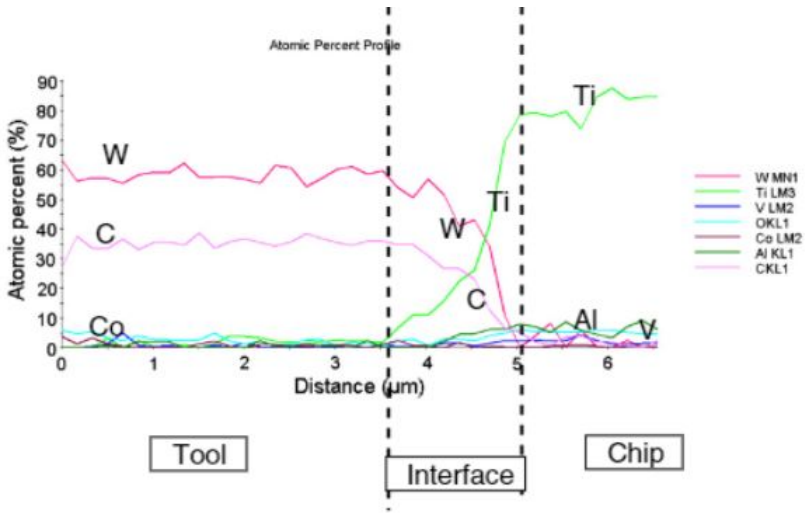

Figure II.10 – Illustration of diffusion profiles conducted on the cutting tool when machining Ti–6Al–4V at V_c = 20 m/min (Nouari and Makich, 2013).

3.1.2.e Oxidation wear

Oxidation wear comes from the formation of an oxide layer due to a chemical reaction between the machined material and the material of the tool. It is usually justified by conducting an Energy Dispersive Spectroscopy (EDS) analysis indicating the presence of oxygen at the surface. Fig. II.11 shows the EDS analysis illustrated oxidation obtained at the flank wear when the coating exposed. The work material is a nickel based alloy Hastelloy C-22HS (V_c= 180 m/min, feed rate = 0.15 mm/tooth and the axial depth =1 mm) .

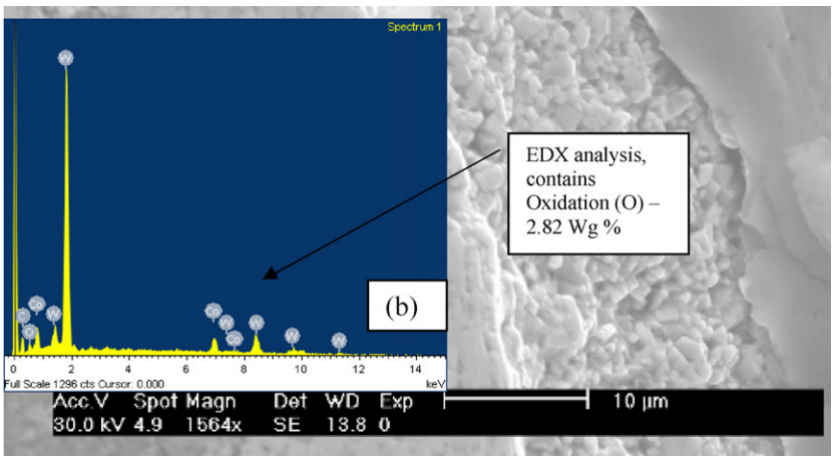

Figure II.11 – Illustration of an EDS analysis illustrated oxidation obtained at the flank wear when the coating exposed (V_c= 180 m/min, feed rate = 0.15 mm/tooth and axial depth=1 mm) (Kadirgama et al., 2011).

In this context, Zhu et al. (2013) have summarized the main causes, mechanisms, types and consequences of the cutting tool wear when machining nickel based superalloys in different cutting operations (turning, milling, drilling) given in the following Fig. II.12.

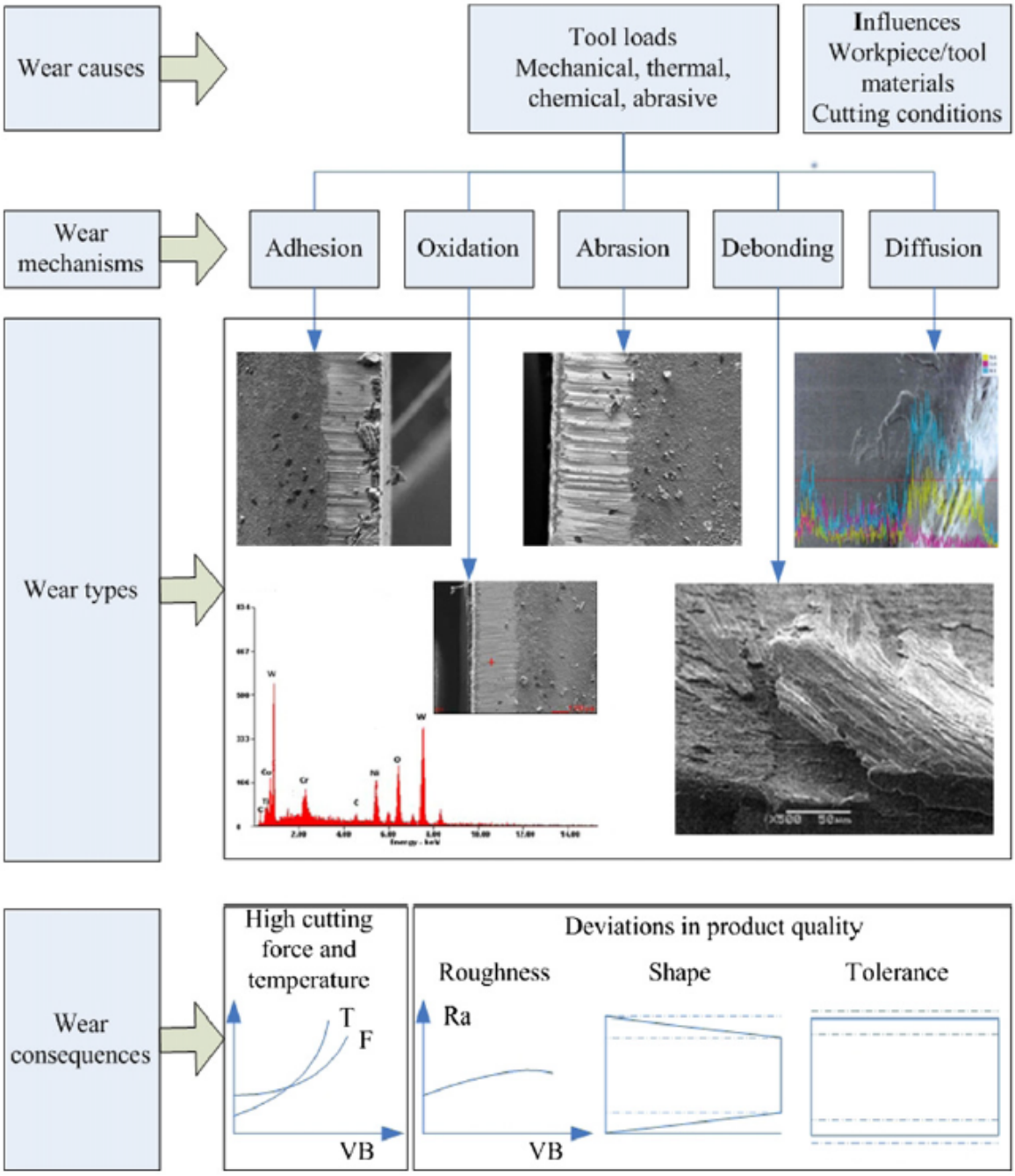

Figure II.12 – An overview of the causes, mechanisms, types and consequences of the tool wear in cutting of nickel based superalloys (Zhu et al., 2013).

3.2 Machining cooling/lubrication approaches

Machining cooling approaches essentially contributes to improving the machinability of materials with poor cutting ability and increasing cutting tool life. This applies to provide an external action at the cutting area. The external action may occur in mechanical and/or thermal form (heating or cooling). In what follows, we will list the main assisted machining strategies that were extensively reported in the literature review.

3.2.1 Laser machining approach

The laser machining approach consists in locally preheating the workpiece in order to reduce the flow stress of the material for ease of machining via a laser beam positioned upstream of the tool. The laser source and the cutting tool are driven by the same speed V.
Fig. II.13 displays the principle of laser assisted machining.

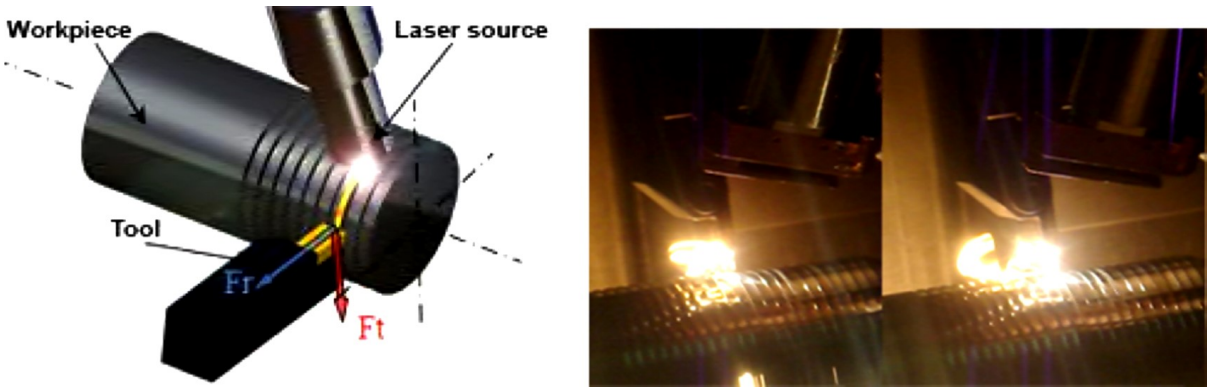

Figure II.13 – Illustration of Laser turning principle (Ayed et al., 2014).

Although the laser machining approach is not frequently employed in the industrial field, this technique has been widely studied in many research issues for different work materials (Germain et al., 2011; Braham-Bouchnak et al., 2013).

3.2.2 High pressure machining approach

The High Pressure machining approach involves delivering a jet of coolant at high pressure between the rake face of the tool and the chip. The pressure of the jet may exceed several hundred bars. The relevance of this process is closely dependent on the good choice of jet parameters such as the pressure, the diameter and the inclination of the nozzle. Fig. II.14 depicts an example of a cutting tool employing for water jet cooling condition.
Owing to its advantages and ease of implementation, this technique has been industrialized.

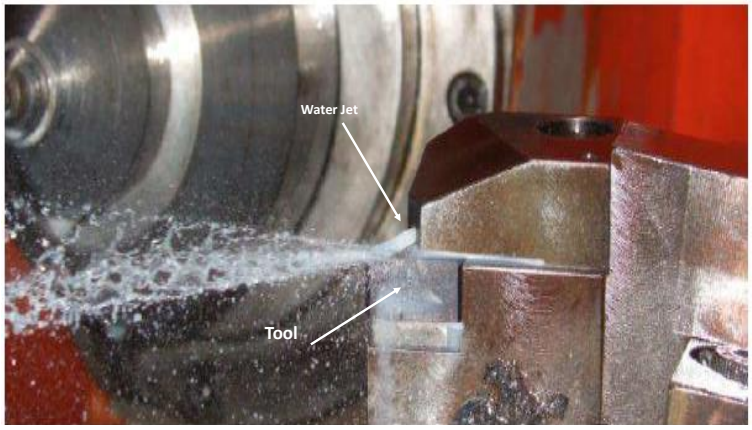

Figure II.14 – Illustration of the High Pressure machining approach (Braham Bouchnak, 2010)

.

3.2.3 Vibration machining approach

Ultrasonic machining approach, also known as vibratory machining process, consists of exciting the cutting tool with low amplitude vibrations (7.5 to 30 μm) and high frequencies (10 to 30 KHz) (Ahmed et al., 2007). Researchers applied this approach when using different materials such as steels and ceramics. Fig. II.15 presents an example of an ultrasonically turning system.

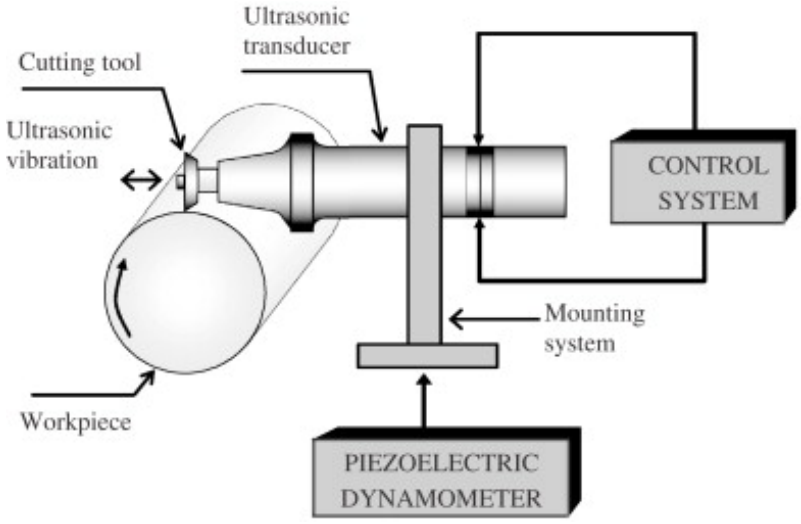

Figure II.15 – Illustration of the ultrasonically turning system (Ahmed et al., 2007)

.

Recently, Khajehzadeh et al. (2020) reported that the Ultrasonic Assisted Turning (UAT) in the case of AISI 4140 decreases the generated tensile residual stress amplitude. Authors declared that the residual stresses distribution is governed by the choice of the workpiece speed as well as the amplitude vibrations.

3.2.4 Cryogenic machining approach

The cryogenic machining approach is based on delivering a jet of cryogenic fluid (liquid nitrogen LN_2 or carbon dioxide LCO_2) at the cutting zone in order to reduce the cutting temperature and therefore minimize the adverse effects of high temperature regard the tool wear and the residual stresses as well (Ayed et al., 2017). Fig. II.16 presents an example of LN_2 Cryogenic system.
Furthermore, the supply of cryogenic fluids provides the benefits of dry machining since that LN_2 or LCO_2 promotes ecological protection. In addition, the chips are not contaminated by the cutting fluid and thereby chip recycling is much easier (Pusavec et al., 2014).
It is worth mentioning that generally speaking, the LCO_2 is not defined as a cryogenic fluid with temperature of -78 °C at ambient pressure. However, it is assimilated to a cryogenic fluid because it has similar use as the liquid nitrogen for a machining application.
More details will be provided in the next paragraphs concerning both cryogenic fluids characteristics in addition to their effect on the machinability and surface integrity.

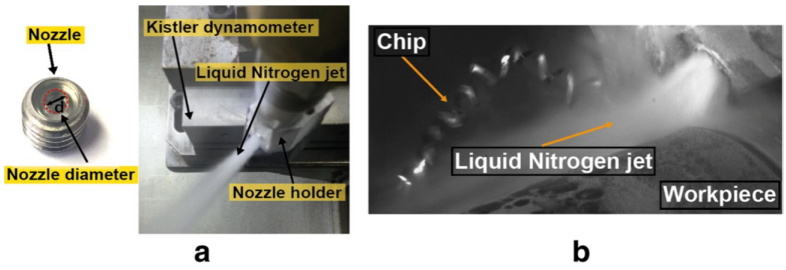

Figure II.16 – Illustration of LN_2 Cryogenic system: (a) Experimental setup; (b) High-speed camera acquisition (Ayed et al., 2017).

3.3 Cryogenic fluids characteristics: LCO_2 and LN_2

Both cryogenic fluids have their specific characteristics in terms of the mechanisms for providing the low temperatures that are very important factor influencing their use as coolants. The main properties for supplying the LN_2 and LCO_2 can be deduced from the phase diagrams displayed in Fig. II.17.

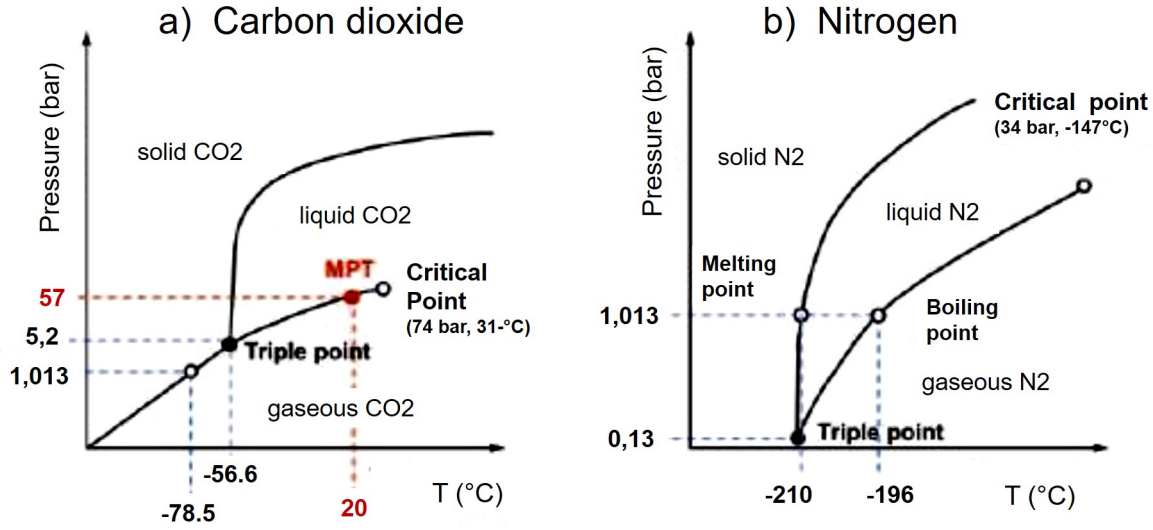

Figure II.17 – Illustration of schematic phase diagrams for: (a) Carbon dioxide; (b) Nitrogen (Stoll et al., 2014).

3.3.1 Liquid carbon dioxide: LCO_2

Fig. II.17.a presents the phase diagram for CO_2. As it can be seen below -56.6 °C and at pressure from 0 to 5.2 bar, CO_2 is either solid or gas. To obtain the liquid state, the pressure of CO_2 must be maintained higher than 5.2 bar. In cutting process, CO_2 is frequently stored at room temperature and at a pressure of 57 bar as observed in Fig. II.17.a. CO_2 is delivered from the tank through pipes into the cutting region. At the exiting from the delivering network, the LCO_2 expands and the pressure decreases to reach the atmospheric pressure to 1.013 bar. In this condition, the temperature of the fluid reaches -78.5 °C according to the Joule-Thomson effect. Phase transformation took place to form solid carbon dioxide (snow) and gaseous phase. After serving as a coolant, the solid particles sublimate to the air and no residue remains.
It is worth noting that CO_2 can also be in the supercritical form (P> 74 bar and T> 31 °C). At theses critical conditions, the CO_2 becomes a solvent, essentially used in commercial issues, particularly in the chemical extraction process owing to its low toxicity and low environmental effect. This state of CO_2 can also be used in machining assistance, in particular when it is mixed with MQL (An et al., 2020). In the current work, supercritical state of CO_2 will not be studied.

3.3.2 Liquid nitrogen: LN_2

Fig. II.17.b revealed the phase diagram for N_2. The triple point is the state where all the phases are present at 0.13 bar of pressure and at -210 °C of temperature. The liquid phase of nitrogen LN_2 occurred at very low temperature holding -196 °C. In general, to maintain the liquid state of nitrogen, the latter is stored in isolated tanks at high pressure around 15 bars. In machining process, when delivering the LN_2 at the cutting zone, the pressure drops to 1.013 bar and the nitrogen boils at -196 °C. So that, the heat dissipated is absorbed and the nitrogen gas state becomes a part of the ambient air. The nitrogen is toxic-free and safe as it evaporates and does not contaminate the working environment and non-combustible as well Nalbant and Yildiz (2011). Never-

theless, it should be noted that in certain cases the nitrogen forms a cushion depending on the delivering parameters that control the liquid state of nitrogen and therefore the cooling effect is reduced (Hong et al., 2001).

Table II.3 summarizes the characteristics of LN_2 and LCO_2 employed during the machining process reported by (Blau et al., 2015).

Table II.3 – Characteristics of LN_2 and LCO_2 employed during the machining process (Blau et al., 2015).

	LCO_2	LN_2
Feasible temperature	-78°C	-196°C
Range of cooling effect	Formation of low temperatures during expansion at tool exit	Cooling effect including the storage tank, feeding tubes and the cutting tool
Handling/integration into machine tool	Without any problems	Vacuum insulation of total feeding system (tubes) necessary
Tools	Standard tool with only few modifications	Special tool design with insulated supply

4 The effect of cryogenic machining

4.1 Effect on tool wear

In machining, the interactions between the machining material and the machined material generate very complex physical phenomena. Indeed, this manufacturing process is a thermomechanical process highly coupled in which heat, friction phenomena and plastic deformations play a crucial role in terms of wear (List, 2004).
Dhananchezian and Kumar (2011), reported the effect of LN_2 cryogenic cooling on tool wear, especially tool flank wear. According to the tests carried out during the machining of the Ti64, they revealed that the evolution of the tool flank wear, after 5 min of machining, is less important under LN_2 cryogenic conditions. Fig. II.18 shows the comparison between the wet machining and cryogenic machining in terms of tool flank wear when varying the cutting speed.

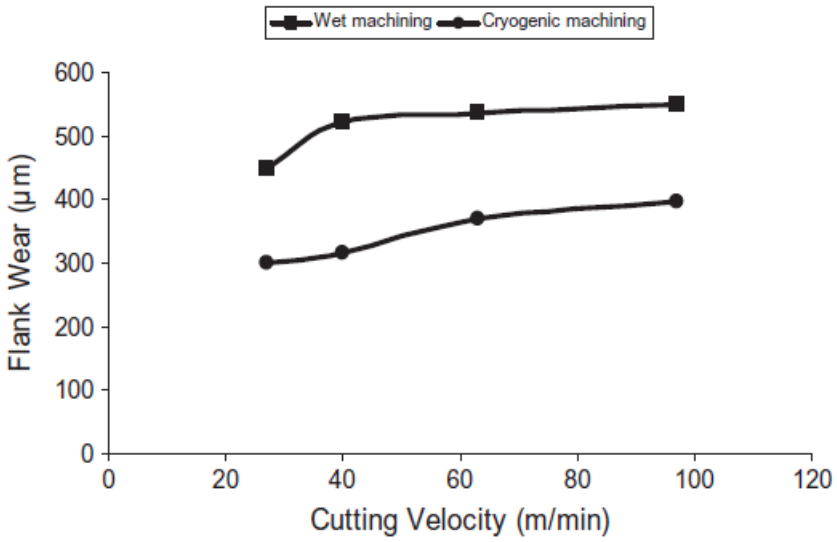

Figure II.18 – Comparison of tool flank wear when machining Ti64 under wet and LN_2 cryogenic conditions after 5 min of cutting (Dhananchezian and Kumar, 2011).

For instance, for a cutting speed V_c= 63 m/min and a feed rate f = 0.159 mm/rev, the flank wear was equal to 536 μm and 370 μm in the case of wet and cryogenic coolants respectively. In fact, a decrease in flank wear was noted with a gain of 31% in the cryogenic case compared to conventional lubrication. This is due to the fact that the liquid nitrogen jet contributes to lowering the cutting temperature and subsequently to control the wear mechanisms that are thermally activated.
Similar results have been reported by (Bordin et al., 2015) in the case of turning Ti64 in dry and cryogenic conditions varying the cutting speeds (50 m/min and 80 m/min) and the feed rates (0.1 mm/rev and 0.2 mm/rev). Authors highlighted that the LN_2 coolant promotes a significant reduction in tool wear damage as displayed in Fig. II.19. Hence, longer tool life was obtained under LN_2 cryogenic condition.

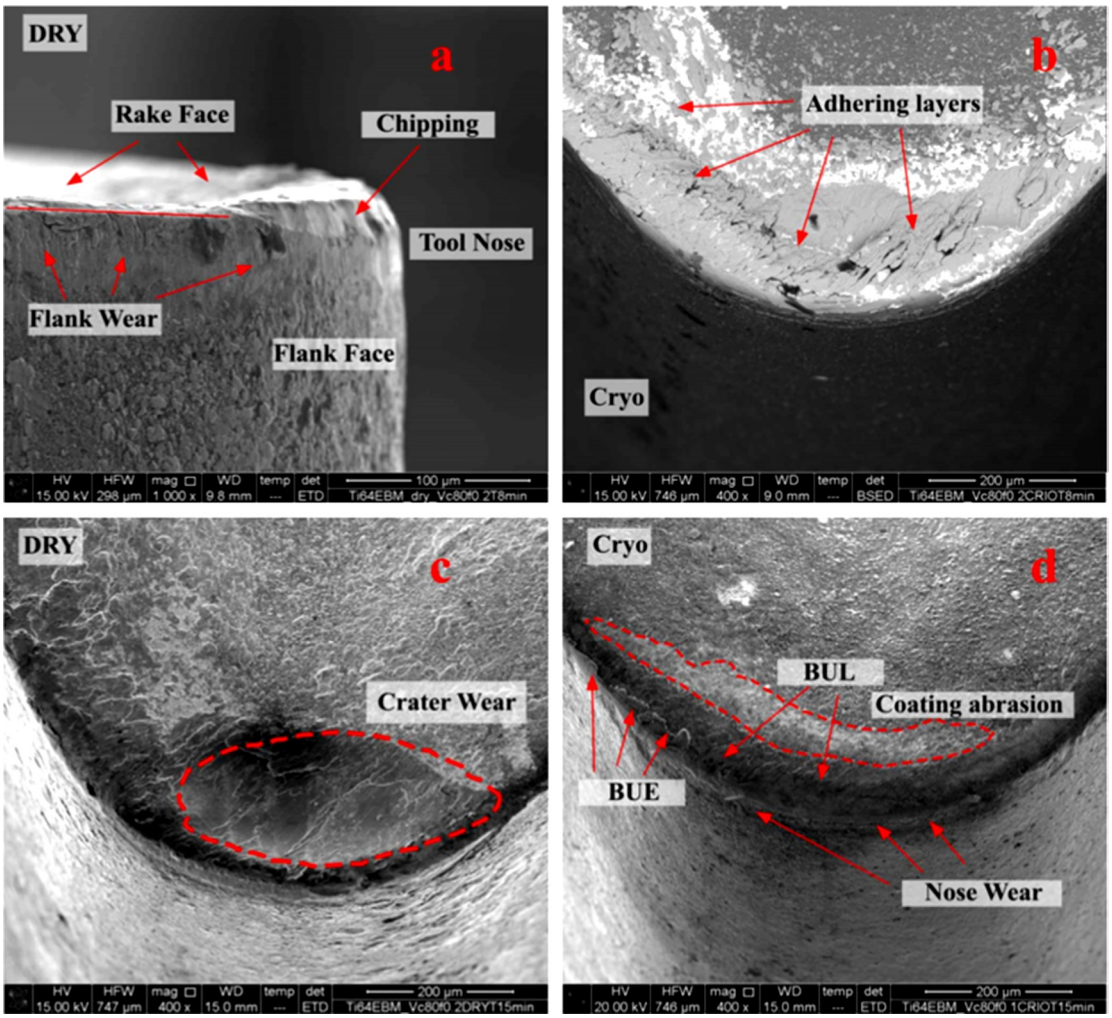

Figure II.19 – Illustration of tool wear damage when turning Ti64 after 8 min of machining under dry and cryogenic conditions (V_c= 80m/min and f =0.2 mm/rev) (Bordin et al., 2015).

Hong et al. (2001) found an identical effect with regard to LN_2 cryogenic fluid influence on tool life during machining Ti64. Results obtained have proved a noticeable improvement in tool life in the case of cryogenic machining of the titanium alloy Ti64. Authors also determined the order of the effectiveness of the cooling method (from lowest to best) as follows: dry, cryogenic cooling of the flank face of the tool, conventional cooling, cryogenic cooling of the rake face of the tool and cryogenically cooling both sides of the tool simultaneously (Fig II.20).

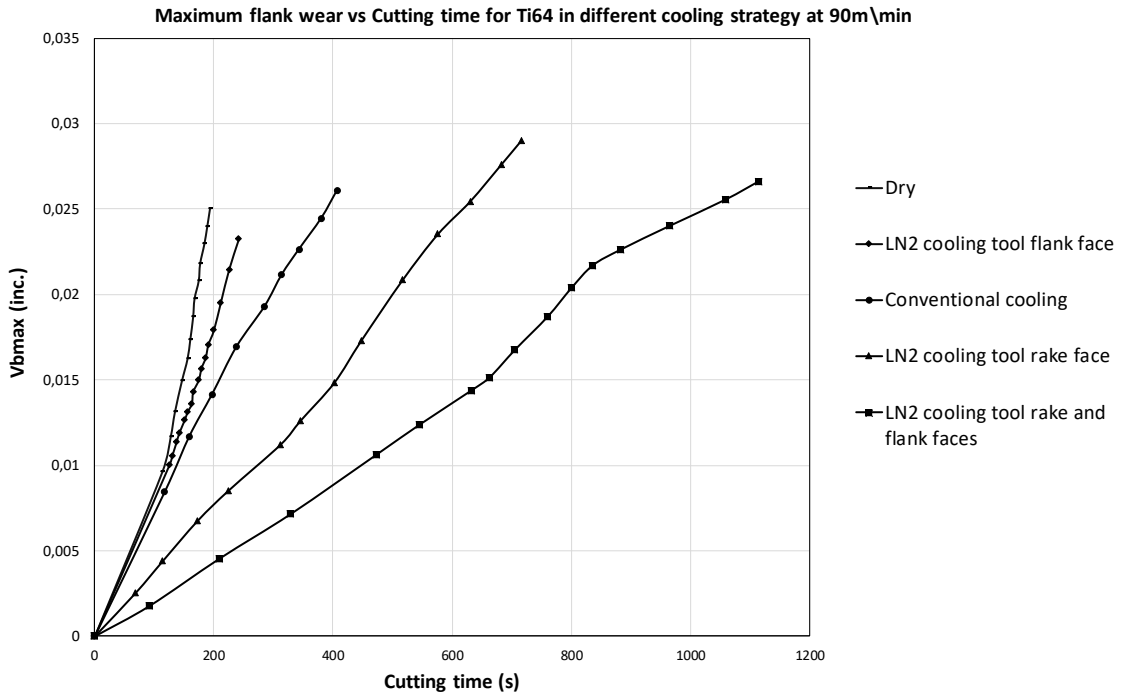

Figure II.20 – Comparison of tool life obtained during machining Ti64 under miscellaneous cooling approaches (Hong et al., 2001).

Kaynak (2014) extensively focused on the machinability of nickel based alloy Inconel 718 under LN_2 cryogenic condition in comparison with dry and MQL methods during turning operation. Regard the LN_2 delivery, a couple of nozzles were used to supply the LN_2 simultaneously at the rake and flank faces of the cutting tool. The obtained results showed a good agreement with the previous studies concerning the tool flank wear decrease compared to dry and MQL approaches until reaching 4 min of cutting.

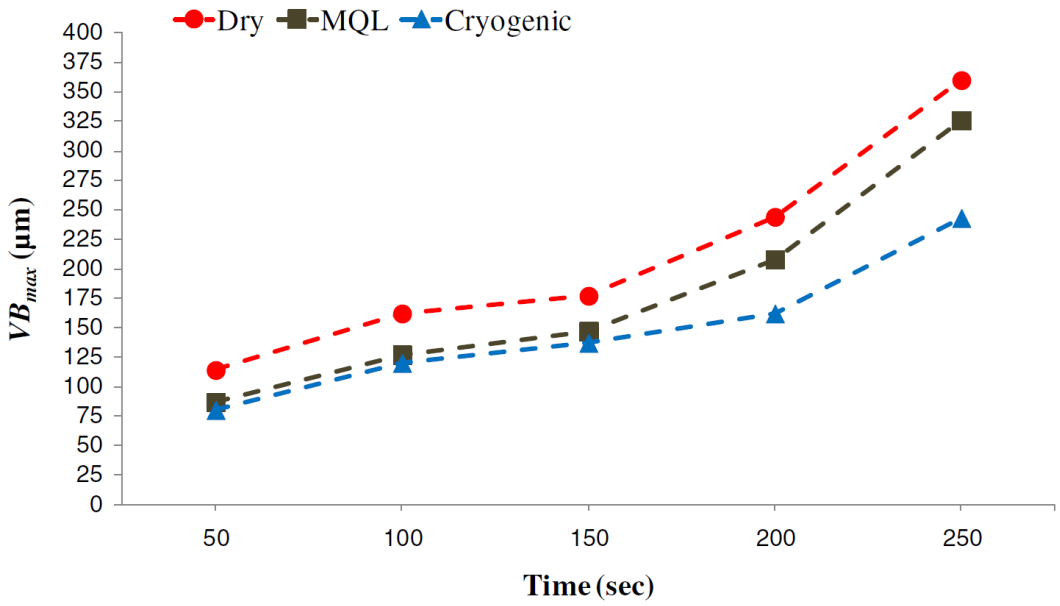

Figure II.21 – Tool flank wear evolution during machining Inconel 718 under : dry, MQL and LN_2 cryogenic conditions (Kaynak, 2014).

Although the flank wear is a fundamental parameter to determine the life of the cutting tool, the crucial factor generating the failure of the cutting tool in the case of LN_2 cryogenic cooling strategy was the notch wear (Kaynak, 2014; Musfirah et al., 2017). Under cryogenic conditions, there is an inverse effect after 100 s in machining (Fig II.22). Indeed, during a very short machining time (less than 100 s), the notch wear curve has the lowest slope compared to those of dry and MQL conditions. However, this parameter shows a very rapid increase after 100 s inducing the end of tool life.

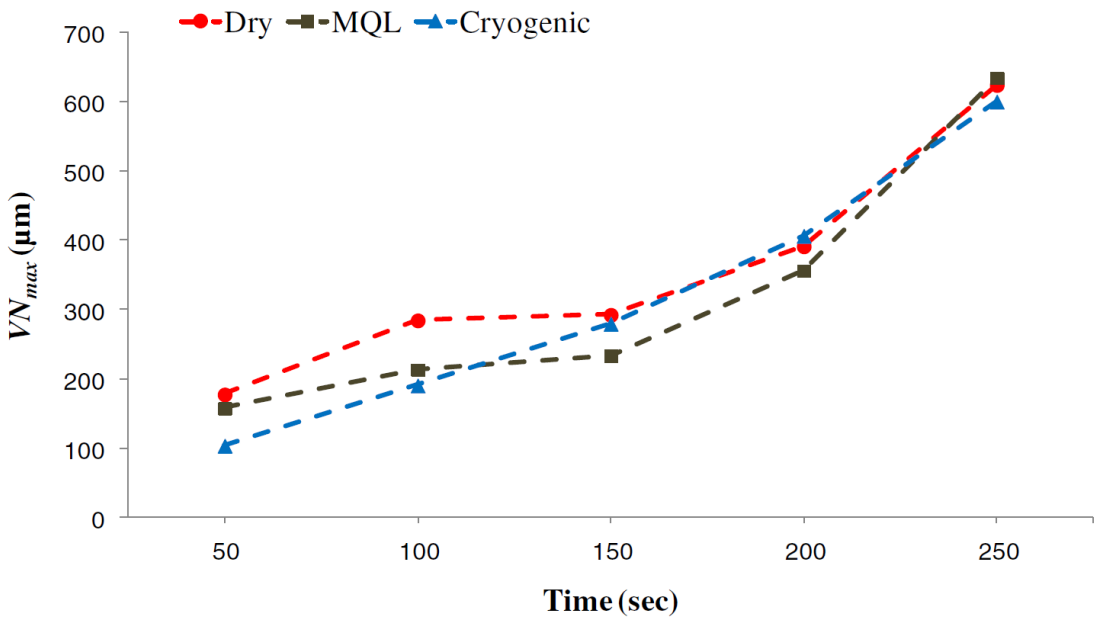

Figure II.22 – Notch wear evolution during machining Inconel 718 under: dry, MQL and LN_2 cryogenic conditions (Kaynak, 2014).

According to (Musfirah et al., 2017), the evolution of the notch wear is essentially owing to the mechanisms of abrasion and adhesion that were more important in the case of LN_2 strategy. Hence, the resistance of the cutting tool was strongly deteriorated.

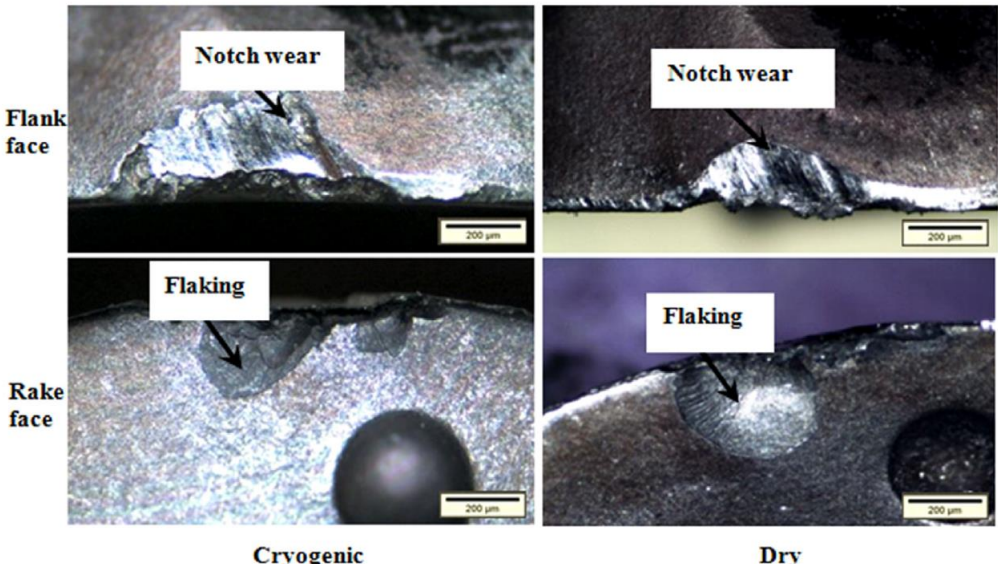

Figure II.23 – Illustration of a comparison of tool wear under two conditions: dry and cryogenic coolant (Musfirah et al., 2017).

Behera et al. (2017) have pointed out a comparative study of several cooling environments during machining Inconel 718 namely cryogenic condition, High pressure jet (HPJ), Minimum quantity lubrication (MQL) and Minimum quantity lubrication using nanofluid (nMQL) considering as a reference dry condition. The Nano minimum quantity lubrication nMQL consists of applying an amount of nanofluids (NF) to the cutting zone. NF is prepared by mixing (nano particles) NPs with the base fluid to improve the thermal as well as the tribological properties of the base fluid. In this work, authors have established a parametric study varying different cutting parameters: the cutting speed "V_c", the feed rate "f" and the effective rake angle "γ". They have recorded several responses such as the cutting forces, surface roughness and in particular the tool flank wear. Actually, with respect to the tool flank wear, experiments showed that the most dominant mechanism under all cooling strategies is the coating peeling-off as obviously illustrated in Fig II.24.
In addition, the measurements of tool flank wear have revealed that the lowest values were recorded in LN_2 cryogenic and nMQL (using the nanofluid) machining environments whereas the highest tool flank wear value of 275.6 μm at -10 ° of rake angle was obtained in dry condition. Under nMQL condition, the tool flank wear decreased until 129.6 μm while in LN_2 cryogenic condition, the tool flank wear was reduced to 99.5 μm. Overall, the authors have classified the different cooling environments with regard to the tool flank wear reduction when varying the cutting parameters that were previously mentioned (from the best to the worst): nMQL, LN_2 cryogenic, HPJ and MQL. They have reported that nMQL cutting fluid exhibits a boosting effect in terms of enhancement of the thermal and tribological properties of the coolant and thus increasing tool life and improving the surface finish of the machined part.

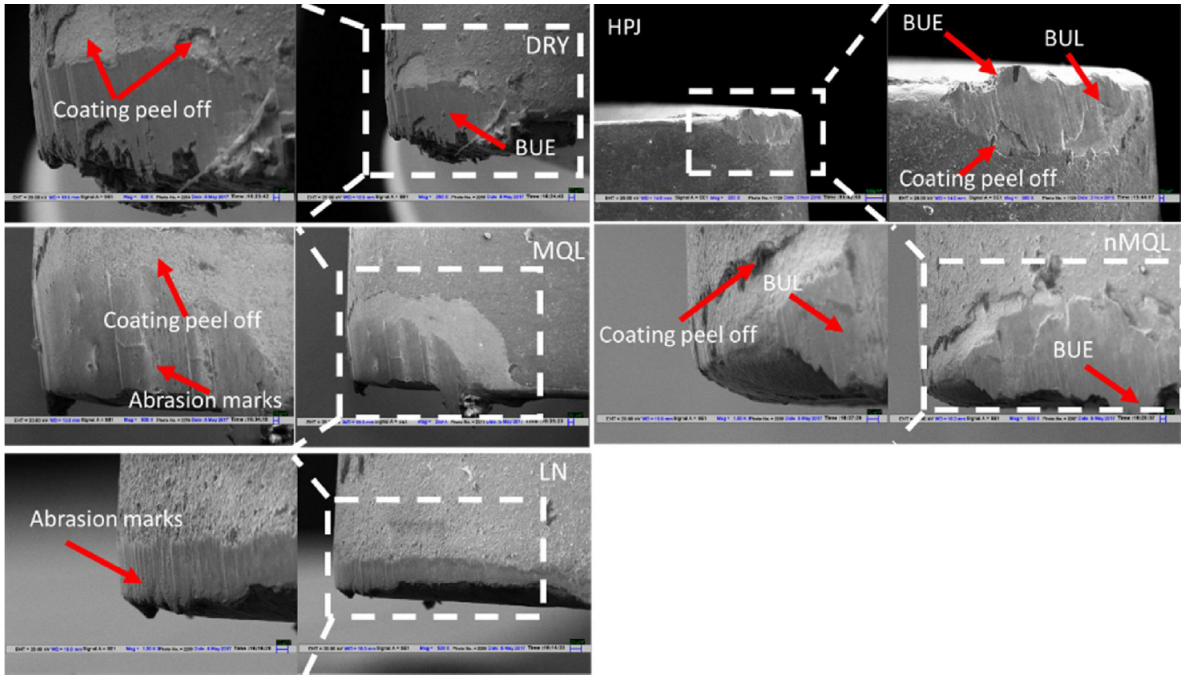

Figure II.24 – Illustration of tool flank wear when machining Inconel 718 under: HPJ, cryogenic, MQL, nMQL and dry machining environments (V_c=80 m/min, f= 0.2 mm/rev, γ =1 °) (Behera et al., 2017).

Few researches have investigated the effect of cryogenic machining using carbon dioxide CO_2 as a cutting fluid performed on several workpiece materials for instance hardened steel, Ti64 and Inconel 718. Bagherzadeh and Budak (2018) have carried out experiments using different coolant environments. They operated several configurations namely a combination of minimum quantity carbon dioxide and oil (CMQL) delivered from the rake face, CO_2 and MQL delivered from rake and flank faces respectively as well as only CO_2 delivered from rake face using two different nozzles (thin nozzle and modified nozzle) when machining Ti64 and Inconel 718 in turning operations. Each trial has been repeated three times for better repeatability. Results showed that in the case of Ti64 machined part, tool life improvement percentage was quantified compared to the case of using CO_2 condition with a thin nozzle: 177 %, 345 % and 392 % in CO_2+MQL, CMQL and CO_2 (modified nozzle) respectively (Fig II.25).
Nevertheless, in the case of Inconel 718 machined part, results showed that no improvement detected in terms of tool life in the case of CO_2+MQL condition compared to the case of using CO_2 condition with a thin nozzle while improvement percentage in tool life was recorded: 30 % and 14 % in CMQL and CO_2 (modified nozzle) respectively, compared to the case of using CO_2 condition (Fig. II.26).
Consequently, one could conclude that depending on the cutting parameters, this alternative of cryogenic coolant using either CO_2 or CMQL exhibit a great enhancement with respect to tool life.

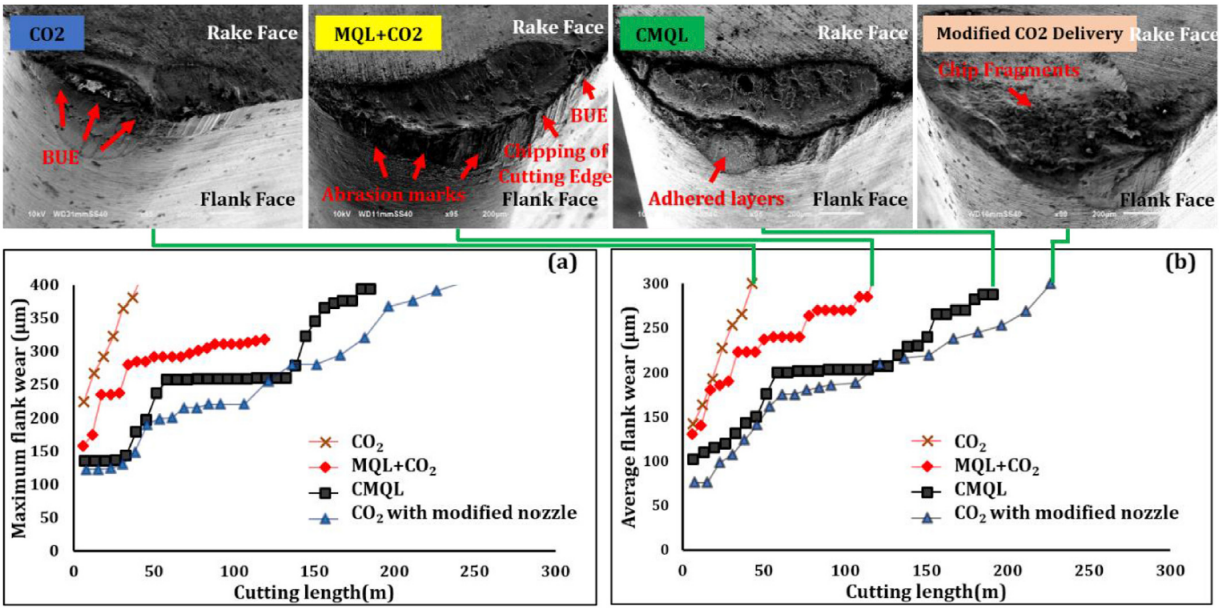

Figure II.25 – Tool flank wear progress as a function of cutting length when machining Ti64 under: CO_2, CO_2+MQL, CMQL and CO_2 (modified nozzle): (a) Maximum flank wear; (b) Average flank wear (V_c=150 m/min, f=0.2 mm/rev, a_p=1 mm, uncoated carbide inserts TPGN160308) (Bagherzadeh and Budak, 2018).

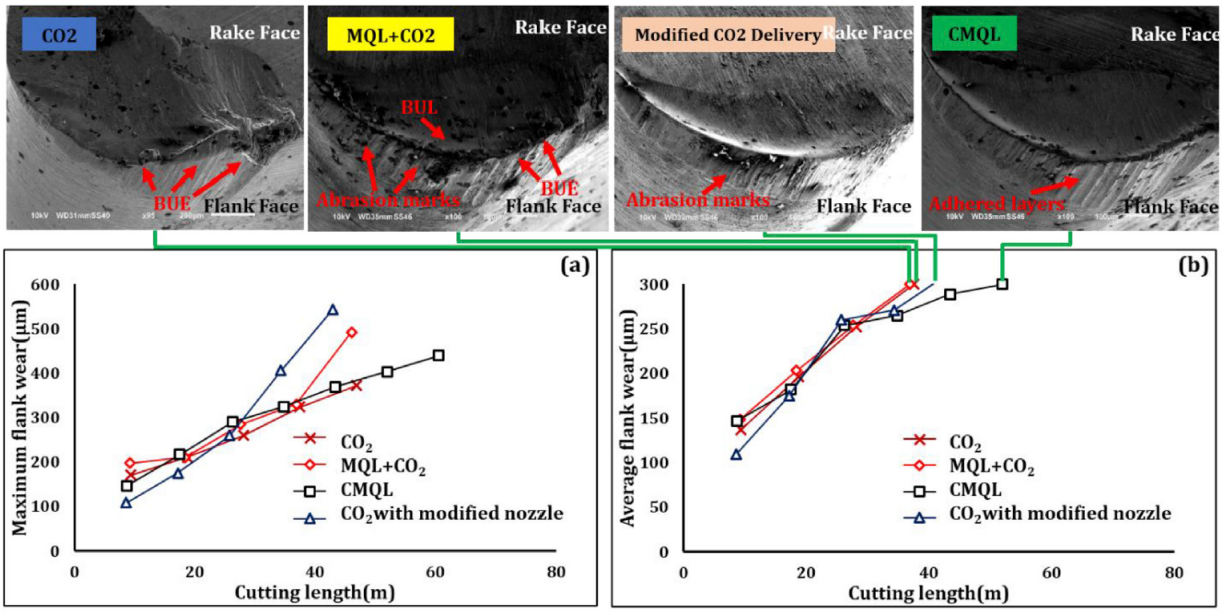

Figure II.26 – Tool flank wear progress as a function of cutting length when machining Inconel 718 under: CO_2, CO_2+MQL, CMQL and CO_2 (modified nozzle): (a) Maximum flank wear; (b) Average flank wear (V_c=100 m/min, f=0.2 mm/rev, a_p=1mm, Uncoated carbide inserts TPGN160308) (Bagherzadeh and Budak, 2018).

4.2 Effect on cutting forces

Concerning the cutting forces, cryogenic machining (LN_2 or LCO_2) showed a significant effect on the evolution of these variables. Some studies have revealed that cryogenic machining have induced higher axial forces while others have found different results. For instance, Ucak and Cicek (2018) have shown that the LN_2 cryogenic cooling fluid in drilling operation of Inconel 718 induces the elevation of the cutting forces. Authors have explained this by the fact that the use of LN_2 (-196 °C) leads to considerably reduce the cutting temperatures. This makes the material of the workpiece harder at the surface generating higher cutting forces. As it can be seen in Fig. II.27, axial forces showed the highest values in the case of LN_2 cryogenic machining compared to dry and wet machining either when using uncoated or coated drills.
This finding is in complete agreement with (Hong et al., 2001,a) in the case of turning Ti64.

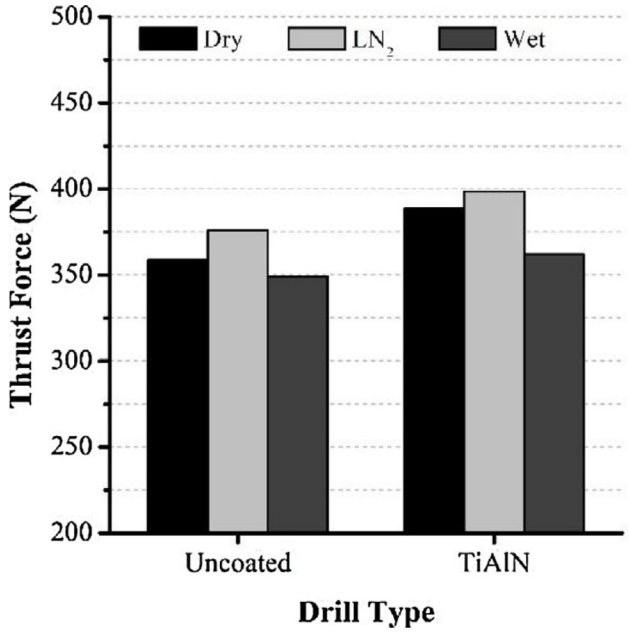

Figure II.27 – Thrust forces evolution when drilling Inconel 718 in dry, wet and LN_2 conditions (Ucak and Cicek, 2018).

Regarding the effect of LCO_2 cryogenic fluid, Ross and Manimaran (2020) have underlined that all cutting forces components have decreased in milling operations of a nickel based alloy (Nimonic-80A) under various speed–feed combinations fixing the nozzle orientation at 45 °. Fig. II.28 illustrates the correspondent results. For instance, the feed forces disclosed in LCO_2 condition 7–10 % and 3–6 % higher values compared to wet and MQL conditions respectively. Experimental outcomes highlighted that LCO_2 reduced the friction coefficient on the tool–chip interface to decrease the cutting forces components.

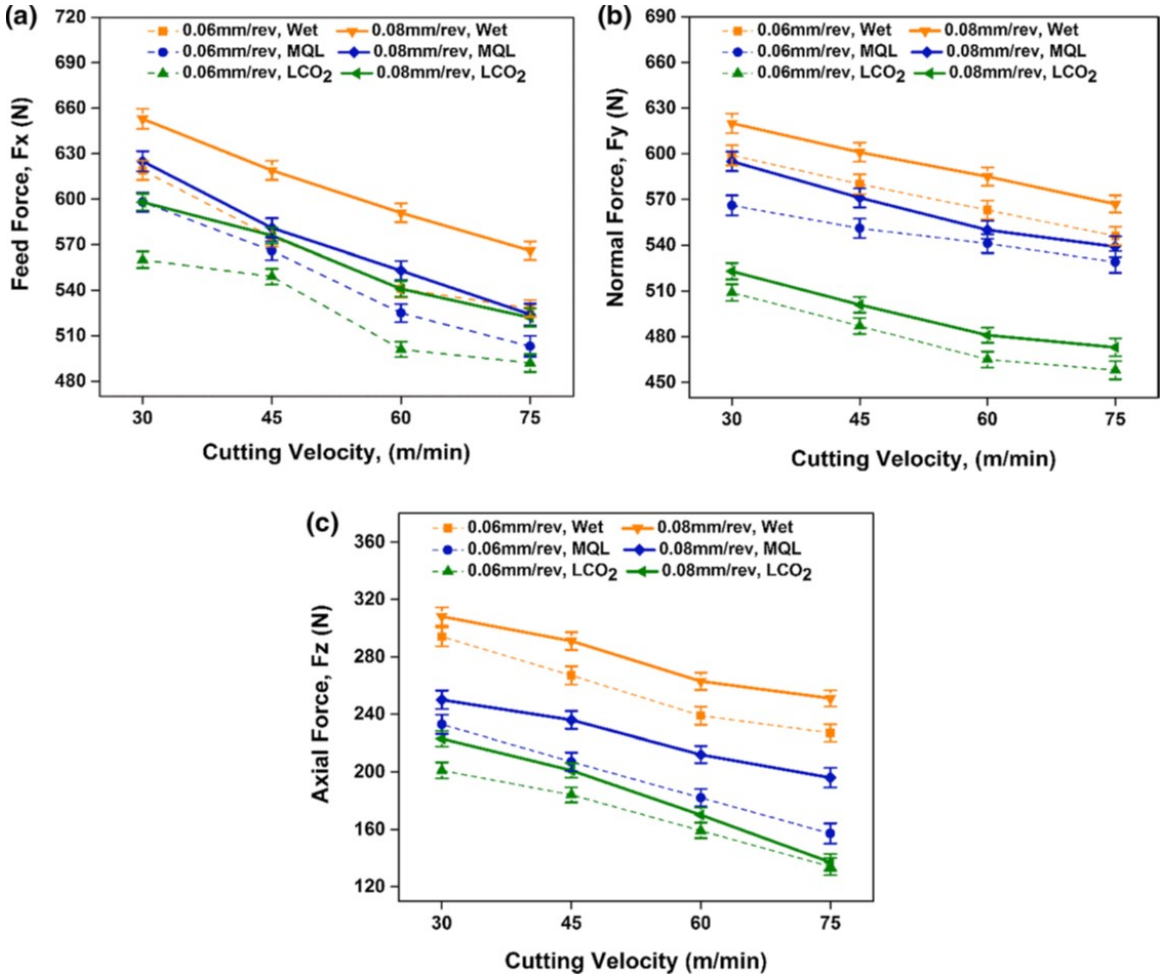

Figure II.28 – Cutting forces evolution under various machining environment: (a) feed force F_x; (b) normal force F_y and (c) axial force F_z (Ross and Manimaran, 2020).

Jerold and Kumar (2012) investigated the difference between the two cryogenic fluids effectiveness namely LN_2 and CO_2 when machining AISI 1045 steel in turning operations. Regard the cutting forces, both cryogenic coolants (LN_2 and CO_2) decrease significantly the cutting forces providing better cooling and lubrication aspects by reducing the friction between tool-chip interface. In particular, the carbon dioxide showed better performance compared to liquid nitrogen. The authors explained this fact by the high pressure jet of the former coolant allowed to penetrate the chip-tool interface decreasing drastically friction. Moreover, the application of LN_2 at very low temperature induced higher surface hardness of the workpiece that may explain the slight rise the cutting force values in comparison with CO_2. It was reported that the main cutting force is decreasing respectively by about 17-38 % and 2-12 % in CO_2 condition than conventional and LN_2 machining conditions. Furthermore, LN_2 coolant as a cutting fluids was advantageous by about 14-34 % in comparison with wet condition.

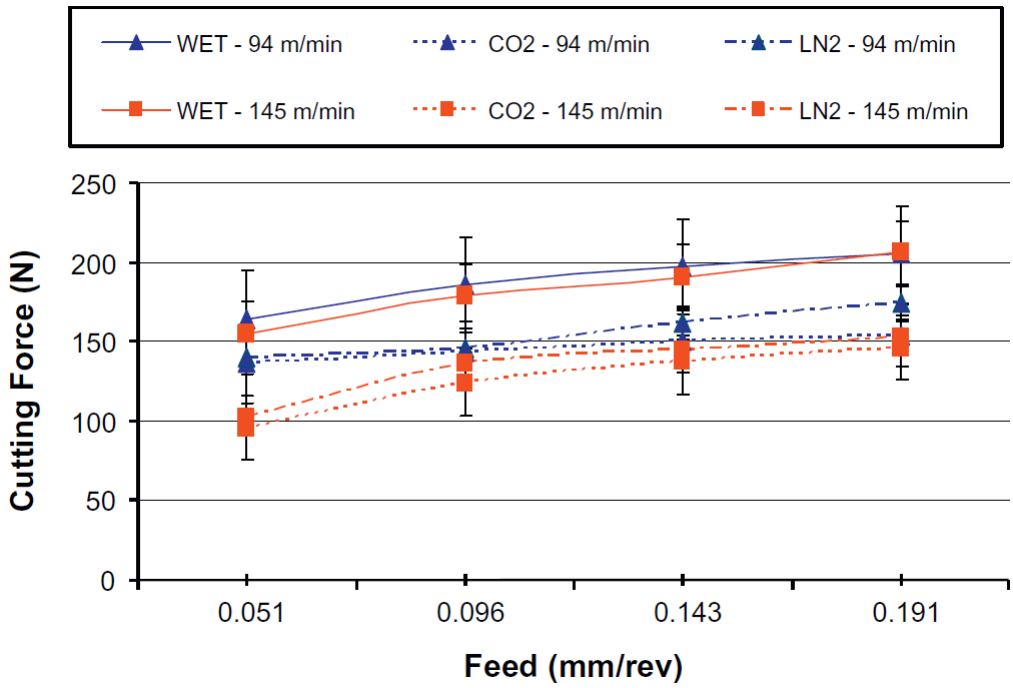

Figure II.29 – Main cutting forces evolution when varying feed rate at different cutting speed in different machining conditions (Jerold and Kumar, 2012).

Overall, it could be noted that according to literature review results, they are some contradictions about the effect of cryogenic machining on the cutting forces. Some studies found that cryogenic coolants reduced the cutting forces values due to the reduction of the friction. However, others showed that the rise of the cutting forces is caused by the increase of the hardness of the work material. Therefore, the explanation of such behaviors could not easily be revealed since several parameters (work material, cryogenic coolants and cryogenic set-up) are very different to be able to justify these contradictions.

4.3 Effect on the cutting temperature

As a whole, the acquisition of the cutting temperature during the machining process arise some difficulties owing to the small size region involved. Besides, the material deformation region in machining is sub-millimeter size. So that, the assessment of the cutting temperature using the thermocouples imply inaccurate measurements, it helps to have an order of magnitude. Another technique that has shown better estimation of cutting temperature consists of the infrared cameras. However, regard the cryogenic machining, this technique discloses certain limits. Indeed, during the cryogenic cutting, the cooling rate is high and the time of the cooling period is in milliseconds. Available infrared cameras on the market own a limited frame rate and a fairly long integration time. At this line, Lu et al. (2013) reported that infrared cameras are not sufficiently fast to detect the rapid temperature evolution occurring under cryogenic condition.

Aramcharoen and Chuan (2014) have examined the efficiency of LN_2 cryogenic fluid during milling operation of Inconel 718. In particular, authors have figured out the measurement of cutting temperatures obtained in different machining configurations. To do this, they had resorted to using infrared cameras. Thus, a significant reduction

has been evaluated in the case of cryogenic conditions in comparison with dry machining. Indeed, the maximum temperature obtained under cryogenic conditions is of the order of 200°C (473 K). However, this parameter reaches a higher value which is 570°C (843 K) in the case of dry machining. This result highlights the effectiveness of the LN_2 cryogenic fluid as a cooling method (Fig II.30). Nevertheless, the fact of employing infrared camera during the machining process when cooling with LN_2 raises many questions. When machining using LN_2 as a coolant, its evaporation when exposing to the air leads to high amount of gas phase that may dramatically disrupt the infrared camera and thus wrong measurements.

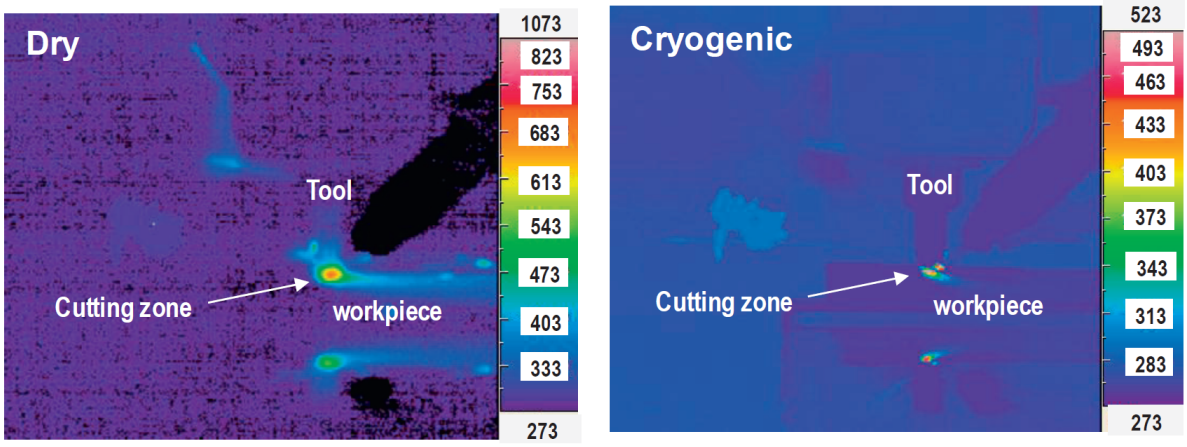

(a) (b)

Figure II.30 – Illustration of cutting temperature measured by means of an infrared camera during milling operation of Inconel 718: (a) dry; (b) cryogenic given in Kelvin (Aramcharoen and Chuan, 2014).

Lower cutting temperature have been obtained under LN_2 cooling condition when drilling Inconel 718 in comparison with dry and wet machining conditions (Ucak and Cicek, 2018). K-type thermocouples that were employed are suitable to measure temperature in the range from -200°C to 1200°C. Five thermocouples were positioned along the thickness of the drilled holes in all machining conditions. Fig. II.31 displayed the positions and the dimensions of the thermocouples located on the workpiece.

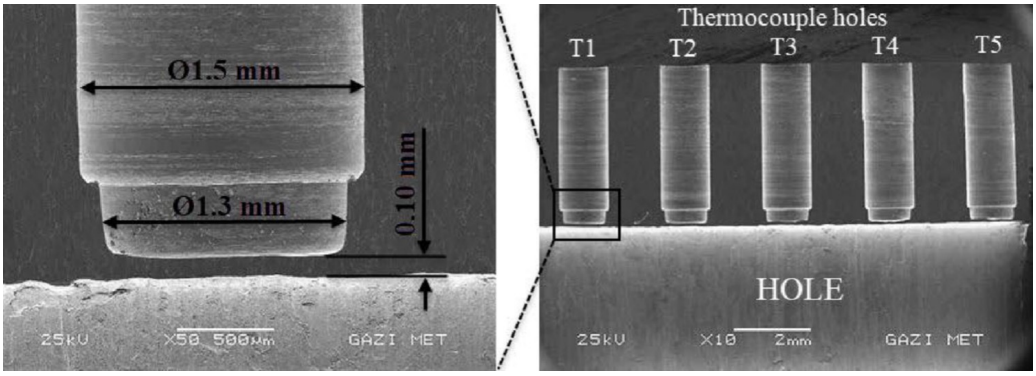

Figure II.31 – SEM images of the cross section of the workpiece showing positions and dimensions of thermocouple holes (Ucak and Cicek, 2018)

.

Fig. II.32 discloses the maximum cutting temperature measured with each thermocouple under all drilling conditions. As it can be seen, the LN_2 reduced significantly the cutting temperature assessed for each position of the thermocouples. For instance, the maximum temperatures measured at T5 position, cryogenic cooling decreases the cutting temperatures by 12.5 % and 66.3 % when using uncoated and by 54.3 % and 81 % when using TiAlN coated drills compared to wet and dry conditions, respectively.

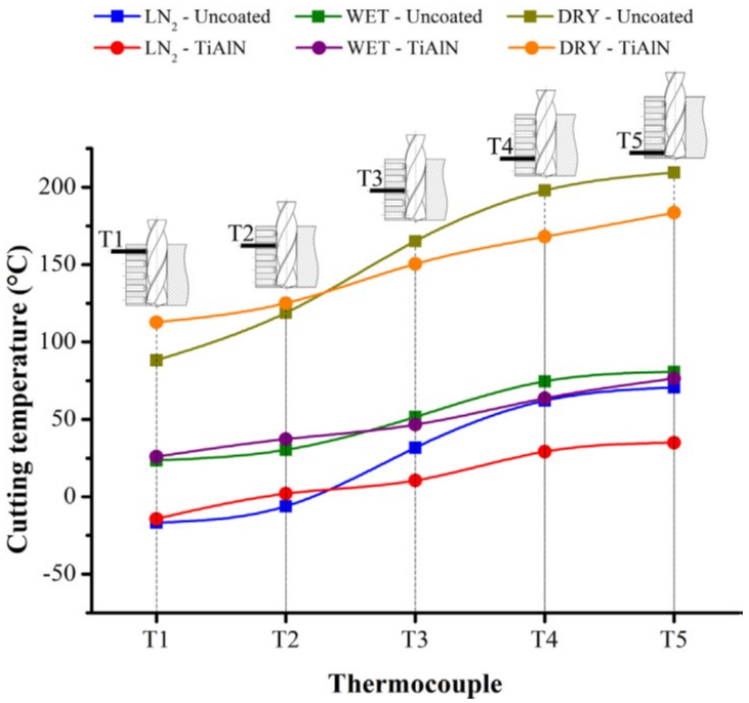

Figure II.32 – Cutting temperature values under different machining conditions (Ucak and Cicek, 2018).

4.4 Effect on friction coefficient

Tribological aspect constitutes an important issue in cutting process owing to its drastic influence on the cutting forces and the cutting temperatures as well. Therefore, one is interested in lowering as possible the friction coefficient in order to improve the machinability of the work materials. In this context, researches examined the effect of the cryogenic coolant regard the friction coefficient.

Courbon et al. (2013) investigated the lubrication efficiency of LN_2 cryogenic fluid when machining Inconel 718 and Ti64. Authors studied the tribological behavior of a carbide insert in contact with the two previous materials. They used an open tribometer equipped with a TiN coated carbide tool rubbing in one side on an Inconel 718 bar and in the other side on a Ti64 bar. Results have revealed that in the case of Ti64, the friction coefficient hardly changes. However, a good improvement has been detected in the case of Inconel 718 where the friction coefficient has decreased as displayed in Fig. II.33 and Fig. II.34. This could be explained by the fact that the tribo-chemical behavior of both materials is different: titanium has a higher tribo-chemical affinity with nitrogen than Inconel 718 (Courbon et al., 2013).

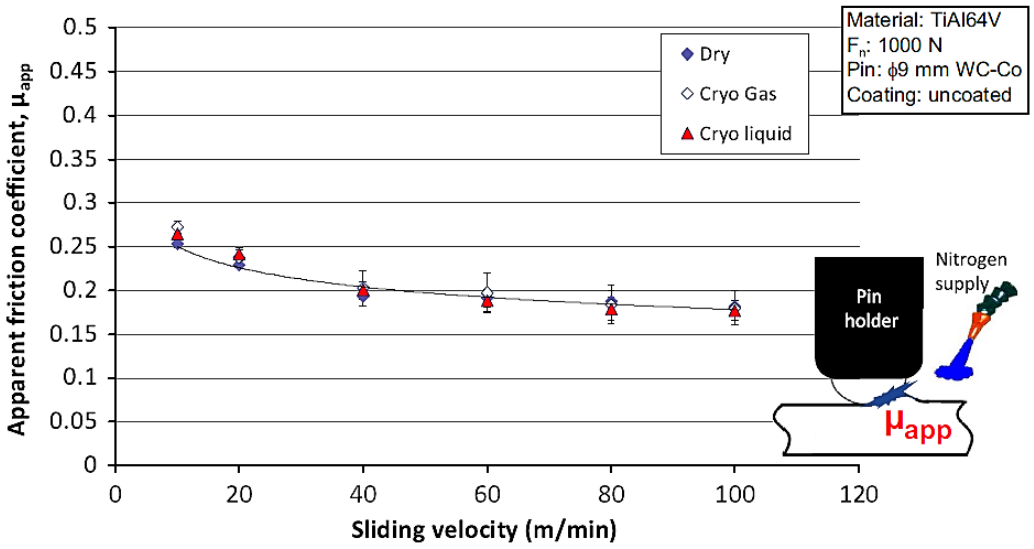

Figure II.33 – Friction coefficient evolution at the interface between tool-chip versus the sliding velocity (Ti64) (Courbon et al., 2013).

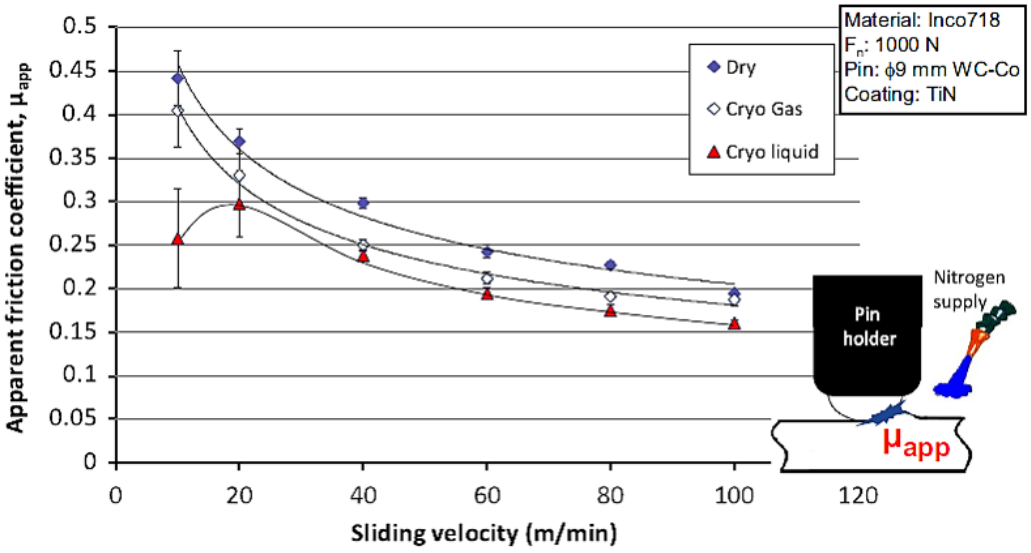

Figure II.34 – Friction coefficient evolution at the interface between tool-chip versus the sliding velocity (Inconel 718) (Courbon et al., 2013).

Recently, Courbon et al. (2020) have studied the effect of LCO_2 on the friction coefficient when cutting Ti64 and AISI1045 with carbide tools. Results have shown that applying only LCO_2 did not change the friction coefficient compared to dry machining while combining LCO_2+MQL decreased significantly the friction coefficient from 0.5 to 0.1 compared to the other machining conditions in the case of AISI1045. In contrast, in the case of Ti64, neither LCO_2 nor the combination LCO_2+MQL have reduced the friction coefficient.
It could be deduced that the effect of the cryogenic coolants on the friction coefficient depends on the work material.

4.5 Effect on surface integrity

Surface integrity is a very important parameter that must be well controlled by machining as it affects the service life of parts during their use. In the aeronautical sector, many components of the aircraft are severely subjected to very high temperatures, heavy mechanical loads and hostile environment. Several fracture analyses of the dynamic parts showed that the latter break by fatigue because of the cracking that initiates and propagates from the surface. Therefore, one must pay a lot of attention to the surface integrity of the machined parts. In what follows, we will discuss the effect of cryogenic machining on the surface integrity (surface roughness, micro-hardness and residual stresses) of manufactured components.

4.5.1 Surface roughness

The surface roughness is a major parameter to characterize the surface quality of the machined part. At this line, many studies have examined the effect of cryogenic cooling on surface roughness induced. Most of these studies have shown the positive effect of this cooling approach on surface quality of the machined parts (Bordin et al., 2017; Rotella et al., 2014; Dhar and Kamruzzaman, 2007). For instance, Dhar and Kamruzzaman (2007) have focused on the LN_2 performance in turning operations of AISI-4037 steel under different machining configurations (cutting parameters: f and V_c and cooling conditions: dry, wet and LN_2 cryogenic conditions). LN_2 provided the best surface finish in comparison with dry and wet machining for all tested cutting speeds and feed rates values. Fig . II.35 presents an example of the outputs obtained for a fixed cutting speed (V_c = 264 m/min) and a feed rate (f= 0.13 mm/rev) under the three machining environment. These results are consistent with those found by (Bordin et al., 2017; Rotella et al., 2014) who conducted experimental investigations to evaluate the performance of cryogenic machining versus dry and MQL machining conditions of titanium alloy Ti64.

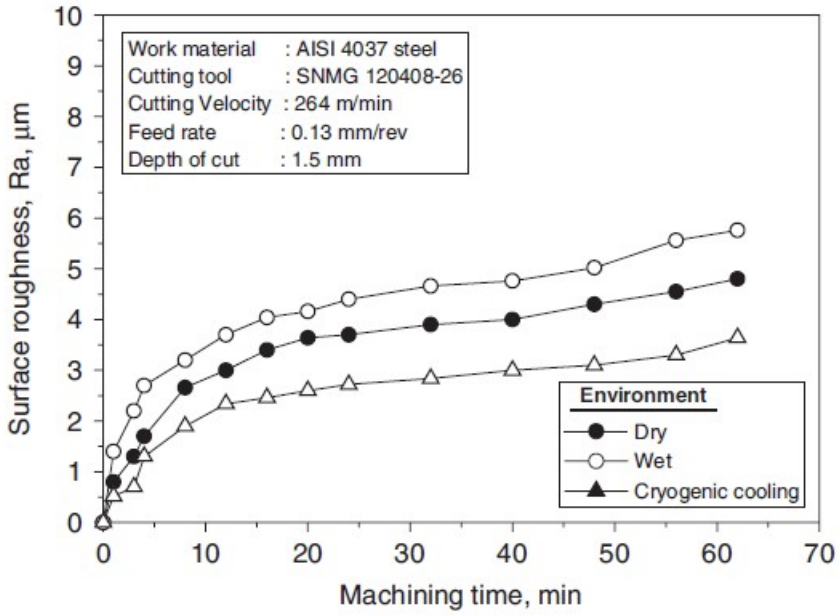

Figure II.35 – Illustration of the surface roughness evolution during machining time under dry, wet and LN_2 cryogenic conditions at V_c=264 m/min and f= 0.13 mm/rev (Dhar and Kamruzzaman, 2007).

Nevertheless, Iturbe et al. (2016) have figured out an opposite effect of LN_2 cryogenic condition when machining Inconel 718. The surface roughness parameters (R_a and R_t) showed much higher values when comparing with the conventional lubrication (Fig. II.36). Authors have explained this result by the fact that the high values of tool wear picked up under the cryogenic condition affects significantly the surface condition of the machined parts.

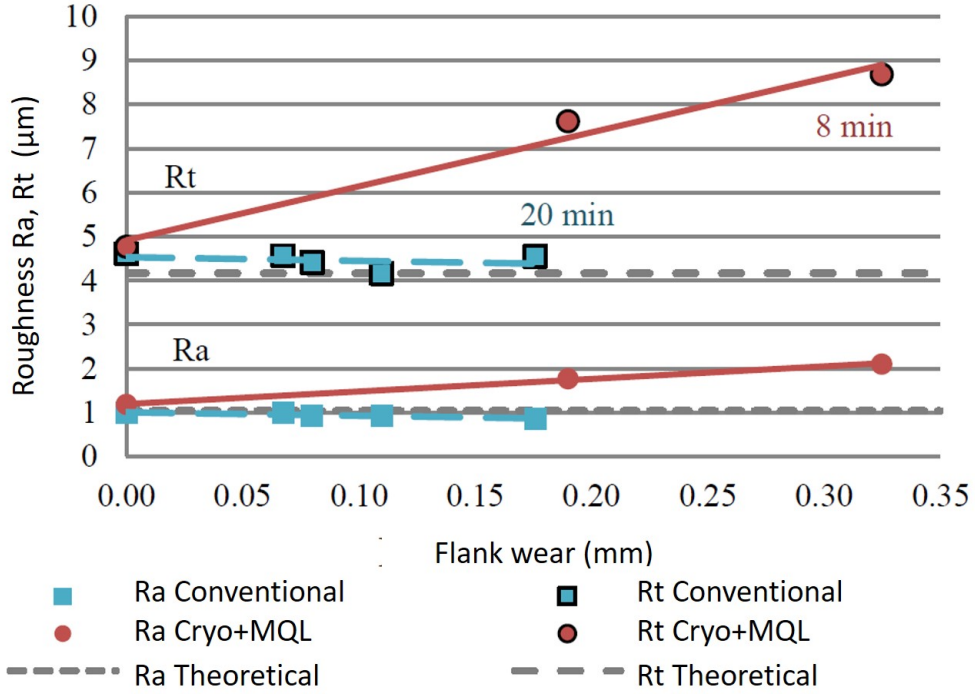

Figure II.36 – Illustration of surface roughness evolution versus tool flank wear during the machining of Inconel 718 in turning operations under conventional and Cryo+MQL cooling strategies (Iturbe et al., 2016).

Lately, Jamil et al. (2021) have carried a comparative study between several machining cooling strategies namely MQL, LN_2 and CO_2 considering as a reference dry conditions. As compared to dry milling, the improvement in surface quality was about 53.8 %, 39.7 %, and 32.8 % in CO2-snow, LN2 and MQL sustainable cooling strategies, respectively. Fig. II.37 summarizes the obtained results under all cooling strategies.

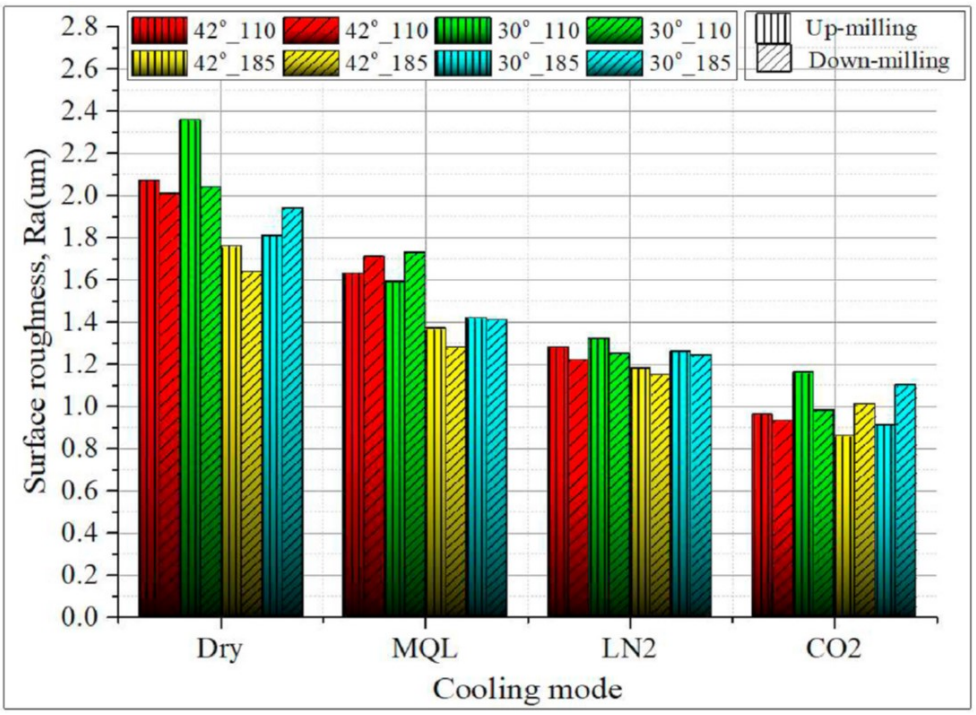

Figure II.37 – Illustration of surface roughness obtained under dry, MQL, LN_2 and CO_2 cooling conditions showing the effect of milling parameters and cooling modes (Jamil et al., 2021).

4.5.2 Residual stresses

Several studies have reported the effect of machining processes on the surface integrity of machined parts, in particular residual stresses. The common results that have been reported in the literature review in the case of steels (Leadebal Jr et al., 2018), titanium alloys (Ayed et al., 2017) and nickel based alloys (Pusavec et al., 2010) revealed that LN_2 cryogenic condition either reduced the tensile residual stresses at the surface (and at the subsurface) or generated compressive residual stresses depending on the work materials.

Leadebal Jr et al. (2018) have investigated the cryogenic effect on surface integrity of AISI D6 steel compared to dry machining. Authors have tested different LN_2 cryogenic delivery positions namely delivering LN_2 on the tool flank face, on the rake face and on both faces simultaneously.

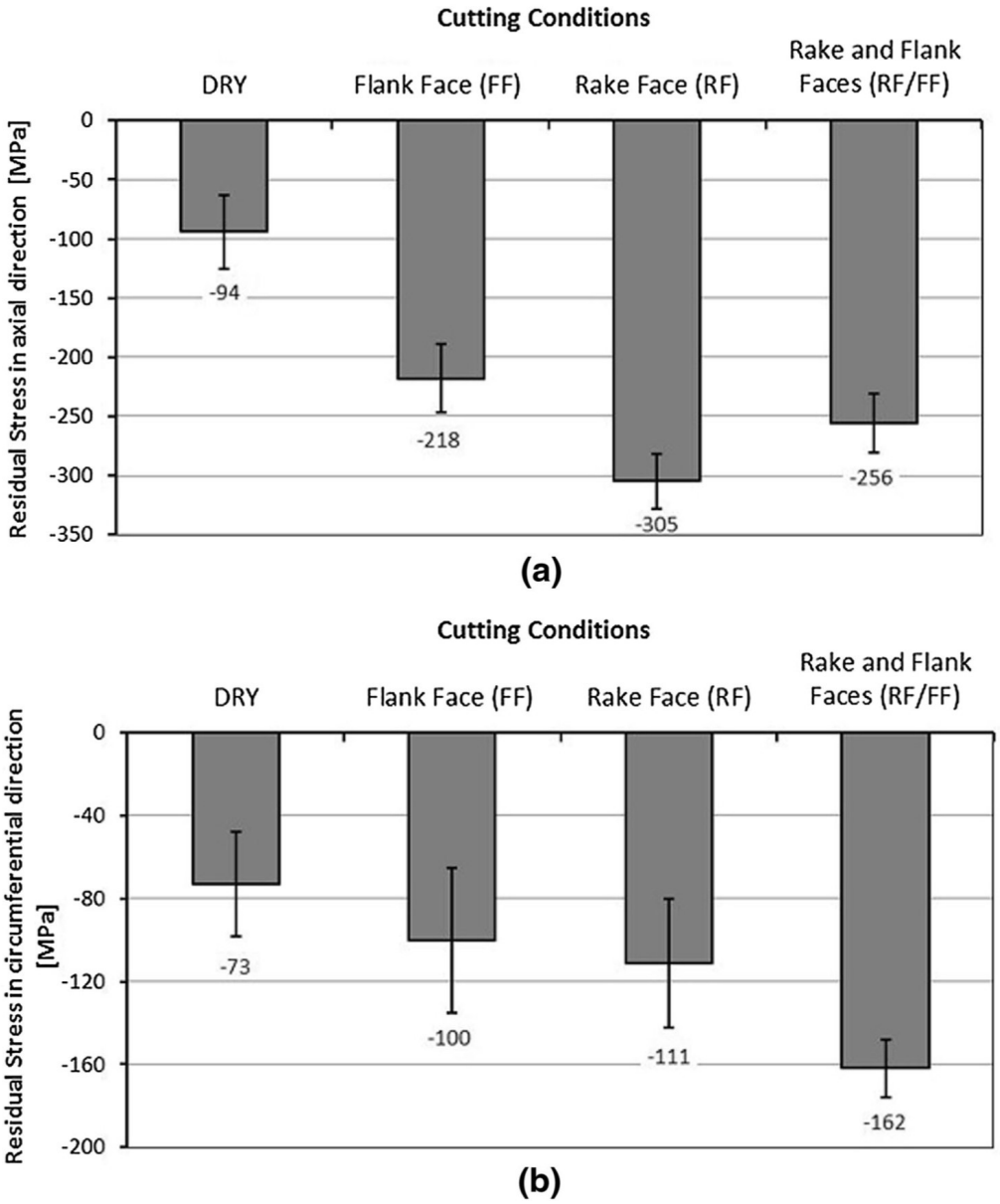

Figure II.38 – Illustration of the residual stresses profiles measured along : (a) Axial direction; (b) Cutting direction (Leadebal Jr et al., 2018).

Results figure out that, when comparing to dry condition, all cryogenic configurations led to higher compressive residual stresses on the surface along the cutting and the feed directions using fresh tools. Axial residual stresses exhibit higher compressive values compared to hoop stresses in all cutting conditions relatively important when LN_2 is applied on the tool rake face. Nevertheless, hoop residual stress reveals the highest compressive value when LN_2 is applied on both tool faces.

Ayed et al. (2017) has disclosed the influence of cryogenic machining conditions on turning operations of Ti64. They revealed that the residual stresses are extremely influenced by machining cooling methods. The most efficient result is obtained in the case of cooling with the cryogenic fluid. This may be justified by the fact that cooling at cryogenic temperatures induces a significant decrease in temperatures in the cutting zone. Subsequently, decrease the tendency to generate thermal loads generating tensile

residual stresses (Fig. II.39).

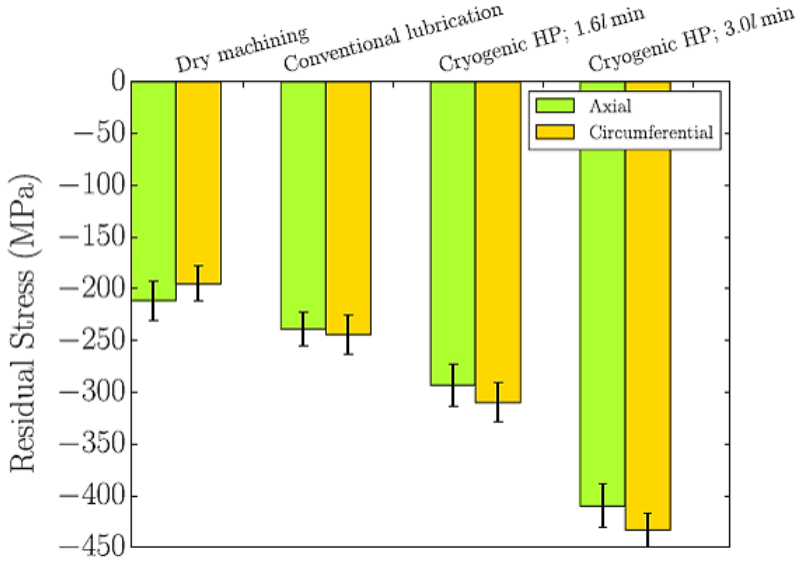

Figure II.39 – Illustration of the effect of several cooling strategies on residual stresses when machining Ti64 in turning operations (Ayed et al., 2017).

Pusavec et al. (2011) have extensively investigated LN_2 cryogenic performance when machining Inconel 718, in particular its influence on the residual stresses. The cutting parameters : V_c = 60 m/min, f=0.05 mm/rev and a_p =0.63 mm were chosen in such a way that cutting forces, cutting temperature and tool lives induced optimum values. With respect to residual stresses, the profiles were measured at the surface and at the sub-surface of the machined part when machining using new tools. Results have shown that LN_2 induced the lowest tensile residual stresses near the surface and the highest compressive residual stresses at the depth of the machined surfaces as illustrated in Fig. II.40. The compressive zone below the surface is thicker for the case of cryogenic conditions, extending the compressive zone from 40 μm to 70 μm (for 185 %) compared to dry condition. The same explanation previously stated was announced to justify these results (Ayed et al., 2017).

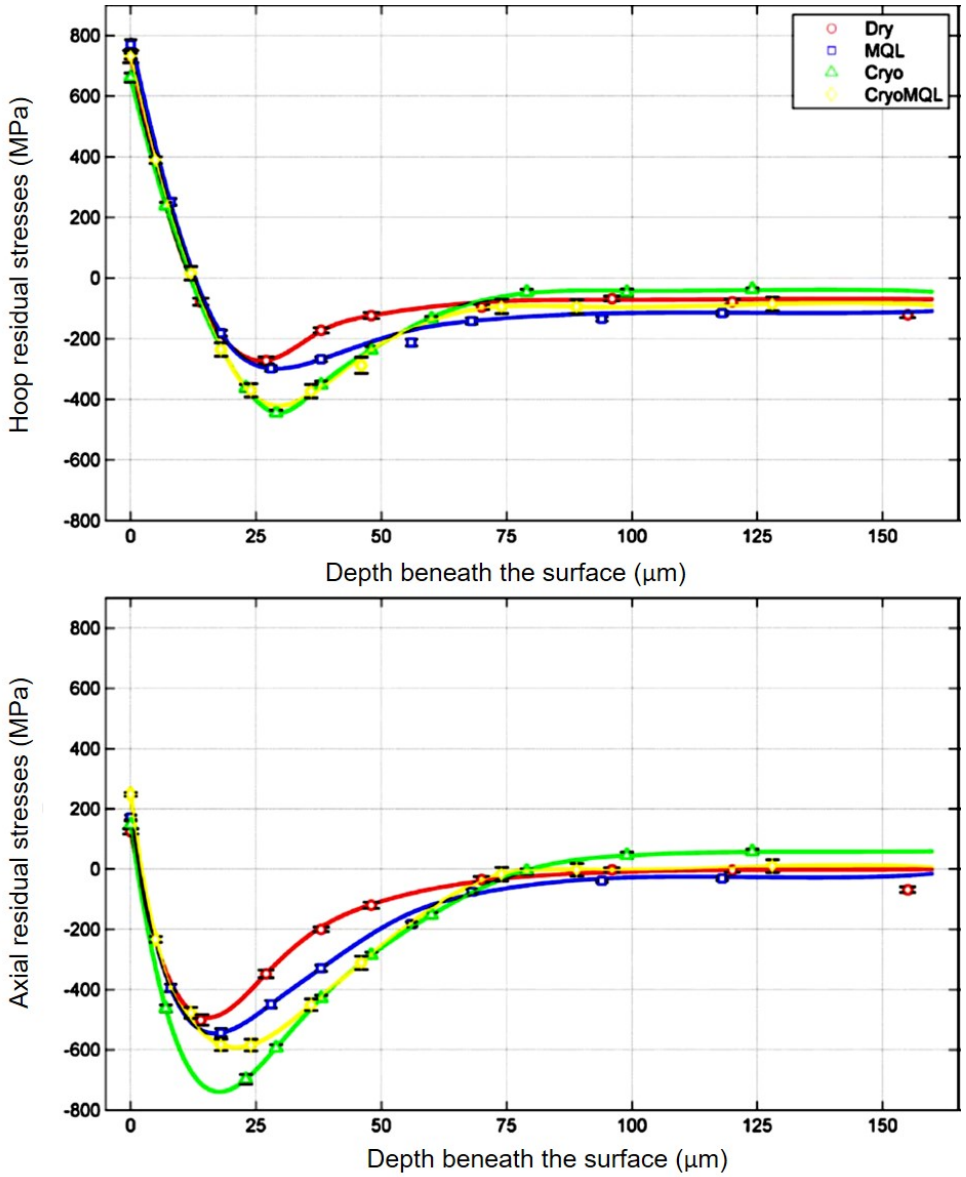

Figure II.40 – Illustration of residual stresses on the surface and along the depth of the machined surface in turning operations of Inconel 718 under different cooling strategies (V_c = 60 m/min, f=0.05 mm/tr and a_p =0.63 mm) (Pusavec et al., 2011).

Similar tendency has been pointed out by (He et al., 2016) reporting that LN_2 cryogenic condition produced lower tensile residual stresses on the surface and the subsurface of the machined workpiece in comparison with those obtained in dry machining.
Concerning the LCO_2, few studies have examined its effect on residual stress distribution. Ross and Manimaran (2020) underlined the LCO_2 influence on surface residual stress in comparison with wet and MQL cooling strategies conditions of a nickel based alloy Nimonic-80A. The main result consists of LCO_2 cooling strategy decreased significantly the thermal effect and fastened the mechanical work, causing higher compressive residual stresses (Fig. II.41).

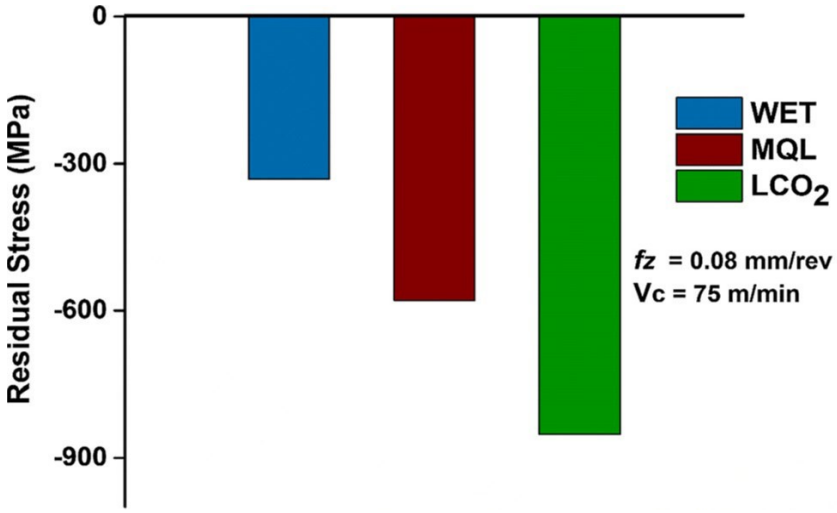

Figure II.41 – Illustration of residual stress on the machined surface under different environmental conditions at $V_c = 75$ m/min and $f_z = 0.08$ mm/rev (Ross and Manimaran, 2020).

4.6 Summary of the literature review

Table II.4 – Summary of the previous studies showing the effect of the cryogenic coolants LN_2 and LCO_2 performances compared to different cooling methods.

References	Work material	Cooling conditions	Machining operations	Main conclusions
Dhananchezian and Kumar (2011)	Ti64	Wet-LN_2	Turning	Tool wear: LN_2 decreased the flank wear by 27-39% over wet machining Surface roughness: LN_2 decreased the R_a to be 35% compared to wet condition
Bordin et al. (2015)	Ti64	Dry-LN_2	Turning	Tool life: Both conditions induced similar tool lives Surface integrity: LN_2 induced lower surface roughness and thinner affected layer of the machined parts compared to dry machining
Hong et al. (2001)	Ti64	Dry-Wet-LN_2	Turning	Tool life: When delivering LN_2 on both rake and flank faces, tool lives obtained was around 950 s versus 167 s in dry and 290 s in wet conditions
Kaynak (2014)	Inconel 718	Dry-MQL-LN_2	Turning	Cutting forces: At $V_c = 120$ m/min, cryogenic cooling induced the least forces among the three conditions Surface roughness: At $V_c = 120$ m/min, LN_2 condition generated the best surface quality
Behera et al. (2017)	Inconel 718	Dry-HPWJ MQL-LN_2	Turning	Under nMQL condition, the tool flank wear decreased until 129.6 μm while in LN_2 cryogenic condition, the tool flank wear was reduced to 99.5 μm
Musfirah et al. (2017)	Inconel 718	Dry-LN_2	Milling	Tool life: Cryogenic coolant decreased tool life about 50 % compared to dry machining

Iturbe et al. (2016)	Inconel 718	Wet Cryo+MQL	Turning	Tool life: Shorter tool life under Cryo+MQL (<10 min) compared to wet (20 min) Surface quality: poor surface roughness induced under Cryo+MQL condition
Pusavec et al. (2011)	Inconel 718	Dry MQL LN_2 LN_2+MQL	Turning	Surface integrity: LN_2 machining generated lower surface roughness The compressive zone below the surface is thicker in LN_2 condition, extending the compressive zone from da =40μm to da =70μm compared to dry machining

5 Conclusion

In this chapter, one has discussed the general aspects of the cryogenic cooling approach highlighting the characteristics of the two cryogenic fluids (LN_2 and LCO_2) commonly employed in anterior studies. Subsequently, the impact of the cryogenic assisted strategy on machining performance (tool life, cutting forces and surface integrity) have been revealed. At this line, a very interesting result has been identified that consists of showing significant gain in the cryogenically assisted machining of certain difficult-to-cut materials such titanium alloys and steels. In contrast, Inconel 718 has exhibited multiple problems during cutting process in terms of tool life and surface integrity of the machined component. Besides, it is worth mentioning that the previous studies when dealing with machining of Inconel 718, authors compared the cryogenic machining performance with dry and MQL cooling strategies. However, a comparison with conventional lubrication was rarely revealed although that this cooling condition is the most used in industrial applications owing to its advantages regard tool life. Moreover, in many cases the information about the machining time is not mentioned. Thus, the tool wear state is not clear and the judgment of the cooling strategy efficiency is not well discerned.
For these reasons, we attribute a great attention to investigate the cryogenic performance when machining Inconel 718. A comparative study between the two cryogenic fluids namely LN_2 and LCO_2 considering as a reference the conventional lubrication (wet) is carried out.

In order to extract additional information concerning the poor machiniability of Inconel 718 under cryogenic conditions, the mechanical characterization of the work material at cryogenic temperature is studied. This could be a key factor to discriminate certain mechanisms and/or phenomena causing the mediocre performance of cryogenic cooling conditions when machining Inconel 718. In fact, the very low temperature of cooling with LN_2 (-196 °C) could affect significantly the work material behavior during machining. In particular, the uncut surface is subjected to low temperature of the cryogenic fluid prior to the cut operation allowing to obtain the stabilized state of the cryogenic fluid.

The main objective of this PhD study is to evaluate to the influence of cryogenic machining on fatigue resistance of Inconel 718. Knowing that most of the airplane components which are produced from nickel based alloys, are subjected to cyclic loads during service. Therefore, controlling the manufacturing process will promote better efficiency regard the fatigue behavior of the machined parts. In other words, providing better surface integrity could improve the fatigue performance as reported in literature. At this line, cryogenic machining may be a good alternative to fulfill these requirements. In this context, an original approach is developed in this PhD work. We focus on adapting the cryogenic drilling process to study its effect on fatigue resistance.

Bibliography

Ahmed, N., Mitrofanov, A., Babitsky, V., Silberschmidt, V., 2007. Analysis of forces in ultrasonically assisted turning. Journal of Sound and Vibration 308, 845–854. URL: doi:https://doi.org/10.1016/j.jsv.2007.04.003. vibro-Impact Systems.

Alexis, P., 2013. Experimental quantitative studies that the solidification of the superalloys 718 in investment casting. Theses. Ecole Nationale Supérieure des Mines de Paris. URL: https://pastel.archives-ouvertes.fr/pastel-00998532.

An, Q., Cai, C., Zou, F., Liang, X., Chen, M., 2020. Tool wear and machined surface characteristics in side milling ti6al4v under dry and supercritical co2 with mql conditions. Tribology International 151, 106511. doi:https://doi.org/10.1016/j.triboint.2020.106511.

Aramcharoen, A., Chuan, S.K., 2014. An experimental investigation on cryogenic milling of inconel 718 and its sustainability assessment. Procedia CIRP 14, 529 – 534. URL: doi:https://doi.org/10.1016/j.procir.2014.03.076. 6th CIRP International Conference on High Performance Cutting, HPC2014.

Ayed, Y., Germain, G., Salem, W.B., Hamdi, H., 2014. Experimental and numerical study of laser assisted machining of ti6al4v titanium alloy. Finite Elements in Analysis and Design 92, 72–79.

Ayed, Y., 2013. Approches expérimentales et numériques de l'usinage assisté jet d'eau haute pression : étude des mécanismes d'usure et contribution à la modélisation multi-physiques de la coupe. Ph.D. thesis. URL: http://www.theses.fr/2013ENAM0056.

Ayed, Y., Germain, G., Melsio, A.M., Kowalewski, P., Locufier, D., 2017. Impact of supply conditions of liquid nitrogen on tool wear and surface integrity when machining the ti-6al-4v titanium alloy. International Journal of Advanced Manufacturing Technology 93. doi:10.1007/s00170-017-0604-7.

Bagherzadeh, A., Budak, E., 2018. Investigation of machinability in turning of difficult-to-cut materials using a new cryogenic cooling approach. Tribology International 119, 510 – 520. URL: doi:https://doi.org/10.1016/j.triboint.2017.11.033.

Behera, B.C., Alemayehu, H., Ghosh, S., Rao, P.V., 2017. A comparative study of recent lubri-coolant strategies for turning of ni-based superalloy. Journal of Manufacturing Processes 30, 541 – 552. URL: doi:https://doi.org/10.1016/j.jmapro.2017.10.027.

Blau, P., Busch, K., Dix, M., Hochmuth, C., Stoll, A., Wertheim, R., 2015. Flushing strategies for high performance, efficient and environmentally friendly cutting.

Procedia CIRP 26, 361–366. URL: doi:https://doi.org/10.1016/j.procir.2014.07.058. 12th Global Conference on Sustainable Manufacturing – Emerging Potentials.

Bordin, A., Bruschi, S., Ghiotti, A., Bariani, P., 2015. Analysis of tool wear in cryogenic machining of additive manufactured ti6al4v alloy. Wear 328-329, 89–99. URL: doi:https://doi.org/10.1016/j.wear.2015.01.030.

Bordin, A., Sartori, S., Bruschi, S., Ghiotti, A., 2017. Experimental investigation on the feasibility of dry and cryogenic machining as sustainable strategies when turning ti6al4v produced by additive manufacturing. Journal of Cleaner Production 142, 4142 – 4151. URL: doi:https://doi.org/10.1016/j.jclepro.2016.09.209.

Braham Bouchnak, T., 2010. Etude du comportement en sollicitations extrêmes et de l'usinabilité d'un nouvel alliage de titane aéronautique : le TI555-3. Ph.D. thesis. URL: http://www.theses.fr/2010ENAM0051. thèse de doctorat dirigée par Furet, BenoîtLebrun, Jean-Lou et Germain, Guenaël Mécanique Paris, ENSAM 2010.

Braham-Bouchnak, T., Germain, G., Morel, A., Lebrun, J.L., 2013. The influence of laser assistance on the machinability of the titanium alloy Ti555-3. International Journal of Advanced Manufacturing Technology 68, 2471–2481. URL: https://hal.archives-ouvertes.fr/hal-02486086, doi:10.1007/s00170-013-4855-7.

Bushlya, V., Zhou, J., Lenrick, F., Avdovic, P., Ståhl, J.E., 2011. Characterization of white layer generated when turning aged inconel 718. Procedia Engineering 19, 60 – 66. URL: doi:https://doi.org/10.1016/j.proeng.2011.11.080. 1st CIRP Conference on Surface Integrity (CSI).

C. Slama, G. Cizeron, 1997. Etude du comportement structural de l'alliage nc 19 fe nb (inconel 718). J. Phys. III France 7, 665–688. URL: https://doi.org/10.1051/jp3:1997148, doi:10.1051/jp3:1997148.

Courbon, C., Pusavec, F., Dumont, F., Rech, J., Kopac, J., 2013. Tribological behaviour of ti-6al-4v and inconel 718 under dry and cryogenic conditions : Application to the context of machining with carbide tools. Tribology International 66, 72 – 82. URL: doi:https://doi.org/10.1016/j.triboint.2013.04.010.

Courbon, C., Sterle, L., Cici, M., Pušavec, F., 2020. Tribological effect of lubricated liquid carbon dioxide on tial6v4 and aisi1045 under extreme contact conditions. Procedia Manufacturing 47, 511–516. doi:10.1016/j.promfg.2020.04.139.

Dhananchezian, M., Kumar, M.P., 2011. Cryogenic turning of the ti–6al–4v alloy with modified cutting tool inserts. Cryogenics 51, 34 – 40. URL: doi:https://doi.org/10.1016/j.cryogenics.2010.10.011.

Dhar, N., Kamruzzaman, M., 2007. Cutting temperature, tool wear, surface roughness and dimensional deviation in turning aisi-4037 steel under cryogenic condition. International Journal of Machine Tools and Manufacture 47, 754–759. URL: doi:https://doi.org/10.1016/j.ijmachtools.2006.09.018. tehran International Congress on Manufacturing Engineering (TICME2005).

Dudzinski, D., Molinari, A., 1997. A modelling of cutting for viscoplastic materials. International Journal of Mechanical Sciences 39, 369 – 389. URL: doi:https://doi.org/10.1016/S0020-7403(96)00043-4.

Ezugwu, E., Bonney, J., Fadare, D., Sales, W., 2005. Machining of nickel base inconel 718 alloy with ceramic tools under finishing conditions with various coolant supply pressures. Journal of Materials Processing Technology 162-163, 609–614. URL: doi:https://doi.org/10.1016/j.jmatprotec.2005.02.144.

Ezugwu, E., Tang, S., 1995. Surface abuse when machining cast iron (g-17) and nickel-base superalloy (inconel 718) with ceramic tools. Journal of Materials Processing Technology 55, 63 – 69. URL: doi:https://doi.org/10.1016/0924-0136(95)01786-0. conference of the Irish Manufacturing Committee on advanced manufacturing technology.

Ezugwu, E., Wang, Z., Machado, A., 1999. The machinability of nickel-based alloys: a review. Journal of Materials Processing Technology 86, 1 – 16. URL: doi:https://doi.org/10.1016/S0924-0136(98)00314-8.

Éric, F., Pierre, M., 2016. Théorie de l'usure mécanismes d'usure. Techniques de l'ingénieur Frottement et usure base documentaire : TIB464DUO. fre.

Farhat, Z., 2007. Caractérisation de modèles de frottement aux interfaces piece-outil-copeau en usinage - Application au cas de l'usinage des aciers et de l'inconel 718. Ph.D. thesis. Ecole centrale de Lyon. URL: http://www.theses.fr/2007ECDL0033. 2007ECDL0033.

Gael, L.C., 2012. Milling of Inconel 718 : Surface integrity, temperature measurement and analytical model of peripheral milling. Theses. Université de Lorraine. URL: https://tel.archives-ouvertes.fr/tel-00917010.

Germain, G., Dal Santo, P., Lebrun, J., 2011. Comprehension of chip formation in laser assisted machining. International Journal of Machine Tools and Manufacture 51, 230–238. URL: doi:https://doi.org/10.1016/j.ijmachtools.2010.11.006.

He, Z.H., Zhang, X.M., Ding, H., 2016. Comparison of residual stresses in cryogenic and dry machining of inconel 718. Procedia CIRP 46, 19 – 22. URL: doi:https://doi.org/10.1016/j.procir.2016.03.130. 7th HPC 2016 – CIRP Conference on High Performance Cutting.

Hong, S.Y., Ding, Y., cheol Jeong, W., 2001a. Friction and cutting forces in cryogenic machining of ti–6al–4v. International Journal of Machine Tools and Manufacture 41, 2271 – 2285. URL: doi:https://doi.org/10.1016/S0890-6955(01)00029-3.

Hong, S.Y., Markus, I., cheol Jeong, W., 2001b. New cooling approach and tool life improvement in cryogenic machining of titanium alloy ti-6al-4v. International Journal of Machine Tools and Manufacture 41, 2245 – 2260. URL: doi:https://doi.org/10.1016/S0890-6955(01)00041-4.

Hongbo, D., Gaochao, W., 2015. Effect of deformation process on superplasticity of inconel 718 alloy. Rare Metal Materials and Engineering 44, 298–302.

Imran, M., Mativenga, P.T., Gholinia, A., Withers, P.J., 2014. Comparison of tool wear mechanisms and surface integrity for dry and wet micro-drilling of nickel-base superalloys. International Journal of Machine Tools and Manufacture 76, 49 – 60. URL: doi:https://doi.org/10.1016/j.ijmachtools.2013.10.002.

Iturbe, A., Giraud, E., Hormaetxe, E., Garay, A., Germain, G., Ostolaza, K., Arrazola, P., 2017. Mechanical characterization and modelling of inconel 718 material behavior for machining process assessment. Materials Science and Engineering: A 682, 441 – 453. URL: doi:https://doi.org/10.1016/j.msea.2016.11.054.

Iturbe, A., Hormaetxe, E., Garay, A., Arrazola, P.J., 2016. Surface integrity analysis when machining inconel 718 with conventional and cryogenic cooling. Procedia CIRP 45, 67 – 70. URL: doi:https://doi.org/10.1016/j.procir.2016.02.095. 3rd CIRP Conference on Surface Integrity.

Jamil, M., Zhao, W., He, N., Gupta, M.K., Sarikaya, M., Khan, A.M., R, S.M., Siengchin, S., Pimenov, D.Y., 2021. Sustainable milling of ti–6al–4v: A trade-off between energy efficiency, carbon emissions and machining characteristics under mql and cryogenic environment. Journal of Cleaner Production 281, 125374. URL: doi:https://doi.org/10.1016/j.jclepro.2020.125374.

Jerold, B.D., Kumar, M.P., 2012. Experimental comparison of carbon-dioxide and liquid nitrogen cryogenic coolants in turning of aisi 1045 steel. Cryogenics 52, 569 – 574. URL: doi:https://doi.org/10.1016/j.cryogenics.2012.07.009.

Kadirgama, K., Abou-El-Hossein, K., Noor, M., Sharma, K., Mohammad, B., 2011. Tool life and wear mechanism when machining hastelloy c-22hs. Wear 270, 258 – 268. URL: doi:https://doi.org/10.1016/j.wear.2010.10.067.

Khan, S., Soo, S., Aspinwall, D., Sage, C., Harden, P., Fleming, M., White, A., M'Saoubi, R., 2012. Tool wear/life evaluation when finish turning inconel 718 using pcbn tooling. Procedia CIRP 1, 283–288. doi:10.1016/j.procir.2012.04.051.

Kaynak, Y., 2014. Evaluation of machining performance in cryogenic machining of inconel 718 and comparison with dry and mql machining. The International Journal of Advanced Manufacturing Technology 72, 919–933. URL: https://doi.org/10.1007/s00170-014-5683-0, doi:10.1007/s00170-014-5683-0.

Khajehzadeh, M., Boostanipour, O., Reza Razfar, M., 2020. Finite element simulation and experimental investigation of residual stresses in ultrasonic assisted turning. Ultrasonics 108, 106208. URL: doi:https://doi.org/10.1016/j.ultras.2020.106208.

Leadebal Jr, W.V., de Melo, A.C.A., de Oliveira, A.J., Castro, N.A., 2018. Effects of cryogenic cooling on the surface integrity in hard turning of aisi d6 steel. Journal of the Brazilian Society of Mechanical Sciences and Engineering 40, 15.

Li, B., 2012. A review of tool wear estimation using theoretical analysis and numerical simulation technologies. International Journal of Refractory Metals and Hard Materials 35, 143–151. URL: doi:https://doi.org/10.1016/j.ijrmhm.2012.05.006.

List, G., 2004. Etude des mécanismes d'endommagement des outils carbure WC-Co par la caractérisation de l'interface outil copeau : application à l'usinage à sec de l'alliage d'aluminium aéronautique AA2024 T351. Ph.D. thesis. URL: http://www.theses.fr/2004ENAM0041. thèse de doctorat dirigée par Girot, Franck Sciences de l'ingénieur. Mécanique Paris, ENSAM 2004.

Lu, T., Dillon, O.W., Jawahir, I.S., 2013. A thermal analysis framework for cryogenic machining and its contribution to product and process sustainability , 262–267Available Open Access publishedVersion at urn:nbn:de:kobv:83-opus4-73249.

Magalhaes, D., Kliauga, A., Ferrante, M., Sordi, V., 2017. Plastic deformation of fcc alloys at cryogenic temperature: the effect of stacking-fault energy on microstructure and tensile behaviour. Journal of Materials Science 52, 1–13. doi:10.1007/s10853-017-0979-8.

Mohan, R.P.V., Satyanarayana, M.K., V., S.S., Nagender, N.S.V., 1992. Effect of ternary additions on the room temperature lattice parameter of ni3al. physica status solidi (a) 133, 231–235. URL: http:https://doi.org/10.1002/pssa.2211330203, doi:10.1002/pssa.2211330203.

Musfirah, A., Ghani, J., Haron, C.C., 2017. Tool wear and surface integrity of inconel 718 in dry and cryogenic coolant at high cutting speed. Wear 376-377, 125 – 133. URL: doi:https://doi.org/10.1016/j.wear.2017.01.031. 21st International Conference on Wear of Materials.

Nalbant, M., Yildiz, Y., 2011. Effect of cryogenic cooling in milling process of aisi 304 stainless steel. Transactions of Nonferrous Metals Society of China 21, 72–79. doi:10.1016/S1003-6326(11)60680-8.

Niang, A., 2010. Contribution à l'étude de la précipitation des phases intermétalliques dans l'alliage 718. Ph.D. thesis. Institut National Polytechnique de Toulouse (INP Toulouse). URL: http://oatao.univ-toulouse.fr/7259/.

Nouari, M., Makich, H., 2013. Experimental investigation on the effect of the material microstructure on tool wear when machining hard titanium alloys: Ti–6al–4v and ti-555. International Journal of Refractory Metals and Hard Materials 41, 259–269. URL: doi:https://doi.org/10.1016/j.ijrmhm.2013.04.011.

Ogata, T., 2014. Evaluation of mechanical properties of structural materials at cryogenic temperatures and international standardization for those methods. AIP Conference Proceedings 1574, 320–326. doi:10.1063/1.4860643.

Pusavec, F., Deshpande, A., Yang, S., Saoubi, R.M., Kopac, J., Dillon, O.W., Jawahir, I.S., 2014. Sustainable machining of high temperature nickel alloy inconel 718: part 1 predictive performance models. Journal of Cleaner Production 81, 255 – 269. doi:https://doi.org/10.1016/j.jclepro.2014.06.040.

Pusavec, F., Hamdi, H., Kopac, J., Jawahir, I., 2011. Surface integrity in cryogenic machining of nickel based alloy—inconel 718. Journal of Materials Processing Technology 211, 773 – 783. URL: doi:https://doi.org/10.1016/j.jmatprotec.2010.12.013.

Pusavec, F., Krajnik, P., Kopac, J., 2010. Transitioning to sustainable production – part i: application on machining technologies. Journal of Cleaner Production 18, 174 – 184. URL: doi:https://doi.org/10.1016/j.jclepro.2009.08.010.

Reed, R., 1998. Low temperature tensile properties of fe ni alloys , 25–32.

Ross, K.N., Manimaran, G., 2020. Machining investigation of nimonic-80a superalloy under cryogenic co2 as coolant using pvd-tialn/tin coated tool at 45 nozzle angle. ARABIAN JOURNAL FOR SCIENCE AND ENGINEERING 45. doi:10.1007/s13369-020-04728-8.

Rotella, G., Dillon, W., Umbrello, D., Settineri, L., Jawahir, S., 2014. The effects of cooling conditions on surface integrity in machining of ti6al4v alloy. The International Journal of Advanced Manufacturing Technology 71, 47–55. URL: https://doi.org/10.1007/s00170-013-5477-9, doi:10.1007/s00170-013-5477-9.

Srinivasan, A., Hanemann, T., Weiss, K.P., Freudenberger, J., Heilmaier, M., Kauffmann, A., 2020. Dislocation-based serrated plastic flow of high entropy alloys at cryogenic temperatures. Acta Materialia 200, 980–991. doi:10.1016/j.actamat.2020.09.052.

Srinivasan, A., Sas, J., Weiss, K.P., Chen, H., Szabó, D.V., Schlabach, S., Haas, S., Geissler, D., Freudenberger, J., Heilmaier, M., Kauffmann, A., 2018. Peculiarities of deformation of cocrfemnni at cryogenic temperatures. Journal of Materials Research 33, 1–14. doi:10.1557/jmr.2018.252.

Stoll, A., Busch, K., Hochmuth, C., Pause, B., 2014. Modern cooling strategies for machining of high-temperature materials. Innovations of Sustainable Production for Green Mobility: Energy-efficient Technologies in Production , 299–316.

Sundararaman, M., Mukhopadhyay, P., Banerjee, S., 1988. Precipitation of the δ-ni3nb phase in two nickel base superalloys. Metallurgical Transactions A 19, 453–465. URL: https://doi.org/10.1007/BF02649259, doi:10.1007/BF02649259.

Ter-Ovanessian, B., 2011. Etude comparative de différents superalliages base Ni pour ressorts de systèmes de maintien. Ph.D. thesis. Institut National Polytechnique de Toulouse (INP Toulouse). URL: http://oatao.univ-toulouse.fr/7075/.

Thellaputta, G.R., Chandra, P.S., Rao, C., 2017. Machinability of nickel based superalloys: A review. Materials Today: Proceedings 4, 3712 – 3721. URL: doi:https://doi.org/10.1016/j.matpr.2017.02.266. 5th International Conference of Materials Processing and Characterization (ICMPC 2016).

Ucak, N., Cicek, A., 2018. The effects of cutting conditions on cutting temperature and hole quality in drilling of inconel 718 using solid carbide drills. Journal of Manufacturing Processes 31, 662–673. URL: doi:https://doi.org/10.1016/j.jmapro.2018.01.003.

Yin, Q., Zhanqiang, L., Wang, B., Song, Q., Cai, Y., 2020. Recent progress of machinability and surface integrity for mechanical machining inconel 718: a review. The International Journal of Advanced Manufacturing Technology 109. doi:10.1007/s00170-020-05665-4.

Zhu, D., Zhang, X., Ding, H., 2013. Tool wear characteristics in machining of nickel-based superalloys. International Journal of Machine Tools and Manufacture 64, 60 – 77. URL: doi:https://doi.org/10.1016/j.ijmachtools.2012.08.001.

Zixing, W., Dianhua, Z., Qun, D., Guosheng, C., Wei, X., 2012. The Microstructure and Mechanical Properties of Inconel 718 Fine Grain Ring Forging. Wiley-Blackwell. pp. 343–349. URL: doi:10.1002/9781118495223.ch26.

Chapter III

Mechanical characterization of Inconel 718 at cryogenic temperature

1 Introduction . . . 114
2 Description of the work material . . . 116
2.1 Heat treatment and chemical composition . . . 116
2.2 Microstructure observations . . . 118
2.2.1 Optical Microscope(OM) . . . 118
2.2.2 Scanning Electron microscopy (SEM) . . . 119
2.2.3 Electron Back Scatter Diffraction (EBSD) . . . 120
2.3 Samples preparation . . . 121
3 Mechanical characterization of Inconel 718 at low temperature . . . 122
3.1 Experimental procedure . . . 122
3.1.1 Experimental equipment . . . 122
3.1.2 Experimental methodology . . . 129
3.2 Results and discussions . . . 131
3.2.1 Stress-strain curves . . . 131
3.2.2 Mirco-hardness measurements . . . 134
3.2.3 Metallographic analysis . . . 137
3.2.3.a Microstructure observations . . . 137
3.2.3.b EBSD analysis . . . 140
4 Conclusion . . . 144

1 Introduction

Nickel based alloys are mostly used as disc material in gas turbine and in jet engines under high thermal loads up to 650 °C (Si et al., 2015). For this reason, previous studies have widely investigated the mechanical behavior of Inconel 718 at high temperature performed using uniaxial quasi-static compression tests. In particular, most of researchers have investigated the thermo-mechanical behavior of Inconel 718 at very high temperature covering the range of 920 °C to 1040 °C and at low strain rate values from 0.001 s^{-1} to 1 s^{-1} (Lin et al., 2015). The choice of these parameters intervals is essentially based on the hot forming process of Inconel 718 for instance the forging process. Nevertheless, another aspect that was extensively examined in the literature review dealing with the high temperature behavior of Inconel 718 consist in the machining process, particularly the chip formation mechanism for modeling requirements (Iturbe et al., 2017). In this context, Iturbe et al. (2017) have deeply investigated the flow stress behavior of Inconel 718 in order to develop a reliable model under high strain rates (up to 100 s^{-1}) and over wide range of temperatures (up to 1050°C). The working temperature examined in this study does not cover the cryogenic temperature range encountered in the cutting process using cryogenic fluid.
It is well known that during the machining process, the temperature in the secondary shear zone could achieve very high values holding even 900°C depending on the cutting speed, the cutting tool material as well as the cooling strategy (Czán et al., 2017). At the beginning of the cryogenic machining, the workpiece material is subjected to very low temperature up to -196 °C. One is interested in examining this temperature level when characterizing the mechanical behavior of Inconel 718.
Few projects have focused on the effect of cryogenic temperature on the mechanical properties of the work material . For instance, Camilo et al. (2017) have performed tensile tests at low temperature on three materials namely AA1050, commercially pure Cu and Cu–15Zn alloy. The findings have led to conclude that the three materials showed an elevation of both strength and ductility at the cryogenic temperature. Fig. III.1 displayed the correspondent results.

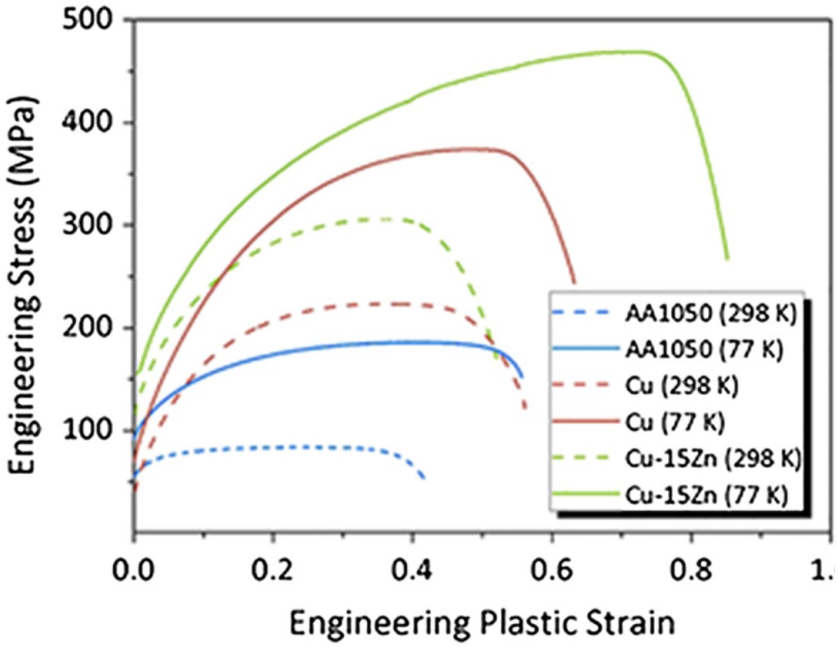

Figure III.1 – Engineering stress vs the plastic strain curves for the three materials (Camilo et al., 2017).

Jiang et al. (2016) have tested three kinds of nickel based alloys with different chemical composition where the rates of the composed elements (Ni Cu Cr Mo Ti Al Nb) have been diversified. Compression tests have been conducted at strain level of 60 %, at strain rate of 0.001 s^{-1} and at a temperature of -150 °C. They concluded that the yield strength and the compression ultimate strength of the three alloys were enhanced under cryogenic environment. Recently, Sharath Chandra et al. (2020) reported that Inconel 718 yield strength and UTS are least affected by low temperatures (up to -70 °C). They have claimed that both material yield strength and the UTS decreased by decreasing the tested temperature as illustrated in the Fig. III.2.

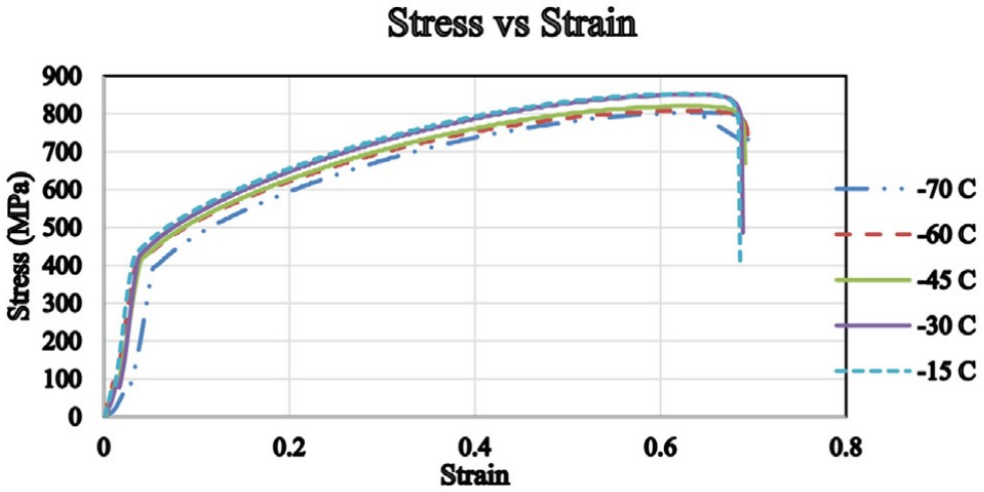

Figure III.2 – Stress-strain curves at sub zero temperatures (Sharath Chandra et al., 2020).

It is important to point out that the strain rate occurred during metal cutting achieved

high levels up to 10^6 s^{-1} (Zhang et al., 2021). In this context, Lee et al. (2011) investigated the dynamic impact behavior of Inconel 718 alloy at temperatures ranging from -150 °C to 550 °C and strain rates covering 1000 s^{-1} to 5000 s^{-1}. Such dynamic experiments are usually performed employing a compressive Split Hopkinson Pressure Bar (SHPB). Results showed that the flow stress is proportional with the strain rate and inversely proportional with the temperature where the highest work hardening rate was observed at the lowest temperature (-150 °C) and the highest strain rate (5000 s^{-1}).

Based on literature review, it appears that no paper has figured out the cryogenic set-up employed during their investigations regardless of the work material. The few cryogenic systems that have been presented are neither financially affordable (Ogata, 2014) nor suitable for Gleeble machine (Fabre, 2013). Indeed, Fabre (2013) showed the liquid nitrogen delivery employed during compression tests under low temperatures. However, such system presents, in our case, a great risque to damage the cell effort of the Gleeble machine since that the liquid nitrogen is not locally supplied to cool down the specimen. Even the tested temperature were not stable in this work.
The current study will present a new cryogenic experimental set-up providing the aimed cryogenic temperature. Besides, we will investigate the cryogenic temperature effect on the flow stress behavior in addition to the microstructure alterations of the deformed samples at cryogenic conditions. For these reasons, the mechanical characterization at low and high temperature under static and dynamic loads will be figured out.
The first part of this chapter will be devoted to the description of the work material. Subsequently, the mechanical characterization methodology will be detailed followed by the experimental results and discussions.

2 Description of the work material

2.1 Heat treatment and chemical composition

The material used in this study is the NiCr19FeNb nickel-based alloy (Inconel 718). During its development, this alloy underwent a structural hardening heat treatment according to the following cycle:

- heating at a temperature from 940 °C to 1010 °C followed by water quenching;
- heating until 720 °C for eight hours;
- cooling until 620 °C with a speed equal to 50 °C/h and maintain for eight hours at this temperature followed by air cooling;

The structural hardening heat treatment aims to precipitate two phases γ' ($Ni_3(Al,Ti)$) and γ'' (Ni_3Nb).
Nickel based alloys are superalloys that exhibit excellent mechanical properties in an extended temperature range up to 700 °C. Compression test has been conducted to identify the ultimate strength and the yield strength at room temperature and at a strain rate of 0.01 s^{-1} (Table III.1). The micro-hardness value was determined using the Vickers method with a 200 gf load .

Table III.1 – Mechanical properties of Inconel 718 at room temperature

Ultimate Compression Strength (MPa)	1630
Yield strength (MPa)	1150
Young modulus (GPa)	206
Hardness ($HV_{0.2}$)	486
Density ($g.cm^{-3}$)	8.19
Thermal conductivity coefficient (W/m.K)	11.2
Average grain size (μm)	27.4

In order to pick out the chemical composition of the work material Inconel 718, Energy Dispersive Spectroscopy (EDS) analyses have been carried out. Fig III.3 and Fig III.4 displayed the correspondent results in addition to the chemical composition of the carbides involved.

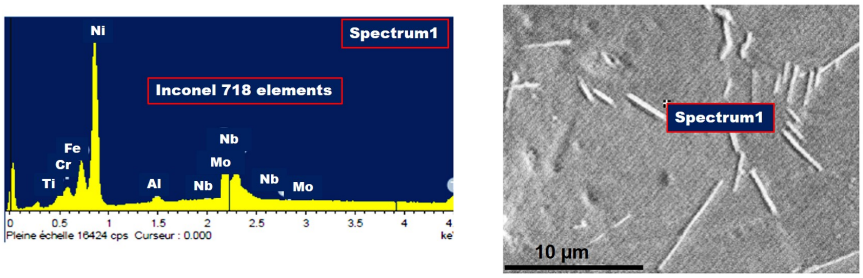

Figure III.3 – EDS analysis carried out at a grain of the austenitic matrix γ in order to identify its chemical composition.

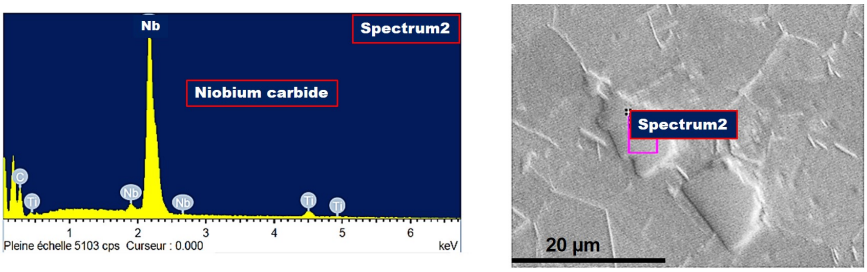

Figure III.4 – EDS analysis carried out at a NbC carbide in order to identify its chemical composition.

Table III.2 summarizes the rate of each element present in the alloy.

Table III.2 – Chemical composition of Inconel 718 (% wt)

Ni	Cr	Fe	Mo	Nb	Ti	Al
53.17	18.41	18.45	2.91	5.51	0.99	0.56

2.2 Microstructure observations

2.2.1 Optical Microscope(OM)

The microstructure of Inconel 718 was visualized using the optical microscope for the purpose of recognizing the structuring of the work material. Metallurgical observations under the optical microscope of Inconel 718 reveals:

— The austenitic matrix γ;
— The δ-phase that exhibits an arbitrary distribution either at the grain boundaries or within the grains. This phase contributes to increasing the creep resistance of Inconel 718;
— The twins are present in a relatively important way. The twinning phenomenon could occur either under thermal loading and/or mechanical loading.

Twinning mechanism is another mode of plastic deformation in addition to the slipping mode; conventionally observed in nickel based alloys metals (Shi et al., 2015). A twin corresponds to a volume of the crystal which has been sheared in homogeneous way (Mackain, 2017). This sheared volume defines an interface with the parent crystal that commonly called "Twin Boundary" as displayed in Fig.III.5.

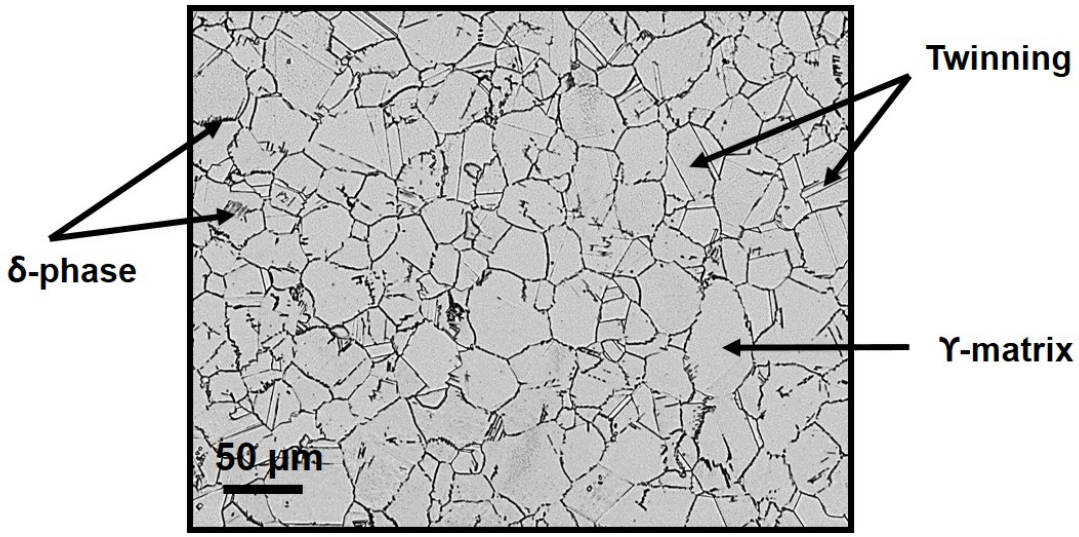

Figure III.5 – Illustration of the microstructure of the raw material at the as-received state.

2.2.2 Scanning Electron microscopy (SEM)

The Scanning Electron microscopy (SEM) is a technique of electron microscope that allows to produce images in high resolution whose principle is to send a beam of electrons on the surface of a sample. The interaction between electron-material gives rise to several types of emitted beams (secondary electrons SE, backscattered electrons BSE and Auger electrons) which will be picked up by detectors allowing finally to build the images. Complementary analyses could be conducted using the SEM equipment. For instance, the EDS mainly employed for chemical composition analysis and the EBSD to characterize the material texture.

The observation of the microstructure using the SEM equipment underlines the same composition mentioned in Section 2.1 namely the γ austenitic matrix, the δ phase, the twins in addition to the MC type carbides. The carbides (intragranular or intergranular) having different shapes. They participate in the slowdown of grains movement at high temperature and actively contribute to the reinforcement of creep resistance. The advantage of this observation is that one could visualize more finely the different morphologies of all phases as displayed in Fig. III.6.

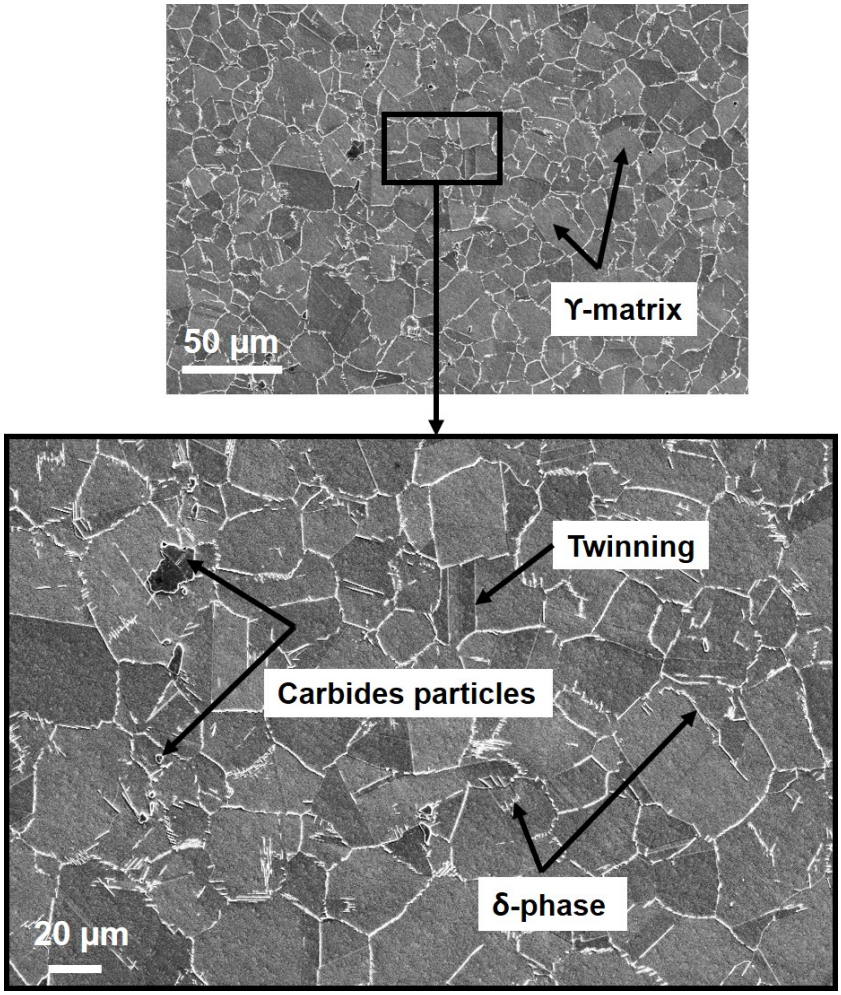

Figure III.6 – Illustration of Inconel 718 microstructure in the as-received state observed by SEM technique using the SE beam.

2.2.3 Electron Back Scatter Diffraction (EBSD)

The Electron Back Scatter Diffraction method (EBSD) allows to characterize the orientation of polycrystalline materials and to analyze the texture of some materials having a preferential orientation due to the forming process. The sample is inclined at an angle of 70 °, with respect to the incident electron beam. The electron-material interaction induces the emission of back scattered electrons which can be diffracted by the diffracting planes that respect the Bragg law. The diffracted cones intersect the phosphorescent screen to form the kikuchi lines that will be indexed thereafter to form "EBSD mapping" (Fig. III.7).

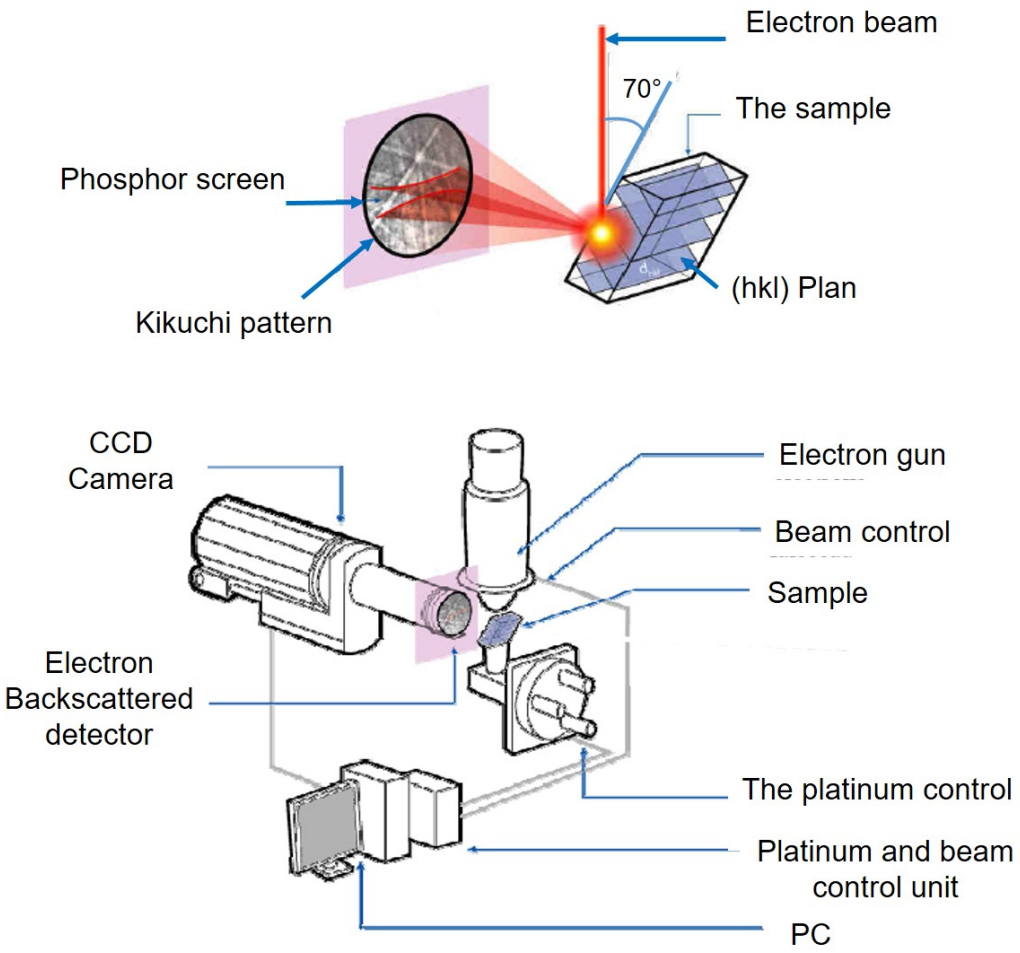

Figure III.7 – Experimental device of scanning electron microscope in EBSD mode (Barbier, 2010).

The EBSD map of the work material in the as-received state before deformation is presented in Fig. III.8. The Fig. III.8 pointed out the random misorientation between grains. It can also be found that the initial microstructure is mainly composed of equiaxed grains and lamella-like straight annealing twins revealing an average grain size of 27.4 μm. A typical microstructure of heat-treated Inconel 718 as reported in literature review (Lin et al., 2015).

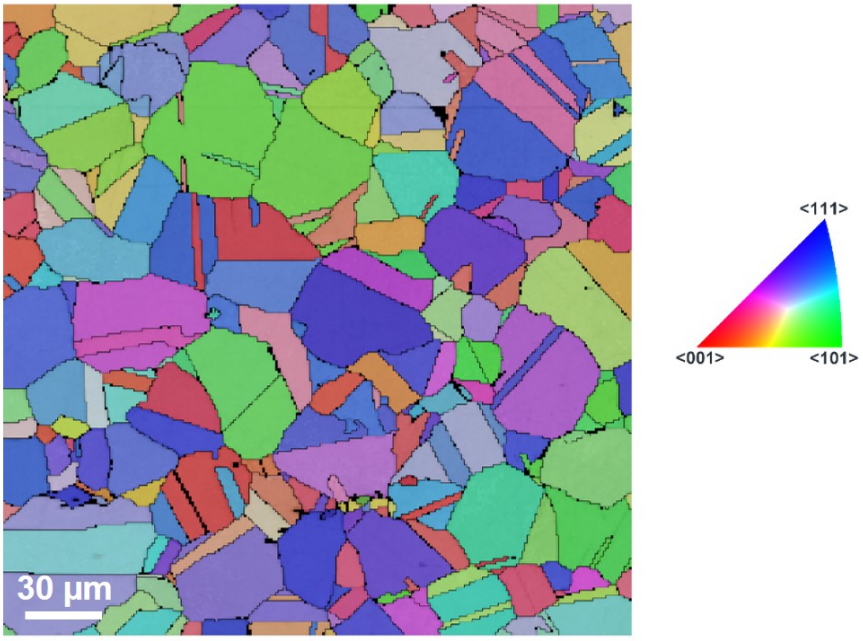

Figure III.8 – Illustration of Inverse Pole Figure (IPF) obtained from EBSD analysis of in the as-received state (Projection axis [001]).

2.3 Samples preparation

Sample preparation is a very important step in order to conduct meticulous metallographic observations. After cutting the samples, one start with the mechanical polishing by means of the Struers machine using SiC silicon carbide abrasive papers with increasing grain sizes (80, 180, 320, 600, 800, 1000, 1200 μm). This step is done under water. Then, diamond polishing (9 μm and 3 μm) and the silica suspension (OP-S) are made using the special felted discs. Subsequently, the samples are cleaned in an ultrasonic bath with ethanol. In fact, in this study, we are interested in observing on a very fine scale. Therefore, we aim to obtain a very clean surface and a perfect finish (mirror polishing). In the case of observations under the light microscope, it is necessary to use an etching solution in order to reveal the microstructure, in particular the grain boundaries. The solution used is the "Eau régale", which consists of a mixture of hydrochloric acid (HCl) and nitric acid (HNO_3), concentrated in a proportion of 75 % and 25 % respectively.

3 Mechanical characterization of Inconel 718 at low temperature

3.1 Experimental procedure

3.1.1 Experimental equipment

In order to study the mechanical behavior of Inconel 718 as well as the microstructure alterations, uniaxial compression trials have been conducted over a wide range of temperature from -188 °C to 900 °C, varying the rate from 10^{-2} s^{-1} until 10 s^{-1}. The experimental system employed during the tests is the simulator Gleeble 3500 thermo-mechanical testing machine. The loading capacity of this machine holds 100 kN. The heating process is induced following the Joule effect by resistance heating achieving a heating rate up to 10 000 °C/s. The heating system is capable of maintaining the temperature up to 1500 °C. Through the heating method, the simulator allows to perform thermal cycles much quicker (5 - 10 times) than the conventional machine using traditional ovens. Therefore, the high heating rates helps to achieve approximately the thermal heating occurred during the cutting process.

In the meanwhile of compression tests, the specimens were placed between two tungsten carbide anvils to ensure the electrical current transfer as well as to preserve a uniform temperature in the specimen when carrying out the compression test (Fig. III.9). Graphite foils were positioned between the anvils and the specimen to prevent friction at the corresponding interfaces (anvil-specimen-anvil) in order to avoid at best the barreling effect.

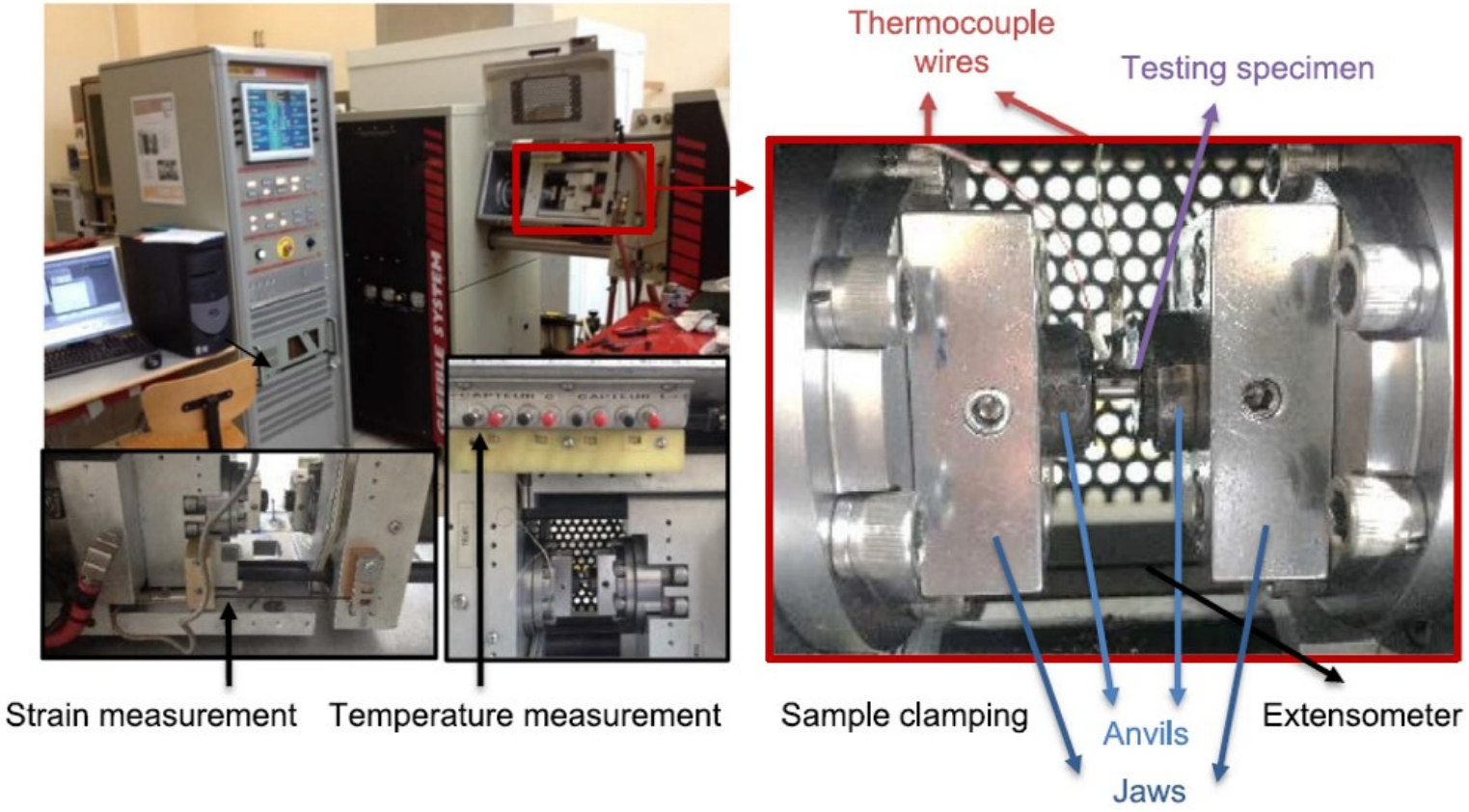

Figure III.9 – Illustration of the experimental set-up of the compression trials using the Gleeble 3500 machine (Iturbe et al., 2017).

During the compression tests, two configurations were exploited when varying the strain rate. Fig. III.10 illustrates both configurations that were employed : at high strain rate ($\dot{\varepsilon}$ >1 s^{-1}) the trials were carried out with uncoupled strategy (configuration A); at low and medium strain rates ($\dot{\varepsilon} \leq 1$ s^{-1}), tests are performed with the coupled strategy (configuration B). Regarding this configuration (B), the two parts of the hydraulic cylinder are coupled and the pneumatic cylinder is desactivated. In contrast, when employing the configuration A, the two parts of the hydraulic cylinder are uncoupled and the pneumatic cylinder is activated in order to maintain the specimen. In this case, in order to control the desired strain, adjustable shims are added between the fixed and the mobile jaws. Also, the shims serve to absorb the energy transmitted during the impact.

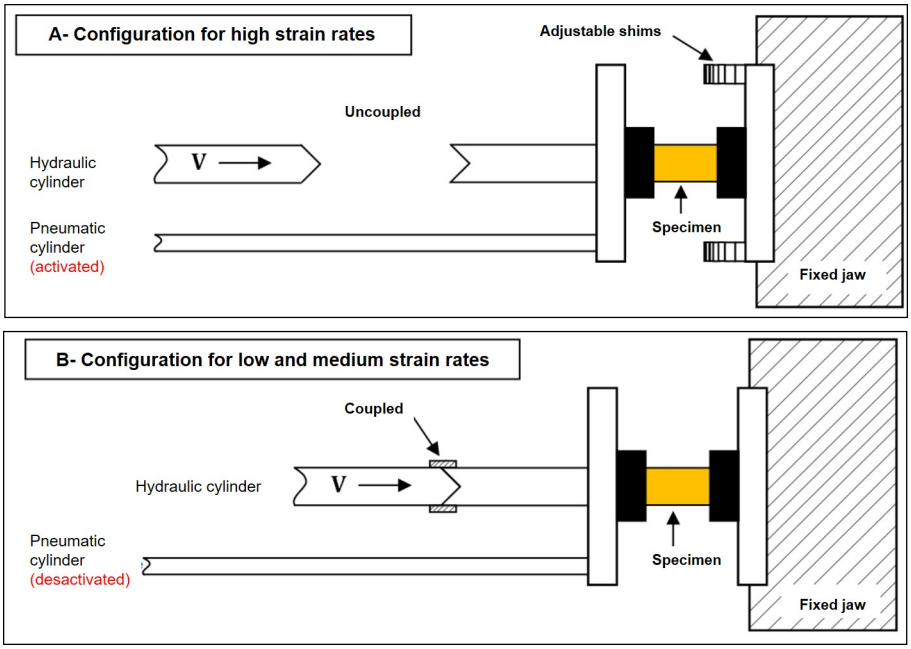

Figure III.10 – Illustration of the two configurations used for the compression tests on Glebble 3500 machine: A-Configuration used for tests performed at high strain rates ($\dot{\varepsilon} > 1$ s^{-1}); B-Configuration used for tests performed at low and medium strain rates ($\dot{\varepsilon} \leq 1$ s^{-1}) (Hor et al., 2013).

At high temperature, in order to avoid the oxidation, the experiments have been performed on a primary vacuum chamber. In addition, for metallographic observations purpose, the microstructure was quenched after test thanks to a cooling system (by a jet of compressed air) allowing achieving cooling rates greater than 230 °C/s.
K-type thermocouples were employed to measure the temperature during the tests. The thermocouples were welded in a centered position on the surface of the specimen (Fig.III.9). The applied thermal load consists of heating the specimen at a constant heating rate of 10 °C/s up to the test temperature (T_{CT}). Subsequently, the temperature is maintained constant for 20 s to homogenize the temperature along the specimen without desoldering thermocouples. The specimen is immediately deformed at a constant strain rate. Once the test is accomplished, heating is ceased and the specimen is instantly quenched in a vacuum in order to avoid microstructure change (Fig.III.11). It is worth mentioning that to avoid microstructural transformation during the thermal loading, one is interested to refer to the TTT-diagram and to identify the maintaining time when heating the specimens (Fig.III.12).

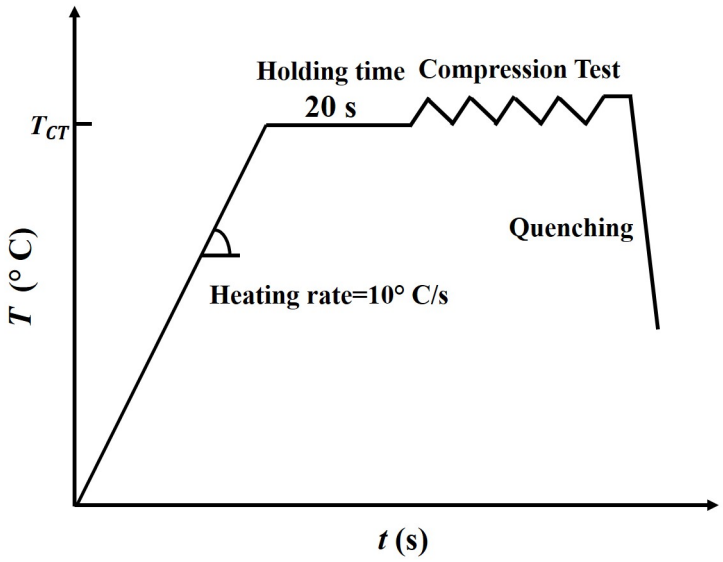

Figure III.11 – Illustration of the thermal cycle applied at high temperature.

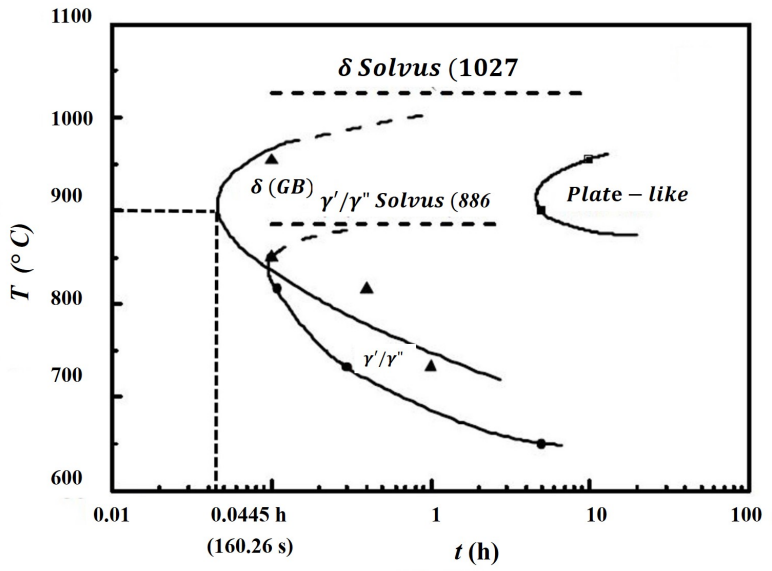

Figure III.12 – Illustration of TTT-diagram of Inconel 718 (Xie et al., 2005).

As for the cryogenic thermal condition, it was relevant to maintain cooling down the specimens along 10 min in order to ensure a stable and homogeneous temperature along the specimens (Yoon et al., 2010). The temperature acquisition has been conducted at the beginning of the trials in order to guarantee that the temperature is maintained at -188 °C as displayed in Fig.III.13.

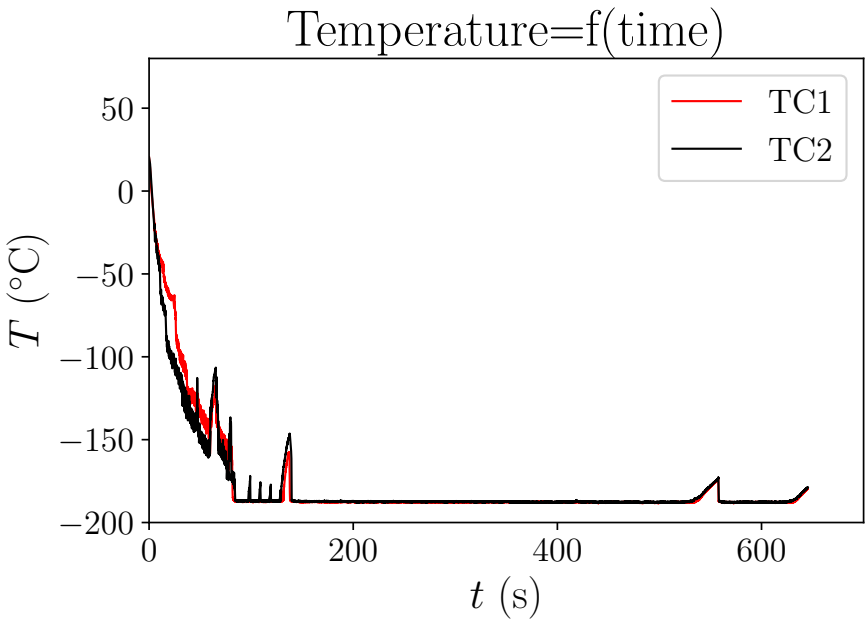

Figure III.13 – Illustration of the thermal cycle applied at cryogenic temperature.

In this study, a cryogenic system has been developed in the laboratory LAMPA in order to carry out compression tests at cryogenic temperature. The most challenging task during the design of the cryogenic system was maintaining the cryogenic temperature before and during the compression tests. Indeed, this system satisfied the expected requirement as mentioned in Fig.III.13.
The cryogenic set-up is essentially composed of funnel from where the cryogenic fluid (LN_2) is supplied to be conveyed through a hosepipe in order to quench the specimen. The latter is fixed in the container between the two anvils during the quenching process as well as the compression test (Fig.III.14). It is interesting to highlight that the container has been manufactured using a 3d-printer. For each cryogenic trial, one container has been produced.

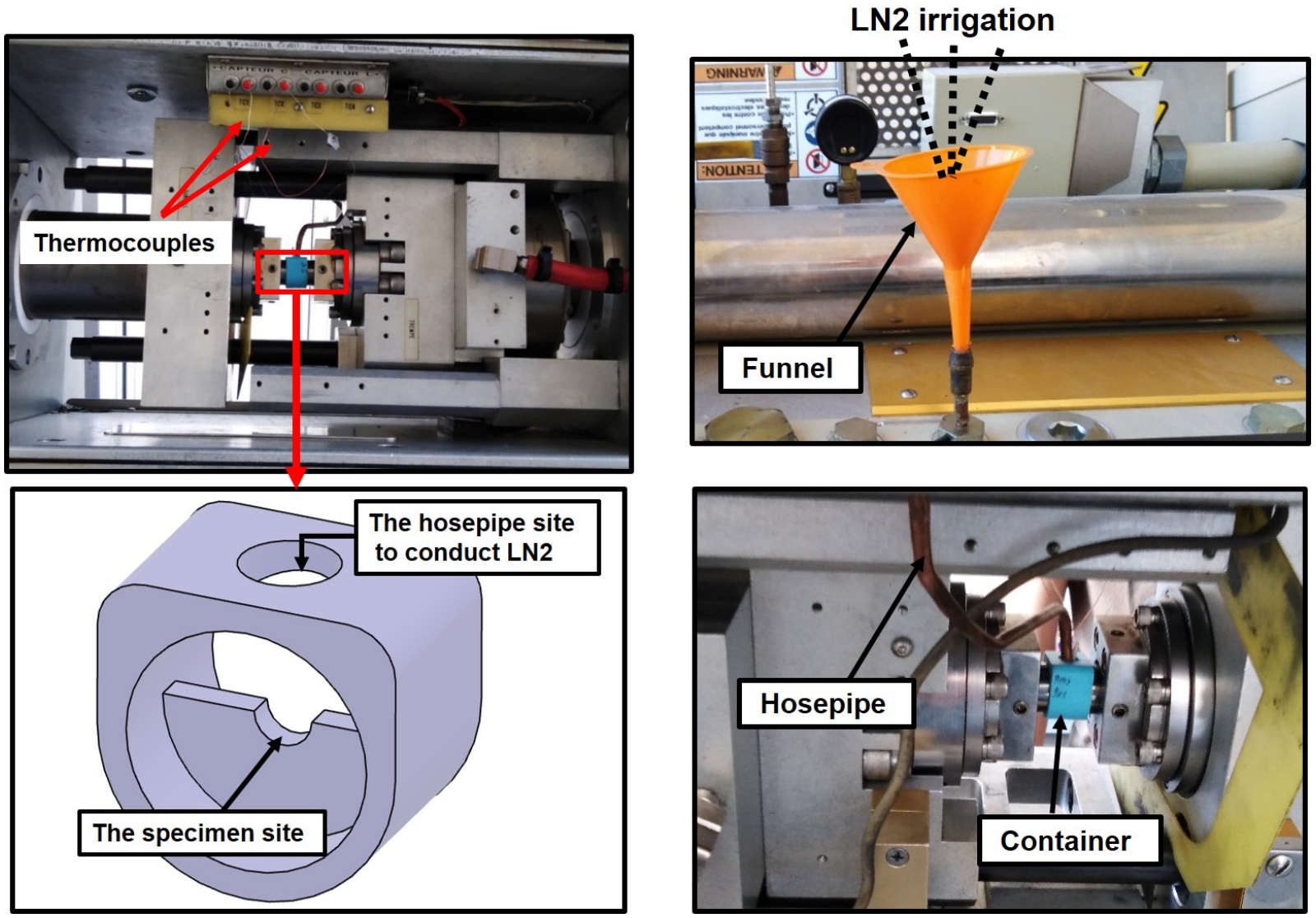

Figure III.14 – Illustration of the cryogenic set-up of the compression trials conducted at cryogenic temperature using the Gleeble 3500 machine: The front view of the Gleeble machine (on the left); The back view of the Gleeble machine (on the right)

In this context, it seems interesting to show the temperature evolution before and after deforming the work material in cryogenic configuration. Fig.III.15 depicts the temperature evolution during the compression test at $T = -188$ °C and $\dot{\varepsilon} = 0.01$ s^{-1}. In this condition, the temperature was maintained at -188 °C before starting the compression test (t<16 s). When applying the mechanical load, the temperature did not evolve until t=22 s to reach almost -50 °C by the end of the test. The temperature increase is essentially due to the self-heating (the conversion of plastic work into heat) and probably the heat exchange with the environment (losses by conduction, convection and radiation from the specimen to its surroundings).

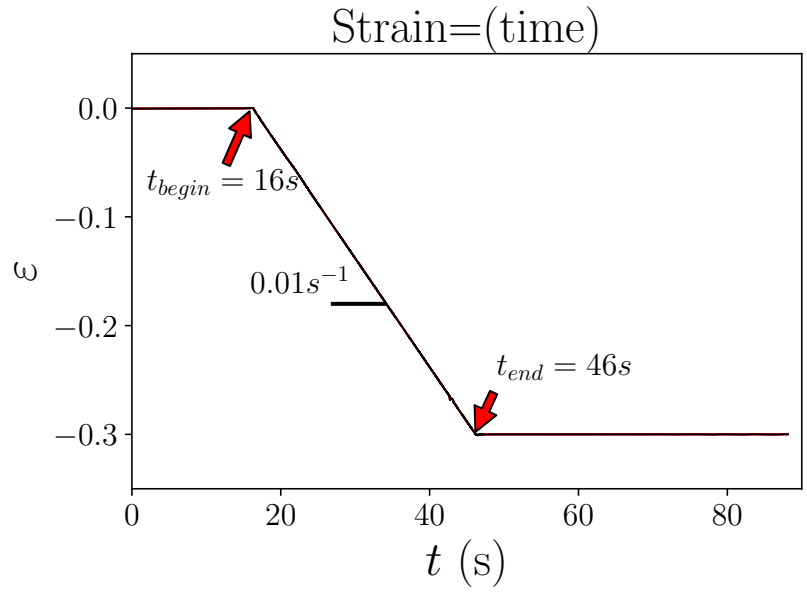

(a)

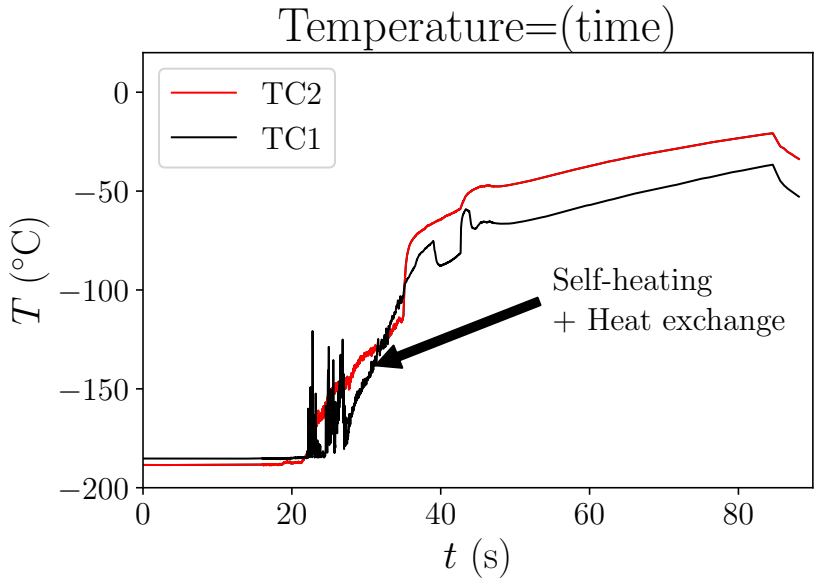

(b)

Figure III.15 – Illustration of temperature evolution during the compression test at $T = -188$ °C and $\dot{\varepsilon} = 0.01$ s^{-1}.

3.1.2 Experimental methodology

In order to characterize the mechanical behavior of Inconel 718 at low and high temperature, an initial experimental plan of the compression tests was fixed. At first, a prior experimental plan has been established revealing the extreme range either concerning the working temperature or the strain rate. It is well known that depending on the cooling strategies (dry, conventional lubrication or cryogenic cooling), the interaction between the cutting tool and the work material during the machining process is thereby altered (Czán et al., 2017). Obviously, the deformation mechanisms and cutting temperature are therefore modified. As previously mentioned that at the beginning of the cryogenic machining, the workpiece material undergoes very low temperature around -196 °C. Hence, one is interested to study low temperature effect on the mechanical behavior of Inconel 718.
According to the results, intermediate temperature was modified as well as the strain rate interval since that the main objective of this campaign is to investigate the influence of both loading (thermal and mechanical) on Inconel 718 behavior, in particular the microstructure alterations induced after cryogenic conditions. The final experimental plan is given below in Fig. III.16. Three repetitions have been preformed for each condition.

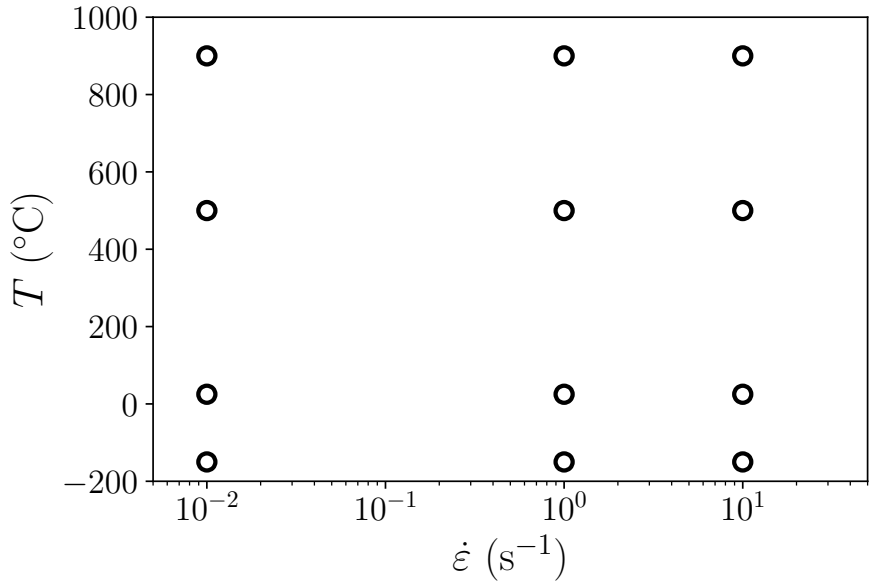

Figure III.16 – Illustration of the experimental plan presenting the working temperature T (°C) and the strain rate $\dot{\varepsilon}$ (s^{-1}) used during the compression tests.

The compression test specimens had a cylindrical shape with an initial diameter equal to 6 mm and an initial length of 9 mm. The specimens were machined using the electro-discharge wire machining (EDM) technique. Afterwards, polishing process was necessary to improve the surface finish of the contact surfaces aiming a better parallelism between anvils and the specimen.

A quartz longitudinal extensometer, positioned on the jaws, was used to measure the displacement. Therefore, it is worth mentioning that the displacement measurement is overestimated. Many parts and contact surfaces are involved in the measuring chain (jaws, anvils and specimen) as displayed in Fig.III.9. The displacement integrates then

the elastic deformation of the jaws and the anvils as well as the deformation of the specimen. Consequently, the stress-strain curves must be corrected considering only the deformation of the testing specimen. Referring to (Hor et al., 2013), the stiffness of the machine (jaws and anvils) was removed in order to estimate the exact deformation of the specimens, knowing the young modulus values for each test temperature. Fig. III.17 shows the curve evolution of the Young modulus versus temperature that has been exploited to correct all the obtained stress-strain curves. However, it appears very hard to find the value of this parameter at cryogenic temperature. Thereby, an extrapolation has been assumed.

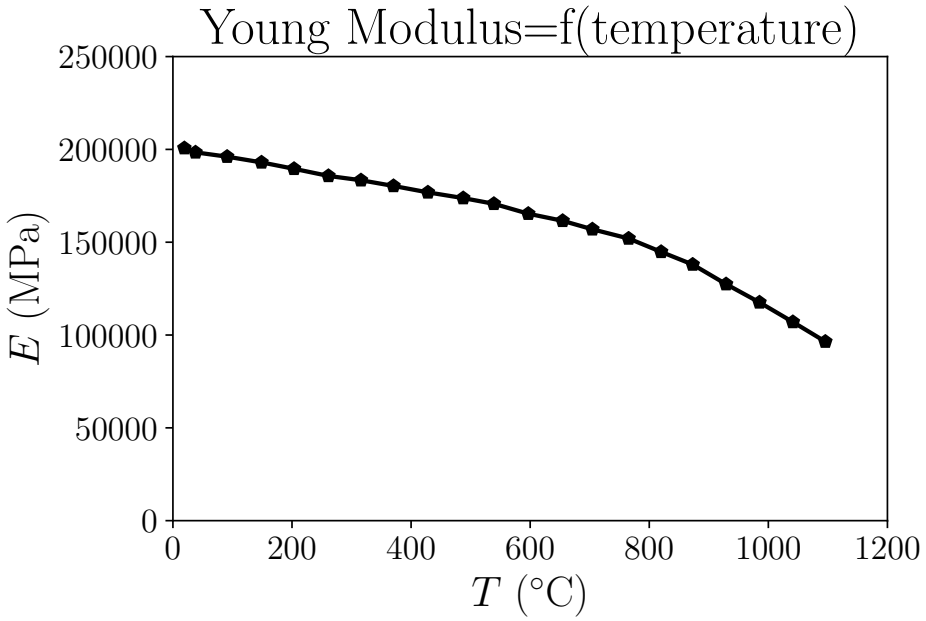

Figure III.17 – Illustration of the evolution of the Young Modulus versus temperature (Fabre, 2013).

Furthermore, it is interesting to declare that when calculating the deformation during the compression test, the strain field is supposed to be homogeneous. Nevertheless, few deformed specimens exhibited barrel shape even if precautions were considered to reduce as possible the friction between the specimen and the interfaces of anvils, so that, the temperature and the strain within the samples were uniform. Consequently, the friction effect was neglected when correction the stress-strain curves.
As previously reported that one is assuming that the deformation occurred in a homogeneous way. Therefore, the expression of the instantaneous strain and stress are assessed using the following formula:

$$\varepsilon = ln(1 + \frac{\Delta l}{l_0}) \tag{III.1}$$

$$\sigma = \frac{F}{S} = \frac{F}{S_0}(1 + \frac{\Delta l}{l_0}) == \frac{4F}{\pi {d_0}^2}(1 + \frac{\Delta l}{l_0}) \tag{III.2}$$

where l_0 and d_0 are respectively the initial length and diameter of the cylindrical specimens. It should be noted that the compression tests have been carried out at a fixed strain level equal to 0.25 in order to be coherent when comparing the deformed microstructure.

3.2 Results and discussions

3.2.1 Stress-strain curves

The stress-strain curves of the superalloy Inconel 718 obtained over a wide range of temperature from -188 °C to 900 °C and strain rates ranging from 0.01 s^{-1} to 10 s^{-1} are shown in the figures below (Fig.III.18, Fig.III.19 and Fig.III.20).

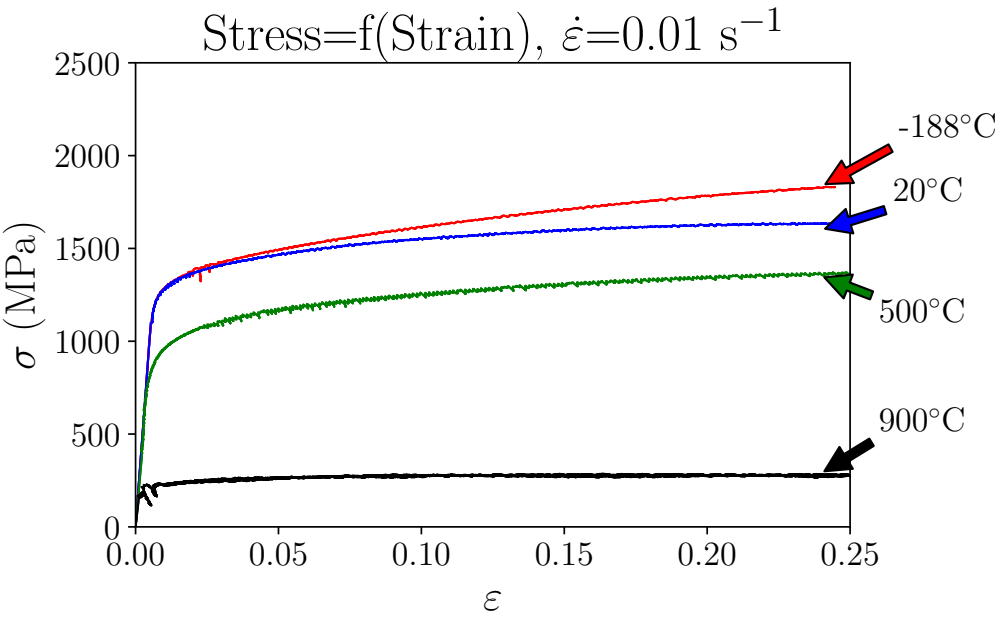

Figure III.18 – Illustration of stress-strain curves obtained at a fixed strain rate $\dot{\varepsilon}$=0.01 s^{-1} over different temperature range.

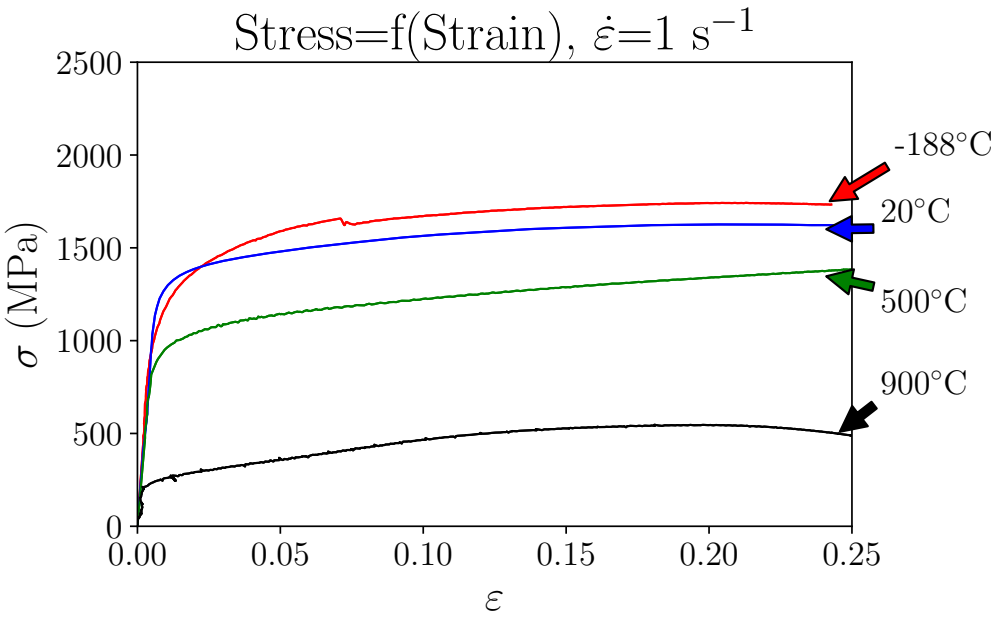

Figure III.19 – Illustration of stress-strain curves obtained at a fixed strain rate $\dot{\varepsilon}$ =1 s^{-1} over different temperature range.

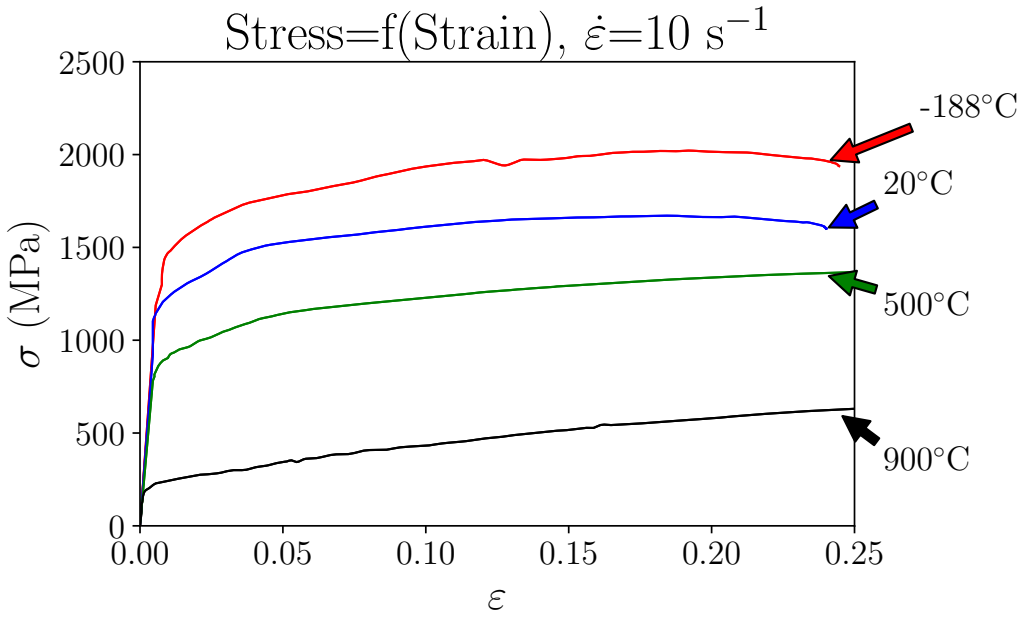

Figure III.20 – Illustration of stress-strain curves obtained at a fixed strain rate $\dot{\varepsilon}$ =10 s^{-1} over different temperature range.

Based on the results, Inconel 718 exhibited thermoplastic behavior regardless of the strain rate range: as the temperature increases, the stress decreases relatively. Obviously, this fact figured out a typical tendency of the temperature effects dominance as long as the temperature increases (Aaron, 2015). This effect is classically justified by the impact of the dislocation mobility rise proportionally to the temperature increase inducing a stress decrease (Yuan and Liu, 2005).
For instance, at low strain rate $\dot{\varepsilon} = 0.01$ s^{-1}, the flow stress decreases significantly when testing temperature increases from -188 °C to 500 °C and dropped significantly at 900 °C. Paturi et al. (2020) reported similar observations confirming that the thermal softening of Inconel 718 became dominating from a temperature of 700 °C. Beneath this level of temperature, the work material maintained its mechanical properties high as illustrated in Fig. III.18, Fig. III.19 and Fig. III.20. Additionally, when examining the stress-strain curves, it is remarkable that the slopes of the majority of the curves are positive indicating that the work hardening phenomena is rather dominant as a function of temperature. The work hardening phenomena is closely related to the increase of the dislocation density (Yuan and Liu, 2005). At a low temperature interval (from -188 °C to 500 °C), the slope of the flow stress curves are positive. However, at high temperature level (900 °C), Inconel 718 revealed a steady state behavior showing an equilibrium between the work hardening and the thermal softening (Fig. III.18). This phenomenon could be promoted by the dynamic recovery (DRV) as reported in (Iturbe et al., 2017). Indeed, the competition between the annihilation of dislocations (DRV) and the dynamic recrystallization (DRX) in addition to the multiplication of dislocations governs the thermo-mechanical behavior of Inconel 718 at this range of temperature (Lv et al., 2020).
At a strain rate equal to 1 s^{-1}, the stress-strain curves exhibited almost similar behavior as the ones obtained at 0.01 s^{-1} except at 900 °C where the flow stress behavior showed a non negligible increase. Most of curves obtained at -188 °C, room temperature (RT) and 500 °C revealed a positive slope indicating a dominant work hardening occurred during the compression deformation. At 900 °C, the behavior of the work material

could be divided into two domains depending on the strain level. At the beginning of the deformation test, a rapid rise of the stress could be observed indicating a strain hardening until reaching a strain value of 0.23. Above this level, the flow stress decreased as long as the strain increases due to the dominance of the thermal softening phenomena. Lin et al. (2015) reported similar observations proving that the thermal softening of Inconel 718 take place usually at high temperature range (above 700 °C). Under dynamic conditions where $\dot{\varepsilon}$ =10 s^{-1}, the cryogenic temperature induced significant rise of the flow stress behavior in comparison with the room temperature. In the same context, Wang et al. (2008) proved the flow stress of Inconel 718 exhibited the highest curve when increasing the strain rate up to 5000 s^{-1} at low temperature (-150 °C) in comparison with room temperature. Additionally, it can be seen that at 900 °C, the strength of the work material increased drastically when increasing the strain rate up 10 s^{-1}. This finding is in agreement with the usually observed deformation characteristics of nickel based superalloys (Iturbe et al., 2017; Yuan and Liu, 2005).
It should be mentioned that none of the tested specimens have failed under the considered test configurations at the fixed strain level of 0.3.

To extract additional information regarding the loading conditions impact on Inconel 718 mechanical behavior, one has evaluated the two coefficients m and n indicating respectively the sensitivity coefficient to strain rate and the strain hardening coefficient. These parameters have been exploited according to Arrhenius law (Deng et al., 2013). At a fixed temperature and a given strain level, the sensitivity coefficient to strain rate m is given following the equation below:

$$m = \frac{dln(\sigma)}{dln(\dot{\varepsilon})_{|T,\varepsilon}} \tag{III.3}$$

The sensitivity coefficient to strain rate m has been assessed for a strain level of 0.1. At a fixed temperature and a given strain rate, the strain hardening coefficient n is deduced from the equation below:

$$n = \frac{dln(\sigma)}{dln(\varepsilon)_{|T,\dot{\varepsilon}}} \tag{III.4}$$

The results are given respectively in Fig.III.21 and Fig.III.22.

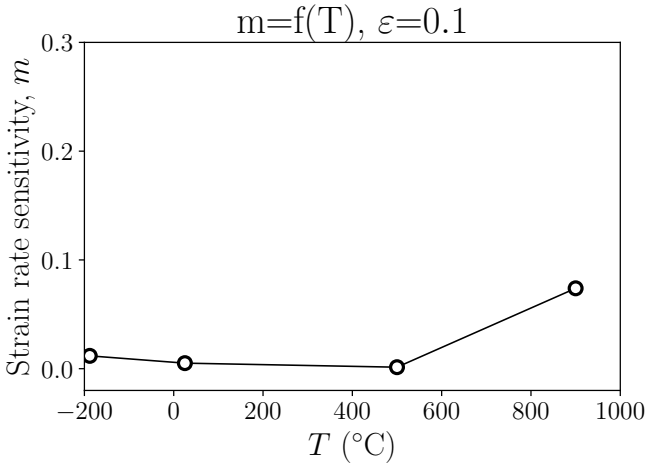

Figure III.21 – Illustration of the sensitivity coefficient to strain rate "m" calculating at a strain level equal to 0.1.

Concerning the sensitivity coefficient to strain rate, m presented very low value at the temperature range from -188 °C up to 500 °C. However, at high temperature of 900 °C, this parameter increased remarkably to confirm that Inconel 718 behaved in a viscous manner at very high temperature. Indeed, the strain rate sensitivity is almost negligible at low temperature domain up to 500 °C. Nevertheless, as long as the temperature became higher, the influence of the strain rate on the material strength increased as well (Fig. III.21). Similar observations have been reported by (Iturbe et al., 2017) confirming that Inconel 718 became much more sensitive to the strain rate above 700 °C. In fact, the strain rate sensitivity is associated to the dislocation movement (Cheng et al., 2013). As the temperature increases, the dislocation mobility increased as well. This statements confirms the high value of m at 900 °C.

As for the strain hardening coefficient, n was evaluated at a strain level of 0.1 from the stress-strain curves. Results showed that all the values of this parameter, at all strain rate intervals and for all temperature domains, revealed positive values confirming the work hardening dominance during the compression tests as previously mentioned. Additionally, as described in Fig.III.22, the strain hardening coefficient n exhibited higher values at 900 °C as long as the strain rate rises (at 1 and 10 s^{-1}). This observation is in agreement with the findings mentioned in the previous section.

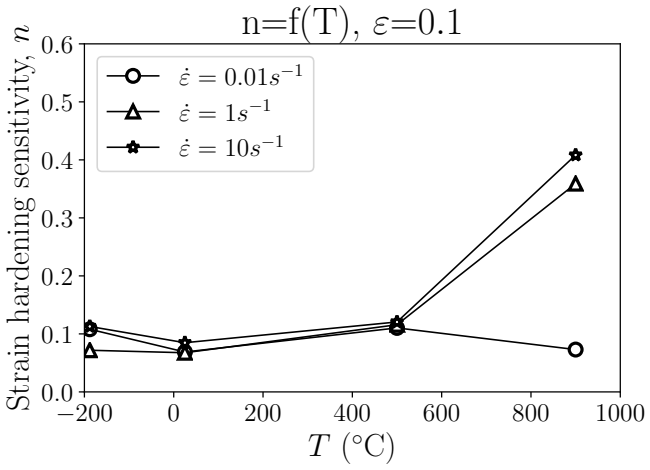

Figure III.22 – Illustration of the strain hardening coefficient "n" over a wide range of strain rate (from 0.01 $s^{-1}$to 10 s^{-1}).

3.2.2 Mirco-hardness measurements

In order to confirm the previous results concerning the strain hardening coefficient n, micro-hardness measurements have been carried out using the Vickers method with a 200 gf load. In this study, the main objective is to examine the effect of cryogenic temperature on the mechanical behavior of Inconel as well as the microstructure evolution further to the compression tests. Therefore, longitudinal and transversal measurements have been conducted at the center of the specimens after deforming the work material at room temperature as well as at cryogenic temperature under both static and dynamic loading ($\dot{\varepsilon}$ = 0.01 s^{-1} and 10 s^{-1}).

Measurements along both directions (longitudinal and transversal) presented almost the same values. For this reason, for each configuration, an average of the measurements was considered. Results are shown in Fig. III.23.

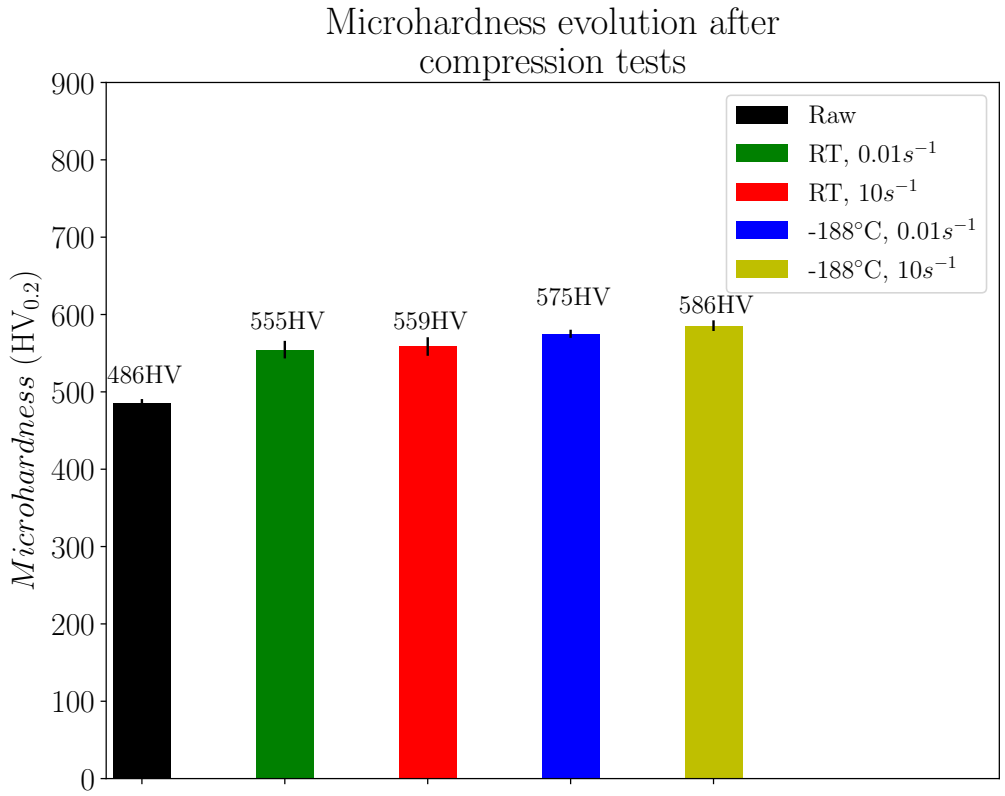

Figure III.23 – Illustration of the micro-hardness profiles obtained after compression tests at low and room temperatures.

In line with the results obtained in the stress-strain curves and the strain hardening coefficient n, two points could be discussed. First, when comparing the micro-hardness of the raw material (486 $HV_{0.2}$) and the deformed specimens, an increase of the micro-hardness after compression tests could be observed ($\leq$ 555 $HV_{0.2}$). Therefore, it could be concluded that work hardening phenomena governed the flow stress behavior of Inconel 718. This finding proved an accordance with the stress-strain curves as well as the strain hardening coefficient n.
Subsequently, it seems to be interesting to compare the micro-hardness values of the deformed specimens at cryogenic and room temperatures. Indeed, at 0.01 s^{-1} and 10 s^{-1}, the micro-hardness measurements showed slightly higher values at cryogenic temperature than those obtained at room temperature. For instance, at a fixed strain rate of 10 s^{-1}, cryogenic temperature induced 586 $HV_{0.2}$ versus 559 $HV_{0.2}$. At cryogenic temperature, a slight rise of the micro-hardness was observed when the strain rate increased from 0.01 to 10 s^{-1} holding respectively 575 $HV_{0.2}$ and 586 $HV_{0.2}$.
According to these observations, one could conclude that cryogenic temperature induced slightly harder material after deformation compared to room temperature, regardless of the strain rate value.

As previously reported, in this research, it could be interesting to evaluate the cryogenic temperature effect on the mechanical behavior of Inconel 718. Therefore, a comparison between the mechanical properties namely, the yield stress as well as the peak stress have been evaluated at cryogenic and room temperatures. Results are given in the figure below (Fig. III.24).

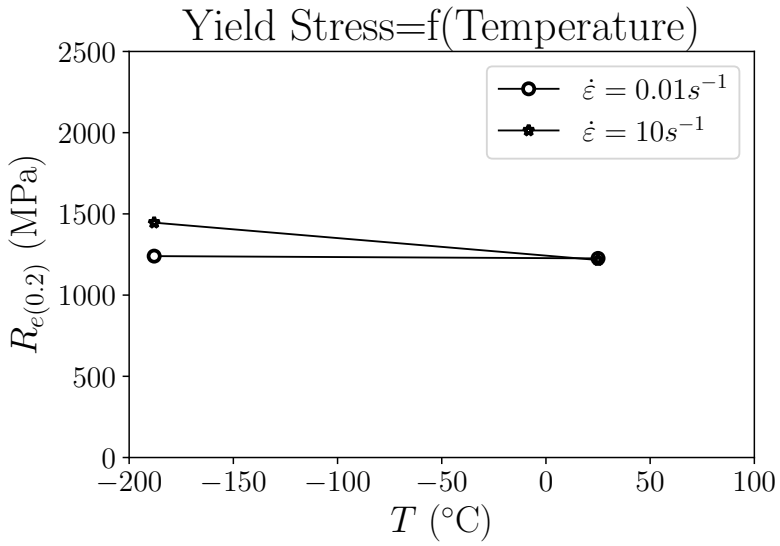

(a)

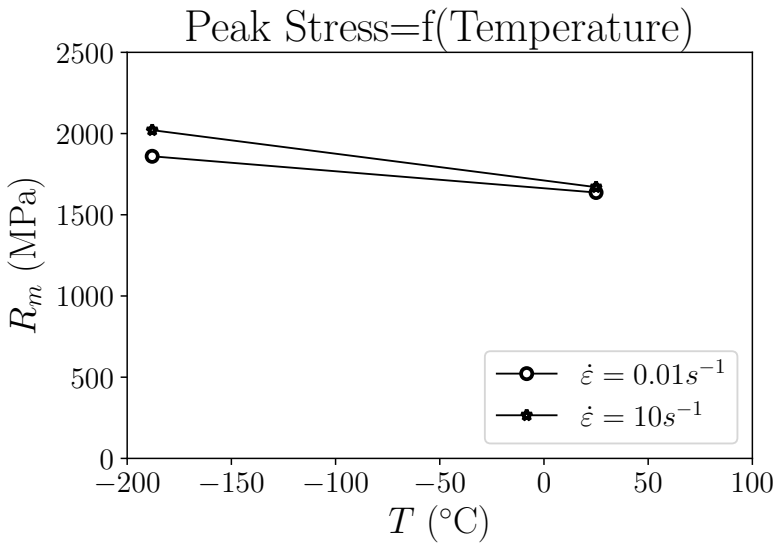

(b)

Figure III.24 – Illustration of the mechanical properties evolution of Inconel 718 along temperature at two strain rates : a) Yield stress "R_e"; b) Peak stress "R_m".

Both cryogenic configurations (at low and high strain rates) induces the highest resistance behavior compared to room temperature. Indeed, a decrease in temperature is associated with an increase in the flow stress, because a decrease in temperature reduces dislocations mobility to overcome obstacles (Ben Boubaker et al., 2020). At $\dot{\varepsilon}$ = 10 s^{-1}, the yield stress increased as the temperature decreased to -188 °C indicating an improvement around 19 % compared to room temperature. Furthermore, the peak stress R_m of Inconel 718 showed the same tendency as the yield stress. For instance, the R_m showed a rise of 351 MPa under cryogenic condition at $\dot{\varepsilon} = 10$ s^{-1} in comparison

with room temperature. This observation could be an explanation for the high values of the cutting forces generated during the cutting process under cryogenic conditions when machining Inconel 718.
The same finding was established by (Jiang et al., 2016; Lee et al., 2011) where authors proved that the highest mechanical properties were generated under cryogenic environments irrespective of the strain rate range.
It could be pointed out that a good correlation might be established between the micro-hardness measurements and the peak stress R_m obtained under cryogenic conditions and the room temperature configurations. Effectively, the R_m exhibited almost the same values at room temperature when varying the strain rate at the same time that the micro-hardness values followed similar tendencies. Furthermore, an increase of the R_m at cryogenic temperature as the strain rate rose has been obtained while the micro-hardness showed an increase as well even if it is not proportional.

3.2.3 Metallographic analysis

3.2.3.a Microstructure observations

In order to export additional information with respect to the microstructural alterations, metallographic observations of the deformed specimens have been performed using the optical microscopy. The deformed microstructures generated under cryogenic conditions and room temperature configurations are given in Fig. III.25 and Fig.III.26.

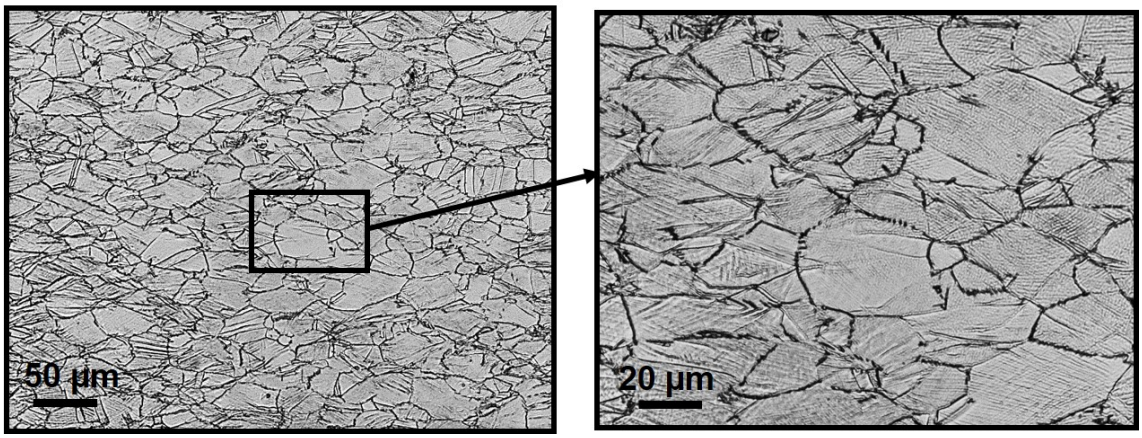

(a)

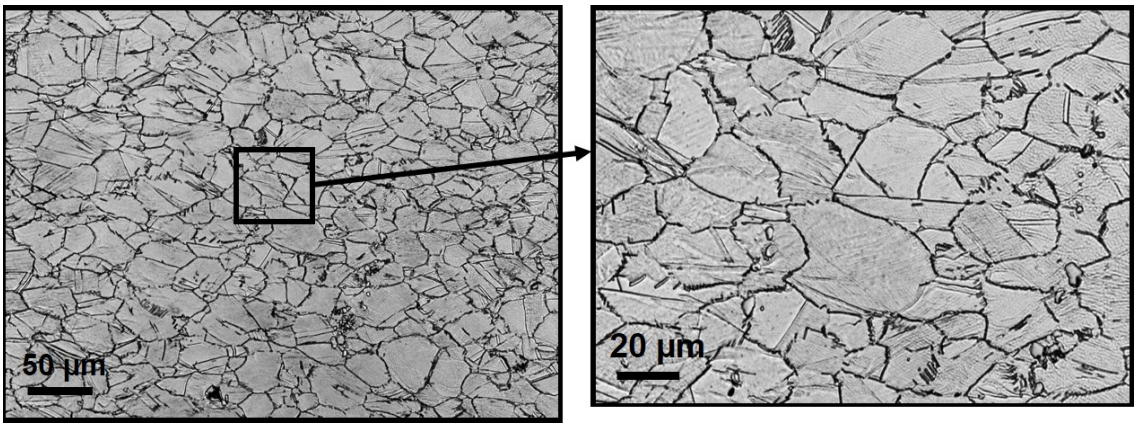

(b)

Figure III.25 – Illustration of metallographic observations of the deformed microstructure at strain rate equal to 0.01 s^{-1} : (a) at room temperature (RT); (b) cryogenic temperature (T=-188°C).

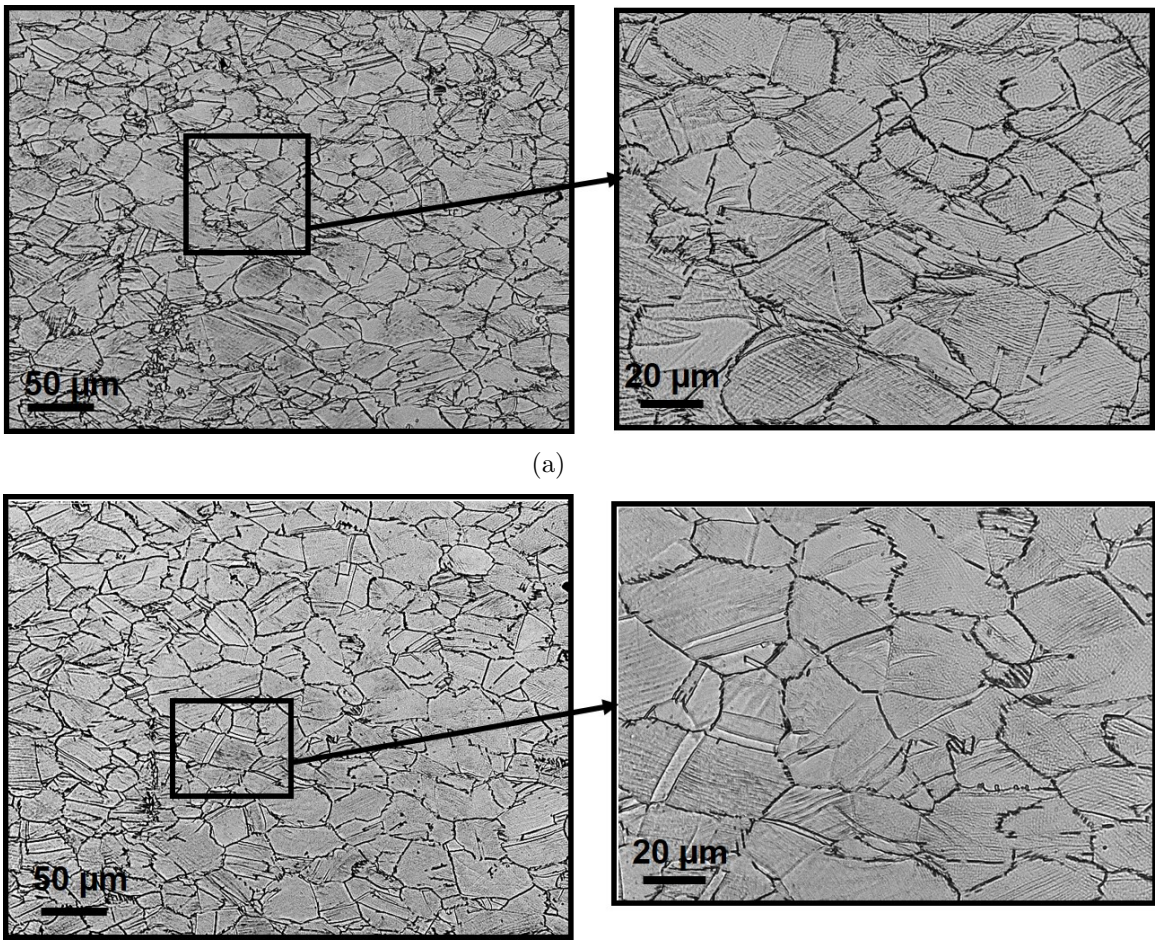

Figure III.26 – Illustration of metallographic observations of the deformed microstructure at strain rate equal to 10 s^{-1} : (a) at room temperature (RT); (b) cryogenic temperature (T=-188 °C).

The deformed specimens underwent the same level of deformation (ε= 0.25) in order to be coherent to extract the temperature influence at a fixed strain rate.
Fig. III.25 highlights the deformed microstructures obtained at strain rate equal to 0.01 s^{-1} at room temperature and low temperature (T=-188 °C). Both conditions generated heavily deformed grains in the center of the specimens. At high magnification, remarkable slip lines could be observed confirming the high level of plastic deformation occurred during the compression tests. Classically, it is well known that the slip lines are mainly resulted from the heavily plastic deformation caused by slip of the crystallographic planes caused by dislocation movement (Kawamura et al., 2021). In the same context, Najafi and Asgari (2005) pointed out another explanation of the main origin of the slip lines. In their study, they focused on the strain hardening mechanisms in an aged nickel based superalloy (AEREX350) during room temperature compression tests. They have figured out that the slip lines observed on the surface of the deformed samples are the signature of the twin deformation clusters.
Compared to the initial microstructure (before deformation), the plastic deformation seems to be not only governed by a slip of the crystallographic planes but also the twinning mechanism. Indeed, both deformed microstructure presented an increase of the twinned grains in comparison with the raw microstructure. Regardless the origin of the slip lines, the latters are good indicators of the high strain hardening previously

highlighted from the stress-strain curves as well as the micro-hardness measurements. Similar findings are observed at higher strain rate (10 s^{-1}) under cryogenic condition and room temperature configuration as illustrated in Fig.III.26. The metallographic observations revealed high plastic deformation occurred after compression tests. Indeed, the twinning rate seemed to be higher compared to raw material in addition to the presence of the slip lines.
Overall, the main conclusion that could be extracted from the optical observations consists of that cryogenic temperature did not show any alteration regarding the microstructure, in comparison with that one obtained at room temperature. Even, SEM observations have been conducted and they highlighted the same findings.
Additionally, when examining the deformed samples, no shear bands have been observed under all testing conditions. No specimen has failed as well.

3.2.3.b EBSD analysis

In this section, the EBSD technique was employed in order to characterize the local plastic deformation of the specimens that have been subjected to compression loading. The EBSD analyses have been performed in the center of the deformed zones of the tested samples.
The Inverse Pole Figures deduced from the EBSD analyses of the deformed specimens: at room and cryogenic temperatures and at low and high strain rates are presented in Fig. III.27 and Fig. III.28.

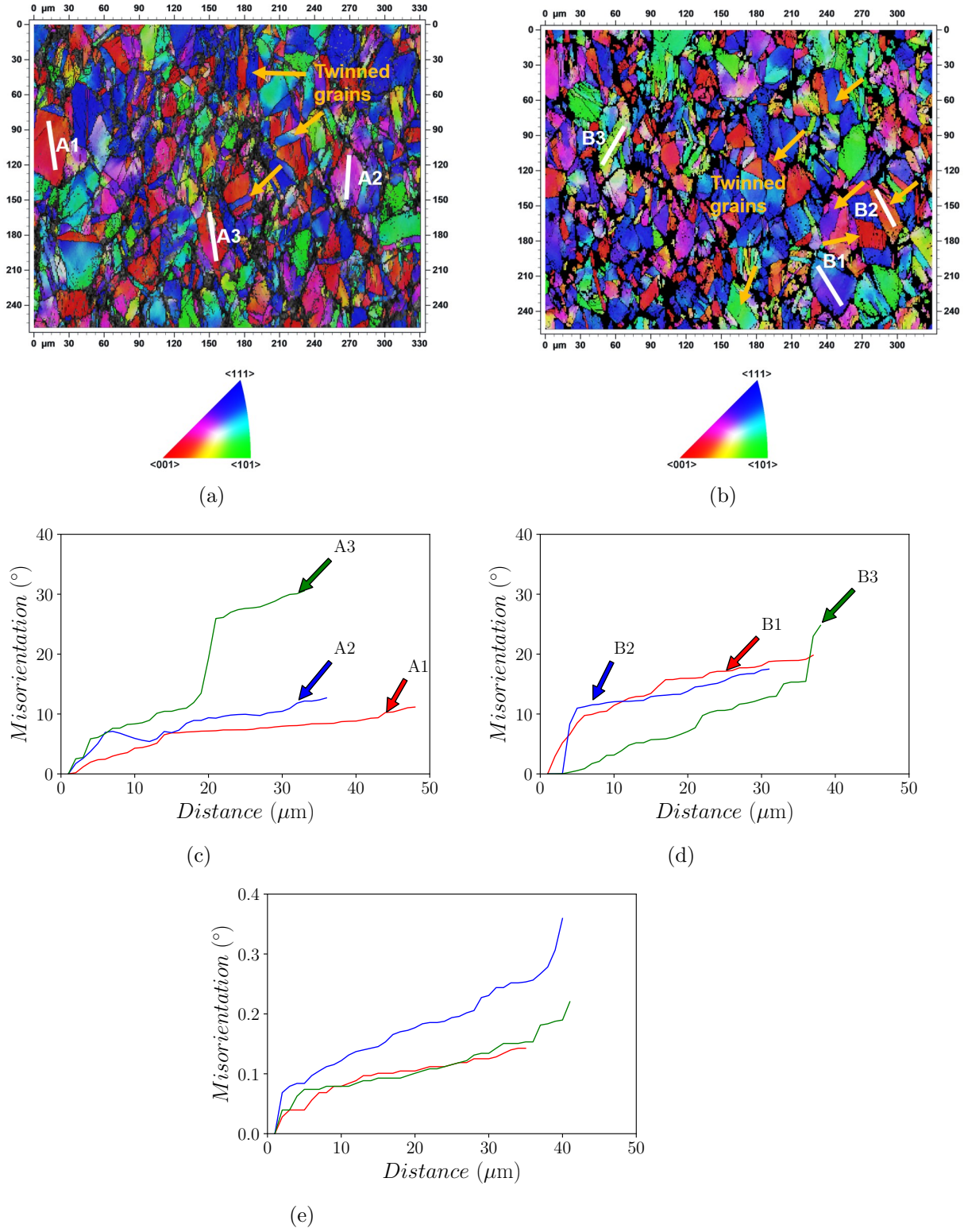

Figure III.27 – Inverse Pole Figure (IPF) obtained from EBSD analyses of the deformed specimens (Projection axis [001]) established at 0.01 s^{-1} in room temperature (a) and cryogenic temperature (b); Misorientation gradients measured inside deformed grains in the case of: (c) Room temperature; (d) Cryogenic temperature; (e) Undeformed grains of a raw specimen.

Conventionally, researchers coordinated the plastic deformation level with the point-to-point misorientations and/or the point-to-origin misorientations within deformed grains (Lv et al., 2020; Lin et al., 2015). In this line, the point-to-origin misorientations within deformed grains are exploited to evaluate the effects of cryogenic temperature as well as the strain rate on the misorientation gradient and thereby plastic deformation intensity. It can be observed that the cumulative misorientations presented large values as defined respectively in the marked lines A2, A3, B1 and B3 at room temperature and at low temperature reaching around 30°.

To identify well the effect of the plastic deformation on the misorientation gradients inside the deformed grains, it was relevant to indicate the misorientation gradients evaluated inside undeformed grains of a raw specimen. Indeed, the corresponding results highlighted that the considered parameter presented extremely low values (did not exceed 0.4°). Nevertheless, there is a sharp rising of the misorientation gradients for the whole deformed specimens having relatively more than 20°.

Moreover, the IPF illustrated the large amount of plastic deformation of the work material in both compression configurations, where grains are severely sheared. Consequently, it could be observed that the misorientations distribution of the polycrystal are impacted. This statement is in a good agreement if comparing the IPF of the raw specimen (Fig.III.8 developed in section.2.2.3) and the deformed specimens (illustrated in the current section).

It is visible that for certain IPF maps, some areas showed dark regions indicating a non-indexation essentially caused by the high intensity of plastic deformation as displayed in Fig. III.27.

In addition, a noticeable increase of the twinned grains could be identified through the Fig.III.27 indicating that the plastic deformation not only governed by dislocation slip but also the twinning mechanism. At this level of analysis, it seems very difficult to distinguish which mechanisms dominate the plastic deformation for two main reasons. Indeed, the scale of the metallographic observations conducted in the present work does not allow these kinds of characterization as well as both plastic deformation mechanisms competed in a very complex way that could be hard to explain. To do this, advanced approaches may be employed such as the Transmission Electron Microscopy (TEM) technique. In this context, Jiang et al. (2016) suggested that under cryogenic environment, the twinning deformation in addition to dislocation slip of three kinds of nickel based alloys when there were subjected to compression loads, occurred alternatively depending on the applied shear stress.

The Fig. III.28 pointed out similar findings concerning the high intensity of plastic deformation occurring under dynamic conditions for a strain rate equal to 10 s^{-1}. In this context, previous studies proved the strain rate impact when calculating the cumulative misorientations (the point-to-origin misorientations) at very high temperature domain up to 1050 °C (Azarbarmas et al., 2016). Consistently, under these conditions (low temperature), no significant influence could be observed concerning the cumulative misorientations assessed along the lines marked in the Fig. III.27 and Fig. III.28.

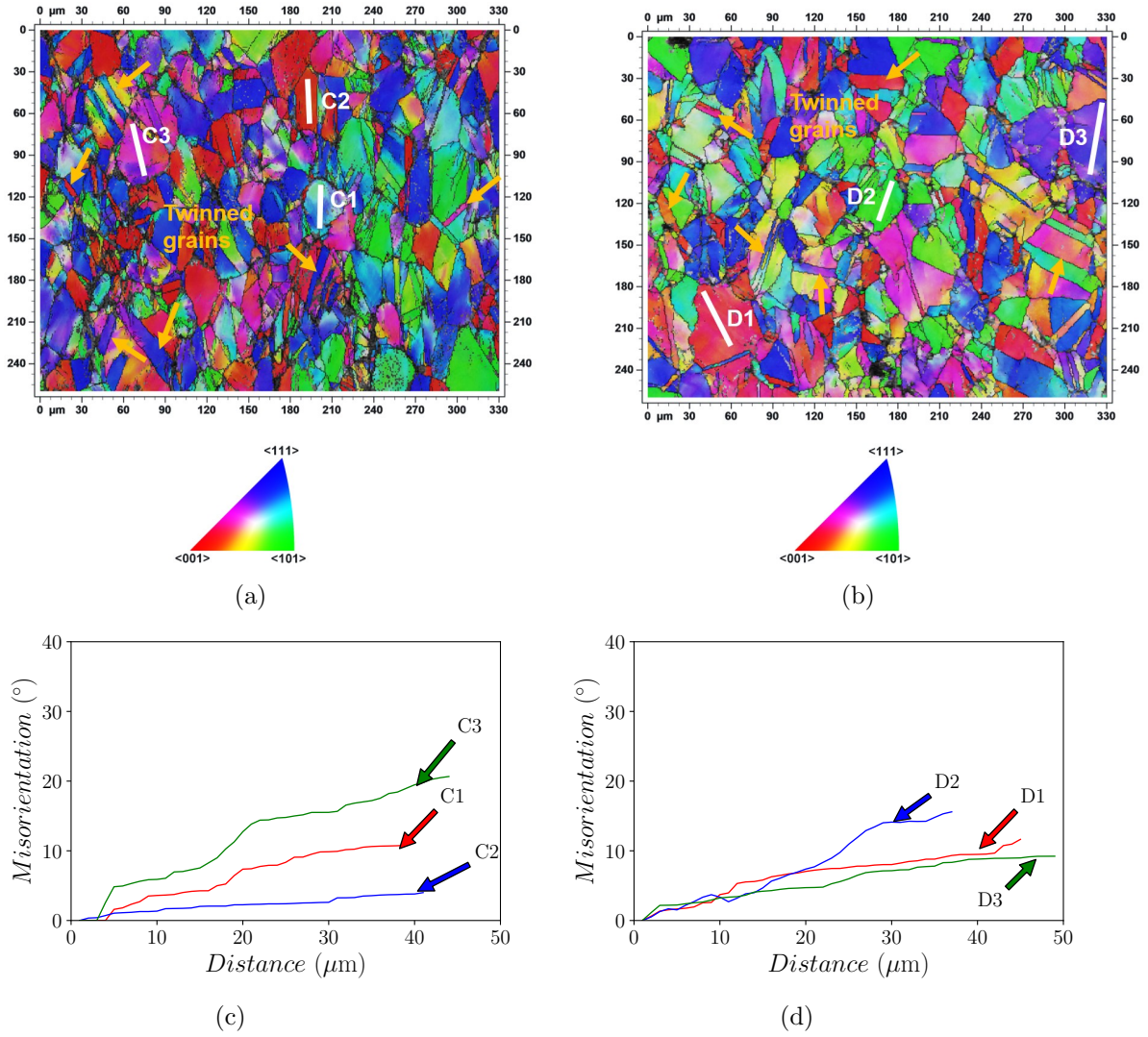

Figure III.28 – Inverse Pole Figure (IPF) obtained from EBSD analyses of the deformed specimens (Projection axis [001]) established at 10 s^{-1} in room temperature (a) and cryogenic temperature (b); Misorientation gradients measured inside deformed grains in the case of: (c) Room temperature; (d) Cryogenic temperature.

4 Conclusion

In this study, an investigation of the thermo-mechanical behavior of Inconel 718 has been conducted covering a wide range of temperature from -188 °C to 900 °C under static and dynamic compression loads. In addition, a new experimental cryogenic set-up has been presented that helped to provide the aimed cryogenic temperature.
The following conclusions are extracted based on the experimental results :

— Inconel 718 exhibits high strain rate sensitivity at high temperature. At cryogenic and room temperature, the sensitivity of the work material to strain rate tends to vanish;

— Regardless of the strain rate, results highlighted that Inconel 718 showed thermoplastic behavior: as the temperature increases, the stress decreases relatively;

— Cryogenic configuration induces the highest resistance behavior at all strain rate range. The mechanical properties namely the yield stress and the peak stress showed higher values in comparison with room temperature configuration;

— The micro-hardness measurements figured out that the strain hardening was the dominant deformation mechanism while the compression tests when comparing the micro-hardness values before and after testings;

— The metallurgical analyses that have been conducted in this work did not probably show any microstructure change under cryogenic conditions compared to room temperature testing conditions;

— As perspective, it seems to be interesting to exploit more sophisticated equipment, particularly the Transmission Electron Microscopy (TEM) method allowing micrographs at the dislocations scale for deeper investigations.

Bibliography

Aaron, M.R., 2015. Plastic Deformation and Ductile Fracture Behavior of Inconel 718. Master. Graduate School of The Ohio State University.

Azarbarmas, M., Aghaie-Khafri, M., Cabrera, J., Calvo, J., 2016. Dynamic recrystallization mechanisms and twining evolution during hot deformation of inconel 718. Materials Science and Engineering: A 678, 137 – 152. URL: doi:https://doi.org/10.1016/j.msea.2016.09.100.

Barbier, D., 2010. Apport de la technique ebsd en mécanique des matériaux. ArcelorMittal Global RD Maizières Automotive Products.

Ben Boubaker, H., Mareau, C., Ayed, Y., Germain, G., Tidu, A., 2020. Impact of the initial microstructure and the loading conditions on the deformation behavior of the ti17 titanium alloy. Journal of Materials Science 55. doi:10.1007/s10853-019-04014-5.

Camilo, M.D.C., Madeira, K.A., Maurizio, F., Luiz, S.V., 2017. Plastic deformation of fcc alloys at cryogenic temperature: the effect of stacking fault energy on microstructure and tensile behaviour. Journal of Materials Science 52.

Cheng, G., Jian, W., Xu, W., Yuan, H., Millett, P., Zhu, Y., 2013. Grain size effect on deformation mechanisms of nanocrystalline bcc metals. Materials Research Letters 1, 26–31. URL: https://doi.org/10.1080/21663831.2012.739580, doi:10.1080/21663831.2012.739580,

Czán, A., Daniš, I., Holubják, J., Zaušková, L., Czánová, T., Mikloš, M., Martikáň, P., 2017. Cutting zone temperature identification during machining of nickel alloy inconel 718. Technological Engineering 14.

Deng, J., Lin, Y., Li, S.S., Chen, J., Ding, Y., 2013. Hot tensile deformation and fracture behaviors of az31 magnesium alloy. Materials and Design 49, 209 – 219. URL: doi:https://doi.org/10.1016/j.matdes.2013.01.023.

Fabre, D., 2013. Characterization of cutting tool wear in cryogenically assisted machining of Inconel 718. Master. Ecole Nationale d'Ingénieurs de Saint-Etienne (ENISE).

Hor, A., Morel, F., Lebrun, J.L., Germain, G., 2013. An experimental investigation of the behaviour of steels over large temperature and strain rate ranges. International Journal of Mechanical Sciences 67, 108 – 122.

Iturbe, A., Giraud, E., Hormaetxe, E., Garay, A., Germain, G., Ostolaza, K., Arrazola, P., 2017. Mechanical characterization and modelling of inconel 718 material behavior for machining process assessment. Materials Science and Engineering: A 682, 441 – 453.

Jiang, S., Sun, D., Zhang, Y., Zhu, X., Wang, M., Zhao, C., 2016. Plastic deformation mechanisms of nicucrmotialnb ni-based alloys at cryogenic temperature. Materials Science and Engineering: A 664, 135 – 145. URL: doi:https://doi.org/10.1016/j.msea.2016.03.133.

Kawamura, M., Asakura, M., Okamoto, N.L., Kishida, K., Inui, H., George, E.P., 2021. Plastic deformation of single crystals of the equiatomic cr mn fe co ni high-entropy alloy in tension and compression from 10 k to 1273 k. Acta Materialia 203, 116454. URL: doi:https://doi.org/10.1016/j.actamat.2020.10.073.

Lee, W.S., Lin, C.F., Chen, T.H., Chen, H.W., 2011. Dynamic impact response of inconel 718 alloy under low and high temperatures. MATERIALS TRANSACTIONS 52, 1734–1740.

Lin, Y., Wu, X.Y., Chen, X.M., Chen, J., Wen, D.X., Zhang, J.L., Li, L.T., 2015. Ebsd study of a hot deformed nickel-based superalloy. Journal of Alloys and Compounds 640, 101 – 113. URL: doi:https://doi.org/10.1016/j.ijheatmasstransfer.2020.120716.

Lv, S., Jia, C., He, X., Wan, Z., Li, Y., Qu, X., 2020. Hot deformation characteristics and dynamic recrystallization mechanism of a novel nickel based superalloy. Advanced Engineering Materials 22. doi:10.1002/adem.202000622.

Mackain, O., 2017. Modélisation du maclage à l'échelle atomique dans les métaux hexagonaux : germination et migration de disconnections dans le zirconium, le titane et le magnésium. Theses. Université de Lyon. URL: `https://tel.archives-ouvertes.fr/tel-01591565`.

Najafi, H., Asgari, S., 2005. Strain hardening mechanisms in aged aerex350 superalloy. Materials Science and Engineering: A 398, 204 – 208. URL: doi:https://doi.org/10.1016/j.msea.2005.03.015.

Ogata, T., 2014. Evaluation of mechanical properties of structural materials at cryogenic temperatures and international standardization for those methods. AIP Conference Proceedings 1574, 320–326. doi:10.1063/1.4860643.

Paturi, U.M.R., Methuku, S., Siripragada, S.S., Sangishetty, Y., Gunda, R.K., 2020. Finite element simulations of machinability parameters in turning of inconel 718. Materials Today: Proceedings URL: doi:https://doi.org/10.1016/j.matpr.2020.08.275.

Sharath Chandra, C., Nagachary, K., Jayahari, L., Hussaini, S., 2020. Characterization of inconel 718 at sub-zero temperatures. Materials Today: Proceedings 26, 3090 – 3093. URL: doi:https://doi.org/10.1016/j.matpr.2020.02.639. 10th International Conference of Materials Processing and Characterization.

Shi, H., Chen, K., Shen, Z., Wu, J., Dong, X., Zhang, L., Shan, A., 2015. Twin boundary characters established during dynamic recrystallization in a nickel alloy. Materials Characterization 110, 52 – 59. URL: doi:https://doi.org/10.1016/j.matchar.2015.10.007.

Si, J., hang Liao, X., qiang Xie, L., rui Lin, K., 2015. Flow behavior and constitutive modeling of delta-processed inconel 718 alloy. Journal of Iron and Steel Research, International 22, 837 – 845. URL: doi:https://doi.org/10.1016/S1006-706X(15)30078-9.

Wang, Y., Shao, W., Zhen, L., Zhang, X., 2008. Microstructure evolution during dynamic recrystallization of hot deformed superalloy 718. Materials Science and Engineering: A 486, 321 – 332. URL: doi:https://doi.org/10.1016/j.msea.2007.09.008.

Xie, X., Xu, C., Wang, G., Dong, J., Cao, W., Kennedy, R., 2005. Ttt diagram of a newly developed nickel-base superalloy- allvac ® 718plusa". Superalloys , 193–202.

Yoon, K.S., Lee, M., Fleury, E., Lee, J.C., 2010. Cryogenic temperature plasticity of a bulk amorphous alloy. Acta Materialia 58, 5295 – 5304. URL: http://www.sciencedirect.com/science/article/pii/S1359645410003459, doi:https://doi.org/10.1016/j.actamat.2010.06.002.

Yuan, H., Liu, W., 2005. Effect of the delta phase on the hot deformation behavior of inconel 718. Materials Science and Engineering, A 408, 281 – 289. URL: doi:https://doi.org/10.1016/j.msea.2005.08.126.

Zhang, D., Zhang, X.M., Nie, G.C., Yang, Z.Y., Ding, H., 2021. Characterization of material strain and thermal softening effects in the cutting process. International Journal of Machine Tools and Manufacture 160, 103672. URL: doi:https://doi.org/10.1016/j.ijmachtools.2020.103672.

Chapter IV

Cylindrical turning operations of Inconel 718 under cryogenic conditions

1 Introduction 149
2 Experimental work 152
2.1 Workpiece Material 152
2.2 Experimental equipment 152
2.3 Experimental Methodology 154
3 Results and discussions 156
3.1 Tool wear mechanisms 156
3.2 Cutting forces 162
3.3 Surface Integrity 166
3.3.1 Surface roughness 166
3.3.2 Microhardness Profiles 172
3.3.3 Surface and subsurface damage 173
3.3.4 Residual stresses 178
3.4 Discussions: correlation between the outcome of the study . . . 181
4 Conclusion 183

1 Introduction

During the machining of Inconel 718 several problems arise as reported in the literature review chapter. In particular, high cutting temperature are generated causing rapid tool wear and thus, poor surface integrity (Ravi and Kumar, 2011). In this context, cryogenic machining is considered as a promising alternative to reduce the tool temperature and wear and to improve the surface integrity (Ayed et al., 2017).
Hong et al. (2001) are among the prior researchers that have reported the effect of LN_2 cryogenic cooling on tool flank wear. Authors carried out experimental turning trials in order to examine the impact of the cryogenic fluid on tool life when cutting a titanium alloy, namely Ti64. They revealed that LN_2 cryogenic condition contributed to lowering the tool flank wear achieving around 15.8 min of tool life when cooling both tool faces (flank and rake faces) at 90 m/min whereas emulsion flooding provided less than 5 min of cutting time. Indeed, they have explained this observation by the fact that the LN_2 jet provides the reduction of the tool temperature and therefore avoiding some tool wear mechanisms, in particular the diffusion.
Subsequently, Iturbe et al. (2016) have deeply studied the possibility to employ the LN_2 cryogenic coolant instead of the conventional lubricant. For this reason, authors chose to use the same cutting parameters as well as the tool geometry established by Kaynak (2014). The experiments were conducted under several cooling conditions. The results indicated that conventional condition induces a tool life superior to 20 min. In contrast, shorter tool life was obtained (less than 10 min) under cryogenic condition. They explained these observations by the fact that the work material Inconel 718 presents an excessive hardening tendency due to the cryogenic temperature effect. Hence, causing the degradation of the tool and thereby shorter tool life.
Recently, Yildirim et al. (2020) extensively focused on the machinability of nickel based alloy 625 under LN_2 cryogenic condition in comparison with MQL and a combination of MQL+Cryo cooling methods during turning operation. Regarding the LN_2 delivery, a nozzle with a 3 mm outlet diameter was used to throw the LN_2 at the rake face of the cutting tool at a distance of 15 mm with a spray angle of 30 °. The obtained results showed that a good agreement with the previous studies concerning the rapid tool wear under LN_2 cryogenic condition. Indeed, tool flank wear measurements exhibited the highest values when supplying only LN_2 whereas the combination between MQL+Cryo induced the lowest tool flank wear at all cutting speed tested.
Results are given in Fig. IV.1.

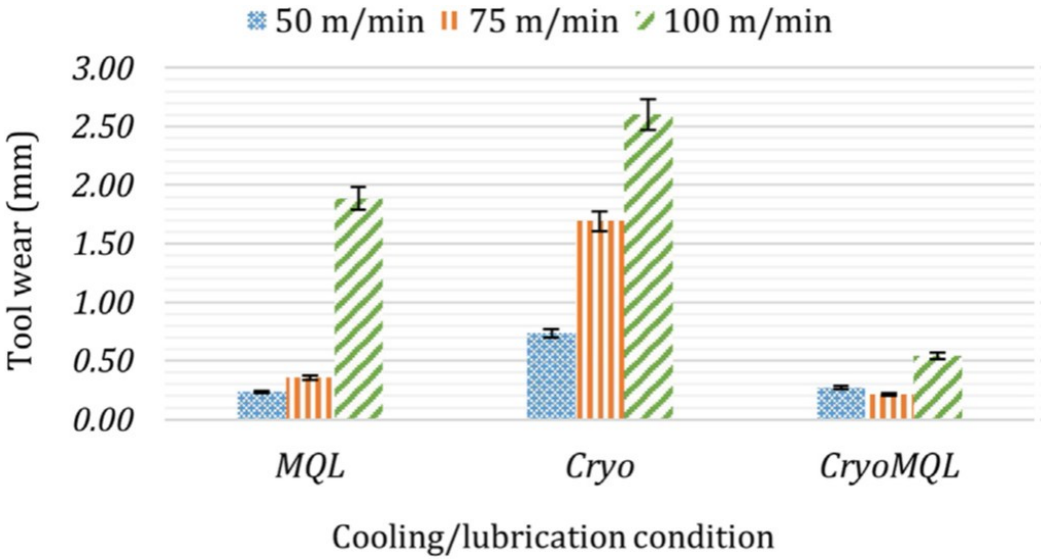

Figure IV.1 – Illustration of tool wear results obtained under MQL, LN_2 and MQL+LN_2 cooling conditions when machining Inconel 718 (Yildirim et al., 2020).

So far, few researches have investigated the influence of cryogenic performance using LCO_2 as a cutting fluid carried out on Inconel 718. In particular, Bagherzadeh and Budak (2018) have conducted experiments using LCO_2 when turning Inconel 718. Their findings revealed an improvement percentage of 14 % of tool life in the case of LCO_2 condition delivered from the rake face and flank face simultaneously using a modified nozzle compared to LCO_2 delivery using thinner nozzle. This result was in agreement with the findings of (Halim et al., 2019) who reported that LCO_2 condition led to almost 71 % longer tool life compared to dry condition during high speed milling of Inconel 718.
Nevertheless, this finding stands in contradiction to (Pereira et al., 2020), who proved longer tool life (19 min) was observed in conventional lubrication in comparison with LCO_2 cooling approaches (both supplying manners:internal and external) inducing the shortest tool life (less than 8 min).
Some authors have also studied the effect of cryogenic cooling on the final surface integrity (surface roughness, residual stresses, microstructural alterations and microhardness) of the machined part. As for the surface finish, the average roughness R_a is a major parameter to characterize the surface condition of the machined part. In this context, Jamil et al. (2021) studied the effect of different cooling strategies during the turning operation of TA6V. They found that the R_a values are the lowest under CO_2 and LN_2 cryogenic conditions in comparison with dry cutting. These results are consistent with those found by Bordin et al. (2017). It seems that the lower surface roughness values reported when using cryogenic cooling are due to the lower tool wear found at those cutting conditions. Nevertheless, Iturbe et al. (2016) figured out an opposite result when machining Inconel 718 in cryogenic conditions. This consequence is closely related to the tool wear picked up during the cutting operation which considerably affects the surface quality of the machined part. Lately, Mehta et al. (2018) carried out cutting experiments in order to evaluate the machining characteristics of Inconel 718 under several conditions (dry, MQL and LN_2). The authors pointed out that the surface quality is improved under cryogenic conditions.
During the material removal process, the machined material is subjected to both mechanical and thermal loads. As a result, several alterations in the machined surface and

the sub-surface can take place namely microstructural changes (such as recrystallization (Zhou et al., 2011)), distorted grains, severe plastic deformation (Herbert et al., 2012) and work hardening (Devillez et al., 2011). These alterations are closely related to the cutting parameters, the cooling conditions and the material to be machined. In the case of Inconel 718, under cryogenic conditions, the machined surface is highly hardened, resulting in a noticeable gradient in hardness compared to the original material (Pusavec et al., 2011). So far, it appears that the effect of cryogenic cutting on the alterations occurring on the machined surface and subsurface microstructure is not developed.

With respect to residual stresses, cryogenic machining produced higher compressive residual stresses in the case of several metallic materials such as AA 7075-T651, Inconel 718, Ni-Ti and AZ31B Mg alloys (Jawahir et al., 2012). In particular, Pusavec et al. (2011) have extensively studied the influence of several cooling strategies (dry, MQL and LN_2-Cryo) on the machining performance of Inconel 718. They found that cryogenic condition exhibited the best residual stresses distribution not only with respect to the highest compressive peak value and the largest compressive depth but also the best cooling effect that leads to lower tensile value. Afterward, Pereira and Delijaicov (2019) examined the effect of cutting parameters on residual stresses of Inconel 718 machined part under dry and LN_2 cryogenic conditions. In order to carry out the residual stress profiles on and beneath the machined surface, X-ray (on the surface) and the hole drilling method (beneath the machined surface) were employed. Results indicated that LN_2 induced higher tensile surface residual stresses compared to dry condition. Surprisingly, authors related this result to higher cutting forces obtained in LN_2 condition while the mechanical loading tends to generate compressive residual stresses. However, below the machined surface, compressive stresses were higher when employing LN_2 as a coolant. In the same context, He et al. (2016) figured out an inverse result claiming that LN_2 coolant generates lower tensile residual stresses on the surface.

Overall, according to the literature review, studies on cryogenic machining of Inconel 718 raise some disagreement regard the tool life improvement. However, even the enhancement did not provide the desired tool life (15 min). With respect to surface integrity (residual stresses, surface roughness), some gaps have been identified. In addition, so far, there is no work that has studied the comparison between cryogenic performance using both cryogenic cutting fluids (LN_2 and LCO_2) when turning Inconel 718 regard the tool life as well as the surface integrity of the machined part.

In this chapter, the evaluation of the efficiency of LN_2 and LCO_2 performance in finish turning operations of Inconel 718 is conducted. First, the experimental process will be presented in detail. Subsequently, the main results will be figured out with respect to Inconel 718 machinability (tool life, tool wear mechanisms, cutting forces) as well as the surface integrity generated (surface roughness, the affected layer and residual stresses profiles).

2 Experimental work

2.1 Workpiece Material

In this study, the same microstructure of Inconel 718 employed during the mechanical characterization (section 2.2) is used during the turning operations. Fig. IV.2 displayed the raw microstructure of the workpiece material. The carbide particles reveal abrasive character while machining (Dosbaeva et al., 2010).

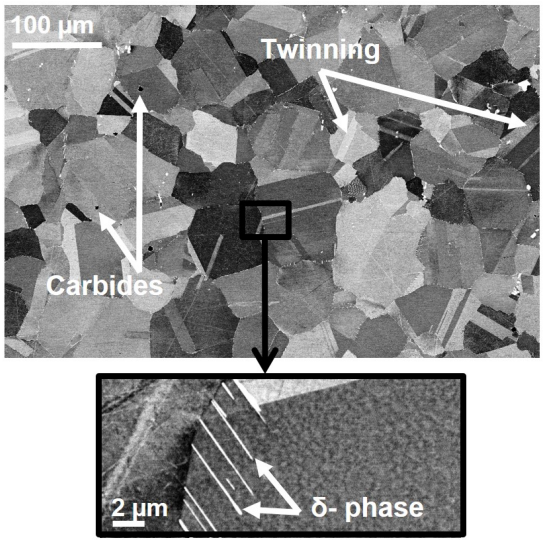

Figure IV.2 – Illustration of Inconel 718 microstructure in the as-received state observed by SEM technique.

2.2 Experimental equipment

Machining experiments have been conducted using the conventional lubrication as well as two cryogenic cutting fluids namely liquid nitrogen LN_2 and carbon dioxide LCO_2. The experiments were carried out using the same test configuration on a horizontal turning CNC lathe Danumeric 2. The conventional lubricant used during these experiments was the HOCUT 3380 supplied at a pressure of 20 bars, cooling the cutting zone. As for the LCO_2 system, it is composed of a bottle of LCO_2 maintained at high pressure equal to 57 bar at room temperature (liquid state) as displayed in Fig. IV.3.c. Concerning the LN_2 cryogenic trials, the cryogenic system consists of a phase separator, the cryogenic control and the liquid nitrogen bottle mounted on the CNC lathe (Fig. IV.3).

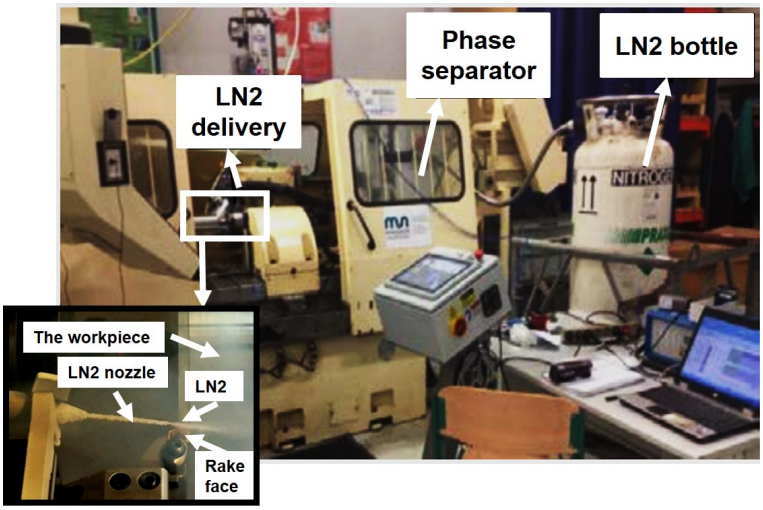

(a)

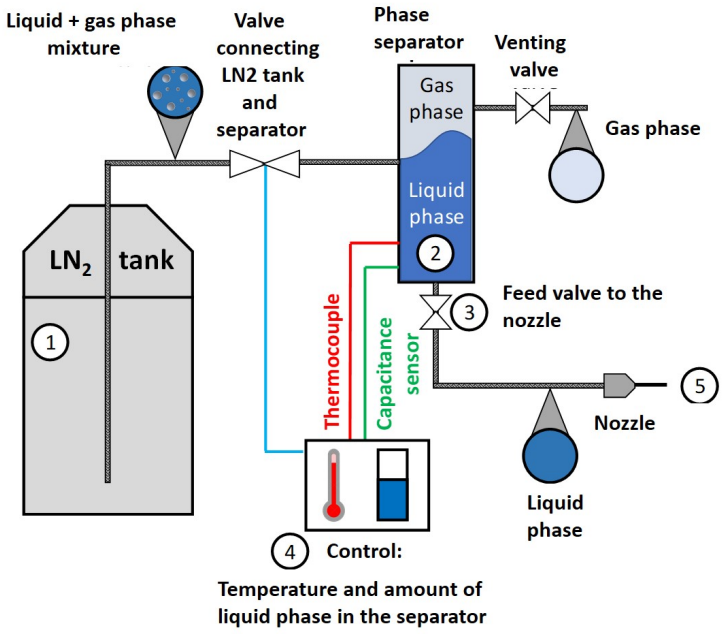

(b)

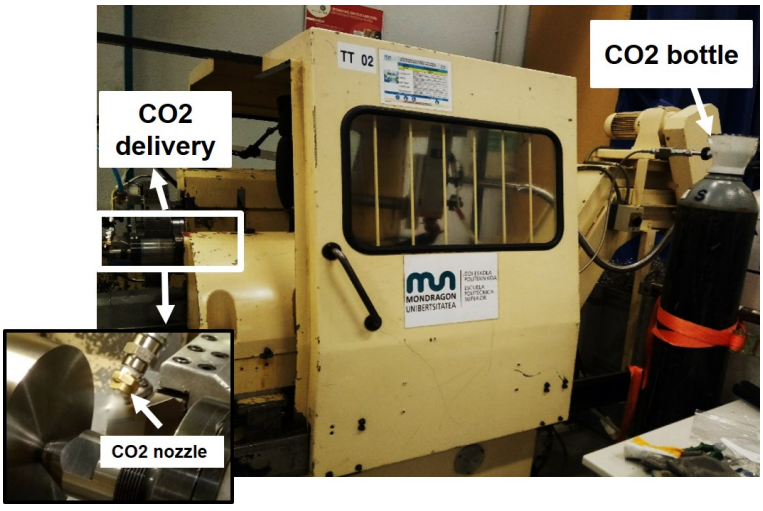

(c)

Figure IV.3 – Experimental set-up for the cryogenic tests: (a) LN_2 set-up; (b) Illustration of the different parts constituting the LN_2 set-up; (c) LCO_2 set-up.

LN_2 spray was activated before starting the cutting process in order to reach stable outlet condition. The parameters of the LN_2 and CO_2 flows are depicted in Table IV.1.

Table IV.1 – LN_2 and LCO_2 flow parameters

	LN_2	LCO_2
The diameter of the nozzle (mm)	1.5	0.4
The pressure (bar)	10	57
Projection angle (°)	15	45
Delivery position	Rake face	Rake face

The choice of LN_2 parameters has been established according to some previous works, in particular (Lequien, 2017). Lequien (2017) has proved that the convective heat transfer coefficient is maximum when the pressure and the nozzle diameter of LN_2 delivery are high whereas the distance projection and the inclination angle should be reduced. In this work, it was relevant to use bigger nozzle diameter, as lower as possible the distance projection and the inclination angle in order to optimize at best the liquid flow of the nitrogen.

2.3 Experimental Methodology

Longitudinal turning experiments were conducted in finishing operations on Inconel 718 bar using the same cutting parameters and the same cutting tool as (Iturbe et al., 2016). In this study, these parameters were fixed whereas the LN_2 set-up has been changed.
Besides the cryogenic coolants (LN_2 and LCO_2), conventional coolant has been employed as a reference in order to evaluate the cryogenic performance when machining Inconel 718. CVD coated carbide inserts from Mitsubishi supplier (DNMG 150612-MS US905) were exploited in the trials (Mitsubishi, 2006) (Fig.IV.4).

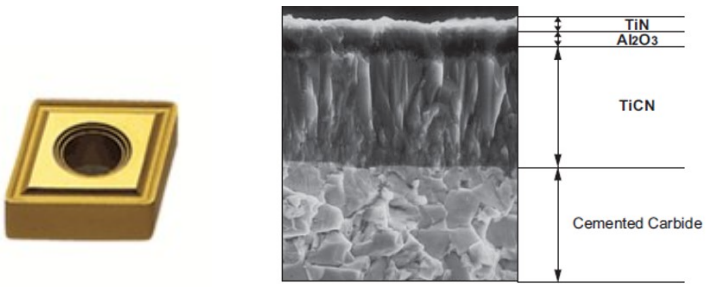

(a) (b)

Figure IV.4 – (a) Tool geometry; (b) Tool coating (Mitsubishi, 2006).

Table IV.2 sets out the machining conditions.

Table IV.2 – Working conditions

Workpiece	Geometry	Cylindrical bar
	Material	Inconel 718
Cutting parameters	Cutting speed (m/min)	70
	Feed (mm/rev)	0.2
	Depth of cut (mm)	0.2
Tool	Tool insert	Coated carbide
	Cutting edge angle (°)	93
	Rake angle (°)	9
	Relief angle (°)	6
	Nose radius (mm)	1.2
Coolants	Conventional	Wet
	Cryogenic	LN_2
	Cryogenic	LCO_2

The trials were carried out until achieving the target cutting time of 15 min or when the maximum tool flank wear defined as $V_{BMAX} = 0.3$ mm was obtained. Each experiment has been performed using a fresh cutting tool edge and has been repeated twice.
Tool flank wear assessment was performed using a LEICA Z16 APO stereo-microscope. Complementary observations of the cutting tools have been carried out using the Scanning Electron Microscopy (SEM). In addition, profilometer measurements using the confocal profilometer, Alicona IFG4 device have been carried out in order to quantify the material loss volume of the tool as well as the adhered material volume. Machining forces were measured using Kistler 9121 dynamometer.
On finishing operations, the surface integrity of the machined part must respond to several quality requirements in terms of surface topography, surface hardness as well as residual stresses. For these reasons, during the experiments, surface roughness was measured in-situ after each cutting test using a Mitutoyo SJ-210 portable rugosimeter. SEM observations of the machined part were carried out after two states of tool wear for each cooling condition: when performing with a new tool cutting edge and a worn tool cutting edge. Electron Backscatter Diffraction (EBSD) technique was used in order to characterize the affected layer of the machined part. All the EBSD analyses were performed using a software called ″Atex″ (Beausir and Fundenberger, 2017).
Microhardness measurements were carried out using the Vickers micro−hardness testing method applying a load of 50 gf and the full load was maintained for 10 s. Two repetitions were conducted for each cooling condition. The microhardness measurements started with 30 μm from the machined surface, followed by five indentations separated of 70 μm and the final four indentations were separated of 100 μm.
Residual stresses measurements were conducted employing the blind hole drilling method according to the ASTM standard using the RESTAN MTS300 hole-drilling equipment. The EA-06-031Re-120 strain gauges were employed and the drill bits with a diameter of 0.8 mm. Regard the depth of drilling, the first five increment were of 10 μm, followed by 5 increments of 20 μm and the final seven increments were of 50 μm.

3 Results and discussions

3.1 Tool wear mechanisms

Tool flank wear was measured throughout the turning operations for all cooling methods (conventional and cryogenic conditions). The trials were stopped when reaching 15 min of cutting in conventional lubrication even if the criterion of maximum flank wear namely $V_{BMAX} = 0.3$ mm was not achieved. Regard the LCO_2 condition, both tests were stopped at 15 min while the tool flank wear levels were notably different. However, under LN_2 cryogenic condition, the trials were stopped when the criterion of V_{BMAX} was reached. Focusing on Fig. IV.5, results indicated that the conventional condition revealed the longest tool life. In fact, the tool flank wear did not surpass 0.12 mm over 15 min of cutting in conventional lubrication. Both repetitions induced the same trend during the cutting process showing a good repeatability.

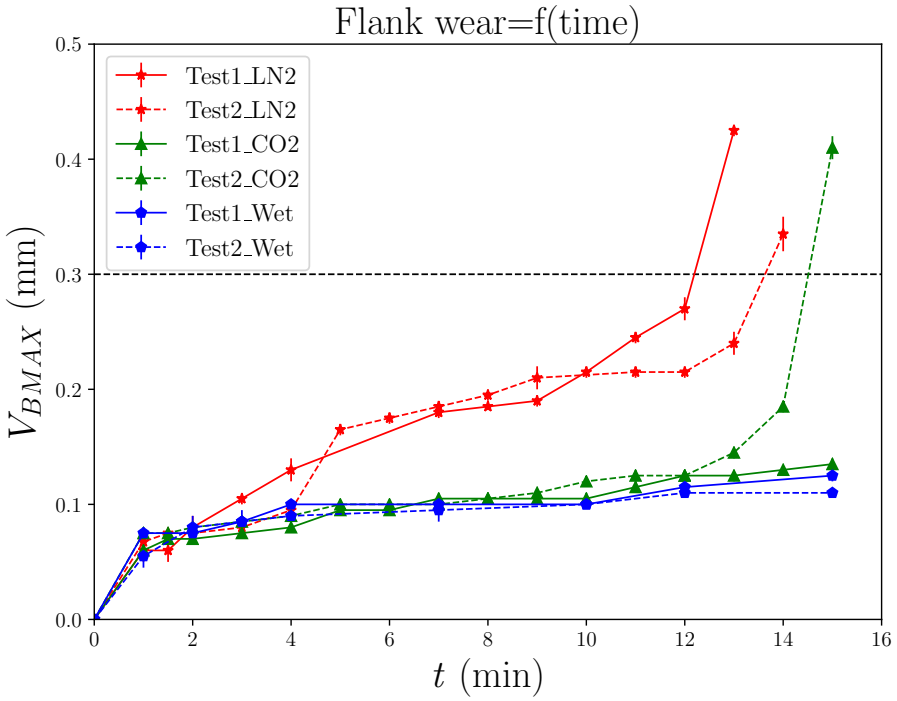

Figure IV.5 – Tool flank wear evolution under Wet, LN_2 and LCO_2 cooling conditions during the tests.

As for the LCO_2 cooling strategy, a similar evolution has been perceived up to 13 min of cutting time. Nevertheless, beyond this duration, the tool flank wear progressed drastically to surpass the criterion at 15 min during the second repetition of LCO_2 experiment. With respect to LN_2 cryogenic condition, tool flank wear increased rapidly from the first 2 and 6 minutes of cutting during test 1 and test 2 respectively causing reduced tool life. In addition, tool flank wear progress in both cryogenic conditions is quite repeatable at the beginning of the machining process. Nevertheless, a significant variability was observed at 11 min and 13 min respectively in LN_2 and LCO_2 cooling strategies when the tool flank wear increased notably. In conventional cooling approach, a homogeneous tool flank wear evolution was observed even after longer machining times. In contrast, during LN_2 cryogenic machining, wear peaks occurred from the beginning of the turning process, indicating that the cutting process is not performed homogeneously while this parameter showed a steady and slow evolution in

LCO_2 cryogenic condition except the last minutes of machining.

Additional analyses have been carried out in order to study the tool wear mechanisms when machining Inconel 718 under conventional lubrication and cryogenic conditions using SEM. Fig. IV.6 shows the SEM observations of the tool wear state on the rake face as well as the flank face obtained in wet condition after 15 min of cutting.

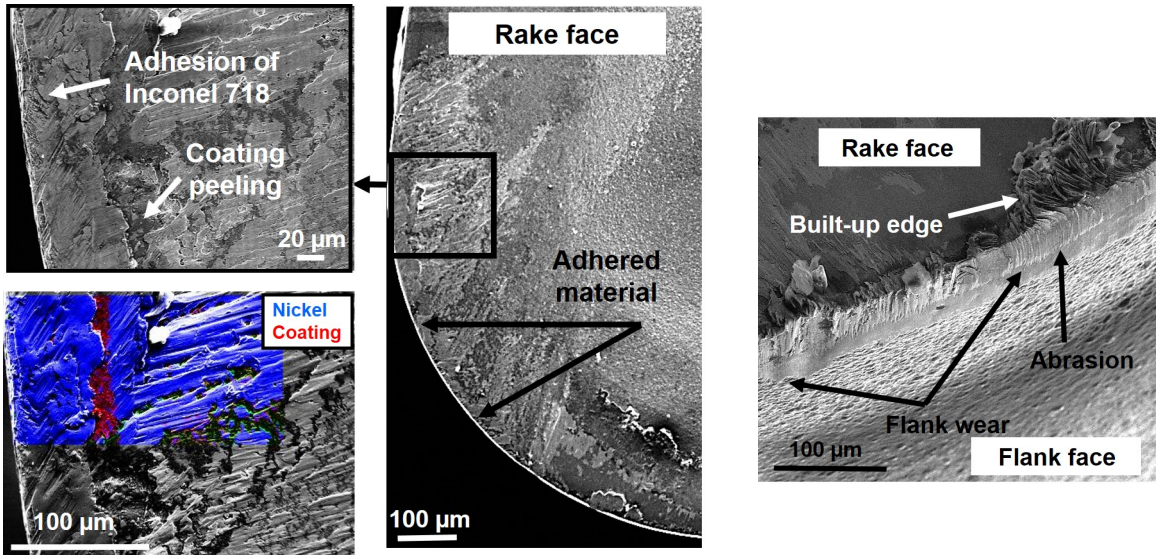

(a) (b)

Figure IV.6 – SEM observations of the tool wear after 15 min of machining in wet condition: (a) Rake face/EDS analysis; (b) Flank face.

The main mechanisms observed consists in adhesion and abrasion wear. Effectively, deposits of workpiece material were stuck on the rake face near the cutting edge revealing the chip rubbing. This observation is proved by EDS analysis showing the adhered material consisted of nickel. In fact, as long as machining time increased, adhered layers were formed progressively to establish built-up edges (BUE) that protect the rake face (Xue and Chen, 2011). However, when achieving stagnation state, the BUE are not stable inducing the peeling of tool coating material.
With respect to tool wear mechanisms under LCO_2 condition, the two tests revealed different mechanisms. The first test exhibits the same trend as the conventional lubrication. Indeed, adhered layers are formed during machining as well as abrasion wear that is mainly caused by the hard carbide particles present in the workpiece material. It is worth mentioning that these two wear mechanisms are closely related (Cantero et al., 2013). Effectively, the adherence of the workpiece material inducing the formation of the BUE leads to tool chipping, because of the instability of BUE that breaks off alternatively tearing out a small lump of the cutting edge (Fig. IV.7).

Nevertheless, the tool wear modes and mechanisms occurred during the second test when using LCO_2 are rather different. Besides the flank wear, drastic crater wear took place caused by the plucking out of the tool coating particles as illustrated in Fig. IV.8.

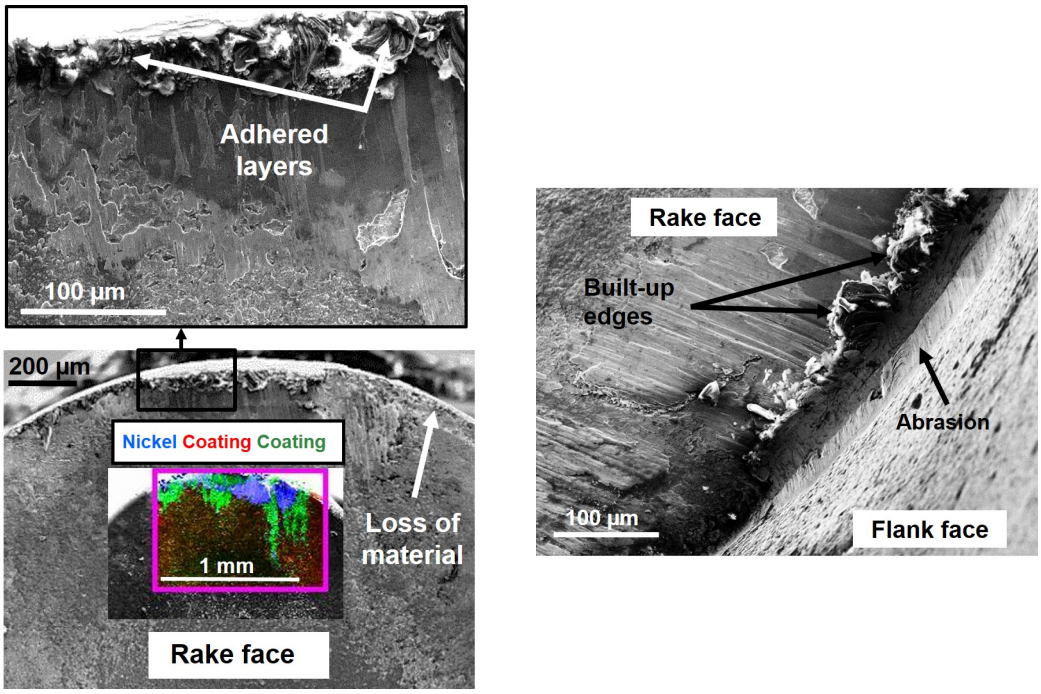

(a) (b)

Figure IV.7 – SEM observations of the tool wear after 15 min of machining in LCO_2 condition during Test 1: (a) Rake face/EDS analysis; (b) Flank face.

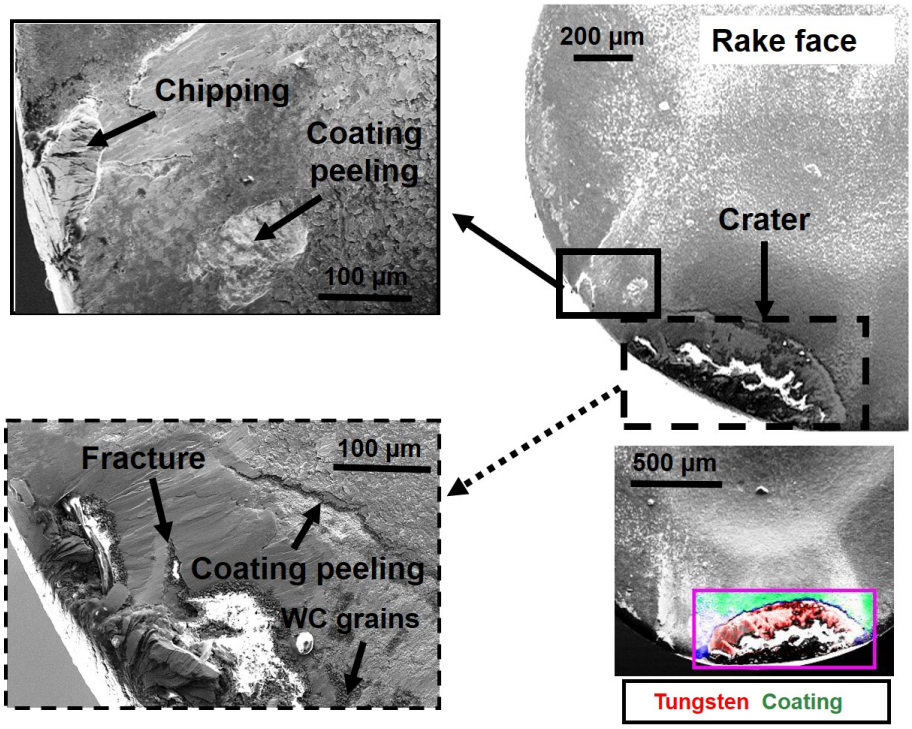

Figure IV.8 – SEM observations of the tool wear after 15 min of machining in LCO_2 condition during Test 2.

Micro-cracks and chipping of the cutting edge have also been observed. Overall, these mechanisms are induced by mechanical loads which developed chipping, fracture and coating peeling as well as the chemical interactions at the tool-workpiece and tool-chip interfaces that caused adhesion (Halim et al., 2019).

Concerning the LN_2 cooling conditions, tool wear mechanisms that have been detected through the SEM observations and the EDS analysis are not far from those obtained during the second test of LCO_2 lubrication. Indeed, during both LN_2 tests, the degradation of cutting tool is primarily caused by adhesion, abrasion and micro-chipping as depicted in Fig. IV.9 and Fig. IV.10.

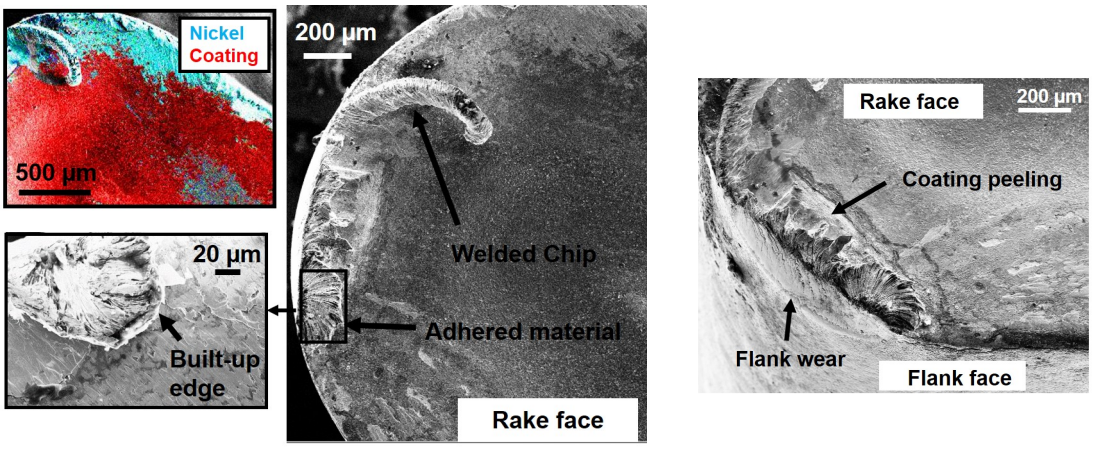

(a) (b)

Figure IV.9 – SEM observations of the tool wear after 13 min of machining in LN_2 condition during Test 1: (a) Rake face/EDS analysis; (b) Flank face.

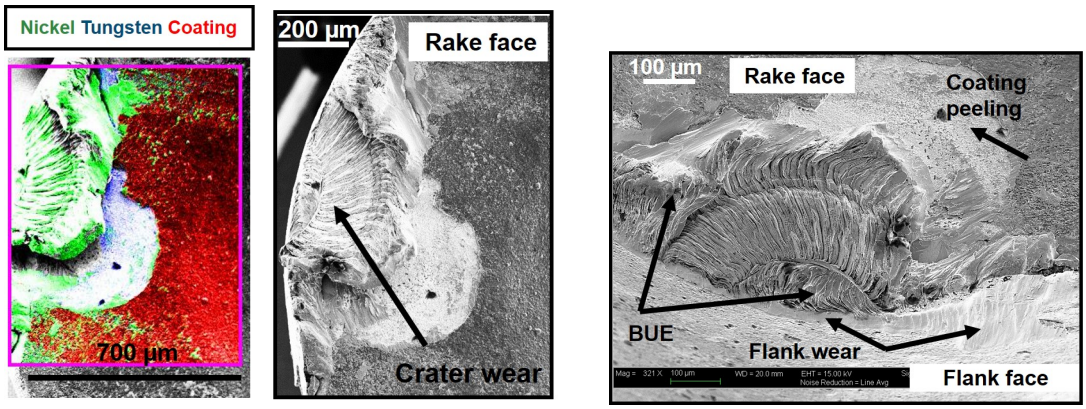

(a) (b)

Figure IV.10 – SEM observations of the tool wear after 14 min of machining in LN_2 condition during Test 2: (a) Rake face/EDS analysis; (b) Flank face.

In particular, welded chips on the rake face have been observed indicating the non-efficient performance of the LN_2 to evacuate properly the chips. It may also be concluded that high temperature obtained during machining contributing to welding the chips reveals that the LN_2 cutting fluid did not cool significantly the tool-chip interface (Liao et al., 2008). Furthermore, due to higher wear of the cutting tool, the friction and the temperature increase in the cutting area leading to serious damage to the tool (Wagner et al., 2015) and thereby rapid wear and reduced tool life (Liang and Liu, 2018).
In order to compare the cutting fluids performances when machining Inconel 718, it is interesting quantifying the material loss of the tool as well as the adhered material

on the tool obtained under all cooling strategies using confocal profilometer, Alicona IFG4. In fact, using a reference surface by scanning a new tool, the adhered and the material loss of the tool could be so far estimated. Results showed that the conventional condition induced the lower value in terms of the volume of adhered material (V_{peaks}) and the volume of material loss ($V_{valleys}$) as given in Fig. IV.11.

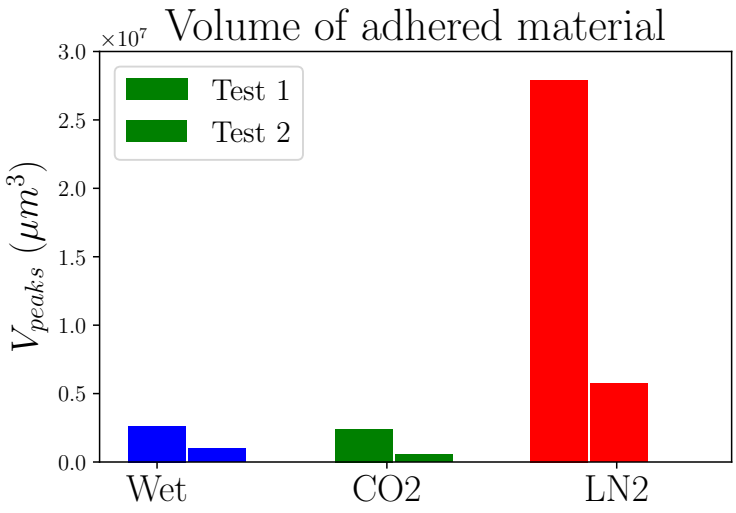

(a)

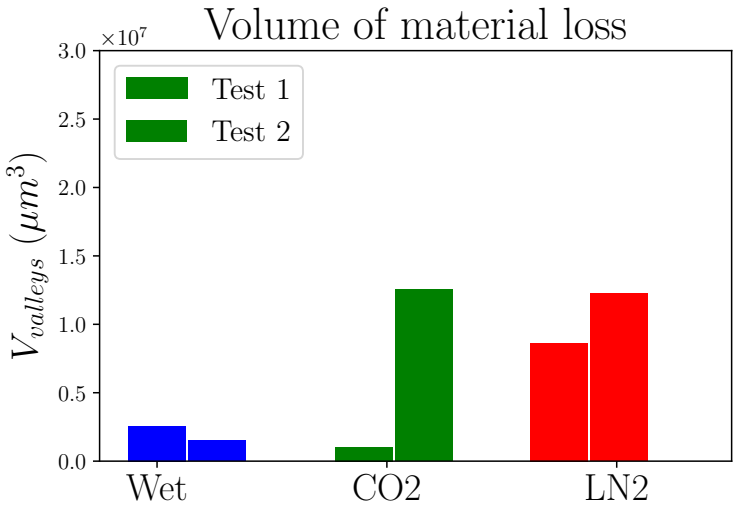

(b)

Figure IV.11 – Assessment of the adhered material volume and the material loss volume using the Alicona- Profilometer measurements: (a) Volume of adhered material; (b) Volume of material loss.

However, under LCO_2 cooling strategy, the material loss volume of the cutting tool was higher compared to the conventional condition but exhibited nearly the same value with respect to the adhered material volume as the former. As for the LN_2 cryogenic condition, in this case, both parameters revealed the highest value either the material loss volume or the adhered material volume. Effectively, this assessment confirms the previous results developed above. Overall, under conventional lubrication, the main wear mechanism was almost adhesion while in both cryogenic conditions not only adhesion was the crucial wear type but also the micro-cracks and chipping of the cutting edge have been revealed.

Another aspect should be stated consisting in that when delivering LN_2 cutting fluid on the tool rake face, it seems complicated to avoid cooling the unmachined workpiece. Consequently, the work material deformation behavior as well as the thermal properties could change by the cryogenic temperature ($-196°$ C). Thereby, the cutting process in this case turns out to be non homogeneous affecting the tool wear resistance. Moreover, when examining the chip morphology obtained under all cooling conditions, there is no significant difference; the chips exhibit almost the same morphology as depicted in Fig. IV.12. These results are in agreement with (Kaynak, 2014). Author deduced that the chip breakability has not been enhanced when varying the cooling strategies.

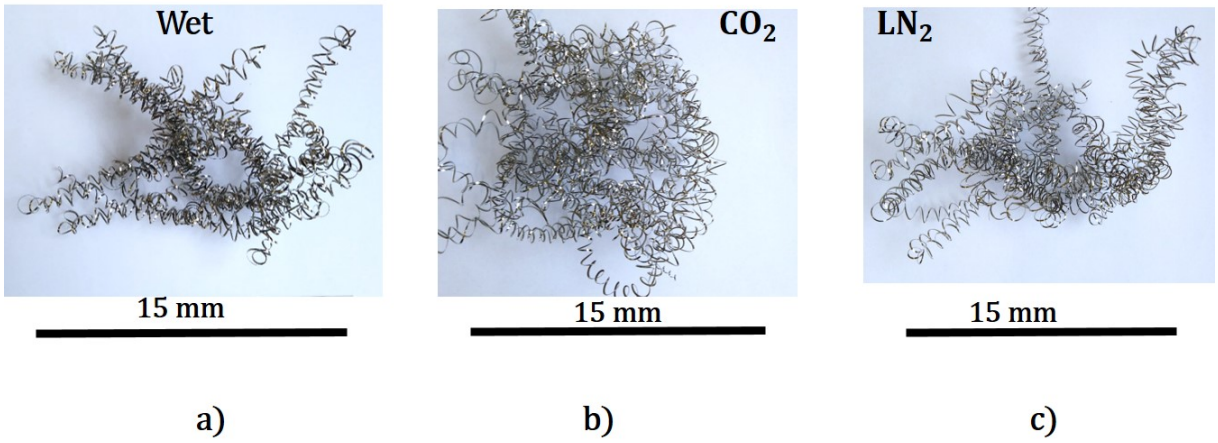

Figure IV.12 – Chip morphology obtained in the three cooling strategies: (a) Wet; (b) LCO_2; (c) LN_2.

3.2 Cutting forces

Assessing the cutting forces is fundamental to control the power consumption during the cutting process as well as to estimate the difficulty of a material to be cut. In fact, the cutting forces are closely related to the cutting conditions such as the material properties of the workpiece, the cutting tool (the geometry, the material, the coating..), the cutting parameters in addition to lubrication approaches. In this study, one is interested to point out the machining forces evolution when cutting Inconel 718 under several cooling strategies namely conventional lubrication and cryogenic conditions using LN_2 and LCO_2. Three components have been evaluated during the turning operations: the cutting forces (F_c), the feed forces (F_f) and the passive forces (F_p). Results showed that all cutting forces components exhibit lower values in conventional cooling condition than in the case of cryogenic conditions (Fig. IV.13).

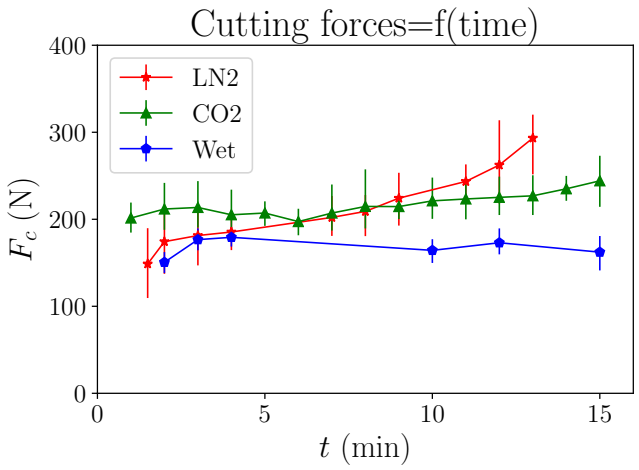

(a)

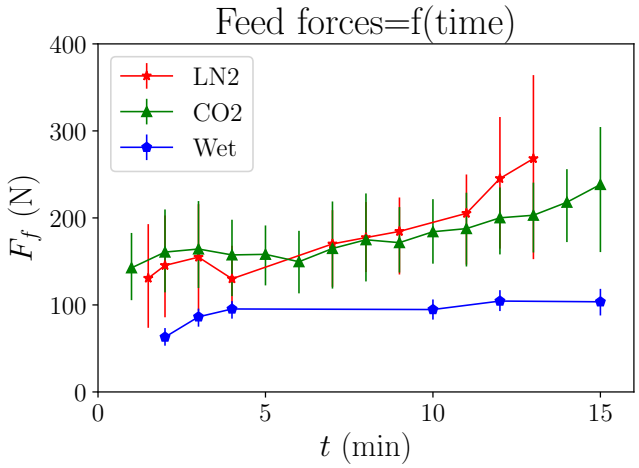

(b)

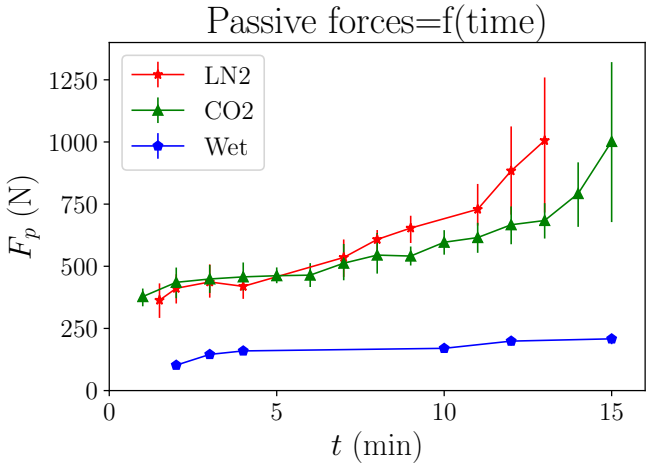

(c)

Figure IV.13 – Illustration of the evolution of cutting forces components under all cooling strategies: (a) Cutting forces; (b) Feed forces; (c) Passive forces.

Indeed, the cryogenic cutting fluids (LN_2 and LCO_2) display very low temperature throughout machining time leading to increase the flow stress of the workpiece material. As a result, the machining forces components heighten significantly. For instance, when examining the cutting forces values obtained in conventional and cryogenic conditions, it is observed that, after 15 min of machining time, 180 N is obtained for the cutting force in conventional cooling, and values of 300 and 250 N are obtained for LN_2 and LCO_2 cooling approaches, respectively. Furthermore, the feed forces show the same tendency where the highest values are achieved in LN_2 cryogenic conditions. However, the passive forces revealed the highest values recorded in all cooling environment compared to the cutting and feed forces reaching over 1200 N after 14 min of machining in LN_2 condition.

Cutting forces values are key factors to indicate the tool wear state. Fig. IV.13 illustrates the cutting forces measurements during the cutting process revealing the effect of tool wear evolution. Obviously, over machining time, the tool wear increases relatively to the cooling environment and therefore cutting forces rise as well. In addition, when comparing between the three components of the cutting forces regardless of the lubrication strategy, one could recognize that the passive force measurements showed the highest values, mostly by the end of the machining process where the tool flank wear increased notably (Grzesik et al., 2018). In addition, when comparing between the different cooling methods, one could notice that passive force progress is slow and steady in conventional condition. Nevertheless, under cryogenic conditions, this parameter evolves drastically at the end of machining. This tendency is more pronounced under LN_2 cryogenic condition than under LCO_2 condition. This result may be attributed to the rapid tool flank wear progress in LN_2 cryogenic strategy mentioning that the passive forces are the most sensitive to tool flank wear as depicted in Fig. IV.14.

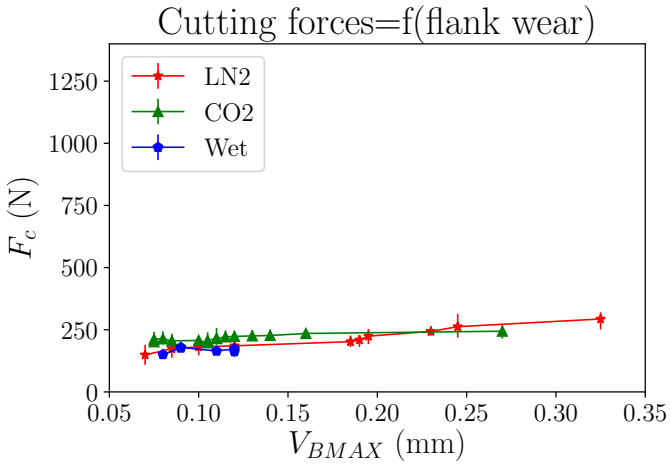

(a)

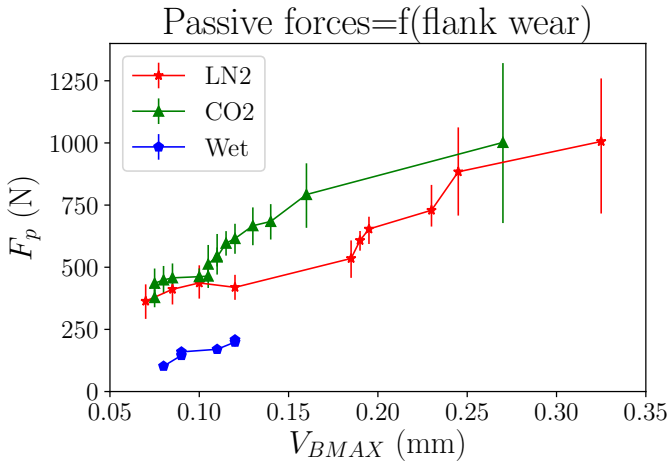

(b)

Figure IV.14 – Correlation between cutting forces components evolution and tool flank wear under Wet, LN_2 and LCO_2 conditions: (a) Cutting forces; (b) Passive forces.

In this context, Arrazola et al. (2014) obtained similar trend when comparing the progress of cutting forces components using unworn and worn tools. They highlighted that passive forces evolution was the most sensitive to tool wear depending on tool geometry as well as the cutting parameters employed.

3.3 Surface Integrity

3.3.1 Surface roughness

Surface finish is a crucial parameter that provides good machining performance of machined parts. Fig. IV.15 illustrates the evolution of surface roughness obtained in conventional and cryogenic conditions.

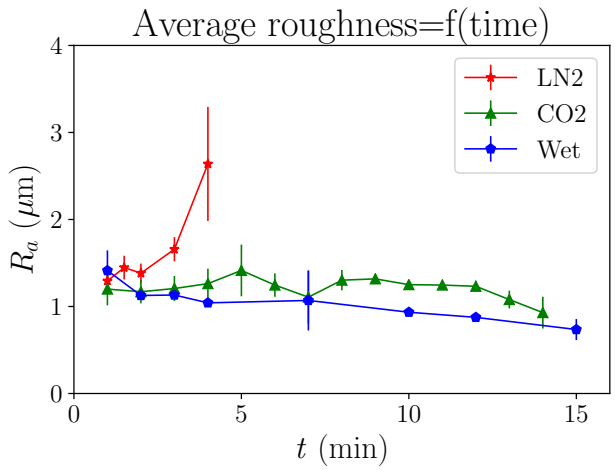

(a)

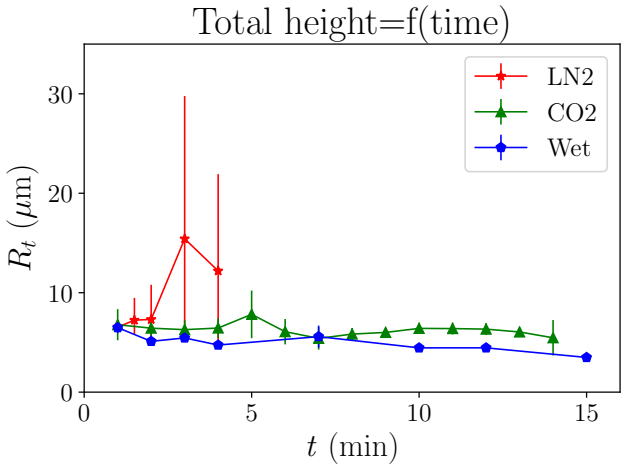

(b)

Figure IV.15 – Surface roughness evolution under Wet, LN_2 and LCO_2 cooling conditions: (a) Average roughness; (b) Total height of the profile.

Results showed that conventional coolant provides the lowest values in terms of the average roughness R_a as well as the total height of the profile R_t. Concerning the LCO_2 condition, it induced approximately the same tendency as the conventional strategy. Nevertheless, in LN_2 cryogenic condition, the surface quality exhibited a mediocre state in comparison with wet and LCO_2 conditions. Actually, under LN_2 cryogenic condition, surface roughness has achieved very high values reaching more than 3 μm of R_a and 20 μm of R_t. In comparison with conventional lubrication, LN_2 cryogenic condition, produces a deterioration of more than 30%.
This denotes that the cooling and lubrication choice affects drastically the expected results with regard to the surface roughness requirements established by industrial manufacturing.
Furthermore, as displayed in Fig. IV.15, the measurements of the surface roughness are not recorded till the end of the cutting process in the case of LN_2 cooling strategy due to the limitations of the equipment as the surface finish was too rough. For this reason, it has been resorted to using the profilometer in order to characterize the LN_2 surface finish measuring the average areal roughness S_a. Fig. IV.16 highlights the increase of S_a measured at different machining times. Indeed, the scanned surfaces reveal the presence of adhered particles on the machined workpiece surfaces that become more important as the machining time increases. This could be the main reason for the worst surface quality obtained in LN_2 cryogenic condition.

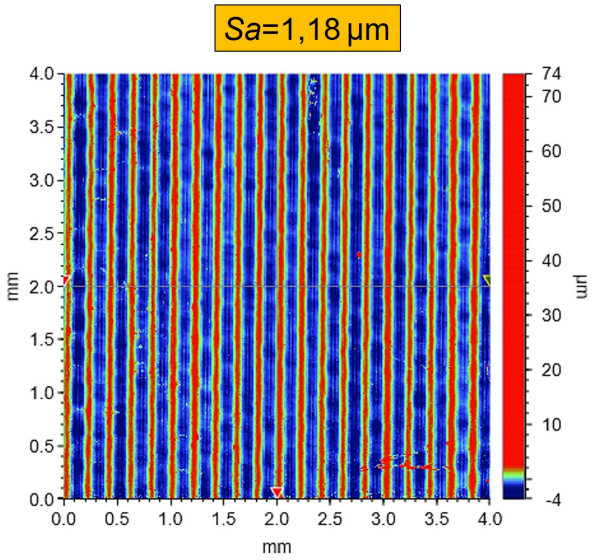

(a)

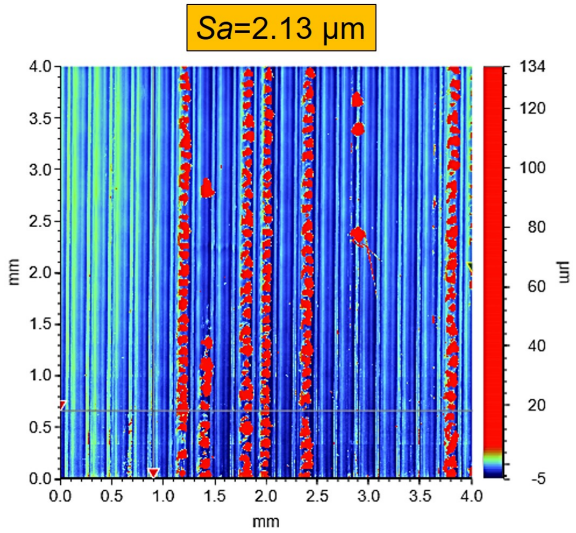

(b)

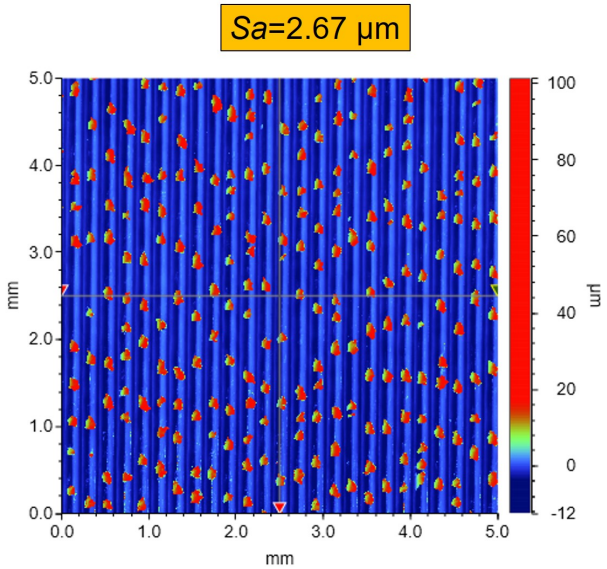

(c)

Figure IV.16 – Surface topography scanned using the Bruker profilometer after machining under LN_2 condition: (a) t=0.5 min; (b) t=5.5 min and(c) t=11 min.

Results showed that the average areal roughness S_a values are in the range of 1.18 μm when the microchips are not present. In contrast, the machined surfaces exhibiting the adhered microchips revealed higher values holding 2.13 μm and 2.67 μm. Overall, whatever the rate of the adhered microchips, the surface finish revealed in this case is poor. To better understand the poor surface quality when machining Inconel 718 under LN_2 cryogenic condition, SEM metallographic observations of the machined surface have been carried out. Fig. IV.17 describes the machined surface obtained after 11 min of cutting under LN_2 cryogenic cooling condition. The major defects observed consist essentially in the adhered material as well as the smearing.

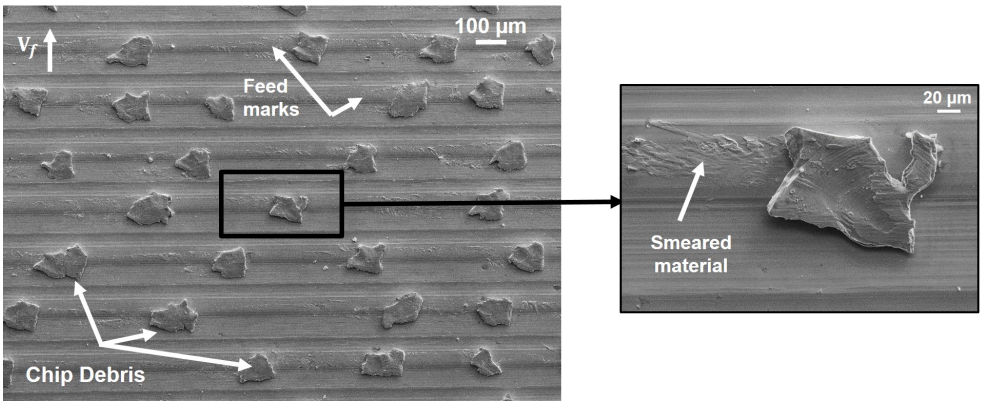

Figure IV.17 – SEM observations of the surface topography after 11 min of machining under LN_2 condition.

Additionally, EDS analyses have been carried out on the adhered material showing that the chemical composition of these particles exhibited the same elements composing the Inconel 718 alloy (Fig. IV.18).

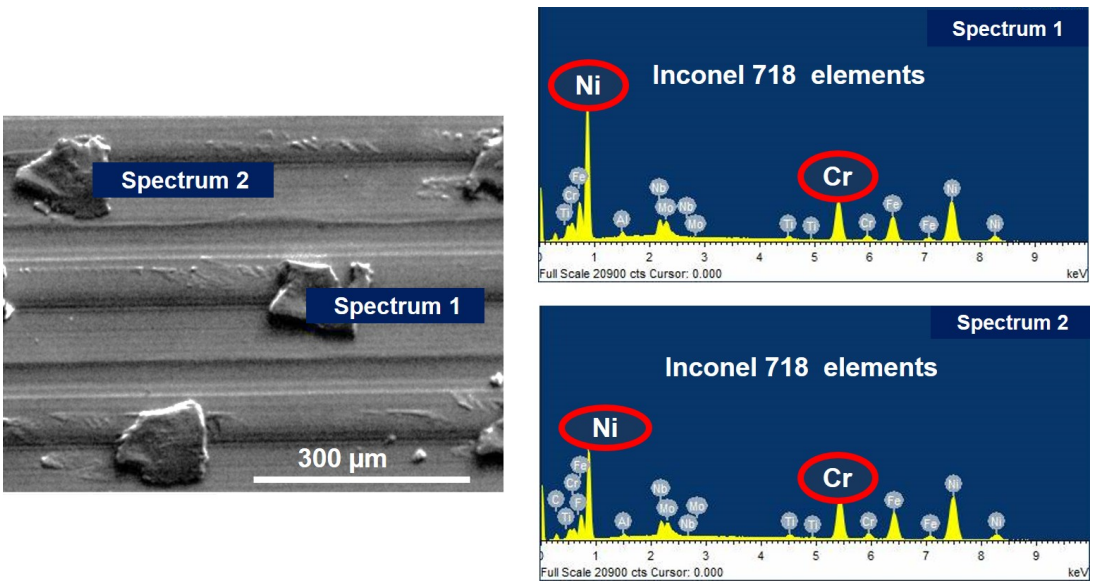

Figure IV.18 – EDS analysis carried out on the machined surface after 11 min of machining under LN_2 condition.

These observations of the machined surface could be explained by the fact that during the chip formation process, the LN_2 cutting fluid did not efficiently evacuate the chip

from the cutting zone. Consequently, the chips were stuffed between the cutting edge and the freshly machined surface. Furthermore, the degree of tool wear affects strongly the machined surface quality knowing that thereby the cutting forces and the cutting temperature increase as well when the tool wear evolves. Indeed, these features have been observed in previous work (Zhou et al., 2012). The study pointed out that the chip debris (the adhered chip) is attributed to the increase of the plastic deformation localized at the cutting tool-work material interface. Another correlation could be established with respect to the significant BUE that has been observed specifically in the case of LN_2 cooling conditions (Subsection 3.1) and the adhered microchips. Indeed, BUE are not stable during the cutting process (Ahmed et al., 2017). In contrast, there are regularly either detached or welded on the freshly machined surface leading to higher surface roughness as described previously.

It is also interesting to correlate the tool flank wear evolution with the surface roughness in all cooling methods namely the conventional and cryogenic lubrication. Under LN_2 condition, as the tool flank wear increases, the surface roughness increases as well as shown in Fig. IV.19. In contrast, in conventional lubrication and LCO_2 condition, the surface roughness decreased slowly since the cutting edge radius increased during machining. Likely, surface roughness produced when turning Inconel 718 could be depended on the non homogeneity of the tool flank wear. In other words, the evolution of tool wear in LN_2 cryogenic machining is not homogeneous leading to poor surface finish.

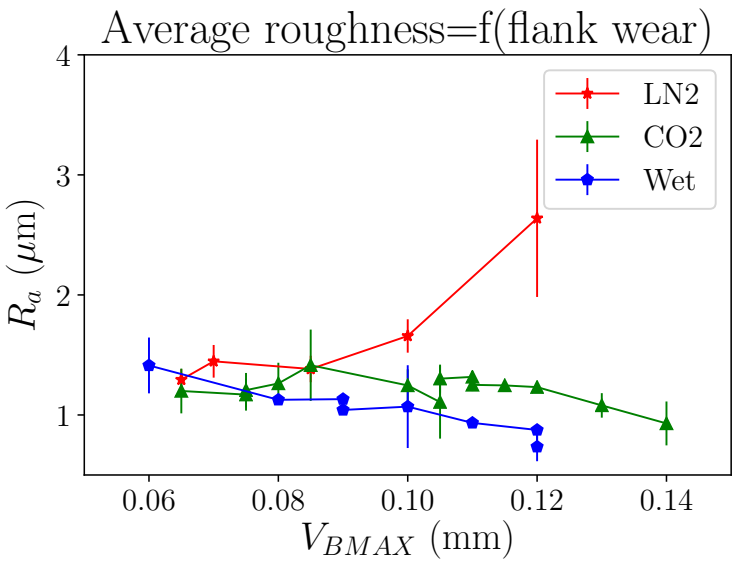

(a)

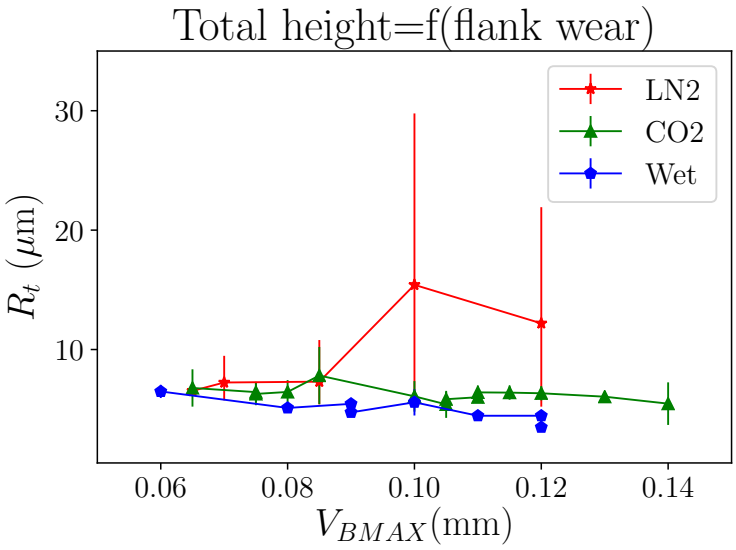

(b)

Figure IV.19 – Surface roughness versus tool wear evolution under Wet, LN_2 and LCO_2 cooling conditions: (a) Average roughness; (b) Total height of the profile.

3.3.2 Microhardness Profiles

This section aims to examine the tool flank wear effect on the microhardess profiles obtained under all cooling conditions. Fig. IV.20 presents the microhardness evolution below the machined surfaces when cutting using semi−worn tools under conventional and LCO_2 cooling conditions and worn tool under LN_2 condition. Knowing that the surface material subjected to mechanical and thermal loads, surface and subsurface properties depend on the coupling effects of both loads.

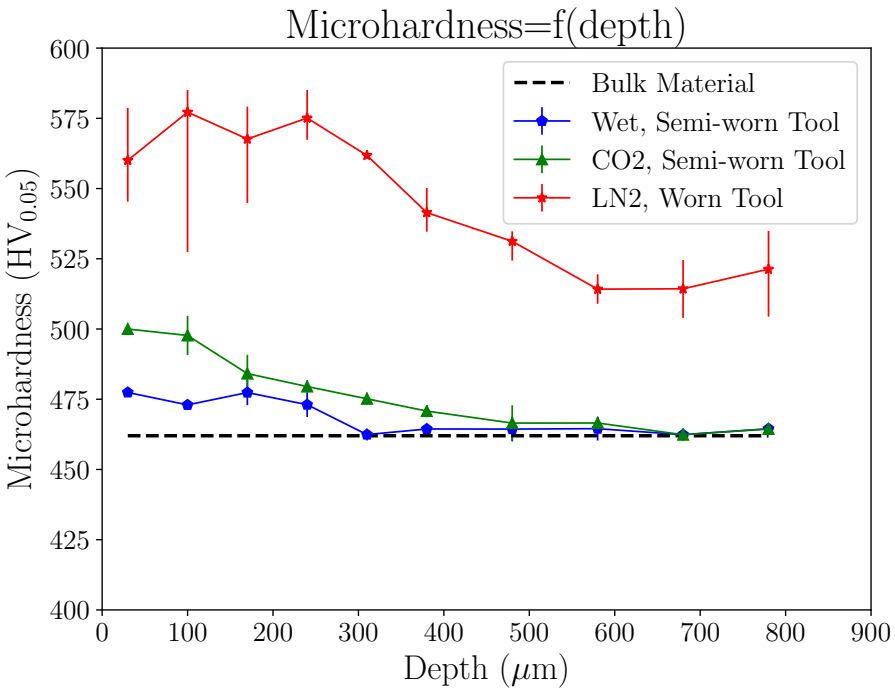

Figure IV.20 – Illustration of the evolution of the microhardness below the machined surfaces using semi−worn tools under conventional and LCO_2 cooling conditions and worn tool under LN_2 condition.

Results indicate that LN_2 cooling approach induced the hardest affected layer along more than 800 μm below the machined surface where the maximum value holds 585 $HV_{0.05}$ while the bulk material exhibits 462 $HV_{0.05}$. Regarding the LCO_2 cooling strategy induced higher strain hardening than the conventional lubrication beneath the machined surfaces. Indeed, the maximum value was measured very close in the near-surface layer of the machined parts holding 500 $HV_{0.05}$ in LCO_2 cooling condition against 477 $HV_{0.05}$ in conventional condition. This could be explained by the fact that the low temperature of the two cryogenic fluids generated harder work material as reported in (Patil et al., 2014). Moreover, it is worth mentioning that higher machining forces were found when using LN_2, and therefore inducing more severe mechanical deformation. The same trend was obtained in (Pusavec et al., 2011) revealing that cryogenic temperature during the machining process caused harder work material.

3.3.3 Surface and subsurface damage

Metallurgical alterations take place during the machining process. Indeed, authors have divided the machined workpiece material globally into two main regions (bulk material and affected zone) induced mainly by the combination of three origins namely the mechanical, thermal as well as chemical effects. The most common defects occurring after machining Inconel 718 on the surface and subsurface consist mainly of deformed grains along the cutting direction (Zhou et al., 2012), cracked carbide particles and surface cavities as reported in literature (M'Saoubi et al., 2012).
Fig. IV.21, Fig. IV.22 and Fig. IV.23 disclose the machined surfaces and subsurfaces alterations induced by machining under the conventional and cryogenic conditions when using new and worn tools along the cutting direction.

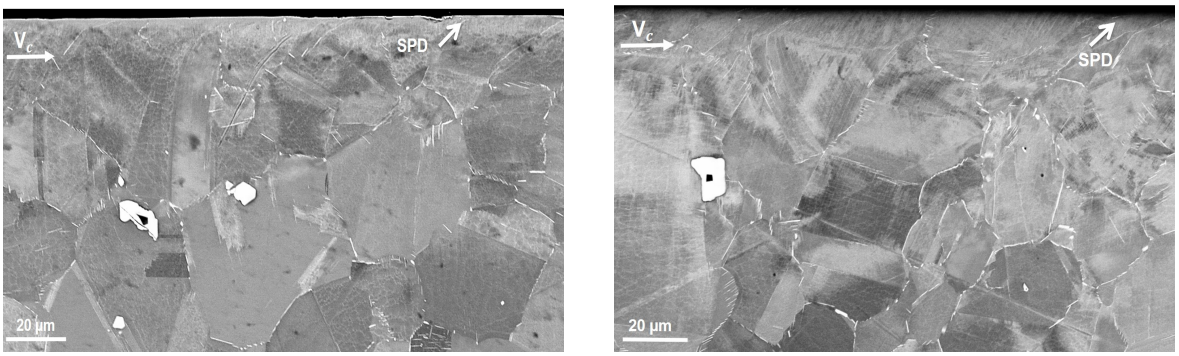

(a) (b)

Figure IV.21 – SEM observations of the machined surfaces in wet condition using new and semi−worn tools: (a) New tool; (b) Semi−worn tool (V_{BMAX}=0.12mm, t=15min).

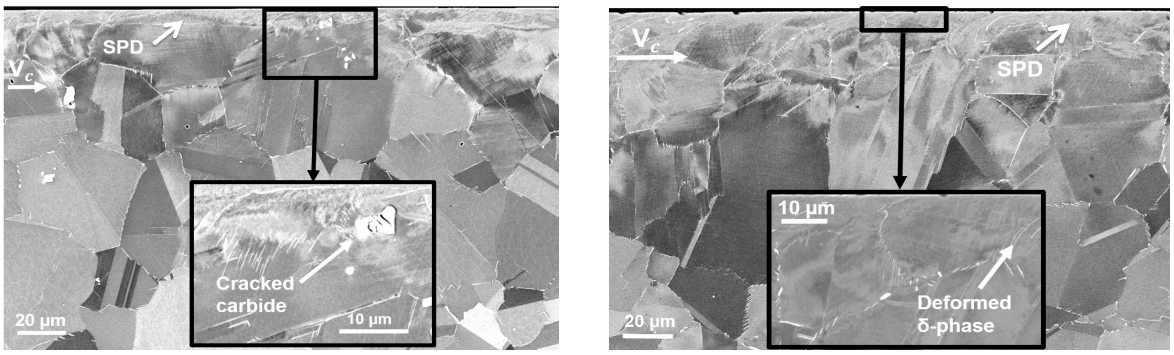

(a) (b)

Figure IV.22 – SEM observations of the machined surfaces in LCO_2 condition using new and semi−worn tools: (a) New tool; (b) Semi-worn tool (V_{BMAX}=0.14 mm, t=15min).

First of all, when focusing on the SEM metallographic observations of the machined surfaces obtained when cutting with new tools, all the cooling strategies have exhibited similar effect generating very thin affected zone. Indeed, very close to the free machined surface, a severe plastic deformation (SPD) could be observed in all cooling conditions. M'Saoubi et al. (2014) pointed out that very close to the free machined surface severe plastic deformation occurs when machining Inconel 718.
SEM observations obtained when machining employing semi−worn and worn tools highlight remarkable difference between surface damage induced when using new and

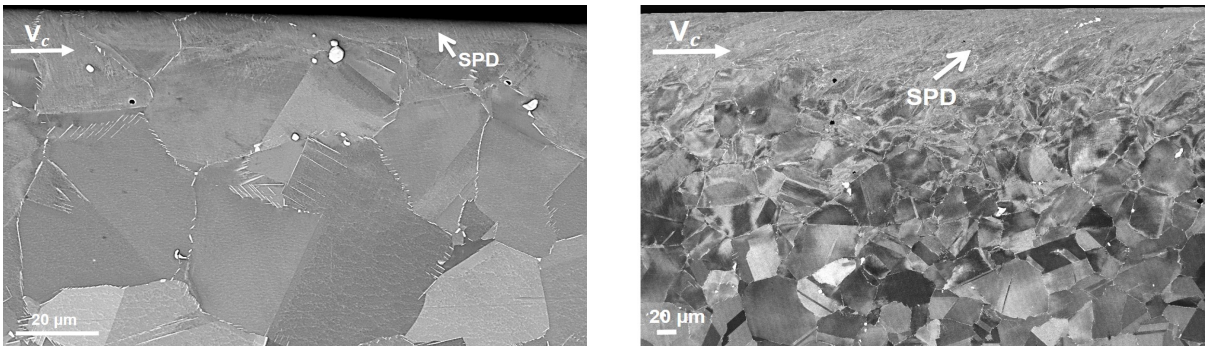

(a) (b)

Figure IV.23 – SEM observations of the machined surfaces in LN_2 condition using new and worn tools: (a) New tool; (b) Worn tool (V_{BMAX}=0.35mm, t=14min).

several state of tool wear. As displayed in the previous figures, an appearance of deeper affected layer is clearly observed compared to the case of the fresh tool. For instance, very close to the machined surfaces, more deformed grains are observed indicating a particular orientation along the cutting direction as reported in (Sharman et al., 2015). Chen et al. (2016) extensively focused on the surface integrity after broaching process of Inconel 718, especially the microstructural damage localized in the subsurface layer. They claimed that at this zone the grains are highly plastically deformed causing cracked carbides.

Similarly, when examining the SEM observations, one could define three regions that compose the work material. The first region consists of a non modified microstructure known as the bulk material. Secondly, a deformed zone reveals the elongation of the grains along the cutting direction due to the intense plastic deformation occurring during the cutting process. The third region is located at the vicinity of the free machined surface indicating a severe plastic deformation much higher than the one obtained in the previous zone where the grains undergo a drastic deformation.

Depending on the cooling conditions that induce miscellaneous tool wear state, the depth of each region is relatively variable. For instance, similar trend was revealed under conventional and LCO_2 conditions. In fact, both cooling conditions have generated approximately the same tool wear level and thereby inducing almost identical effect on the deformed subsurface. By contrast, as long as the tool wear increases, the damage of the machined affected layer is more pronounced as illustrated by the case of LN_2 strategy where the tool flank wear has exceeded the criterion. These observations are in agreement with (Zhou et al., 2011) that have pointed out the tool wear effect on subsurface deformation of nickel based alloy mentioning that tool wear as well as high cutting forces are the major factors considered for plastic deformation occurred beneath the machined surface.

However, it is important to affirm that accurately characterizing the depth of the affected zone turns out to be difficult through the SEM observations. That's why, EBSD analysis will be discussed in the next paragraphs in order to estimate the depth of the affected layer.

The EBSD technique is a complementary characterization to SEM technique for investigating the local plastic deformation produced following the machining process. Machining using new tools regardless the cooling strategy induces similar effect. That's why, in this study, one is content with identifying the effect of tool wear in the case of LCO_2 cooling strategy and subsequently comparing between the three cooling methods

when the tool wear evolved.
Fig. IV.24 gives information about the misorientation gradients measured inside the deformed grains chosen in the region close to the machined surface in the case of LCO_2 cooling strategy when using new and semi−worn tools.

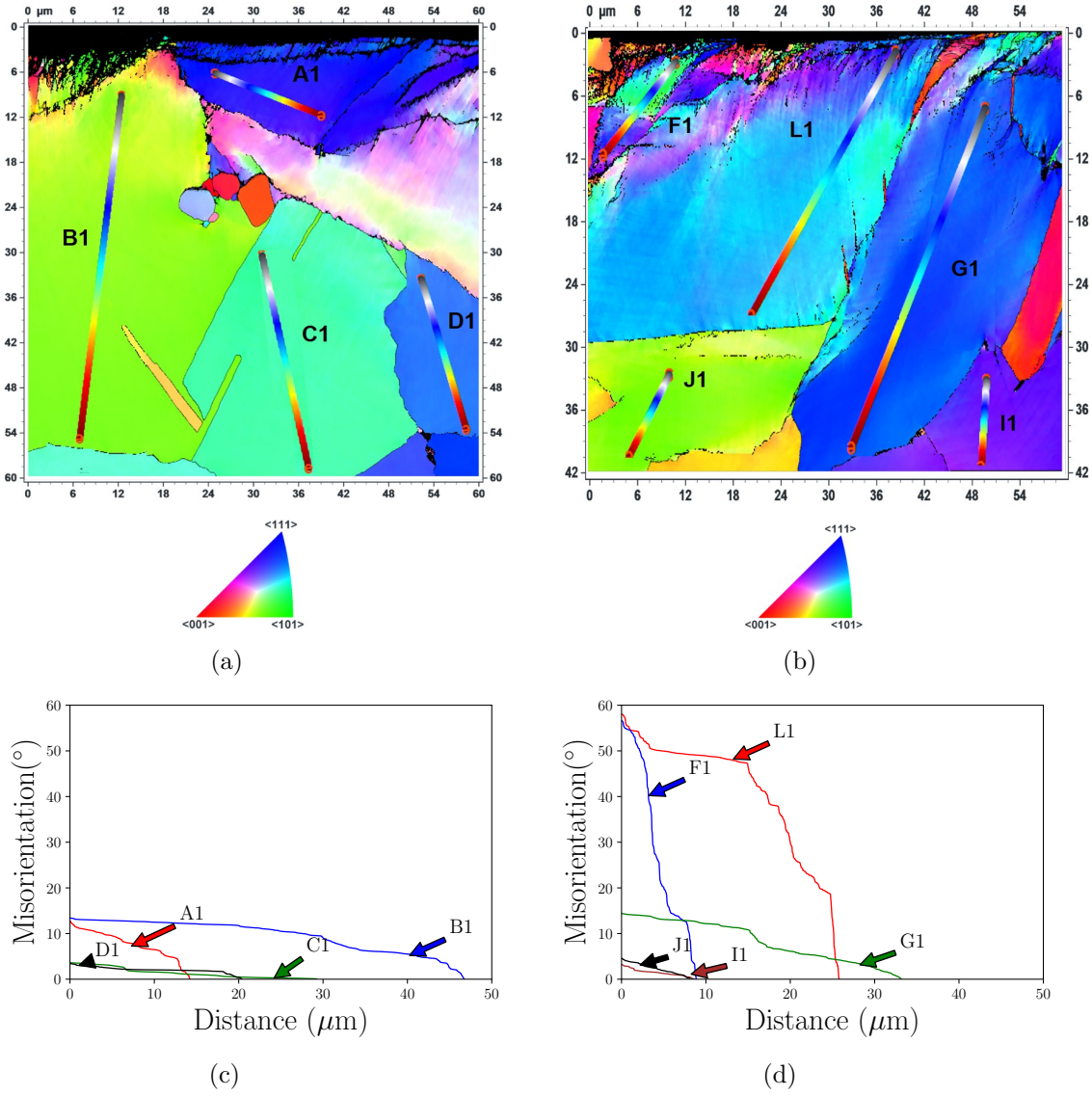

Figure IV.24 – Inverse Pole Figure (IPF) obtained from EBSD analyses of the machined surfaces (Projection axis [001]) established in LCO_2 condition using new tool (a) and semi−worn tool (b); Misorientation gradients measured inside deformed grains (in the direction as indicated by lines) in the case of: (c) New tool; (d) Semi-worn tool.

Accordingly, the regions subjected to large deformation are those that have undergone large grain elongation. Indeed, as long as the depth beneath the surface increases, the misorientation gradients inside the grains decrease. Obviously, when the grains are located very close to the machined surface, the plastic deformation at this position exhibits the highest values revealing a severe misorientation gradients (either using the cumulative or point-to-point method) (Azarbarmas et al., 2016; Mandal et al., 2010). For instance, the cumulative misorientations developed along the L1 and F1 lines exhibit higher misorientation gradient within the deformed grains. It is apparent from Fig. IV.24 that the cumulative misorientation continuously increases to almost 60° (at a distance of 25 μm).
In contrast, as for the grains located far away from the machined surface, the misorientation gradient inside the grains was reduced significantly because of the decrease of the plastic deformation, for instance along the lines I1 and J1. However, when focusing on these two lines, slight difference could be noticed concerning the misorientation gradients values. Although these two lines are located almost at the same depth from the machined surface, each grain was initially oriented differently and thereby the rate of plastic deformation may not be the same. In addition, an important aspect should be identified concerning the non indexed zone that proves the severe plastic deformation occurring very close to the free machined surface.
Moreover, when focusing on the tool wear effect and thereby comparing between the profiles obtained using new and semi−worn tools, one could notice that the highest misorientation gradients inside the deformed grains is attributed to the case that reveals higher tool wear. As the tool wear increases, the cutting forces tend to increase notably and therefore plastic deformation increases as well (Pradhan et al., 2017). In particular, it could be observed that the orientation gradient measured along A1 and F1 inside two deformed grains localized at the vicinity of the two cutting free surfaces (Fig. IV.24) generated using respectively new and semi−worn tools exhibit pronounced difference with respect to the cumulative misorientation plots where larger values are detected in the case of employing semi−worn tool.
In addition, when examining the resulting profiles as displayed in Fig. IV.24 and Fig. IV.25, the latters show clearly the higher values of the cumulative misorientation inside the deformed grains localized at the vicinity of the machined free surfaces when using semi−worn tools as well as worn tool respectively revealed under wet, LCO_2 and LN_2 cooling approaches.

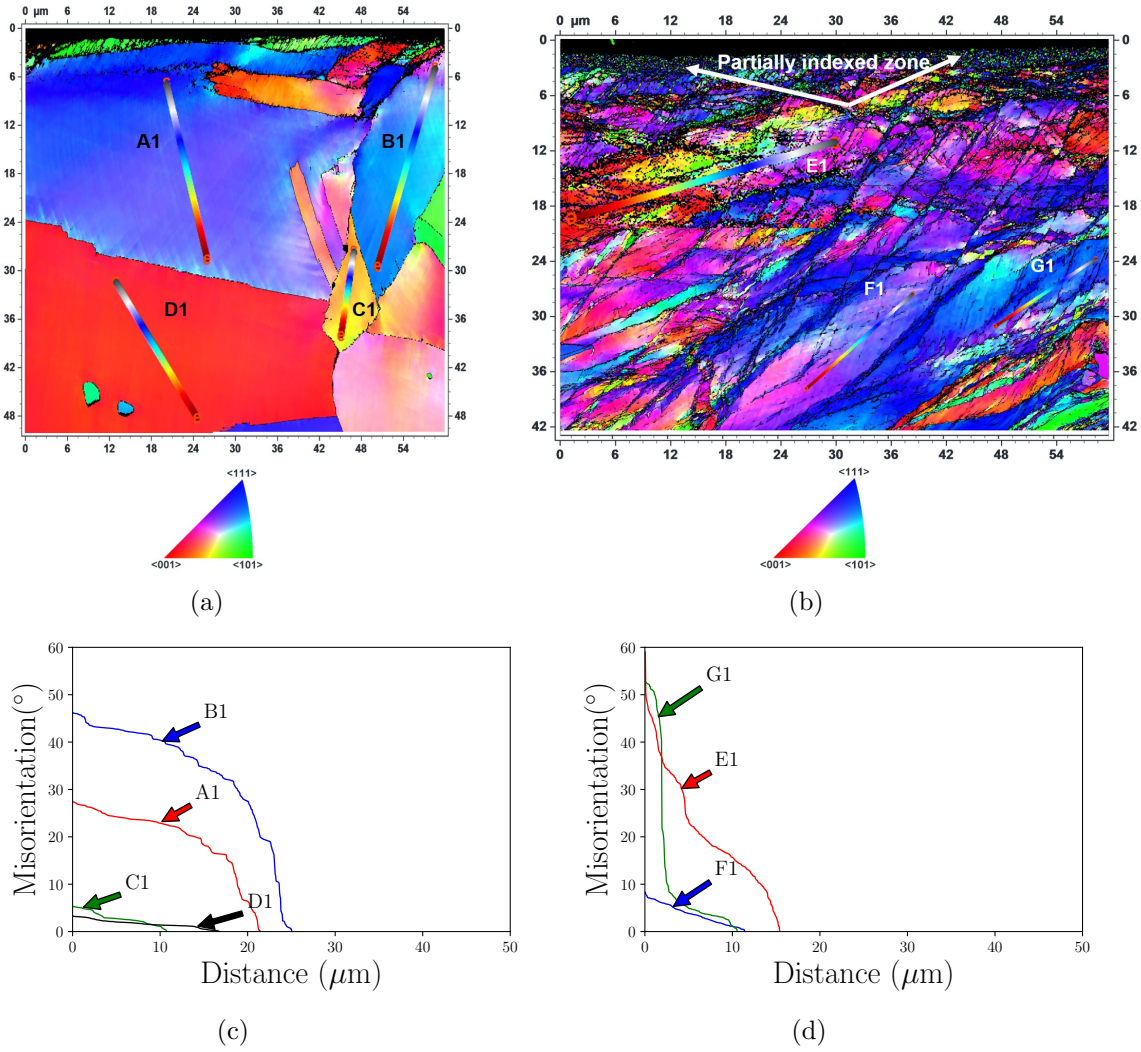

Figure IV.25 – Inverse Pole Figure (IPF) obtained from EBSD analyses of the machined surfaces (Projection axis [001]) established in wet condition using a semi−worn tool (a) and in LN_2 condition using worn tool (b); Misorientation gradients measured inside deformed grains in the case of: (c) Wet, Semi-worn tool; (d) LN_2, Worn tool.

Indeed, this confirms the intense grain rotation and plastic activity in this region induced by the cutting process. Zhou et al. (2011) have pointed out the tool wear effect on the surface integrity, in particular the depth of the plastically deformed layer. They related the deformation depth with the different tool conditions (new, semi−worn tool and worn tool) and the resultant cutting forces. The results figured out that the damage of the subsurface layer during the machining process is mainly governed by the tool wear levels during chip formation. In other words, the tool wear levels have major impact on the subsurface deformation depth as well as microstructure change. In fact, this could be attributed to the parallel progress of the thermal and mechanical loads acting on the machined surface resulting from the tool wear evolution. Effectively, in the case of LN_2 cryogenic condition that exhibited the highest tool wear value (V_{BMAX}= 0.35 mm), other aspect could be easily identified consisting in a thin layer observed in the immediate subsurface of the workpiece that was partially indexed. This is closely related to the heavy plastic deformation occurred at this region inducing distortion of the grains and thereby difficulties to accurately index.

3.3.4 Residual stresses

Residual stresses induced by machining affect strongly the products functional performances for instance the fatigue life (Javidi et al., 2008) as well as the resistance to stress corrosion cracking (Soyama and Takakuwa, 2015). In this study, one is interested to point out the influence of conventional and cryogenic conditions on the residual stress profiles beneath the machined surface when cutting using fresh tools. In addition, this work aims to figure out the effect of tool wear state on residual stress profiles obtained under all cooling conditions.
As depicted in Fig. IV.26, regardless the cooling conditions, tensile residual stresses are dominant near the surface indicating that the thermal effect prevails against the mechanical effect along the cutting direction.

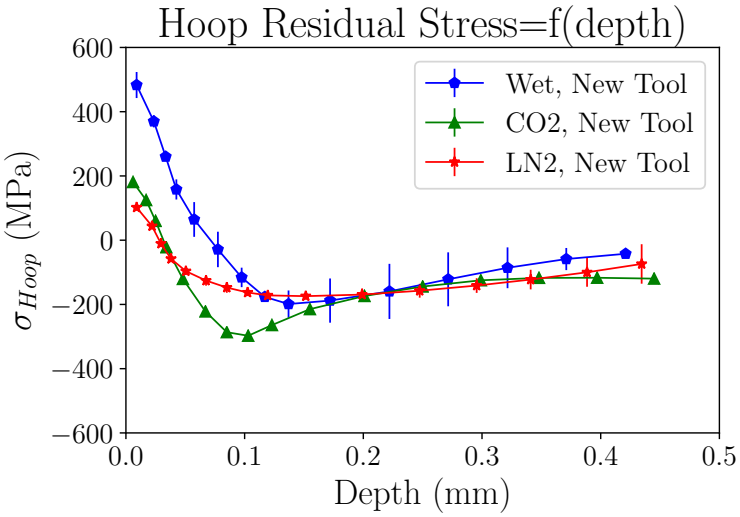

(a)

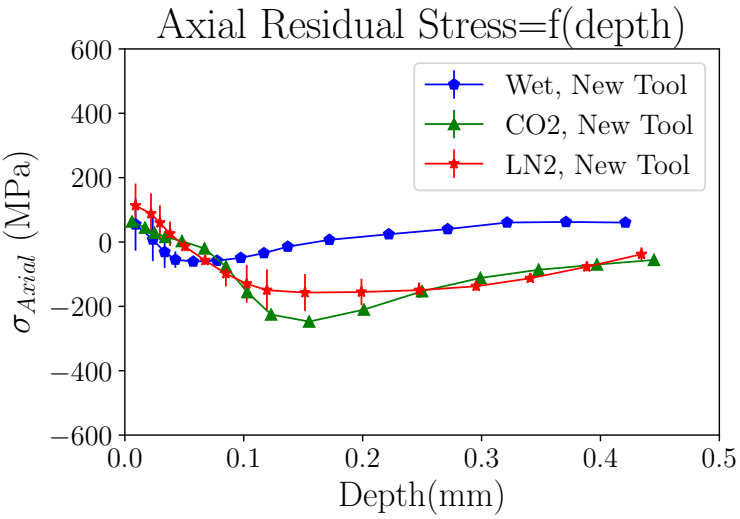

(b)

Figure IV.26 – Residual stress profiles near and beneath the machined surface using a new tool under Wet, LCO_2 and LN_2 cooling conditions measured along: (a) Hoop direction (cutting direction); (b) Axial direction (feed direction).

Actually, one may assert that near the surface, the tensile residual stresses are mainly associated to the thermal load effect. However, the compressive residual stresses beneath the machined surface are induced by the increase of the mechanical load and the plastic deformation flow (Pawade et al., 2008).
Nevertheless, when examining all the cooling strategies, the magnitudes of the tensile residual stress in the hoop direction (cutting direction) were significantly lower under cryogenic conditions compared to conventional lubrication. Obviously, tensile hoop stresses dropped from 483 MPa in wet condition to 180 MPa and 102 MPa respectively under LCO_2 and LN_2 cooling conditions indicating the efficiency of the cryogenic cutting fluids. On the other hand, since the thermal conductivity of the workpiece material is poor and the cooling capacity of the conventional lubrication is limited compared to cryogenic temperature, all these factors result in the domination of the thermal effect especially very close to the machined surface in conventional condition.
Additionally, conventional condition generated the largest tensile hoop stress layer reaching 100 μm below the machined surface and induced a compressive peak holding around -200 MPa. In contrast, LCO_2 cooling condition revealed the largest compressive depth initiating from 35 μm to more than 400 μm and provided the highest compressive peak reaching almost -300 MPa. Concerning the LN_2 condition, beneath the machined surface within 30 μm, hoop stress shifted to compressive values showing larger compressive depth compared to conventional condition. Overall, under cryogenic conditions, as the depth beneath the workpiece surface rose, the tensile hoop stresses rapidly dropped and quickly reached compressive levels before slowly returning to bulk values in the case of machining using new tools.
As for the axial stress profiles (along the feed direction), results indicated very low tensile values near the surface that shifted gradually to compressive trend under wet and LN_2 cryogenic conditions. However, under LCO_2 cryogenic condition, residual stress in the feed direction induced more compressive values from the depth of 50 μm.
When examining the cutting forces values obtained under all cooling conditions using a new tool, both cryogenic approaches revealed the highest values for all cutting forces components (especially the passive forces) showing the dominance of mechanical loading compared to conventional lubrication. This could likely justify the lower tensile residual stresses recorded near the surface and the higher compressive depth obtained under both cryogenic conditions.
Focusing on Fig. IV.27, as the tool wear increased in all cooling conditions, the residual stresses near the machined surface shifted to higher tensile stress range along the cutting direction and the compressive stress state beneath the machined surface increased drastically in both directions (axial and hoop) compared to the results obtained when machining with new tools. For instance, when examining the residual stress profiles generated in conventional lubrication, near the machined surface, the tensile residual stress evolved to achieve around 668 MPa and 214 MPa respectively in the hoop and axial directions while these components revealed lower values in the case of machining using new tools.

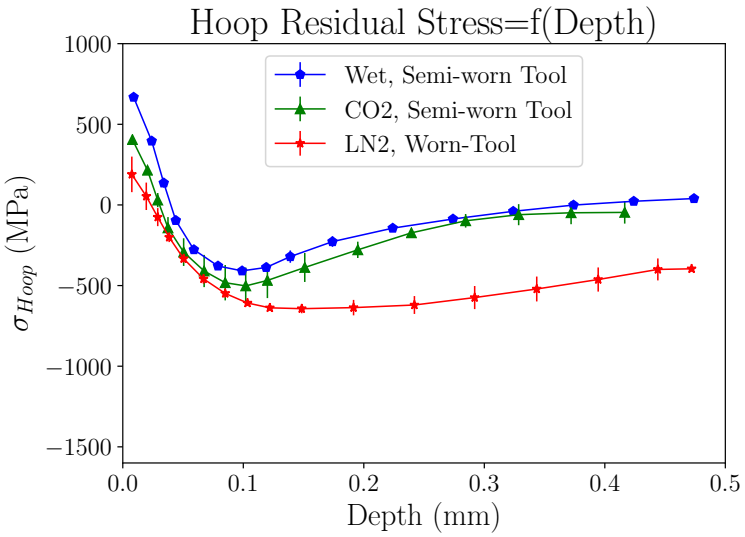

(a)

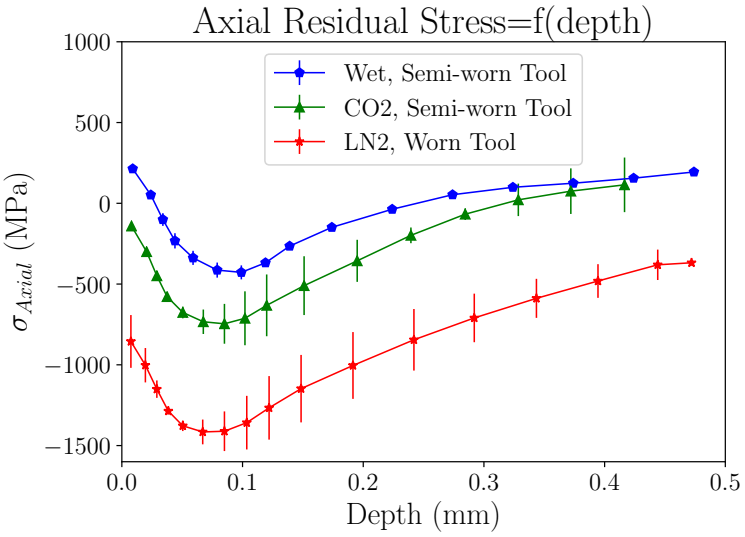

(b)

Figure IV.27 – Residual stresses profiles near and beneath the machined surface using semi−worn tools under conventional and LCO_2 cooling conditions and worn tool under LN_2 condition measured along: (a) Hoop direction; (b) Axial direction.

Besides, residual stresses generated along the hoop direction dropped rapidly to compressive values within 40 μm indicating a compressive peak holding around -408 MPa and then levelling out from 375 μm below the workpiece surface. By contrast, the axial residual stress shifted to compressive value at 34 μm below the surface inducing higher compressive peak holding around -427 MPa.
With regard to the LCO_2 cooling condition, as expected, near the surface, hoop residual stresses rose significantly reaching 405 MPa and then decreased gradually to compressive values at the depth of 50 μm showing higher compressive peak around -468 MPa in comparison with the values obtained in the case of using new tool. Alternatively, along the axial direction, residual stresses tended to be much more compressive from the first increment (10 μm) and penetrated to a deeper depth inducing greater compressive peak holding -746 MPa compared to the result obtained when cutting with a new tool. Another aspect that should be noticed is that when comparing conventional and LCO_2 cooling conditions that exhibited the same tool wear state, results showed better residual stress distribution revealed in the case of LCO_2 strategy indicating the advantage of cryogenic approaches with respect to fatigue resistance.
Concerning the LN_2 cooling method, when examining the residual stress distribution near the surface, in the cutting direction, it is obvious that residual stresses were tensile. Nevertheless, they are surprisingly maintained almost at the same range when using a new tool holding 189 MPa versus 102 MPa respectively. Consequently, one is interested to mention that when machining with severe tool wear, it is well known that temperatures rise drastically near the surface due to the increase of friction contact area between tool flank face and the workpiece. However, LN_2 cryogenic condition that reveals the highest tool wear level induces lower tensile residual stresses along the cutting direction compared to conventional and LCO_2 cooling conditions. In the other hand, along the feed direction, very close to the surface, stresses are much more compressive shifting from 113 MPa to -855 MPa when the tool wear has evolved dramatically.

3.4 Discussions: correlation between the outcome of the study

A knowledge of the machined surface properties is a major issue in order to predict how the structural part will perform in-service. Thus, it is necessary to identify the final characteristics of the machined parts to prevent any undesirable behavior of the components. In this section, a correlation between residual stresses, tool wear, cutting forces as well as the micro-hardness measurements will be established.
The investigation carried out to obtain higher integrity in the machined surface and subsurfaces on Inconel 718 shows that probably two different mechanisms might be involved in the surface generation: thermally influenced plastic deformation and mechanically induced plastic deformation, which govern the type of residual stresses as well as the micro-hardness induced in the machined surfaces (Fig. IV.28).

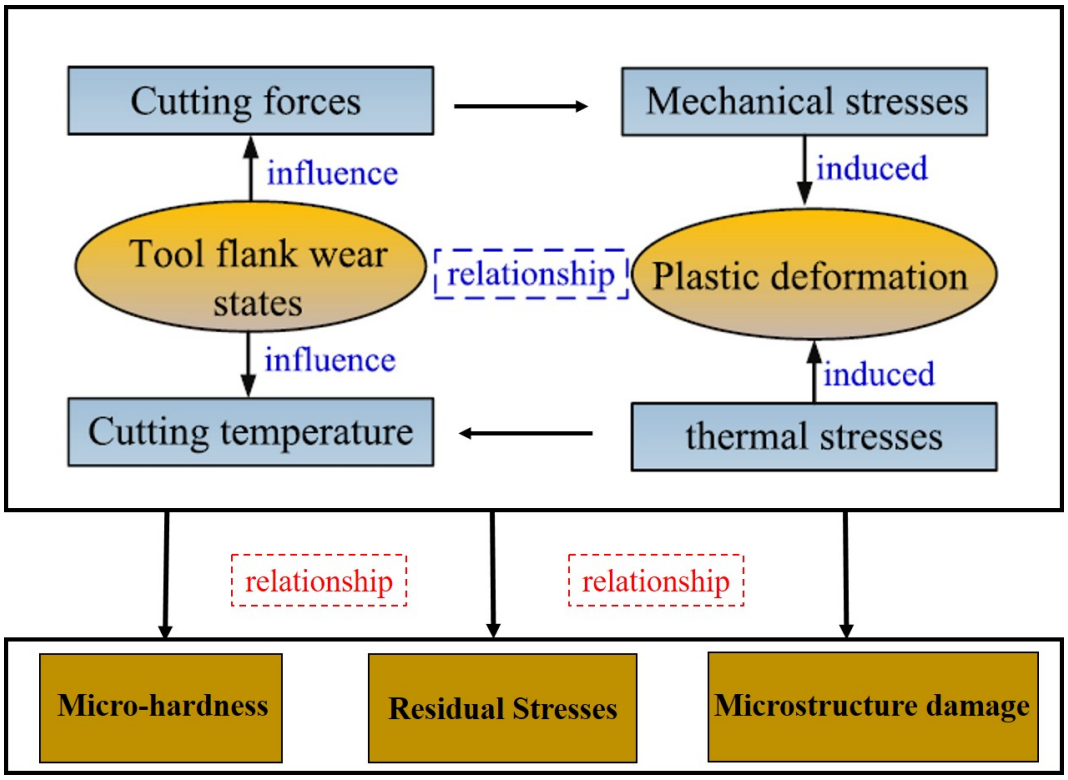

Figure IV.28 – Schematic of the plastic deformation mechanisms considering tool flank wear effect and the impact on the surface integrity (residual stresses, microstructure damage and microhardness).

First and foremost, the measured stress trends are different in axial and hoop directions, confirming that both mechanical and thermal effects contribute to the final residual stress state in a complex way that cannot be easily explained. Probably, the anisotropy obtained when comparing both components with respect to hoop and axial stresses could be explained by the fact that cutting direction undergoes a significant impact of the cutting speed and depth of cut as affirmed by Zhou et al. (2014). Nevertheless, along the feed direction, lower tensile residual stresses were recorded as displayed in Fig. IV.26. The same observation was figured out in (Pusavec et al., 2011) where tensile residual stresses tended to be more important in the cutting direction than in the feed direction.
In addition, the maximum compressive value indicates much higher value than the yield stress about -1415 MPa due to severe strain-hardening as indicated in 3.3.2. In this context, Peng-Lin et al. (2013) reported that the maximum compressive residual stress and its depth penetration rise drastically when worn tools are used due to essentially the significant growth of cutting forces. Indeed, as it was mentioned in 3.2, machining forces evolved dramatically when tool wear has increased, especially the passive forces. Thereby, the residual stresses developed in the workpiece after machining are strongly affected by the increase in cutting forces (Sharman et al., 2006).
Moreover, when comparing residual stress profiles along the feed direction in all cooling conditions, LN_2 cryogenic condition leads to higher compressive value from the machined surface in which the tool wear was the most pronounced. This result could be explained by the notable increase of the passive forces as the cutting tools were worn.
As it can be seen in Fig. IV.27, concerning both cryogenic profiles, it is worth mention-

ing that the depth of the thermally stressed layer is much thinner than the depth of the machined layer affected by mechanical loads compared to those obtained under conventional lubrication. In other words, cryogenic cutting fluids not only ensure efficient contribution to reducing the thermal effect on residual stress fields, but also provides increasing the compressive residual stress range (higher passive forces components). However, it should be noticed that generating compressive residual stresses in the finished product and increasing the passive forces during machining (power consumption) constitute a dilemma and hence a compromise is required.
Furthermore, it was reported that nickel based alloys, for example Inconel 718 are prone to strain hardening during the machining process. Indeed, Pawade et al. (2008) showed that the stress-strain characteristics of the machining affected layer changed significantly compared to the core material. They have proved that, depending on the cutting conditions, the local yield stress beneath the machined surface could increase even more than 1800 MPa whereas the yield stress of the bulk material does not exceed 1000 MPa. In the same context, other researches have investigated the machined surface damage of two nickel based alloys exhibiting different fraction volume of γ' phase (Liao et al., 2018). Their findings reveal that the superficial layers exhibit much higher yield stress values compared to the bulk material achieving even 1.4 times for both alloys.
Consistently, if examining the microstructure damage revealed by the SEM observations and the EBSD analysis, one may correlate the plastic deformation induced under all cooling conditions versus the microhardness measured beneath the machined surfaces. Plastic deformation causes hardening of the machined workpiece layer which is also known as work hardening effect. Indeed, the highest values of the microhardness were obtained in LN_2 condition where the plastic deformation of the affected layer seems to be the most pronounced as displayed in Fig. IV.25.b and Fig. IV.25.d.

4 Conclusion

In this work, a comparative study has been conducted in order to investigate the cryogenic performance using the liquid nitrogen LN_2 and the carbon dioxide LCO_2 when machining Inconel 718 in finish turning operations. The following conclusions are identified based on the experimental results of the present research:

— With respect to tool life, traditional lubrication produced the longest tool life. Concerning the LCO_2 condition, it exhibited similar tendency compared to the wet condition until reaching 14 min of cutting. However, LN_2 cryogenic condition revealed the shortest tool life. Besides, in this condition, welded chips on the rake face have been discerned;

— Cutting forces components (F_c, F_f and F_p) indicated higher values under both cryogenic conditions compared to conventional lubrication revealing that the flow stress of the work material increased due to cryogenic temperature. Additionally, it was noticed that the passive forces are the most sensitive component to tool flank wear rise;

— As for the surface roughness, this parameter indicated analogous trend under conventional and LCO_2 cooling methods presenting lower value compared to LN_2 strategy. In addition, the latter generated the largest values of surface

roughness due to the adhered chips that have been observed;

— In the matter of residual stress, results pointed out that when cutting using new tools, conventional lubrication produced the highest tensile value near the surface along the cutting direction and induced the lowest compressive peak and the lowest compressive depth. In both cryogenic conditions, near the surface, the hoop residual stresses exhibited almost similar values. By contrast, LCO_2 condition produced the highest maximum compressive value as well as the largest compressive depth when cutting with new tools;

— Residual stress profiles obtained when machining using semi−worn tools and worn tool respectively in conventional, LCO_2 and LN_2 cooling approaches, showed that both cryogenic conditions figured out the best performances obtained compared to wet condition. Furthermore, when cutting employing worn tool, much more compressive values have been recorded, especially along the axial direction;

— Regard the affected layer of the workpiece, when using new tools, no significant difference have been observed under all cooling strategies. By contrast, LN_2 cryogenic condition induced the most important damage when machining using worn tool;

— If comparing the tested cryogenic cooling conditions, LCO_2 cooling strategy is the most appropriate since it is able to withstand 15 min with acceptable tool wear and to produce a better surface integrity than LN_2 condition.

Bibliography

Ahmed, Y., Fox-Rabinovich, G., Paiva, J.M., Wagg, T., Veldhuis, S.C., 2017. Effect of built-up edge formation during stable state of wear in aisi 304 stainless steel on machining performance and surface integrity of the machined part. Materials 10.

Arrazola, P., Garay, A., Fernandez, E., Ostolaza, K., 2014. Correlation between tool flank wear, force signals and surface integrity when turning bars of inconel 718 in finishing conditions. Int. J. of Machining and Machinability of Materials 15, 84 – 100.

Ayed, Y., Germain, G., Pubill, M., Kowalewski, P., Locufier, D., 2017. The International Journal of Advanced Manufacturing Technology 93, 1199–1206.

Azarbarmas, M., Aghaie-Khafri, M., Cabrera, J., Calvo, J., 2016. Dynamic recrystallization mechanisms and twining evolution during hot deformation of inconel 718. Materials Science and Engineering: A 678, 137–152.

Bagherzadeh, A., Budak, E., 2018. Investigation of machinability in turning of difficult-to-cut materials using a new cryogenic cooling approach. Tribology International 119, 510 – 520.

Beausir, B., Fundenberger, J.J., 2017. Analysis tools for electron and x-ray diffraction, atex-software URL: `http://www.atex-software.eu`. université de Lorraine-Metz, 2017.

Behera, B.C., Alemayehu, H., Ghosh, S., Rao, P.V., 2017. A comparative study of recent lubri-coolant strategies for turning of ni-based superalloy. Journal of Manufacturing Processes 30, 541 – 552.

Bordin, A., Sartori, S., Bruschi, S., Ghiotti, A., 2017. Experimental investigation on the feasibility of dry and cryogenic machining as sustainable strategies when turning ti6al4v produced by additive manufacturing. Journal of Cleaner Production 142, 4142 – 4151.

Cantero, J., Díaz-Álvarez, J., Miguélez, M., Marín, N., 2013. Analysis of tool wear patterns in finishing turning of inconel 718. Wear 297, 885 – 894.

Courbon, C., Pusavec, F., Dumont, F., Rech, J., Kopac, J., 2013. Tribological behaviour of ti6al4v and inconel718 under dry and cryogenic conditions—application to the context of machining with carbide tools. Tribology International 66, 72 – 82. URL: doi:https://doi.org/10.1016/j.triboint.2013.04.010.

Chen, Z., Peng, R.L., Moverare, J., Avdovic, P., Zhou, J.M., Johansson, S., 2016. Surface integrity and structural stability of broached inconel 718 at high temperatures. Metallurgical and Materials Transactions A 47, 3664–3676.

Devillez, A., Coz, G.L., Dominiak, S., Dudzinski, D., 2011. Dry machining of inconel 718, workpiece surface integrity. Journal of Materials Processing Technology 211, 1590 – 1598.

Dosbaeva, G.K., Veldhuis, S.C., Elfizy, A., Fox-Rabinovich, G., Wagg, T., 2010. Microscopic observations on the origin of defects during machining of direct aged (da) inconel 718 superalloy. Journal of Materials Engineering and Performance 19, 1193–1198.

Ezugwu, E., Wang, Z., Machado, A., 1999. Journal of Materials Processing Technology 86, 1–16.

Grzesik, W., Niesłony, P., Habrat, W., Sieniawski, J., Laskowski, P., 2018. Investigation of tool wear in the turning of inconel 718 superalloy in terms of process performance and productivity enhancement. Tribology International 118, 337 – 346.

Halim, N., Haron, C., Ghani, J., Azhar, M., 2019. Tool wear and chip morphology in high-speed milling of hardened inconel 718 under dry and cryogenic co2 conditions. Wear 426-427, 1683 – 1690. 22nd International Conference on Wear of Materials.

He, Z., Zhang, X., Ding, H., 2016. Comparison of residual stresses in cryogenic and dry machining of inconel 718. Procedia CIRP 46, 19 – 22. 7th HPC 2016 – CIRP Conference on High Performance Cutting.

Herbert, C., Axinte, D., Hardy, M., Brown, P., 2012. Machining Science and Technology 16 .

Hong, S.Y., Markus, I., Jeong, W., 2001. New cooling approach and tool life improvement in cryogenic machining of titanium alloy ti-6al-4v. International Journal of Machine Tools and Manufacture 41, 2245 – 2260.

Hongbo, D., Gaochao, W., 2015. Effect of deformation process on superplasticity of inconel 718 alloy. Rare Metal Materials and Engineering 44, 298 – 302.

Iturbe, A., Hormaetxe, E., Garay, A., Arrazola, P.J., 2016. Surface integrity analysis when machining inconel 718 with conventional and cryogenic cooling. Procedia CIRP 45, 67 – 70. 3rd CIRP Conference on Surface Integrity.

Jamil, M., He, N., Zhao, W., Li, L., Gupta, M.K., Sarikaya, M., Khan, A.M., Singh, R., 2021. Heat transfer efficiency of cryogenic-ln2 and co2-snow and their application in the turning of ti-6al-4v. International Journal of Heat and Mass Transfer 166, 120716. URL: doi:https://doi.org/10.1016/j.ijheatmasstransfer.2020.120716.

Javidi, A., Rieger, U., Eichlseder, W., 2008. The effect of machining on the surface integrity and fatigue life. International Journal of Fatigue 30, 2050 – 2055.

Jawahir, I., Zhengwen, P., Yang, S., Giovanna, R., Yusuf, K., Tao, L., A, D., Domenico, U., O.W., D.J., 2012. Cryogenic processing of materials for enhanced product life, performance and sustainability. 15th International Conference on Advances in Materials and Processing Technology, Australia .

Jozić, S., Bajić, D., Topic, S., 2012. Flank wear in down and up milling. 23rd DAAAM International Symposium on Intelligent Manufacturing and Automation 2012 1, 251–254.

Kaynak, Y., 2014. Evaluation of machining performance in cryogenic machining of inconel 718 and comparison with dry and mql machining. The International Journal of Advanced Manufacturing Technology 72, 919–933.

Kumar, S., Satapathy, B., Pradhan, D., Mahobia, G.S., 2019. Effect of surface modification on the hot corrosion resistance of inconel 718 at 700 c. Materials Research Express 6, 086549.

Lequien, P., 2017. Etude fondamentale de l'assistance cryogénique pour application au fraisage du Ti6Al4V. Ph.D. thesis. Thèse de doctorat dirigée par Poulachon, GérardOuteiro, José Carlos et Rech, Joël Génie mécanique - procédés de fabrication Paris, ENSAM 2017.

Liang, X., Liu, Z., 2018. Tool wear behaviors and corresponding machined surface topography during high-speed machining of ti-6al-4v with fine grain tools. Tribology International 121, 321 – 332.

Liao, Y., Lin, H., Wang, J., 2008. Behaviors of end milling inconel 718 superalloy by cemented carbide tools. Journal of Materials Processing Technology 201, 460 – 465. 10th International Conference on Advances in Materials and Processing Technologies.

Liao, Z., Axinte, D., Mieszala, M., M'Saoubi, R., Michler, J., Hardy, M., 2018. On the influence of gamma prime upon machining of advanced nickel based superalloy. CIRP Annals 67, 109 – 112.

Mandal, S., Bhaduri, A., Vadlamani, S.S., 2010. A study on microstructural evolution and dynamic recrystallization during isothermal deformation of a ti-modified austenitic stainless steel. Metallurgical and Materials Transactions A: Physical Metallurgy and Materials Science 42, 1062–1072.

Mehta, A., Hemakumar, S., Patil, A., Khandke, S., Kuppan, P., Oyyaravelu, R., Balan, A., 2018. Influence of sustainable cutting environments on cutting forces, surface roughness and tool wear in turning of inconel 718. Materials Today: Proceedings 5, 6746 – 6754. International Conference on Emerging Trends in Materials and Manufacturing Engineering (IMME17), March 10-12, 2017.

Mitsubishi, 2006. Highly rigid and light-weight heads prevent vibration and achieve good surface finish Tool news,2006.7.Update B047A.

M'Saoubi, R., Axinte, D., Herbert, C., Hardy, M., Salmon, P., 2014. Surface integrity of nickel-based alloys subjected to severe plastic deformation by abusive drilling. CIRP Annals 63, 61 – 64.

M'Saoubi, R., Larsson, T., J.Outeiro, Guo, Y., Suslov, S., Saldana, C., Chandrasekar, S., 2012. Surface integrity analysis of machined inconel 718 over multiple length scales. CIRP Annals 61, 99 – 102.

Patil, N., Asem, A., Pawade, R., Thakur, D., Brahmankar, P., 2014. Comparative study of high speed machining of inconel 718 in dry condition and by using compressed cold carbon dioxide gas as coolant. Procedia CIRP 24, 86 – 91. New Production Technologies in Aerospace Industry - 5th Machining Innovations Conference (MIC 2014).

Pawade, R., Joshi, S.S., Brahmankar, P., 2008. Effect of machining parameters and cutting edge geometry on surface integrity of high speed turned inconel 718. International Journal of Machine Tools and Manufacture 48, 15–28.

Peng-Lin, R., Zhou, J., Johansson, S., Billenius, A., Bushlya, V., Ståhl, J., 2013. Surface integrity and the influence of tool wear in high speed machining of inconel 718 .

Pereira, W.H., Delijaicov, S., 2019. Surface integrity of inconel 718 turned under cryogenic conditions at high cutting speeds. The International Journal of Advanced Manufacturing Technology .

Pereira, O., Celaya, A., Urbikaín, G., Rodríguez, A., Fernández-Valdivielso, A., de Lacalle, L.N.L., 2020. Co2 cryogenic milling of inconel 718: cutting forces and tool wear. Journal of Materials Research and Technology 9, 8459 – 8468. URL: doi:https://doi.org/10.1016/j.jmrt.2020.05.118.

Pradhan, S., Mandal, S., Athreya, C., Babu, A., de Boer, B., Vadlamani, S.S., 2017. Influence of processing parameters on dynamic recrystallization and the associated annealing twin boundary evolution in a nickel base superalloy. Materials Science and Engineering A 700.

Pusavec, F., Hamdi, H., Kopac, J., Jawahir, I., 2011. Surface integrity in cryogenic machining of nickel based alloy—inconel 718. Journal of Materials Processing Technology 211, 773 – 783.

Ravi, S., Kumar, M.P., 2011. Experimental investigations on cryogenic cooling by liquid nitrogen in the end milling of hardened steel. Cryogenics 51, 509 – 515.

Rotella, G., Dillon, O.W., Umbrello, D., Settineri, L., Jawahir, I.S., 2014. The effects of cooling conditions on surface integrity in machining of ti6al4v alloy. The International Journal of Advanced Manufacturing Technology 71, 47–55.

Sharman, A., Hughes, J., Ridgway, K., 2006. An analysis of the residual stresses generated in inconel 718^{TM} when turning. Journal of Materials Processing Technology 173, 359 – 367.

Sharman, A., Hughes, J., Ridgway, K., 2015. The effect of tool nose radius on surface integrity and residual stresses when turning inconel 718^{TM}. Journal of Materials Processing Technology 216, 123 – 132.

Soyama, H., Takakuwa, O., 2015. Effect of residual stress on the corrosion behavior of austenitic stainless steel. Advances in Chemical Engineering and Science 5, 62–71.

Wagner, V., Baili, M., Dessein, G., 2015. The relationship between the cutting speed, tool wear, and chip formation during ti-5553 dry cutting. The International Journal of Advanced Manufacturing Technology 76, 893–912.

Xue, C., Chen, W., 2011. Adhering layer formation and its effect on the wear of coated carbide tools during turning of a nickel-based alloy. Wear 270, 895 – 902.

Yildirim, C., Kivak, T., Sarikaya, M., Sirin, S., 2020. Evaluation of tool wear, surface roughness topography and chip morphology when machining of ni-based alloy 625 under mql, cryogenic cooling and cryomql. Journal of Materials Research and Technology 9. doi:10.1016/j.jmrt.2019.12.069.

Zhou, J., Bushlya, V., Peng, R., Johansson, S., Avdovic, P., Stahl, J.E., 2011. Effects of tool wear on subsurface deformation of nickel-based superalloy. Procedia Engineering 19, 407 – 413. 1st CIRP Conference on Surface Integrity (CSI).

Zhou, J., Bushlya, V., Peng, R.L., Chen, Z., Johansson, S., Stahl, J.E., 2014. Analysis of subsurface microstructure and residual stresses in machined inconel 718 with pcbn and al2o3-sicw tools. Procedia CIRP 13, 150 – 155. 2nd CIRP Conference on Surface Integrity (CSI).

Zhou, J., Bushlya, V., Stahl, J., 2012. An investigation of surface damage in the high speed turning of inconel 718 with use of whisker reinforced ceramic tools. Journal of Materials Processing Technology 212, 372 – 384.

Chapter V

Fatigue tests of cryogenic drilled samples

1 Introduction . . . 191
2 Experimental work . . . 195
2.1 Work material . . . 195
2.2 Experimental equipment . . . 196
2.3 Description of the drilled batches . . . 197
2.4 Description of the fatigue specimen . . . 198
2.5 Experimental Methodology . . . 199
2.5.1 Staircase method . . . 199
2.5.2 Loading conditions . . . 200
2.5.3 Estimation of the fatigue limit . . . 200
3 Results analysis and discussions . . . 201
3.1 Stress-cycles: S-N curves . . . 201
3.2 Hole topology . . . 207
3.2.1 Surface topology : SEM observations . . . 207
3.2.2 Areal parameters . . . 209
3.3 Microhardness profiles . . . 212
3.4 Surface and subsurface damage . . . 213
3.5 Fractography of broken fatigue specimens . . . 215
3.6 Discussions: summary of the outcome of the study . . . 227
4 Conclusion . . . 229

1 Introduction

Aeronautic industry encounter continuously several challenges to achieve an optimum, reliable and long lasting components with the lowest production cost. Owing to their good mechanical properties over a wide range of temperatures, nickel based alloys, in particular Inconel 718, are frequently used in aircraft engines. Hence, it is very important to enhance as possible the performance of such component as well as the critical structure when operating in service-cycle. In this context, manufacturers search for efficient alternatives for the machining processes to achieve excellent surface integrity of the machined components. It is well known that the surface integrity characteristics significantly affect the fatigue behavior of the work materials (Sun et al., 2018b). Drilling process is widely employed for the airplane components since that building an aircraft requires an assembly. At this line, the main concern is to evaluate the fatigue behavior of Inconel 718 after drilling operations.
From literature, it is understandable that the machining process plays a major role to enhance or to worsen the fatigue strength (Thakur and Gangopadhyay, 2016). Suárez et al. (2019) have examined the influence of four machining process operations on the fatigue limit of Inconel 718 in four-point bending fatigue test. They involved the Abrasive Water Jet (AWJ), Wire Electrical Discharge Machining (WEDM), the conventional milling and the ultrasonic milling (UVAM) to investigate the surface integrity generated by these machining operations in order to evaluate the fatigue life correspondent to each case. Authors found that the WEDM specimens exhibited the highest values of surface roughness (S_a=3.5 μm), tensile surface residual stresses (around 400 MPa near the surface) and the shortest fatigue life (40 000 cycles). In contrast, UVAM specimens showed the highest fatigue life (80 000 cycles), the highest compressive residual stresses (around -800 MPa near the surface) and the lowest surface roughness values (S_a=0.25 μm) (Fig. V.1).

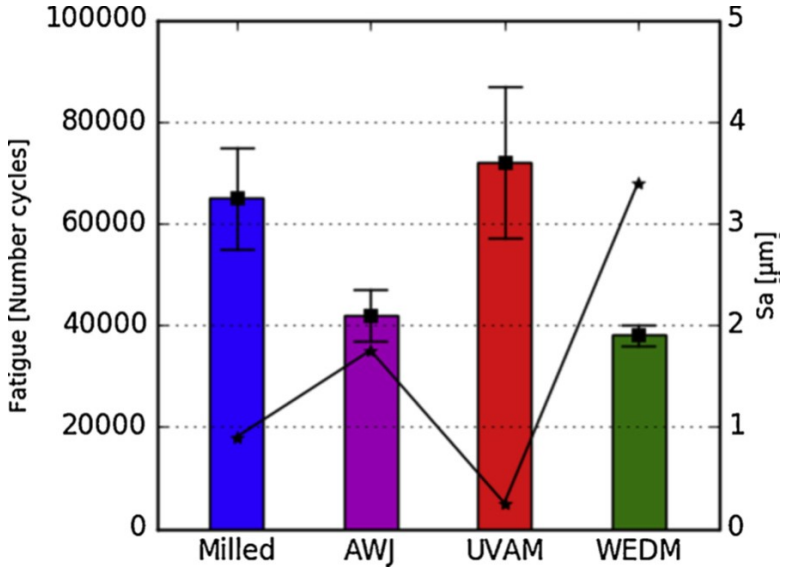

Figure V.1 – Illustration of fatigue results compared to S_a for tested technologies (Suárez et al., 2019).

Although the UVAM operation is considered as the best configuration to provide the highest fatigue limit, the latter did not exceed 80 000 of fatigue cycles and the level of the applied stress was not defined. In the same context, Chen et al. (2016) have pointed

out the fatigue performance of Inconel 718 specimens machined with WEDM process. They have found that the specimens machined by EDM have a noticeable decrease in fatigue life of 30 % compared to the polished specimens holding respectively 175 000 and 225 000 cycles. They have explained this finding by the fact that WEDM produced a damaged surface finish presenting surface craters, micro-cracks and micro-voids. Such defects favor the fatigue crack nucleation in addition to the large surface tensile residual stresses. These factors are proposed to be the major causes for the loss in fatigue life of the EDM specimens.
Javadi et al. (2018) have studied the effect of the surface residual stresses on the fatigue behavior of turned Inconel 718. Fatigue specimens were machined by turning. Rotating bending fatigue (RBF) tests were carried out with a stress ratio R = -1 at room temperature under a stress amplitude of 448 MPa (40 % of the yield stress) and a frequency of 30 Hz where high cycle fatigue lives of 10^6 cycles were targeted to reach. Authors have tested four fatigue batches namely polished samples considered as a reference and the three others are turned varying the cutting parameters (cutting speed, depth of cut and the feed rate) for each batch. Three tested specimens were employed for each configuration. Results have shown that the highest fatigue life (1 850 000) was obtained under a specific turning condition (V_c=67 m/min, f=0.02 rev/mm and a_p=0.3 mm) inducing the best surface integrity in terms of residual stresses distribution even if the surface roughness showed almost similar values (Fig. V.2).

Run#	Surface roughness		Surface residual stresses		Fatigue life
	Ra (µm)	*Rt* (µm)	*Axial* (MPa)	*Hoop* (MPa)	*Nf* (Cycles)
Machined run #1	0.47 ± 0.11	4.51 ± 0.73	-275 ± 25	492 ± 28	1.85×10^6
Machined run #2	0.74 ± 0.13	4.84 ± 1.38	853 ± 32	996 ± 39	5.02×10^5
Machined run #3	0.28 ± 0.05	2.8 ± 0.32	146 ± 28	515 ± 22	8.33×10^5
Polished	0.020 ± 0.002	0.27 ± 0.05	-9 ± 30	-3 ± 43	9.85×10^5

Figure V.2 – Illustration of average values (four replications) of surface roughness, residual stresses, and average fatigue lives (three RBF tests) for the selected turning conditions and the polished specimens (Javadi et al., 2018).

It should be noted that the polished fatigue specimens induced lower fatigue life of 985000 cycles knowing that the surface roughness was fairly low in comparison with the three batches. In the same line, Wang et al. (2017) investigated the influence of the cutting parameters (the cutting speeds and the feed rates) in milling operations on three-point bending fatigue life of Inconel 718. The maximum and minimum stresses were 1000 and 100 MPa, respectively, and the load frequency was fixed at 20 Hz. Their conclusions that have been drawn disclosed that the fatigue life of Inconel 718 could be enhanced when optimizing the cutting parameters. They found that the cutting speed had negligible influence while the feed rate impacted the fatigue life. Indeed, the fatigue life decreased from around 160 000 to 10 0000 cycles when the feed rate was fixed at 0.1 mm/tooth/rev to 0.25 mm/tooth/rev respectively. The obtained fatigue life remains too low in comparison with the industrial requirement (Belan, 2015).
Subsequently, Gribbin et al. (2019) have examined the influence of the microstructure elaborated from several forming process namely the direct metal laser melting (DMLM) varying the direction of the material deposition at a 45 ° (diagonal) and a 90 ° (horizontal) angle with respect to the loading direction. The two other microstructures are: one was wrought and the second was elaborated by DMLM followed by Hot Isostatic

Pressing (HIP) treatment. Fatigue tests were carried out at room temperature and 500°C under rotary beam loading. The applied stresses σ_a varied from 200 MPa to 1200 MPa. Results have shown that the fatigue endurance limit reached around 450 MPa at 10^7 of fatigue cycles for the wrought microstructre. At room temperature, the wrought specimens induced the highest fatigue resistance in comparison with the DMLM (the diagonal and the horizontal). This finding could be explained by the microstructure defects occurred in DMLM specimen such as the porosity in addition to the high content of δ precipitates deteriorating the fatigue behavior.
Afterwards, Zhong et al. (2019) have investigated the high cycle fatigue performance of the nickel based alloys submitting two different heat treatment (only heat treated ST and heat treated + aged ST+A). The fatigue tests have been tested under tension and compression loading (R=-1) and three polished specimens were employed for each applied stress level. Results have figured out that the fatigue limit of the ST+A showed lower value compared to ST state holding a decrease of 6.73 % from 492 MPa to 461 MPa at 10^7 cycles. Authors suggested that the origin of such gab could be likely related to the crack nucleation sources occurring in each specimen category (ST or ST+A).
Another aspect might be worth mentioning with respect to the microstructure influence on the fatigue behavior of Inconel 718. For instance, Belan (2015) have evaluated the effect of carbide particles at high cycle fatigue (HCF) and very high cycle fatigue (VHCF). Their findings disclosed that due to the size of the carbide particles present in the alloy having an average size of 11.79 μm, the carbides did not act as fatigue cracks nucleation sites. Moreover, an interesting study that could be evoked in the current work dealing with the effect of cryogenic temperature of the fatigue performance of Inconel 718. Ono et al. (2004) have investigated the Inconel 718 behavior under fatigue loading at two cryogenic temperatures (4 K and 77 K) and at room temperature (293 K). Results have proved that as long as the fatigue test temperature decreased, the fatigue limits of the tested specimens increased as depicted in Fig. V.3.

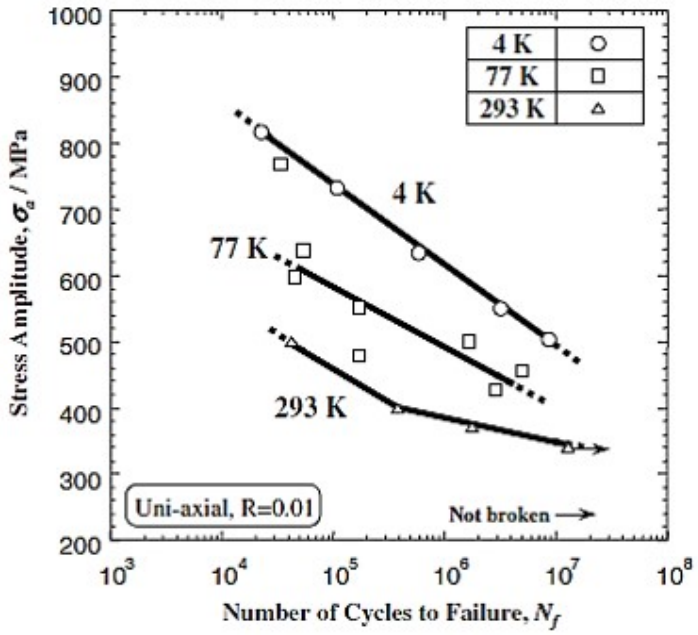

Figure V.3 – Illustration of S-N diagrams at 4 K, 77 K and 293 K for Inconel 718 alloy (Ono et al., 2004).

Concerning the fatigue cracks sites, authors have indicated that the cracks initiated

near the specimen surface. Depending on the level of the applied stress, fatigue cracks regions are fairly different: at high stress level, cracks predominantly initiated from coarse niobium carbides NbC, however at lower stress amplitude, fatigue cracks are mainly initiated around facets structures (Fig. V.4).

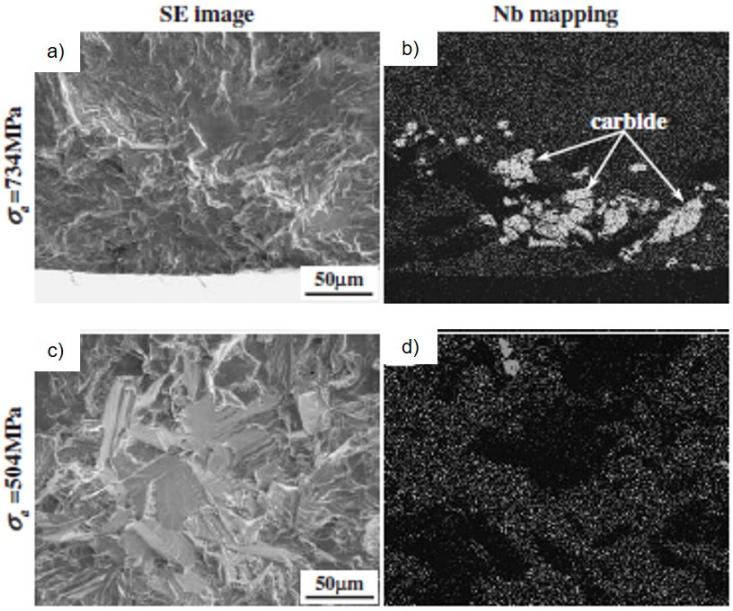

Figure V.4 – Illustration of SEM secondary electron images showing the fatigue crack initiation sites (a), (c), and niobium mapping by EDS (b), (d) respectively. These specimens were fatigue-tested at 4 K. (Ono et al., 2004).

As a general overview of the previous studies that have been investigated the influence of the machining process on the fatigue performance, several comments could be arisen. First, most of the previously mentioned papers have studied the fatigue performance of Inconel 718 at low fatigue cycles ($<10^5$) although the industrial requirements are much higher. Secondly, concerning the influence of machining operations on fatigue performance of Inconel 718, the drilling operation was not developed so far. Finally, none has figured out the cryogenic machining effect (regardless of the operation) on the fatigue behavior either of metallic metals or composites materials. For these reasons, the present study attaches importance to the effect of cryogenic cooling conditions of drilled specimens on fatigue limit at high cycle fatigue regime (2.10^6).
In the first part of this chapter, the material properties involving the microstructure and the tensile properties are briefly presented. Subsequently, the fatigue tests in terms of the experimental set-up including the fatigue specimen geometry, the staircase method as well as the loading conditions are described in detail. The characterization of surface integrity of the drilled specimens that were machined using fresh tools is figured out. Afterwards, the stress-cycles curves (S-N) are presented. Finally, the analyses of the fracture surfaces of the broken specimens are pointed out in order to identify the crack nucleation regions correspondent to each studied case.

2 Experimental work

2.1 Work material

Prior to fatigue testing, monotonic tensile tests were conducted at room temperature in order to determine the tensile properties of the tested material in the rolling direction (RD). Results are given in the Table V.1.

Table V.1 – Mechanical properties of the work material

Young modulus (GPa)	206
R_m (MPa)	1695
$R_{e_{0.1\%}}$(MPa)	1255
Hardness ($HV_{0.05}$)	499

The geometry of the tensile specimens were chosen according to the standard NF EN 2002-001 (AFNOR, 2006) and is illustrated in the Fig.V.5.

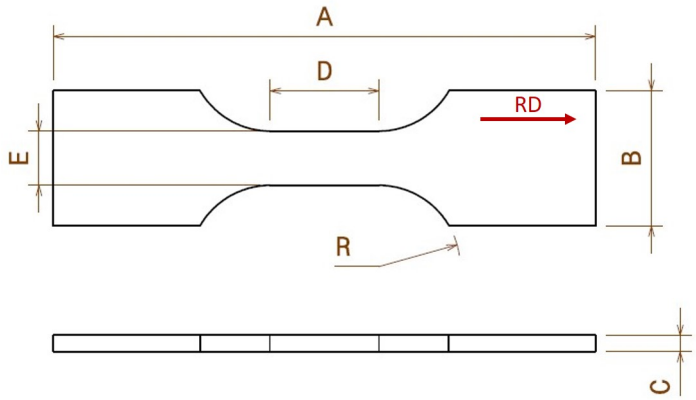

Figure V.5 – Illustration of the tensile specimen.

Table. V.2 sets the dimensions of the tensile specimens

Table V.2 – The dimensions of the tensile specimens

A (mm)	B (mm)	C(mm)	D(mm)	E(mm)	R(mm)
170	40	2	30.94	15	41.13

Additionally, X-Ray Diffraction (XRD) analyses have been conducted out to characterize the texture of the work material using the BRUKER Discover D8 diffractometer. The corresponding inverse pole figures are plotted for the three principal directions namely the rolling direction (RD), the transverse direction (TD) and the normal direction (ND) as illustrated in Fig.V.6. RD poles are preferably located along [111] (red color) whereas the ND poles are aligned with the [011] of the standard stereographic

triangle.

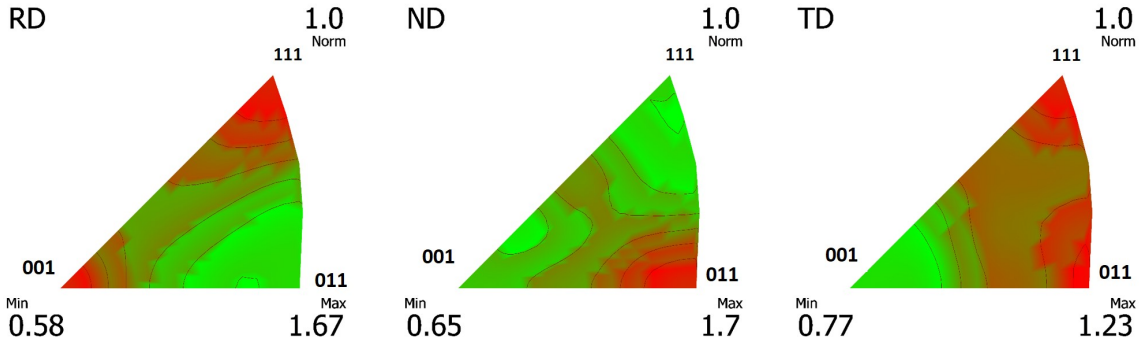

Figure V.6 – Illustration of Inverse pole figures of as-received material for (a) normal direction; (b) rolling direction and (c) transverse direction.

2.2 Experimental equipment

The main goal of this study is to evaluate the effect of cryogenic machining on fatigue endurance life, in particular the drilling operations. Hence, the fatigue specimens have been drilled under conventional and cryogenic cooling conditions using fresh tools. The two cryogenic cutting fluids that were employed are the liquid nitrogen LN_2 and the carbon dioxide LCO_2. The drilling trials were carried out using the same test configuration (cutting parameters, drill bit geometry, set-up) varying the cooling conditions. The cutting configurations are summarized in the Table V.3.

Table V.3 – Working conditions

Workpiece	Material	Inconel 718
Cutting parameters	Cutting speeds (m/min)	30
	Feed (mm/rev)	0.1
	Depth of the hole (mm)	2 (through-hole)
Tool	Drill bit	Coated carbide (TiAlN)
	Point Angle (SIG) (°)	140
	Diameter of the drill bit (mm)	14
	Drill reference	SD103-14.00/14.99-50-16R7
	Exchangeable tip reference	SD100-14.00-M
Coolants	Conventional	Wet
	Cryogenic	LN_2
	Cryogenic	LCO_2
Coolants application	Wet	Internally
	LN_2	Internally
	LCO_2	Internally

The drill geometry and the drill bit are displayed in Fig. V.7.

(a) (b)

Figure V.7 – (a) Illustration of the drill geometry; (b) Illustration of the drill bit (Seco, 2020).

The experimental set-up of the drilling operations of the fatigue specimens is given in Fig.V.8.

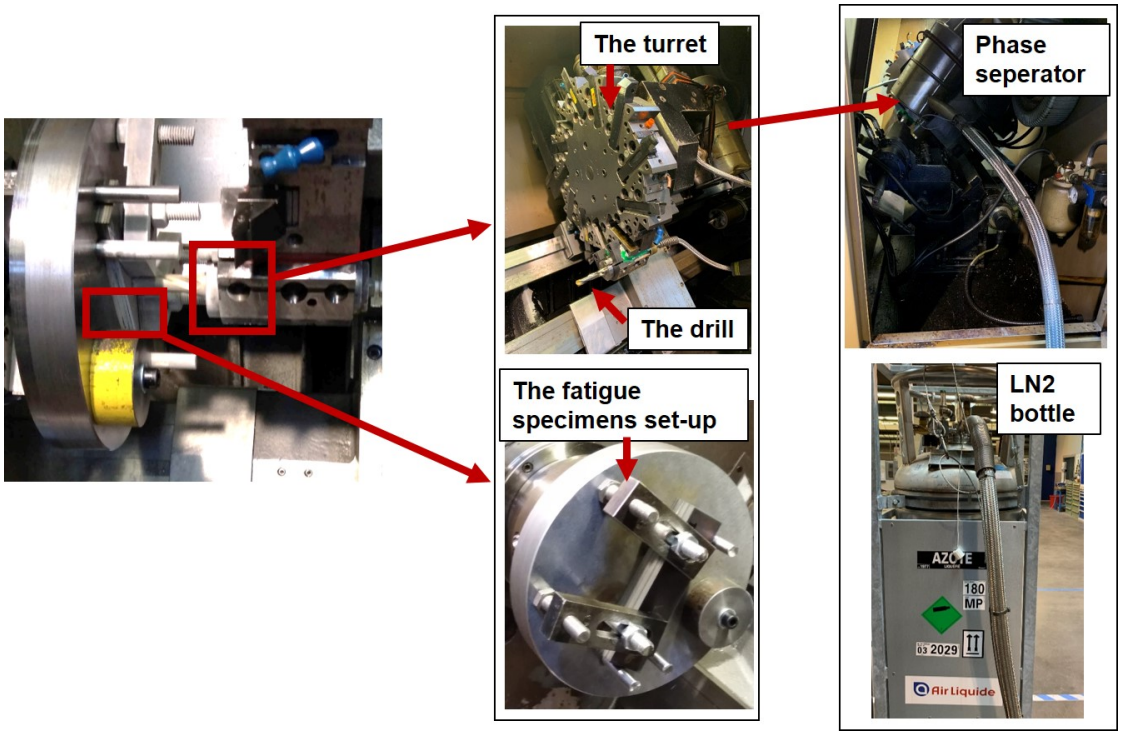

Figure V.8 – Illustration of the experimental set-up of fatigue specimen drilling operation: LN_2 configuration.

2.3 Description of the drilled batches

For each drilling step, a batch composed of 6 specimens was drilled at the same time. The fatigue specimens exploited in this work are drilled in the center.
Before presenting the obtained results of the fatigue campaign, it is relevant to show the chronology of the drilling operations of the fatigue specimens for each cooling strategy. Table V.4 illustrated the mentioned information.

Table V.4 – The chronology of the fatigue specimens drilling.

	Wet	LCO_2	LN_2
First batch (t_1)	Speci n°: 1 to 6	Speci n°: 1 to 6	Speci n°: 1 to 6
Second batch (t_2)	Speci n°: 7 to 12	Speci n°: 7 to 12	Speci n°: 7 to 12
Third batch (t_3)	Speci n°: 13 to 15	Speci n°: 13 to 15	Speci n°: 13 to 18
Fourth batch (t_4)	Speci n°: 16 to 18	Speci n°: 16 to 18	-

The first batch for each condition was carried out using new drill. The second and the third packages have been performed employing the same drills already used during the first batch for each cooling condition. Regard the fourth batch, the wet and LCO_2 conditions were drilled using new drills.

2.4 Description of the fatigue specimen

The design of the fatigue specimens were conceived following the standards AFNOR (AFNOR, 2012). As the specimens are drilled, the stress concentration factor k_t (equal to 2.3) was considered while choosing the applied stress during the fatigue load. The geometry of the fatigue specimens are illustrated below (Fig.V.9). It is worth mentioning that the choice of the fatigue specimens (drilled specimens) was not randomly decided. Indeed, drilled specimens induce higher stresses at the hole surface comparing to the subsurface with a factor of 2.3. Therefore, the influence of the surface is much more significant and thereby the process effect is well discriminated.

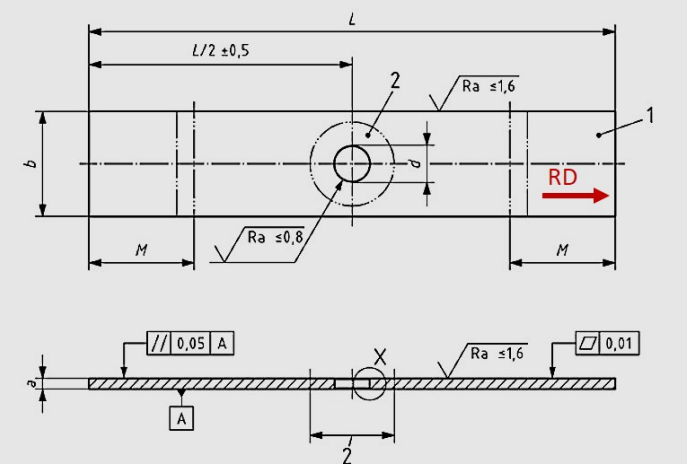

Figure V.9 – Illustration of Fatigue specimen geometry.

Table V.5 sets out the dimensions of the fatigue specimens.

Table V.5 – The dimensions of the fatigue specimens

a (mm)	b (mm)	d (mm)	L (mm)
2	52	14	170

Fatigue experiments have been performed using the INSTRON 3-axes Fatigue machine in tensile load (Fig.V.10).

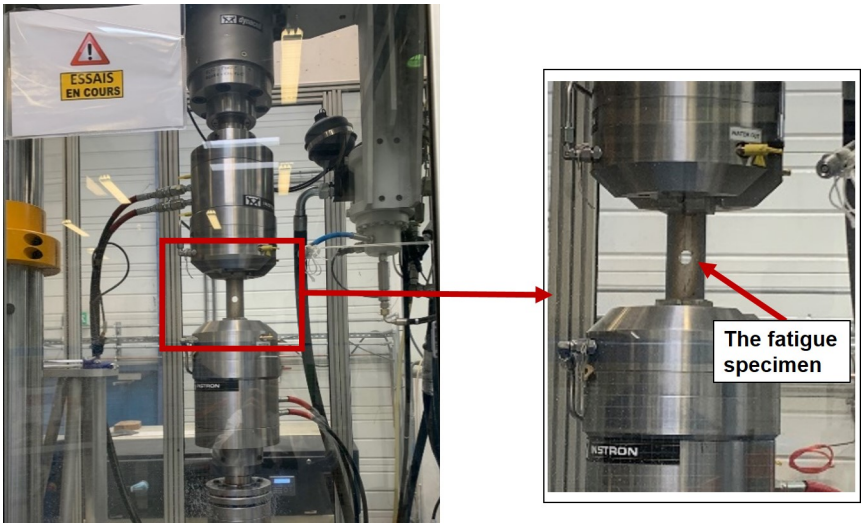

Figure V.10 – Illustration of the fatigue machine INSTRON 3-axes.

2.5 Experimental Methodology

The fatigue test campaigns are greedy in parts and therefore it requires long time to conduct these tests. So that, it was relevant to optimize the experimental test plans. In this work, the main objective of the fatigue experiments is to determine the fatigue endurance limit at high cycle fatigue (HCF) for three batches of specimens since that HCF is very sensitive to process effect. Therefore, the Staircase method was opted as it is a quantitative approach that allows to determine appropriately the fatigue endurance limit and to estimate the correspondent data spread.

2.5.1 Staircase method

The Staircase method consists in testing a batch of specimens (n) subjected to several stress levels at a fixed cycle number (N). The variable parameter of the test is the rupture or non-rupture of the specimens. The specimens should be tested one after the other, because the applied stress of the specimen (i+1) depends on the result of the specimen (i). The first level of the applied stress should correspond to the fatigue endurance limit estimated either through preliminary test or deduced from literature review. In the current work, a Locati test has been conducted as preliminary test. The Locati method consists in testing only one specimen at several applied stress successively at a fixed number of cycle (N) until failure. The stress induced the rupture of the specimen (σ_{Locati}) is then exploited in the Staircase method.
When selecting the step of the applied stress levels (d), the first stress level of Staircase method ($\sigma_{Straicase}$) corresponds to the one inducing the failure of the specimen substructing the step (d) as mentioned in the Equation V.1.

$$\sigma_{Straicase} = \sigma_{Locati} - d \tag{V.1}$$

The next level of stress ($\sigma_{Straicase,i+1}$) is depending on the result of the previous tested

specimen (i) (rupture or non-rupture):

- if the specimen (i) failed,
  then the $(\sigma_{Straicase,i+1})$ will correspond to $((\sigma_{Straicase,i}) - d)$

- if the specimen (i) did not fail at the fixed number of cycle (N),
  then the $(\sigma_{Straicase,i+1})$ will correspond to $((\sigma_{Straicase,i}) + d)$

This procedure is repeated until reaching the fixed number of tested specimens (n) (Dixon and Mood, 1948). In this study, the number of the tested specimens for each condition was fixed to 15.

2.5.2 Loading conditions

The fatigue tests of the drilled specimens were performed at ambient temperature and pressure in laboratory air with a load ratio R=0.1 and at a frequency equal to 20 Hz. Each specimen is exposed to cyclic loads at a predetermined magnitude of the applied stress (σ_a). A maximum fatigue life of 2.10^6 cycles was imposed. The stopping criterion was chosen to be the complete rupture of the specimen or achieving the imposed fatigue life (2.10^6).
As formerly highlighted, the strategy of fatigue experiments was to employ the staircase methods. At this line, the three kinds of batches are detailed below :

— Staircases of 15 specimens drilled under conventional condition;
— Staircases of 15 specimens drilled under LCO_2 condition;
— Staircases of 15 specimens drilled under LN_2 condition.

2.5.3 Estimation of the fatigue limit

The expression of the fatigue endurance limit σ_d and the the standard deviation s were elaborated according to the ASTM Special Technical Publication and the standard ISO 12107/2012 (ISO12107, 2012). They were assessed according to the following equations respectively:

$$\sigma_d = \sigma_0 + d * (\frac{A}{N} \pm \frac{1}{2}) \tag{V.2}$$

$$s = 1.62 * d * \{\frac{(N * B - A^2)}{N^2} + 0.029\} \tag{V.3}$$

- if the event the least frequent is the non-rupture: $+\frac{1}{2}$
- if the event the least frequent is the rupture: $-\frac{1}{2}$

σ_0: corresponds to the lowest value of stress, A and B are coefficients deduced from the standard.

It should be noted that the several analyses that will be presented in the next section namely the hole topology, the micro-hardness measurements as well as the microstructure damage were carried out using the specimens that were machined when the drills

were fresh in order to make sure that the tool wear effect is almost negligible. The aim of these analyses was to compare the influence of the cooling strategies (wet, LCO_2 and LN_2) on the surface integrity after drilling operations.
Fig.V.11 illustrates a schema highlighting the areas where the hole topology analyses were conducted (SEM analyses and areal roughness measurements), the cross sections along the cutting direction to observe the surface and subsurface damage and to perform the micro-hardness measurements

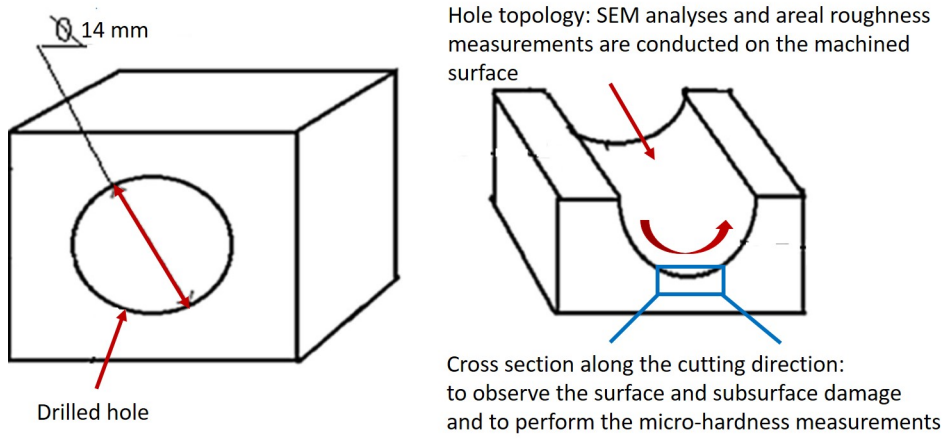

Figure V.11 – Illustration of a schema highlighting the areas where the hole topology analyses were conducted (SEM analyses and areal roughness measurements), the cross sections along the cutting direction (surface and subsurface damage observations and the micro-hardness measurements).

3 Results analysis and discussions

3.1 Stress-cycles: S-N curves

In order to estimate the endurance limit at 2.10^6 reference cycles of the studied material, the Staircase method was employed. The correspondent results are present in the Table V.6, Table V.7 and Table V.8 established respectively for three batches (wet, LCO_2 and LN_2).
O: unbroken specimen, X: broken specimen

Table V.6 – Staircase results of fatigue specimens drilled in wet condition

Specimen n°	2	3	4	5	6	7	8	9	10	12	13	14	15	16	17
σ_a=160 MPa				X		X						X			
σ_a=150 MPa			O		O		X		X		O		X		
σ_a=140 MPa		O						O		O				X	
σ_a=130 MPa	O														O

Table V.7 – Staircase results of fatigue specimens drilled in LCO_2 condition

Specimen n°	3	4	5	6	7	8	9	10	11	12	13	14	15	1	16	17
σ_a=150 MPa	X		X													
σ_a=140 MPa		O		X		X								X		X
σ_a=130 MPa					O		X				X		O		O	
σ_a=120 MPa								X		O		O				
σ_a=110 MPa									O							

Table V.8 – Staircase results of fatigue specimens drilled in LN_2 condition

Specimen n°	6	2	7	8	10	11	12	1	13	14	15	16	17	18
σ_a=120 MPa		X						X						
σ_a=110 MPa	O		X				O		X					
σ_a=100 MPa				X		O				X				O
σ_a=90 MPa					O						X		O	
σ_a=80 MPa												O		

An expected difference related to fatigue resistance could be noticed when examining the staircase results for the three batches. In general, the wet lot exhibited higher level of the applied stress σ_a. As for the LCO_2, this condition induced relatively lower of σ_a and more broken specimens. Nevertheless, LN_2 cooling condition reduced significantly the range of σ_a.
Staircase results are collected in the Stress-cycles (S-N) curves shown in Fig. V.12. The graph displays the fatigue performances of Inconel 718 as a function of cooling strategy of the drilled specimens.

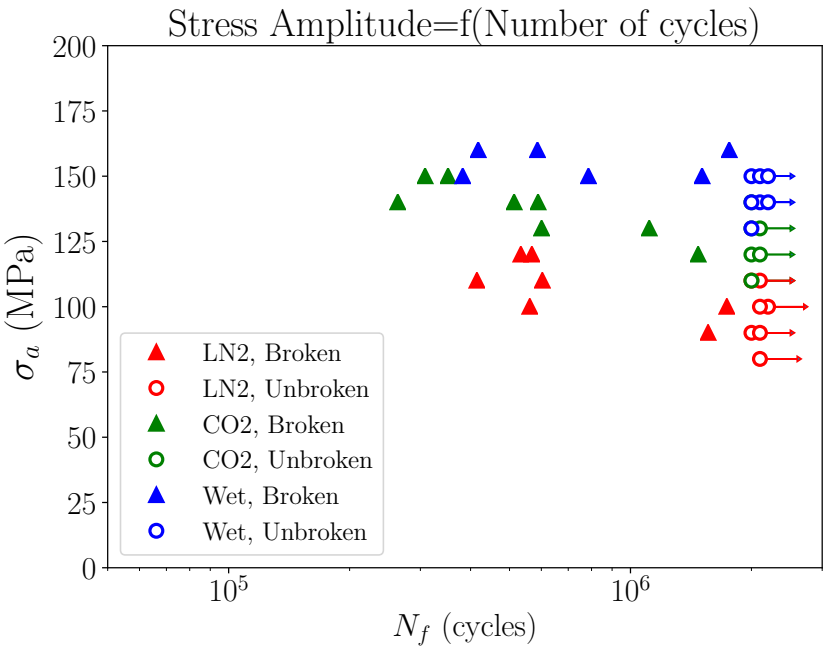

Figure V.12 – Illustration of Stress-cycle (S-N) curves showing the fatigue performances of Inconel 718 as a function of cooling strategy of the drilled specimens.

Results showed that wet condition exhibited the highest fatigue resistance compared to both cryogenic batches. In contrast, the LN_2 condition disclosed the lowest fatigue resistance in comparison with the LCO_2 drilled specimens. Furthermore, the wet lot displayed lower scattering with respect to the fatigue resistance compared to the LCO_2 condition. LN_2 condition exhibited the highest scattering regard to the stress amplitude applied. Conceivably, the fatigue life rises with decreasing the stress amplitude relatively to the studied cases.

At this level, it seems to be interesting mentioning the influence of tool wear on the fatigue results. Now, we will present only the state of tool wear after drilling the first 6 specimens (using fresh tools for each cooling strategy) in order to reveal the efficiency of the cooling strategies from the point of view of fatigue behavior. Fig. V.13 illustrated the tool wear state obtained under wet condition since all cooling conditions produced almost the same tool wear state after drilling the first 6 specimens.

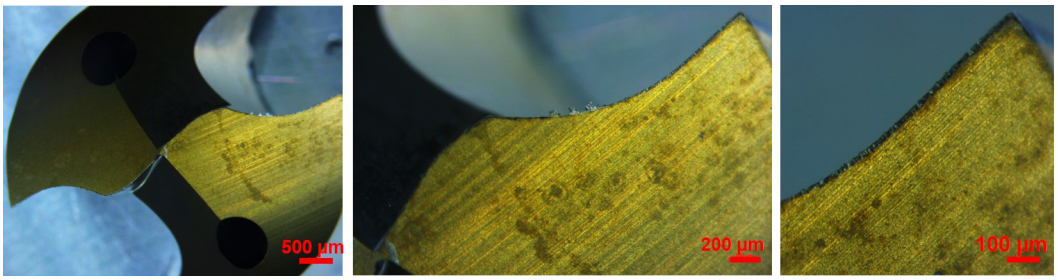

Figure V.13 – Illustration of tool wear state after drilling the first 6 specimens under wet condition.

Table V.6, Table V.7 and Table V.8 depicted the order of the drilled specimens and the correspondent applied stress previously evoked in section. 3.1. Since that the applied stresses σ_a differs from one lot to another, the tool wear effect seems not to be a great contributer to affect the fatigue strength, especially that the tool wear is very low. Effectively, in this context, Li et al. (2014) investigated the tool wear effect on fatigue strength of Inconel 718. Authors reported that tool wear effect is negligible with respect to fatigue limit when tool wear did not exceed V_B= 0.2 mm.
To more figure out the impact of tool wear, one has summarized the stress-cycle (S-N) curves presenting the fatigue performances obtained for each cooling condition as a function of the chronology of drilling the fatigue specimens. Fig. V.14 illustrated the correspondent curves. As it can be seen, under all cooling conditions, fatigue results revealed a random tendency with respect to the different batches (t1, t2, t3 and t4) that dislosed the chronology of the drilling process. In other words, the tool wear states (either new or unnew tools) have not affected the fatigue results especially that the gab was not significant enough to affirm that the tool wear state influenced the fatigue outputs obtained under the three cooling conditions.

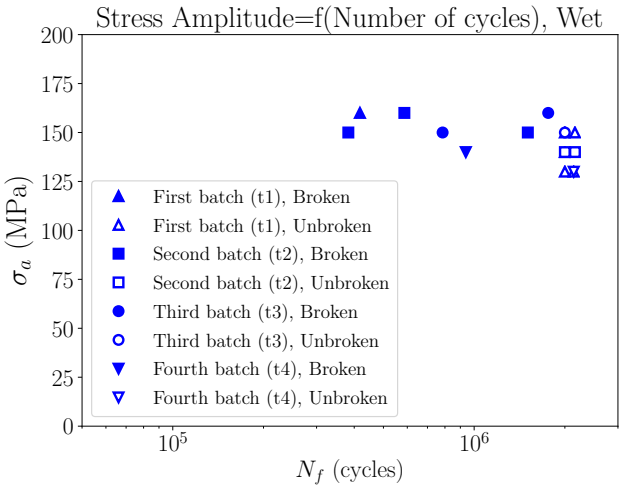

(a)

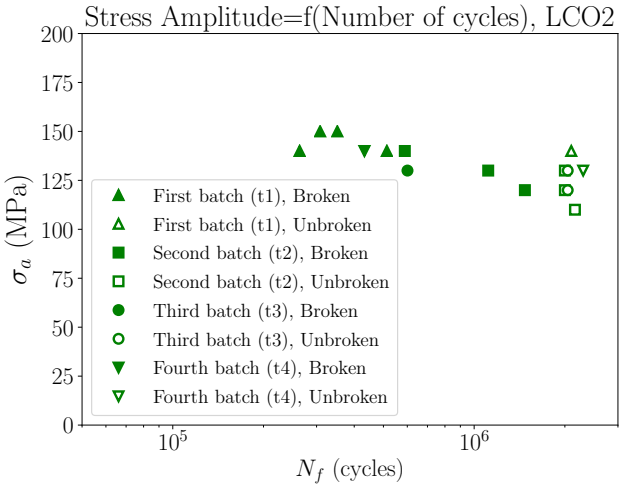

(b)

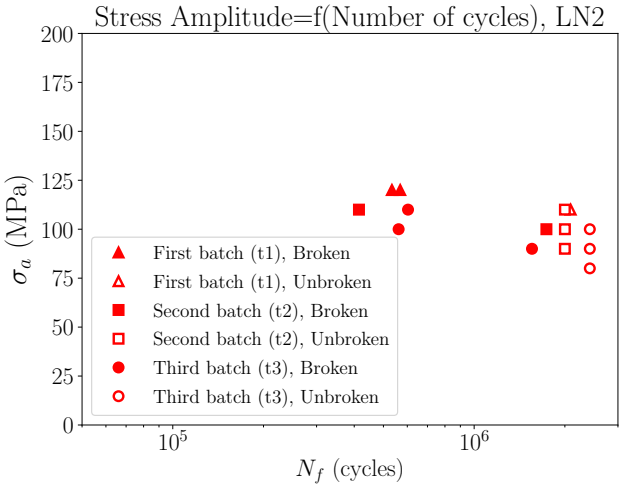

(c)

Figure V.14 – Illustration of Stress-cycle (S-N) curves showing the fatigue performances obtained for each cooling condition as a function of the chronology of drilling the fatigue specimens : (a) Wet; (b) LCO_2 and (c) LN_2.

The fatigue endurance limit σ_d is therefore calculated to well evaluate the cryogenic performance of the drilled specimens. Fig. V.15 illustrated the fatigue endurance limit as a function of the cooling strategy of the drilled specimens.

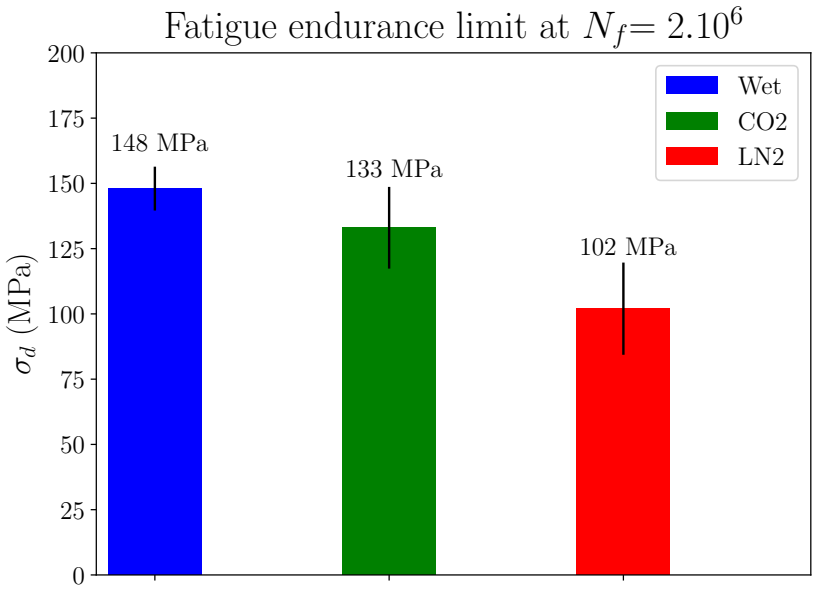

Figure V.15 – Illustration of the fatigue endurance limit as a function of cooling strategy of the drilled specimens.

The fatigue endurance limits σ_d (at 2. 10^6 of fatigue cycles) held 148 MPa, 133 MPa and 102 MPa respectively in wet, LCO_2 and LN_2 conditions revealing standard deviation of 8.4 MPa, 15.65 MPa and 17.66 MPa respectively. So that, cryogenic drilled specimens exhibited lower fatigue endurance limit compared to conventional lubrication revealing more than 10% of deterioration in the case of LCO_2 and around 30% in the case of LN_2. Although the postulate that the scatter when testing fatigue specimens continues to occur and requires too many specimens to be statistically accurate at best, it could be highlighted that the scatter of results might be strongly linked to the drilling process, in particular the cooling conditions. Such discrepancy will be investigated in the next sections.

The S-N curves indicate the fatigue behavior of the drilled specimens. Therefore, it was considered interesting to place these results with the literature review findings. However, there is no previous research that has dealt with the influence of the drilling process at high-cycle fatigue of Inconel 718 nor the effect on the cryogenic cooling strategies on fatigue strength. So that, to be consistent regarding the comparison issue with smooth specimens, the stress concentration factor K_t has been involved following the equation below since that the macroscopic behavior is considered linear (elastic regime) (Aman et al., 2017).

$$\sigma_{d,(smooth-specimen)} = K_t * \sigma_{d,(drilled-specimen)} \tag{V.4}$$

To compare with previous studies, a summary of literature review works has been established as displayed in Fig. V.16.

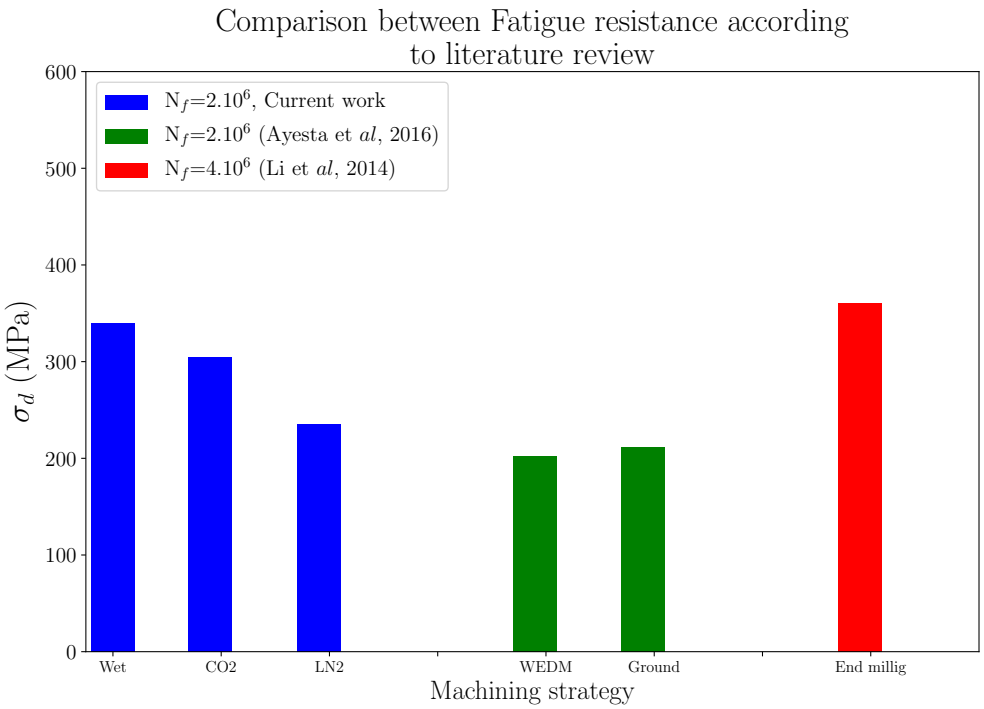

Figure V.16 – Illustration of the machining process effect on fatigue endurance limit reported in literature review (R=0.1).

Globally, the current results are well placed in comparison with literature review findings even if the variable parameters are quite different, notably the machining operation itself. As expected, the drilling operation may reduce notably the fatigue strength since that the hole presents a major source of stress concentration inducing a drop of fatigue limit.
Ayesta et al. (2016) reported the High Cycle Fatigue behavior of WEDM-manufactured and ground specimens of Inconel 718. Authors found that the machining operation may affect the fatigue resistance where ground specimens disclosed 10 % higher compared to WEDM specimens. Indeed, the WEDM-manufactures specimens exhibited high residual tensile stress, surface roughness and microcracks generated in the surface contributing to decreasing the fatigue strength, especially at high-cycle fatigue regime. It should be noted that the ground specimens were polished at the lateral faces. Therefore, the surface roughness disclosed lower values compared to the WEDM specimens.
At the same line, Li et al. (2014) investigated the end-milling influence on the fatigue life of Inconel 718, in particular the tool wear effect. The fatigue tests showed that the four milled samples (tool wear up to V_B= 0.2 mm) did not fail within 4.10^6 cycles in four point bending fatigue testing condition. At this point, one question could be arisen that consists in the number of the tested specimens was not sufficiently representative to evaluate the fatigue behavior of the end milled specimens since that the heterogeneity of the materials is a detrimental factor to affect the reliability of the fatigue outputs.
In this present work, 45 specimens were employed in order to estimate at best the fatigue resistance for the drilled specimens according to the staircase method. The latter is the most efficient approach to characterize the fatigue behavior of metallic materials when the number of the tested specimens are minimized. For each tested batch, one must at least employ from 10 to 15 specimens in order to ensure reliable results (Abroug et al., 2018).

3.2 Hole topology

Hole topology could be a great contributor to the reduction in fatigue life due to surface irregularities and defects generated from the machining process such as grooves, cracks, and debris (Yin et al., 2020).

3.2.1 Surface topology : SEM observations

In this section, SEM observations have been carried out in order to identify the surface topology of the drilled holes under all cooling conditions. Therefore, one could extract additional information to explain the difference obtained with respect to fatigue behavior. Fig.V.17 depicted the surface topology of the drilled specimen obtained in wet condition.

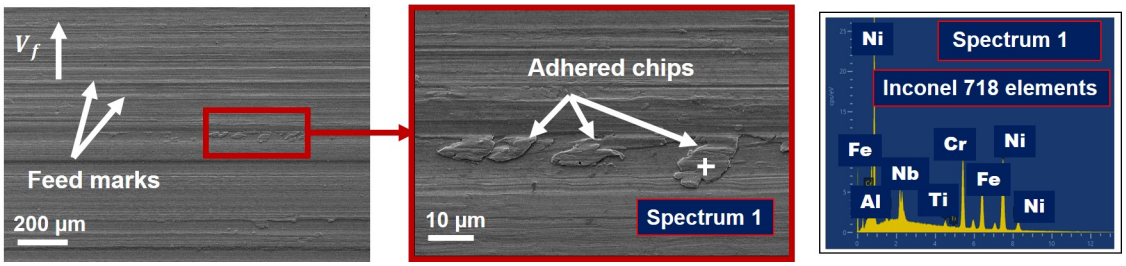

Figure V.17 – Topology of the drilled specimen under wet condition using SEM.

The machined surface of the drilled specimen obtained under wet condition revealed a typical state in terms of feed marks except the presence of some adhered particles. To recognize these particles, EDS analysis was conducted and have shown that the chemical composition consisted of the work material elements. These features are commonly observed when machining Inconel 718 (Axinte et al., 2006). In the LCO_2 condition, additional features were observed as displayed in Fig. V.18.

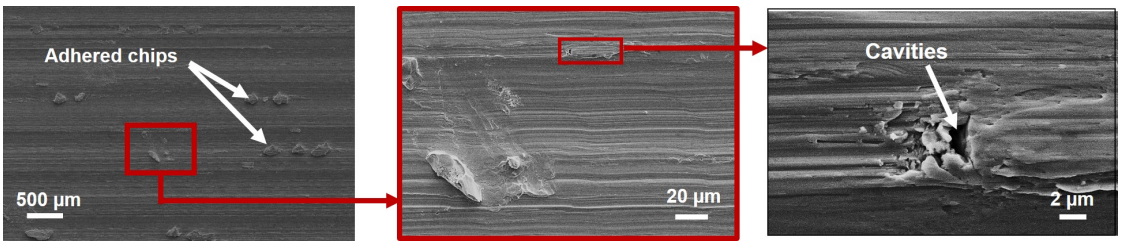

Figure V.18 – Topology of the drilled specimen under LCO_2 condition using SEM.

Apart from the adhered chips, micro-cavities were present on the machined surface of the LCO_2 drilled specimen. These defects have an adverse effect on the fatigue behavior as they are propitious to stress concentration. Yin et al. (2020) reported that the micro-pores are essentially monitored by the carbide particles of the work material, build-up edge (BUE) stuck on the tool tip as well as the adhered chips. Authors added that the formation and the plucking of the BUE results in destabilizing the cutting

process and thus deteriorating the surface morphology.
As for the LN_2 surface morphology of the drilled specimen, much poorer surface finish has been observed revealing huge amount of adhered material on the surface in addition to the smearing. The latter may occur due to high plastic deformation caused by squeezing action between the auxiliary flank face of the tool and the machined surface during the progression of tool (Thakur and Gangopadhyay, 2016).

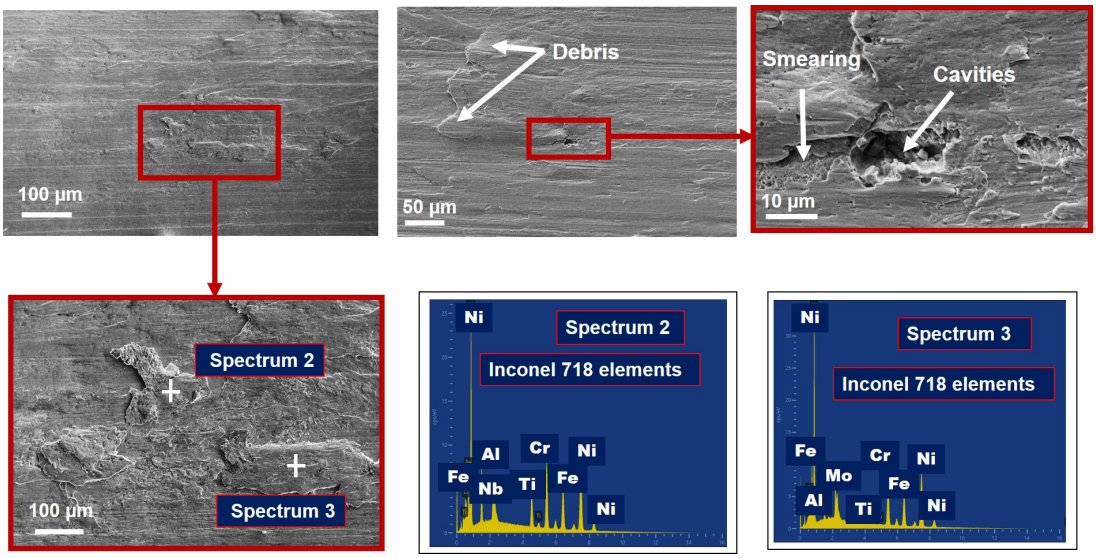

Figure V.19 – Topology of the drilled specimen under LN_2 condition using SEM.

It could be further observed that the LN_2 configuration disclosed larger cavities across the machined surface with a size around 10 μm. Indeed, the surface damage is much more severe by the occurrence of bigger cavities on the machined surface which has in general prominent influence on fatigue strength of the drilled specimens. This observation is closely in agreement with the current results since that the poorest machined surface topology obtained in the LN_2 configuration correspond to the lowest fatigue resistance.
Concerning the presence of accidental machining defects on the machine surface (such debris, smearing and cavities) in processing Inconel 718, it might be interesting to optimize as possible the cutting conditions (cutting parameters, tool cutting, cooling strategy) in order to reduce their effects on fatigue resistance as they present a potential danger over the life of the components.

3.2.2 Areal parameters

Surface irregularity induced by machining process affects the fatigue resistance. Classically, the surface roughness R_a is the most commonly considered when characterizing the fatigue behavior of machined components (Sun et al., 2016). However, this parameter do not reflect the state of the surface topography if the machined surfaces exhibit heterogeneity. Effectively, according to the SEM observations that were just presented, the machined surfaces obtained after the drilling operation under all cooling conditions revealed debris as well as cavities randomly distributed on the surface. Therefore, one is interested to measure the areal surface parameters namely the average areal roughness S_a in addition to the total areal roughness S_q.
Using the Brucker profilometer, scan analyses of the holes drilled under wet, LCO_2 and LN_2 cooling strategies have been conducted. Fig. V.20 displayed the correspondent analyses.

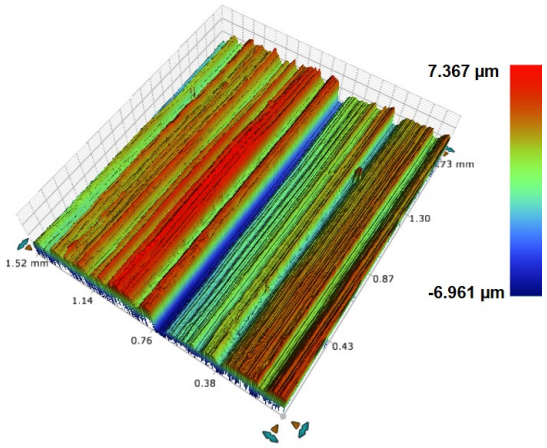

(a)

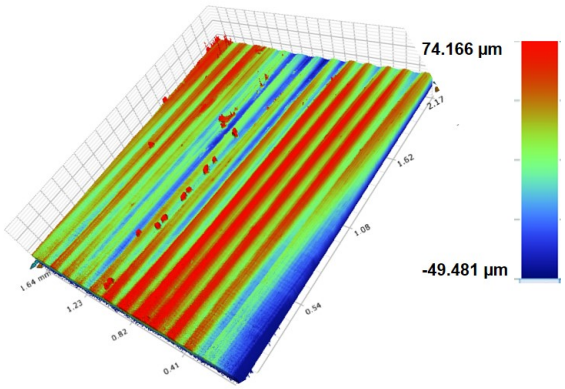

(b)

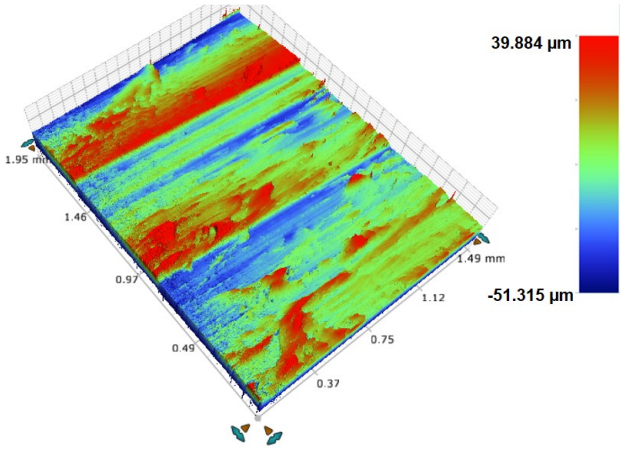

(c)

Figure V.20 – Surface topgraphy scanned using the Brucker profilometer of the drilled specimens under all cooling strategies : (a) Wet; (b) LCO_2 and (c) LN_2.

Table V.9 sets out the areal parameters assessed using the profilometer equipment.

Table V.9 – Areal parameters evaluated from the profilometer analyses

	Wet	LCO_2	LN_2
S_a (μm)	1.47	1.42	2.03
S_q (μm)	1.85	1.8	2.63
σ_d (MPa)	148	133	102

Results showed that the S_a and S_q revealed similar values in both configurations wet and LCO_2. Nevertheless, LN_2 cooling strategy exhibited the highest values of S_a and S_q inducing a damage of 38 % and 42 % respectively in comparison with the wet condition. In this context, Novovic et al. (2004) have examined the effect of surface topography generated from machining process on fatigue performance. Authors reported that for a critical range of lower roughness leads to longer fatigue life. Similar finding has been pointed out by (Sun et al., 2016). Sun et al. (2016) have studied the fatigue performance of titanium drilled samples showing that the decrease in fatigue life is most likely caused by the poor surface integrity of the workpiece. They have estimated that this statement was essentially related to the rougher surfaces which may provide stress concentrations causing fatigue crack initiation sites, and thereby reduction in fatigue limit.
Overall speaking, the fatigue result obtained for the three fatigue batches seems to be consistent with the areal roughness measurements. Indeed, the smoother is the topography of the drilled specimens, the higher was the fatigue resistance. At this line, a correlation between the measured areal parameters (S_a and S_q) and the fatigue limits of the three fatigue batches was established in order to figure out the link between these parameters and the fatigue limits.
It can be deduced that the areal surface parameters could exhibit a correlation with the fatigue resistance. Obvious tendency might be observed when examining the results illustrated in Table V.9: the lowest values of S_a and S_q experienced in the case of wet and LCO_2 batches correspond with the highest values of fatigue resistance achieved in the same configurations. In contrast, LN_2 configuration that revealed the lowest fatigue resistance induced the worst surface topography in terms of S_a and S_q. This finding is in total agreement with (Holmberg et al., 2021).

3.3 Microhardness profiles

The micro-hardness profiles in depth of the affected layer near the sample surface have been measured on the cross-sections and are compared with the micro-hardness of the raw material. Results are given in Fig. V.21.

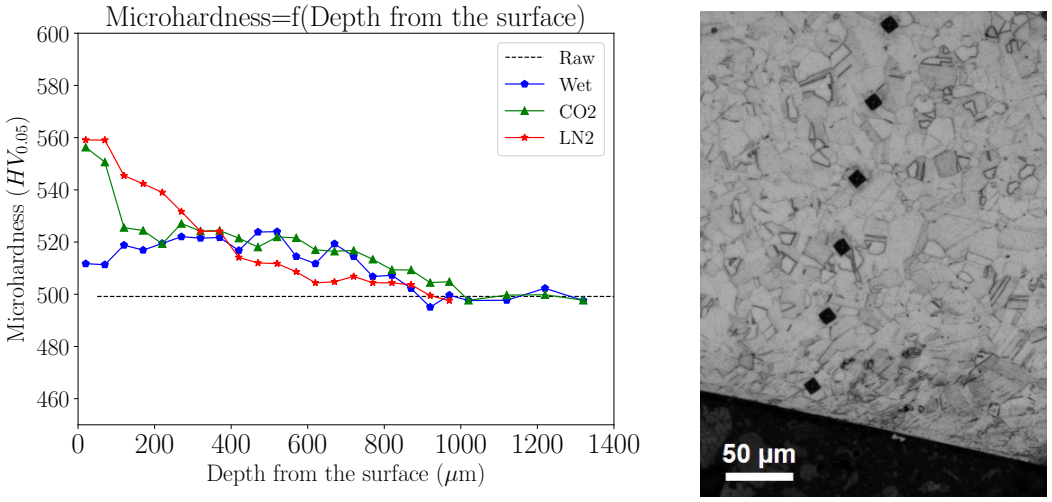

(a) (b)

Figure V.21 – (a) Illustration of micro-hardness profiles of drilled specimens under all cooling machining strategies; (b) Illustration of the correspondent indentations of the micro-hardness profiles.

Both cryogenic conditions showed higher values of microhardness close to the surface than the conventional condition. Compared with the raw material, both cryogenic approaches revealed higher values of almost 60 $HV_{0.05}$ near the surface (12 %) whereas wet condition induced only 10 $HV_{0.05}$ when comparing with the raw material microhardness. This could be explained by the fact that higher machining forces are induced when using cryogenic fluids and therefore causing more severe mechanical deformation (Pusavec et al., 2011). Concerning the fatigue behavior of the current studied cases, it could be assumed that the cryogenic temperature induced harder work material and probably acquiring brittle behavior. Consequently, the fatigue resistance seems to be adversely affected. This tendency is reflecting quite well the fatigue resistances obtained in wet, LCO_2 and LN_2 batches. Nevertheless, one question arise concerning the appropriateness of relying solely on this parameter. Indeed, as previously mentioned, both cryogenic conditions induces similar results regard the micro-hardness. In contrast, the fatigue resistances are significantly different even if they showed lower values compared to the wet batch. For these reasons, it is worth excavating further to explain the origins of the fatigue behavior difference.

3.4 Surface and subsurface damage

As well known that the drilling operation is a confined area, the work material is subjected to high mechanical and thermal loads which may affect the microstructure of the workpiece material at the surface and the subsurface. Therefore, SEM observations of the machined surface and subsurface of the drilled specimens have been conducted on the cross-section along the cutting direction for the three cooling conditions. The main target of these analyses is to figure out if the several cooling strategies revealed any difference in terms of microstructure alterations.
Fig. V.22 illustrated the microstructure damage of the cross section of the drilled fatigue specimens under wet condition.

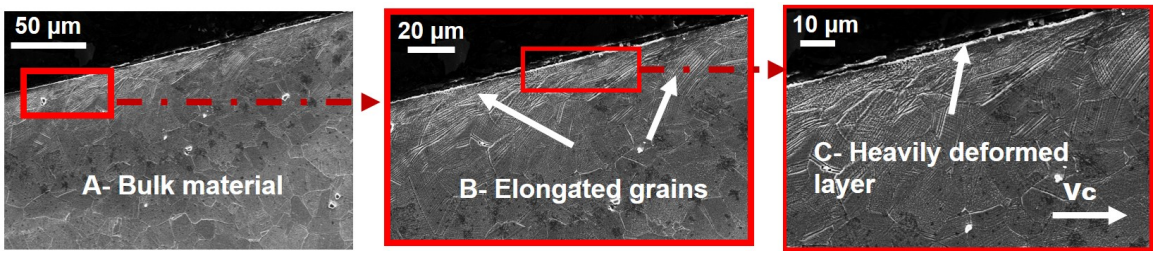

Figure V.22 – Surface and subsurface damage of cross section of the drilled fatigue specimens under wet condition.

As it can be observed that the affected layer induced during the drilling process revealed three typical zones (Imran et al., 2015):

- Zone A: a non modified microstructure known as the bulk material;
- Zone B: a deformed zone reveals the elongation of the grains along the cutting direction;
- Zone C: a severe plastic deformation SPD much higher than the one obtained in the previous zone where the grains undergo a drastic deformation.

As for the LCO_2 condition, the affected layer exhibited thicker SPD layer in comparison with the previous condition in addition to cracked carbides present close to the machined surface as displayed in Fig. V.23.

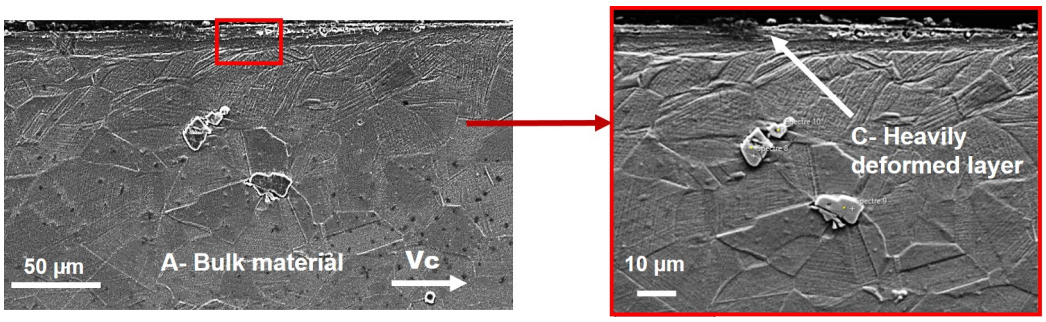

Figure V.23 – Surface and subsurface damage of cross section of the drilled fatigue specimens under LCO_2 condition.

Anterior study have reported that the white layer experienced in the machined surface could be very harmful with respect to fatigue resistance (Guo and Schwach, 2005).

Authors pointed out that the samples that did not exhibit a white layer are much more able to hold out against fatigue crack initiation and propagation. Hence, longer lifetime were obtained in comparison with the ones that presented white layer.
Concerning the LN_2 drilled specimen, apart from the typical zones that were observed under all cooling conditions, additional features were present at the vicinity of the machined surface. Fig. V.24 shows the correspondent observations that were depicted.

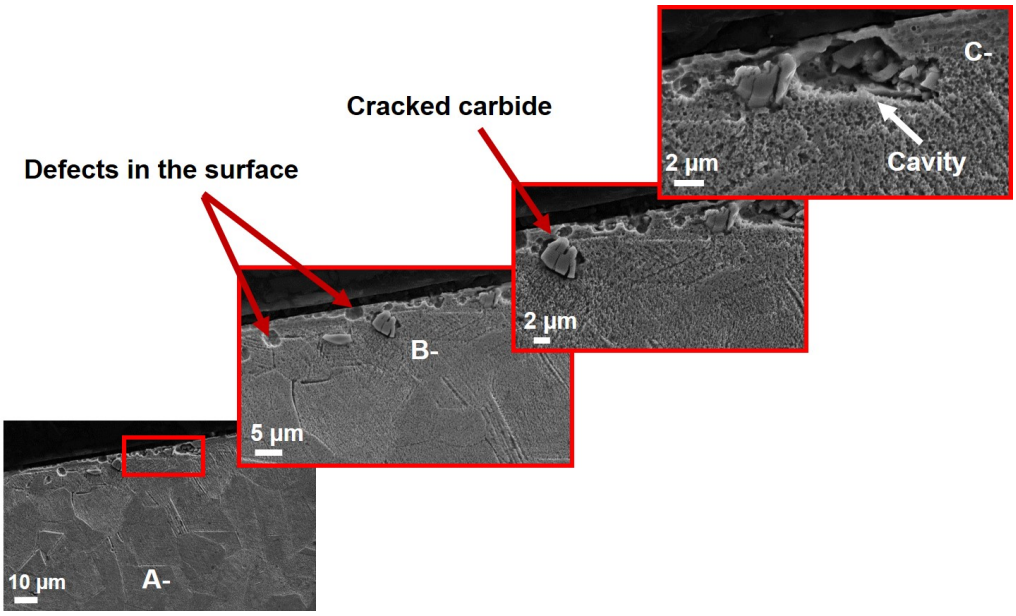

Figure V.24 – Surface and subsurface damage of cross section of the drilled fatigue specimens under LN_2 condition.

Remarkable defects existed very close to the machined surface for instance cracked carbides in addition to frequent cavities were generated in the LN_2 machining strategy. Such defects are obviously source of stress concentration causing the reduction of fatigue life. In this context, some previous studies found that local defects especially the ones present at the vicinity of the sample surface affects negatively the fatigue strength of the component (El Khoukhi et al., 2019).

Overall speaking, the heterogeneity (defects, cavities, cracked carbides) observed along the cross section of the drilled specimens microstructure in the case of LN_2 cooling strategy is probably the key factor the explain the degradation of the fatigue strength obtained in the LN_2 case. In other words, there are greater stress concentrations present on the machined surface caused by the previously mentioned features which likely resulted in fatigue crack nucleation sites, and thereby a subsequent drop in fatigue life of the samples. Nevertheless, the microstructural observation carried out in the case of wet as well as LCO_2 drilled specimens have shown almost the typical aspects induced during machining process namely plastic deformation in the subsurface and relatively thin layer. Both conditions resulted in less affected material microstructure which seems to give rise to longer fatigue life of the drilled specimens.

In the next section, to figure out the influence of the different cooling conditions of the drilled fatigue specimens, an investigation regard the fractographies analyses is developed.

3.5 Fractography of broken fatigue specimens

To export additional information helping to identify the origin of the fatigue endurance limits difference revealed in the S-N curves, it is worth examining the failure surfaces of the broken fatigue specimens. Table V.10 summarizes the broken specimens outputs for the three kinds of batches whose failure surface will be presented in this section.
It is important to highlight that the main target of this investigation consisted in identifying the crack initiation sites for the three kinds of batches and try to explain the difference of fatigue limit observed.

Table V.10 – Summary of the broken specimens outputs for the three kinds of batches whose failure surface will be presented in this section

Cooling Conditions	Wet	LCO_2	LN_2
σ_a=160 MPa	586 775		
σ_a=160 MPa	1.76 10^6		
σ_a=130 MPa		600 883	
σ_a=130 MPa		1.11 10^6	
σ_a=120 MPa			533 534
σ_a=100 MPa			1.73 10^6

It was relevant to show the fractographies of the failed specimens with the correspondent criterion. For each lot, the applied stress was fixed and the cycles to failure range: short fatigue life (around 600 000 cycles) and long fatigue life ($> 10^6$) will be presented. So that, the crack initiation sites could be distinguished depending on the fatigue life range for each batch.
However, in the LN_2 case, this condition was not possible to fulfill since that the scatter was too high to show fracture surfaces of broken specimens subjected to the same applied stress inducing respectively short and high fatigue lives.
The fractography observation have been conducted using the SEM equipment. Obviously, crack initiation for the failed specimens took place from the drilled hole edges as displayed in Fig. V.25.

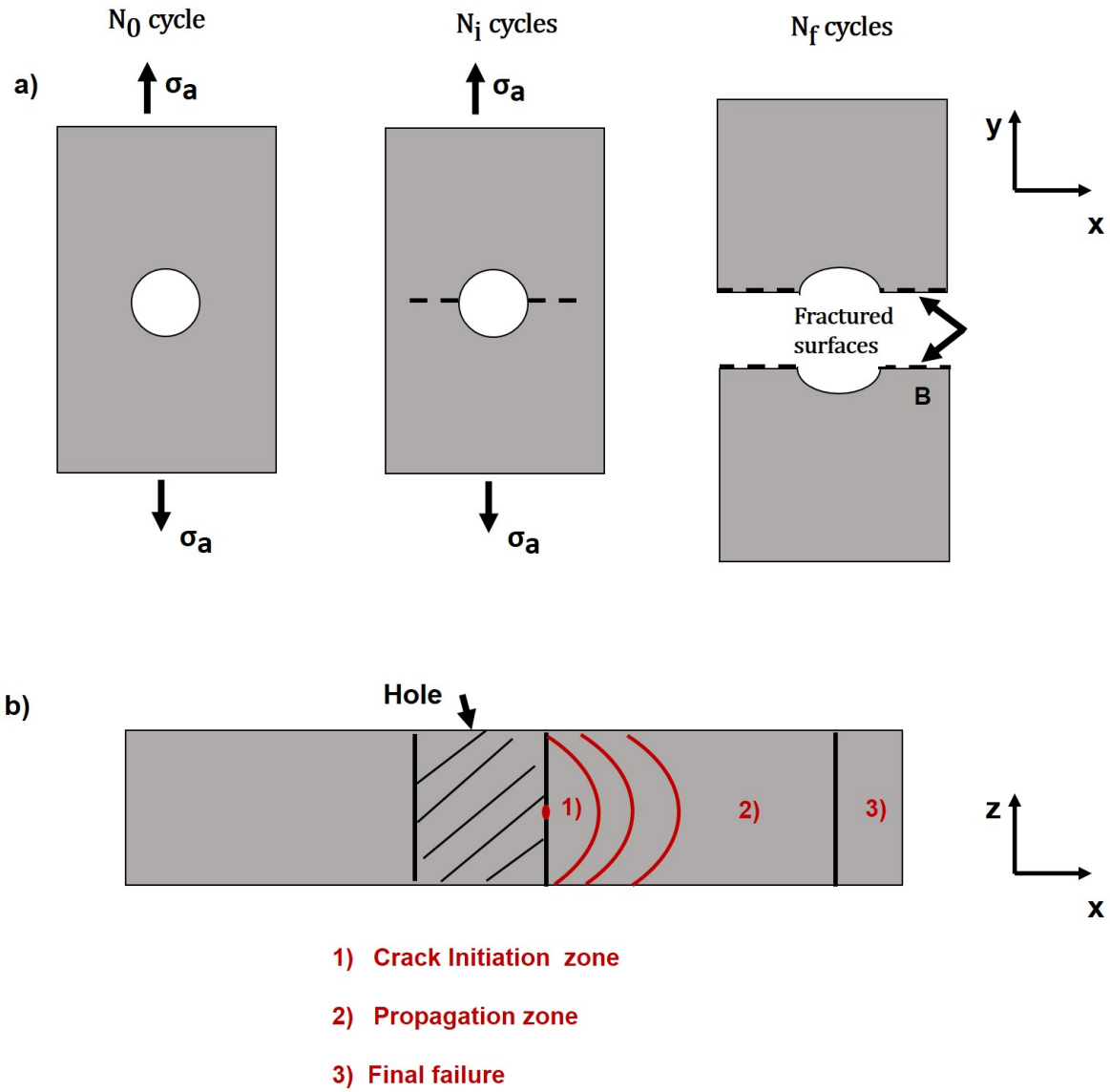

Figure V.25 – Illustration of the fatigue steps site at the macroscopic scale : (a) in the plane (xy); (b) in the plane (xz).

A general observation that could be mentioned is that the fractured surfaces (regardless of the cooling condition) are essentially composed of two specific characteristics :

— Fatigue zone revealing smooth surface induced during the fatigue loading cycles;
— Final failure or the catastrophic rupture exhibiting a rough surface.

Basically, apart from the work material or the loading conditions (loading, loading ratio, specimen geometry...), the rupture by fatigue exhibits three phases namely (Fig. V.25.b):

1. Crack Initiation phase: Germination and growth of multiple micro-cracks, their coalescence resulting in the formation of a macro-crack;
2. Propagation phase: The macroscopic crack propagates according to the laws of fracture mechanics;
3. Final failure phase: The final break comes abruptly. The crack is spreading and the straight section tore off.

In this work, the attention is dedicated essentially to the crack initiation phase as the comparative study focused on the effect of the drilling process on the fatigue limit. Fig. V.26 shows the fractography of the broken specimen (n°7) obtained in wet condition. The specimen was subjected to σ_a=160 MPa inducing a fatigue life of N_f= 586 775.

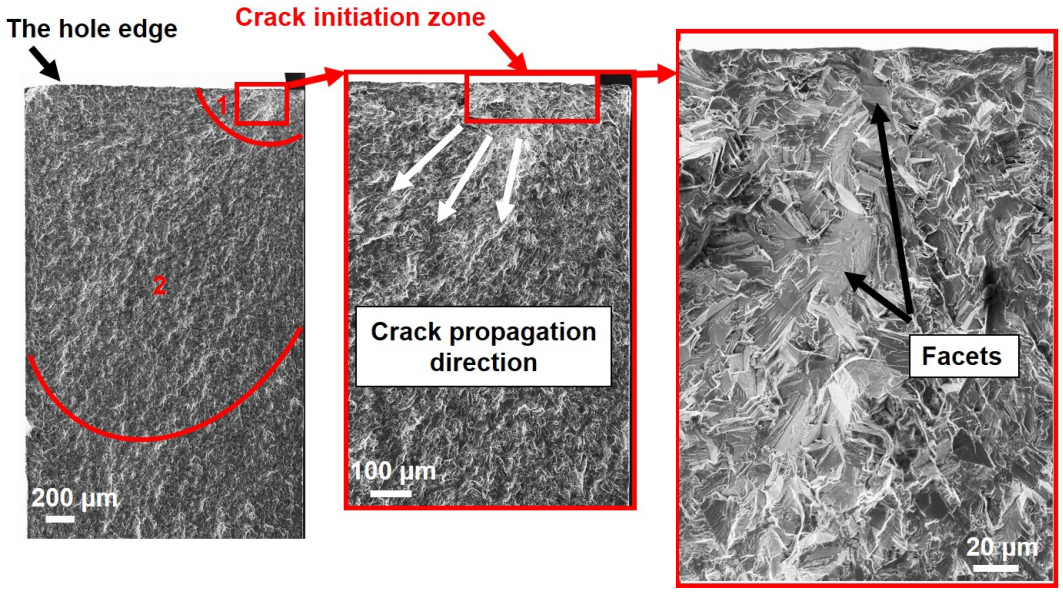

Figure V.26 – Illustration of the fractured surfaces of the broken specimen n°7 drilled in wet condition (N_f= 586 775, σ_a=160 MPa).

It can be seen that the fatigue cracks initiated near the specimen surface where faceted structures were observed around the crack initiation site. The facet could be induced either by the grain boundary decohesion (intergranular) or the accumulation of the local plastic fatigue deformation inside the grain (intragranular) leading to fatigue crack initiation.
In this context, Price and Kunc (1986) have extensively studied the occurrence of faceted fatigue fractures in nickel superalloys. They have reported that the main conditions of the facets structrure of fatigue fracture are not only the coarse grain size and thin sections but also low stress levels with respect to the yield stress. The latter condition seems to be convenient with this study case since that the loading stress levels are too low compared to the yield stress of the work material.
Currently, the majority of manufacturing processes induce defects that promote the fatigue crack initiation namely porosities and inclusions. Indeed, such features provide stress concentration inducing the crack initiation and thereby the propagation causing the material failure as reported in (Qian et al., 2020). Therefore, EDS analyses were carried out in order to identify if these features exist in the initiation site close to the surface and in the subsurface.
Fig. V.27 illustrates the EDS analysis that has been conducted on the fractured surface of the specimen n°7 at the vicinity of the surface as it was assumed that the crack initiation sites took places very close to the surface (around the facets structures). It can be observed that the several analyzed zones proved that neither inclusions nor strange particles such as oxide particles have been detected. This finding might confirm that the facets play major role for the crack initiation.

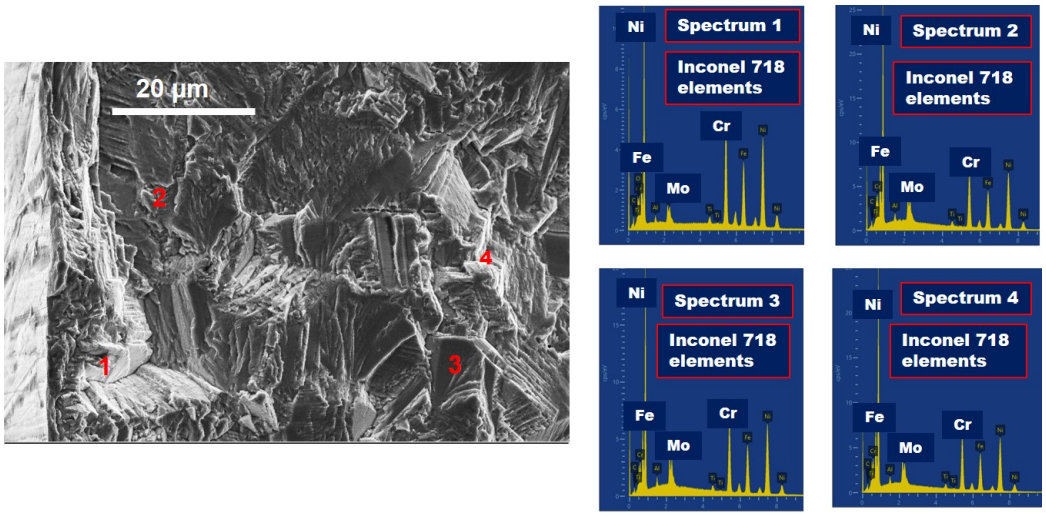

Figure V.27 – Illustration of the EDS analysis conducted on fractured surfaces of the broken specimen n°7 drilled in wet condition (N_f= 586 775, σ_a=160 MPa).

At the same line, Forsman (2012) figured out when examining the fracture fatigue mechanisms of Inconel 718 that casting defects has not been found to initiate cracks at any testing temperature. In contrast, facet initiations prevailed the crack initiation sites at room temperature and high temperature as well.

Subsequently, an observation of the fracture surface of a broken specimen that underwent the same loading conditions as the previous one. However, the achieved cycles number to failure was significantly higher (N_f= 1.76 10^6). Fig. V.28 figured out the correspondent results.

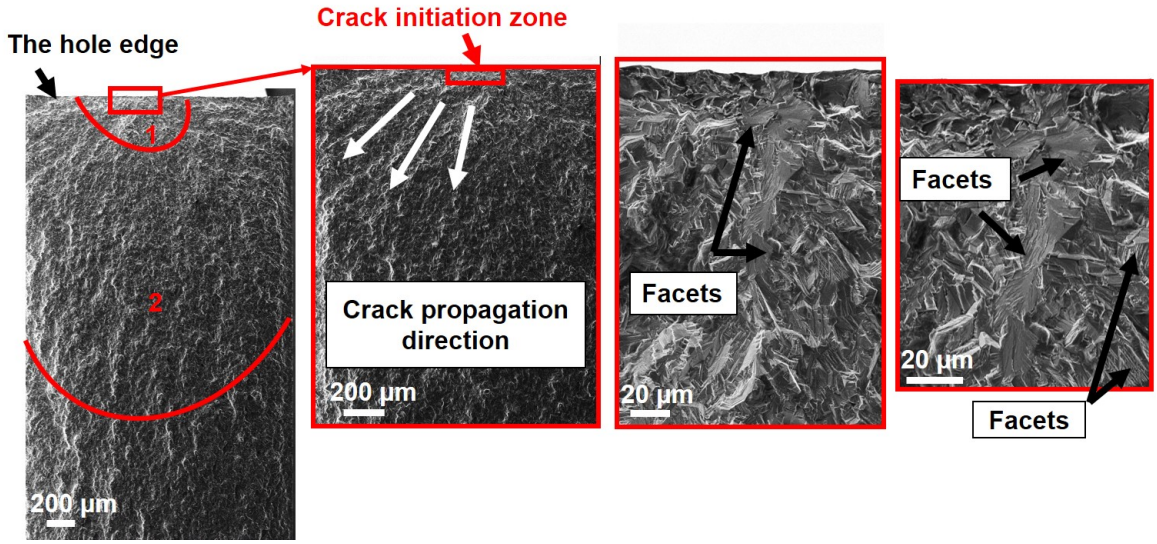

Figure V.28 – Illustration of the fractured surfaces of the broken specimen n°14 drilled in wet condition (N_f= 1.76 10^6, σ_a=160 MPa).

It can be observed that even at higher cycle fatigue life, similar observations could be depicted. Indeed, very close to the surface, facets structures were identified. The facet surfaces that initiated the crack are probably triggered from coarse grain size as illustrated in the Fig. V.28. The larger facet surface seems to be the true initiation

point as the identification of the crack initiation sites are essentially recognized by the tear ridges. When examining the tear ridges propagation, it was judging that these features derived from the larger facet surface located very close to the hole edge.

For the LCO_2 broken specimens, Fig. V.29 illustrated the fractured surfaces of the specimen n°13 that was subjected to 130 MPa of σ_a inducing N_f= 600 883.

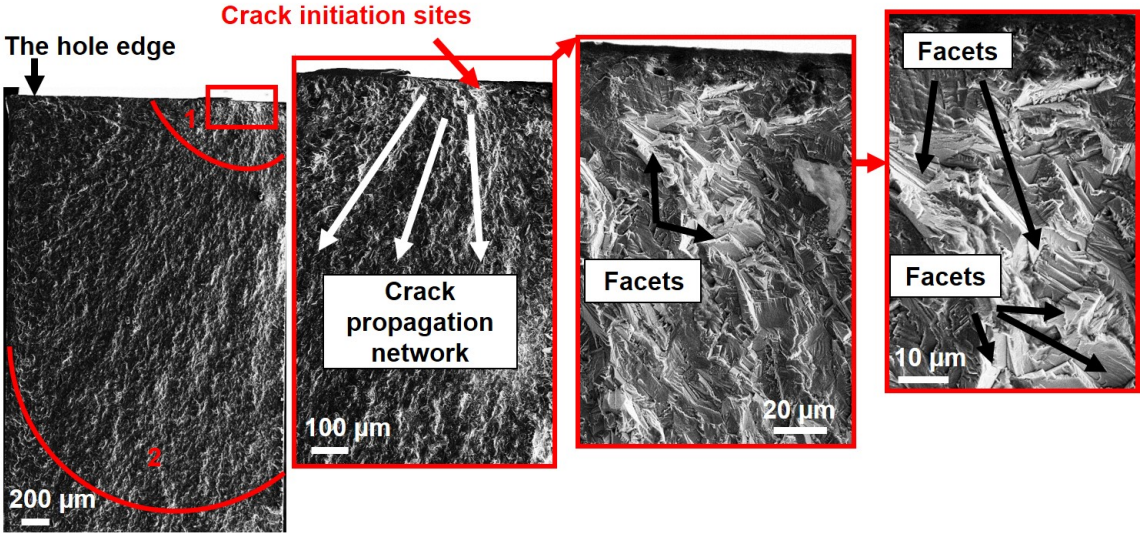

Figure V.29 – Illustration of the fractured surfaces of the broken specimen n°13 drilled in LCO_2 condition (N_f= 600 883, σ_a=130 MPa).

It can be deduced that the LCO_2 broken specimen case seems to be very similar to the previously described fractographies revealed in the wet condition. Relying on the Fig. II.2, one could judge that the crack initiation sites are localized in the facet structure. Indeed, crack initiation sites have been assumed to be dominated by facet initiations due to locally some small deformation occurring during each load. Basically, fatigue fracture could take place at very low magnitudes of stresses where the response of material towards applied loads is assumed to be elastic. In a macroscopic manner, this elastic approximation is completely true, but locally some small deformation must occur during each single load cycle. These deformations, even if small, are further added as long as more cycles are applied until causing the failure.

The study of the fatigue fracture surfaces of the broken specimen n°9 drilled in LCO_2 condition (N_f= 1.11 10^6, σ_a=130 MPa) displayed an initiation appearing typically at faceted structure characterized by smooth surfaces (Fig. V.30). Even at higher fatigue life cycle (and the same level of stress amplitude), the crack initiation sites have been seen again to be governed by facet structures where the accumulation of the plastic deformation contributed significantly to promote crack nucleation (Waqas Tofique et al., 2016).

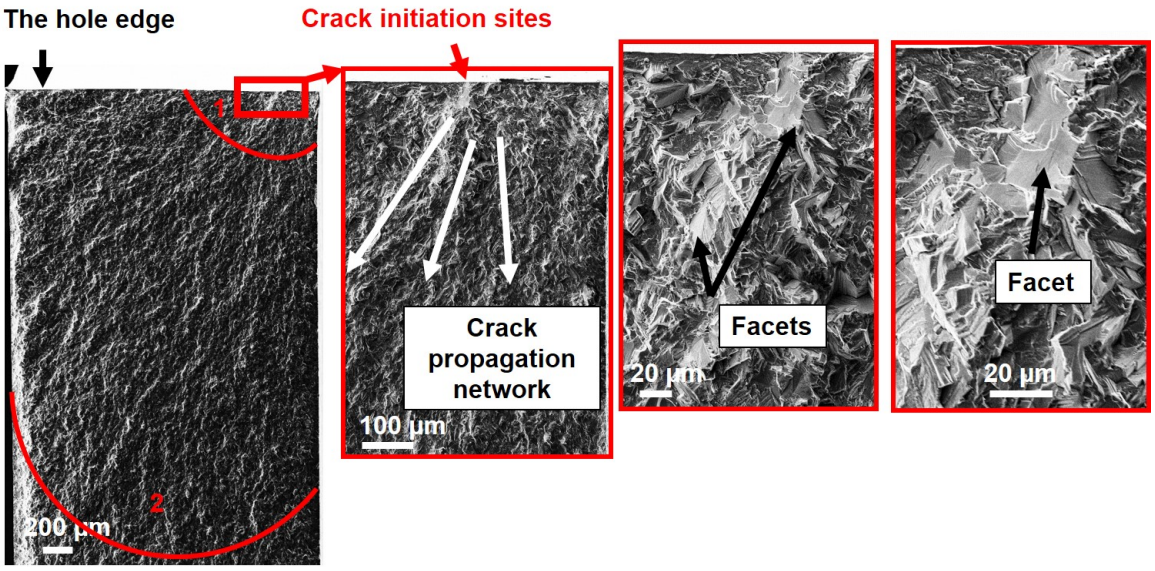

Figure V.30 – Illustration of the fractured surfaces of the broken specimen n°9 drilled in LCO_2 condition (N_f= 1.11 10^6, σ_a=130 MPa).

At the same line, Ma et al. (2010) examined the fatigue and fracture surface of nickel based superalloy Inconel 718 up to the very high cycle regime under rotary bending tests at room temperature. Authors proved that with a low stress level, the most easily way of the facets formation can be induced by the localized plastic deformation during crack nucleation.

Noted that the most of the investigated broken specimens (either wet or LCO_2 batches) were found to reveal that most of the crack sites initiated at the hole edge (the surface) or in the subsurface (very close to the surface) where the initiation sites had a facet like appearance. In close to all studied cases, the initiations sites had a very comparable appearance which implies that the initiation mechanisms are likely also analogous.
It is worth to point out that the determination of the exact initiation sites is however difficult. In some cases, it was hardly discernible to identify the true sites of the crack nucleation. Therefore, complementary EDS analyses were performed on additional broken specimen n°8 drilled in LCO_2 condition (N_f= 588 758, σ_a=140 MPa). This investigation may help to examine some zones that would be susceptible to initiate cracks. Results are shown in Fig. V.31.

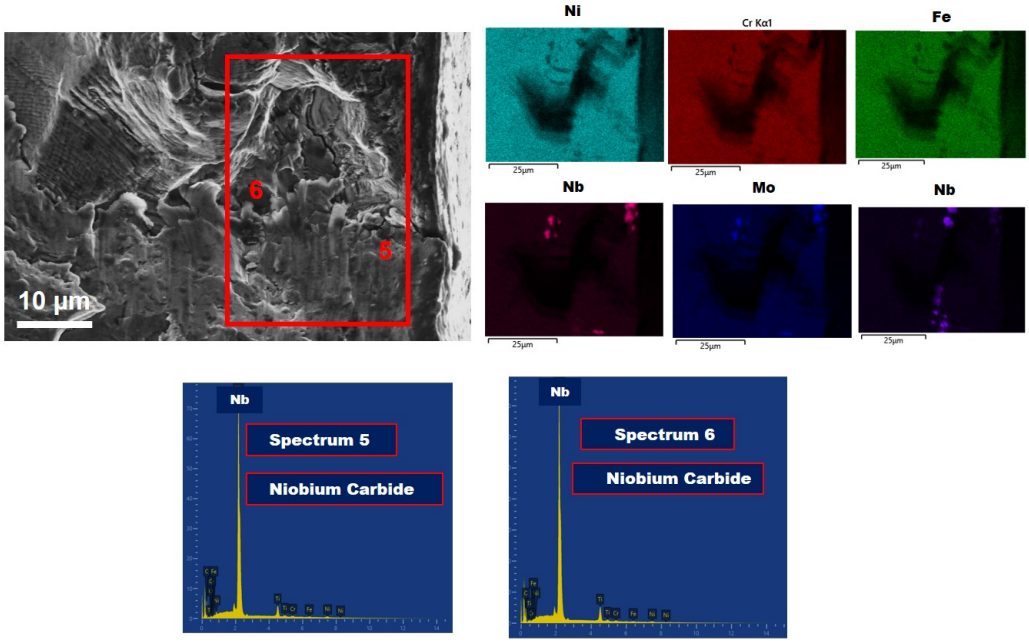

Figure V.31 – Illustration of the EDS analyses conducted in the fractured surfaces of the broken specimen n°8 drilled in LCO_2 condition (N_f= 588 758, σ_a=140 MPa).

EDS analyses displayed that NbC carbide could be as well the source of crack nucleation of Inconel 718 under fatigue load. These particles are brittle and might be the cause of crack nucleation. In this context, Ono et al. (2004) reported that fatigue cracks initiation sites have been found to occur near the specimen surface. Authors figured out that facet structures in addition to coarse NbC carbides were observed around the crack initiation sites depending on the stress level applied.

Concerning the third lot namely the broken specimens drilled under LN_2 condition, fractographic analyses revealed a drastic difference with respect to the fatigue crack initiation regions in comparison with the previous cases. Fig. V.32 showed the fractured surface of the broken specimen n°2 drilled in LN_2 condition inducing N_f= 533534 when the applied stress level σ_a was equal to 120 MPa.

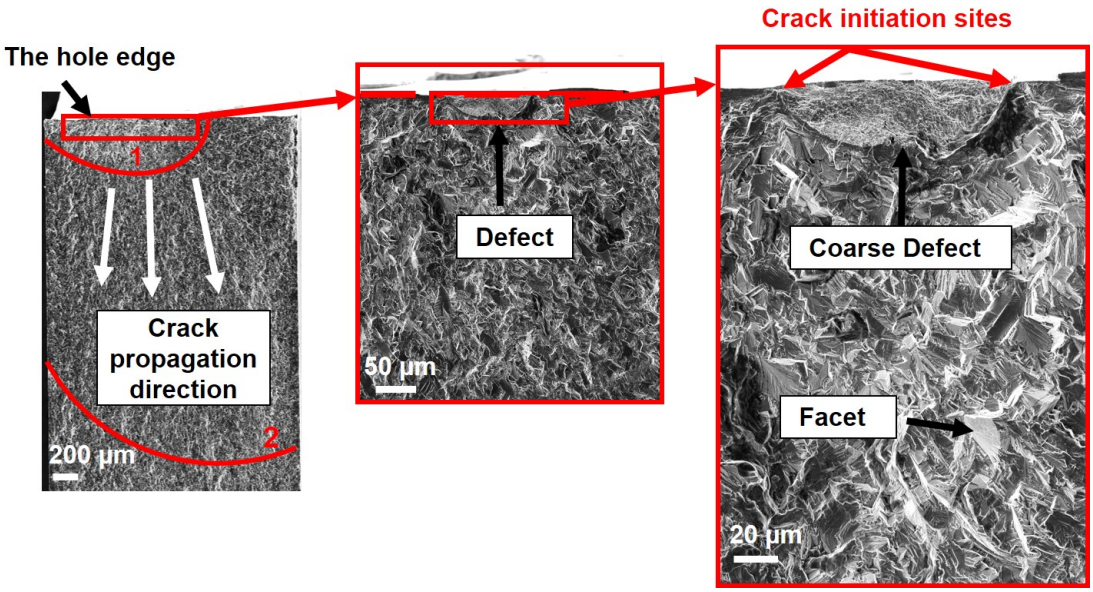

Figure V.32 – Illustration of the fractured surfaces of the broken specimen n°2 drilled in LN_2 condition (N_f= 533 534, σ_a=120 MPa).

Obviously, it can be seen that fatigue cracks initiated near the specimen surface. As illustrated in Fig. V.32, it might be judged that the crack source region preferentially initiated from the coarse defects. Such defects are likely generated during the drilling process under LN_2 cooling condition. The large defect existing near to the surface observed in the LN_2 drilled specimen considerably shortens its lifetime. It has been extensively recognized that fatigue resistance is sensitive to defect position as well as defect size. These two parameters act in competitive way. Bonneric et al. (2020) reported that the defect position is the winner from a point of view that the major cause of fatigue failure is the surface assuming that the essential cause of the surface cracks is the interaction with the external environment that could have a large impact on crack nucleation.

EDS analyses were carried out at the defect position and showed the presence of Inconel 718 elements as illustrated in Fig. V.33. This observation could be explained by the fact that the peeling of material was generated during the drilling process.

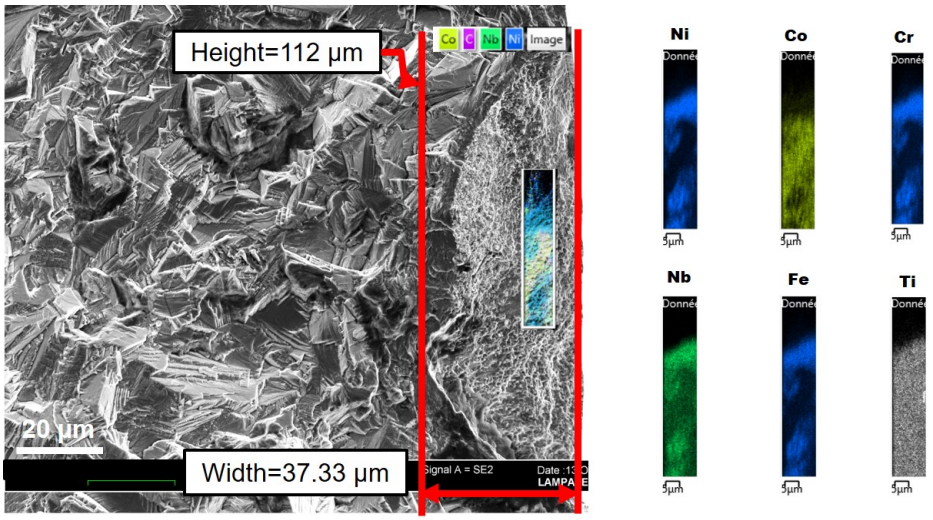

Figure V.33 – Illustration of the EDS analyses conducted in the fractured surfaces of the broken specimen n°2 drilled in LN_2 condition (N_f= 533 534, σ_a=120 MPa).

Subsequently, an observation of the fracture surface of a broken specimen n°8 drilled in LN_2 condition is presented in Fig. V.34. This specimen was subjected to 100 MPa of σ_a leading to a fatigue lifetime N_f equal to 1.73 10^6.

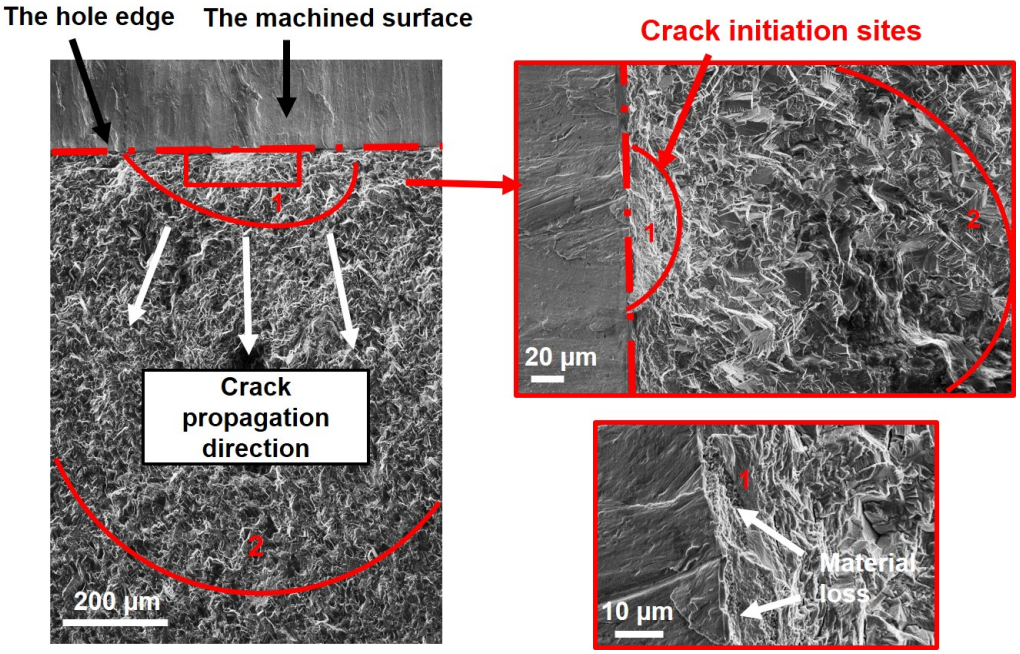

Figure V.34 – Illustration of the fractured surfaces of the broken specimen n°8 drilled in LN_2 condition (N_f= 1.73 10^6, σ_a=100 MPa).

As it can be observed, cracks initiated predominantly within the defects experienced at the hole edge. According to literature review findings, the fatigue behavior of materials is driven significantly by the state of the surface since that the initiation of cracks appears predominantly at the surface of the fatigue specimens (Moussaoui et al., 2015). Consequently, it could be concluded that the observation mentioned previously (in Fig. V.33 and Fig. V.34) implicates that drilling operation under LN_2 cooling condition de-

teriorated the surface topology of the machined surfaces. Hence, fatigue resistance is adversely affected revealing a significant reduction in comparison with the conventional lubrication and the LCO_2 strategy as well.
It seems worth mentioning that in case of the LN_2 fatigue specimens, all the broken specimens were analyzed in order to verify if the defects that have been observed occurred for all tested specimens or they are randomly present. Effectively, when examining all the surface fractographies, similar findings were figured out. For the majority of LN_2 failed specimens, coarse defects were identified revealing the same aspects of the fracture surfaces. This observation confirms that the LN_2 drilling condition generated the most deteriorated surface finish. Moreover, in the case of the LCO_2 and conventional cooling conditions, such defects did not exist in the surface fracture.

Conventionally, researchers investigates the effect of the defect size on the fatigue limit via Kitagawa-Takahashi diagrams (Abroug et al., 2018; El Khoukhi et al., 2019). The Kitagawa-Takahashi diagram reflects that in the presence of defect, fatigue limit decreases in a stepwise manner with the increase of the defect size. However, in this work, it is not possible to proceed the same way since that the output of the staircase method are not sufficient to draw the Kitagawa-Takahashi diagrams. In other word, for the considered LN_2 batch, one staircase allowed to estimate only one point of the curve. Therefore, another correlation could be established according the finding of the present work. One could relate the the effect of the size defect on the fatigue lifetime of the LN_2 drilled specimens. To do this, at first, the area of each defect present in the fracture surface of the broken specimens drilled in the LN_2 cooling condition are given in Fig. V.35. It should be mentioned that the calculation of the defects area were established using the software Image-J.

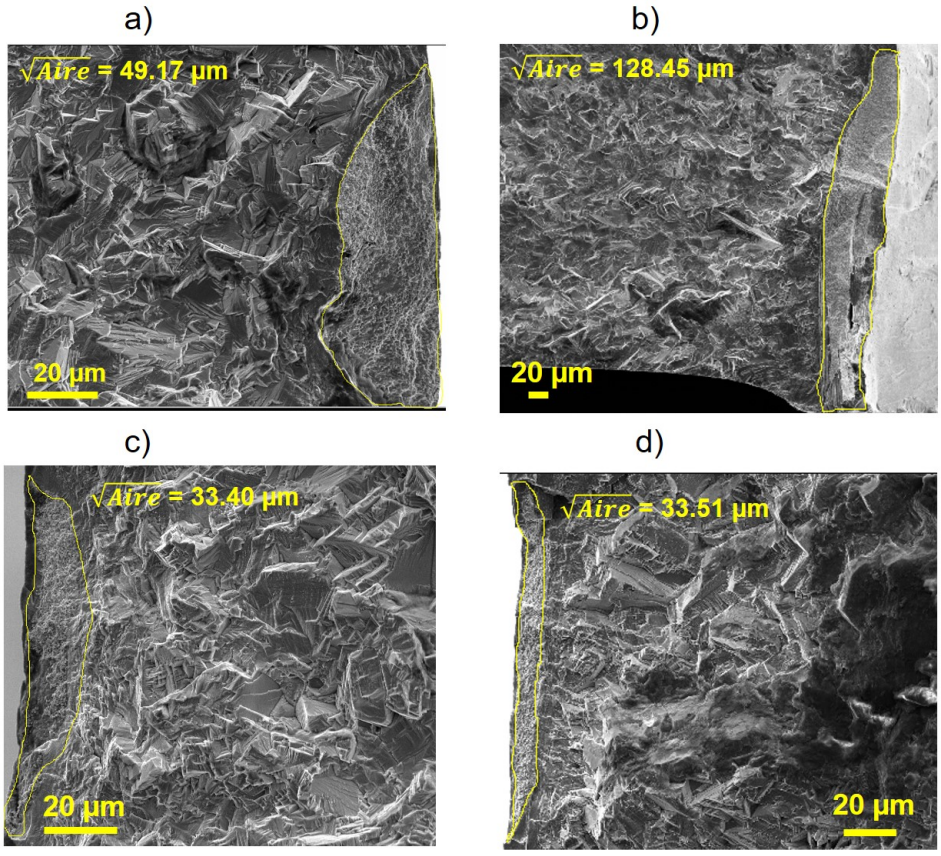

Figure V.35 – Illustration of the probable crack initiation sites experienced from the defects close to the surface of the LN_2 failed specimens : a) Specimen n°2: N_f=533534; b) Specimen n°7 : N_f=414 773; c) Specimen n°8: N_f= 1.73 10^6; d) Specimen n°15 : N_f= 1.56 10^6.

Afterwards, the applied stresses σ_a is then plotted versus the fatigue lifetime taking into account the square root of the defect area. Results are shown in the Fig. V.36.

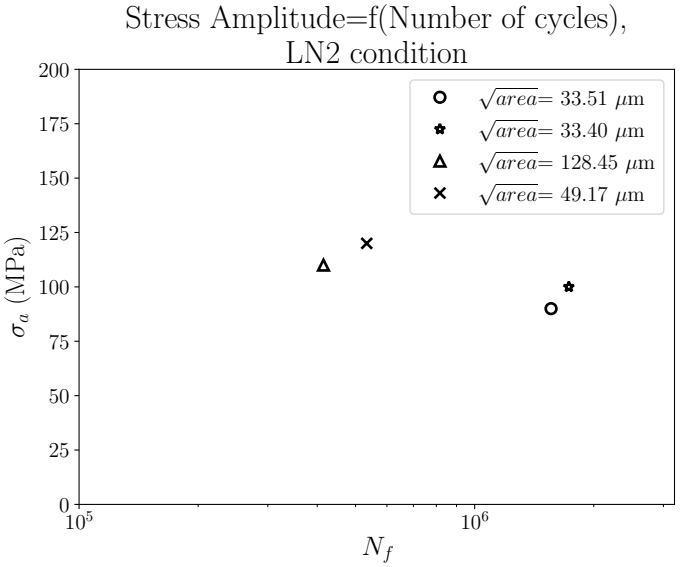

Figure V.36 – Illustration of applied stresses versus fatigue lifetime of the LN_2 failed specimens taking into account the square root of the defect area.

It can be observed that the fatigue lifetime is dependent on the defect size: as the size defect increases, the fatigue lifetime decreases. At this line, authors define a critical size where the sensitivity to the fatigue limit is then significant (El Khoukhi et al., 2019). The latter reported that the main difference in fatigue resistance is attributed to the defect size as well as its position. This interpretation correlates well with the current results mainly for two reasons. First, if comparing the three studied cases namely : wet, LCO_2 and LN_2 fatigue specimens. It could be judged that the presence of defects at the vicinity of the surface in the case of LN_2 lot generated the worst fatigue behavior in terms of fatigue limit compared to the wet and LCO_2 cases. Secondly, when examining the LN_2 batch, fatigue lifetime is strongly linked to the defect size. Indeed, broken specimens revealing larger defect experienced shorter fatigue lifetime.

Overall, fracture surface investigations and EDS analyses have figured out that the cooling strategy during drilling operation of the fatigue specimens affected drastically the fatigue behavior inducing several aspects (defects, fatigue failure mechanisms..). Let us recall that wet and LCO_2 strategies generated comparable fatigue limits. Hence, one could not easily distinguish the fatigue mechanisms related to the crack initiation sources in the case of the wet and LCO_2 cooling approaches. Effectively, it has been pointed out that similar aspects governed the fatigue behavior of the drilled specimens under both conditions (wet and LCO_2). Fatigue cracks initiated often around facet structure very close to the surface. In contrast, LN_2 exhibited unlike fatigue crack initiation zones where coarse defects localized at the surface causing the rapid failure of the specimens (Fig. V.37).

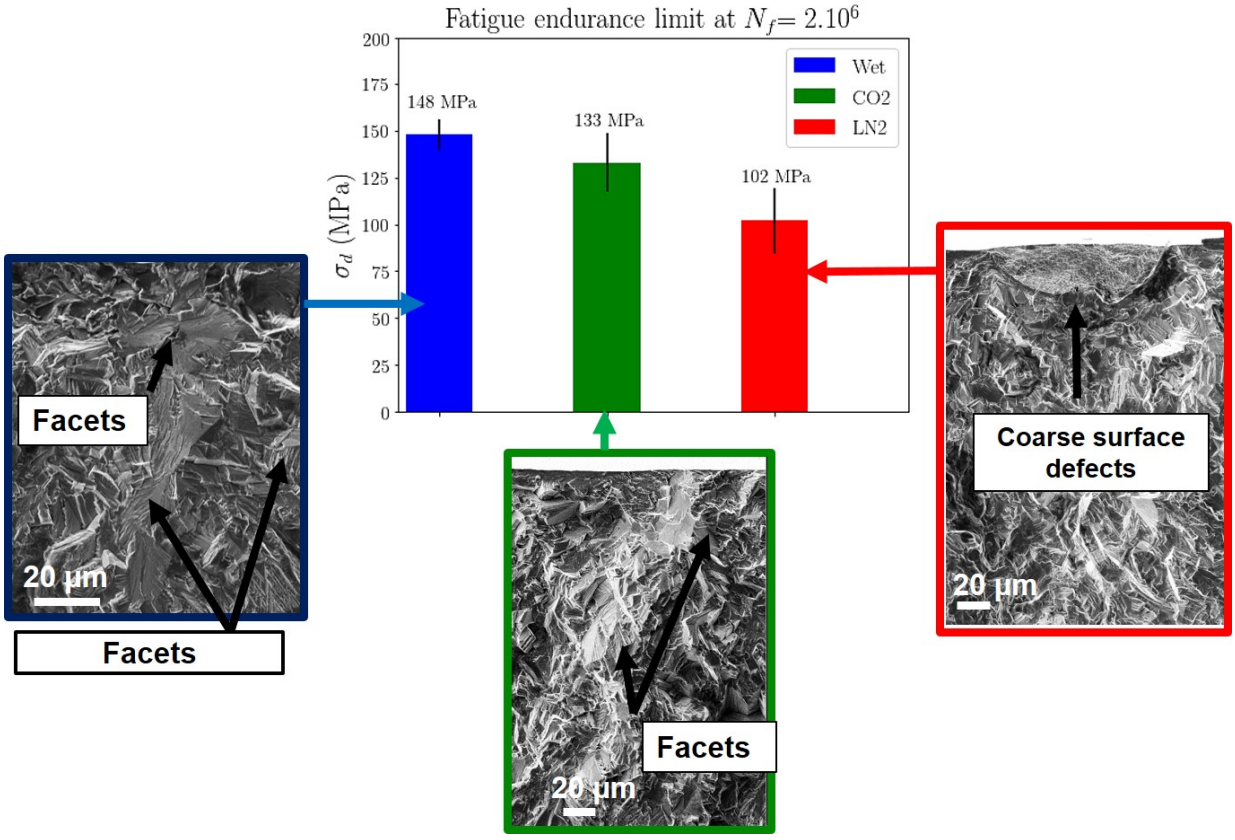

Figure V.37 – Illustration of the fatigue endurance limit obtained for the three fatigue batches linked with the fatigue failure mechanisms observed in the surface fracture.

3.6 Discussions: summary of the outcome of the study

It is widely reported about the existence of a strong correlation between the manufacturing process and the fatigue behavior of the components and critical structure (Davies et al., 2014). For instance, the machining process affects significantly the surface integrity of the workpiece which is a predominant factor to monitor the fatigue performance. In particular, depending on the mechanical and thermal loads encountered in the machining process, the surface integrity of the machined parts experience some alterations with respect to the metallurgical aspects (surface and subsurface roughness, microstructure change, microhardness evolution) as well as the mechanical aspects (residual stresses) in addition to the topological properties (surface roughness) as illustrated in Fig. V.38.

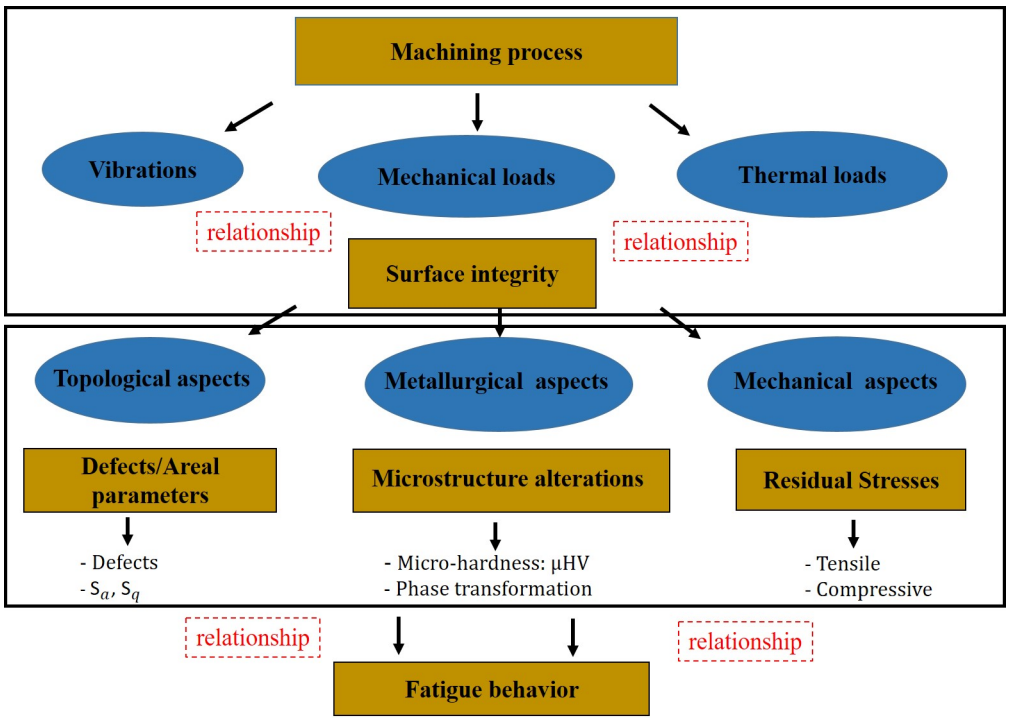

Figure V.38 – Illustration of the fatigue endurance limit obtained for the three fatigue batches linked with the fatigue failure mechanisms observed in the surface fracture.

In this section, a correlation between the hole topology, the micro-hardness measurements, microstucture damage as well as the fracture surfaces of the broken specimens will be established.
At first, it should be noted that although the residual stresses are very interesting to assess when characterizing the surface integrity in order to predict the fatigue behavior, these parameters were not evaluated in the current work. In fact, evaluating the residual stresses distribution of drilled samples arise some difficulties. To access to the machined surface of the drilled holes, one needs to cut the sample. The cut of the sample induces the release of the residual stresses induced by drilling operation. So that, it is necessary to combine two methods : the experimental (XRD) and numerical (such as the contouring approach). In this context, Pagliaro et al. (2011) explains in details the strategy to measure the inaccessible residual stresses using several methods and superposition. As this procedure requires much longer time, it was not possible to conduct it.

The investigation carried out has driven to several conclusions deduced from each cooling condition performance. Table V.11 presents a summary showing a comparison of the output of this study related to each batch.

Table V.11 – Summary of the output of the study

Cooling conditions	Wet	LCO_2	LN_2
σ_d MPa	148 MPa	133 MPa	102 MPa
Areal parameters	S_a=1.47 μm S_q=1.85 μm	S_a=1.42 μm S_q=1.80 μm	S_a=2.03 μm S_q=2.63 μm
Hole topology	debris	debris micro-cavities	debris large cavities smearing
Microhardness (near the surface)	512 $HV_{0.05}$	556 $HV_{0.05}$	560 $HV_{0.05}$
Microstructure damage	typical affected layer	typical affected layer	typical affected layer defects at the surface cracked carbides
Crack initiation sites	Facets	Facets	Coarse defects

As it could be deduced from the Table V.11, wet lot revealed the highest fatigue strength compared to the cryogenic ones (LCO_2 and LN_2). If examining the output obtained in this condition, one could affirm that the conventional lubrication generated the best surface integrity : the lowest values of S_a and S_q and the least damage present on the machined surface. In addition, fracture surfaces of the failed specimens have shown that the crack nucleation origins are almost occurring around facets structure.

As for the LCO_2, similar observations have been noticed in comparison with the wet condition. Remarkable difference concerned the hole topology in terms of defects that were occasionally seen. Regard the fracture surface, cracks originate from initiation facets in a most of analyzed cases where facets nucleated cracks at the surface as well as the sub-surface. In summary, it was very difficult to draw conclusions regarding the mechanism behind the initiation of facets at the surface and subsurface observed in wet and LCO_2 specimens. Price (1984) has investigated the correlation between the yield

stress and the fatigue limit for several materials (Nickel based alloys, steel alloys and aluminum alloys) with respect to facet fractured. Author found that for some nickel based alloys such as Inconel 625, two kinds of steels alloys exhibited comparable fatigue limit values and the yield stresses. However, Inconel 718, Udimet 700 and two kinds of aluminum alloys revealed very low fatigue limits in comparison with their yield stress values. Additionally, he related this finding to facet structured formation. Indeed, concerning the first category, these alloys are unfavorable to exhibit facet structure in the crack nucleation zones. Nevertheless, the second category are rather prone to facet structures. Consequently, it was suggested that the facet structures control the fatigue resistance. These finding correlate well with the current study results. Indeed, both batches (wet and LCO_2 drilled specimens) manifested facet structures in the fatigue fractographies leading to low fatigue resistance compared to the yield stress.

Regard the LN_2 study case, the weak fatigue strength could be attributed to the combination of several parameters namely the machined surface that exhibited poor surface state revealing frequent defects such as cavities, smeared material and debris which are favorable to stress concentration and thus causing fatigue cracks nucleation.
Furthermore, an interesting finding was depicted related to the fracture surfaces, it seems to be that facet structure are excluded to dominate the crack initiation sites. In contrast, the coarse defects observed at the vicinity of the surface are very likely the greatest weakness in the LN_2 drilled specimens to initiate fatigue cracks leading to the drop of the fatigue limit. This statement is an interesting conclusion that may explain the significant gab induced concerning the fatigue performance for the three batches.

4 Conclusion

In this chapter, fatigue tests have been conducted at high-cycle fatigue regime for three batches of fatigue specimens drilled in cryogenic and conventional cooling strategies. The following conclusions are extracted from the experimental investigations:

— Results showed that wet drilling induced the highest fatigue resistance whereas the LN_2 generated the lowest fatigue limit;

— The experimental analyses proved that LN_2 cryogenic condition induced the worst surface integrity in terms of S_a and Sq in addition to the presence of the large cavities on the machined surface;

— Fractographic analyses have revealed that the fatigue cracks originated from facets structure in a dominating majority of investigated cases of drilled specimens in wet and LCO_2 cooling conditions;

— The majority of the LN_2 fatigue fracture surfaces disclosed large surface defects regardless of the applied stress and the fatigue lives. These defects are likely convenient and favorable to crack initiation;

— As perspectives, the evaluation of residual stresses distribution related to the drilling process could evaluated in order to export additional information to explain the fatigue resistance difference of the three batches of the drilled spec-

imens.

Bibliography

Abroug, F., Pessard, E., Germain, G., Morel, F., 2018. Hcf of aa7050 alloy containing surface defects: Study of the statistical size effect. International Journal of Fatigue 110, 81 – 94. URL: http://www.sciencedirect.com/science/article/pii/S0142112318300124, doi:https://doi.org/10.1016/j.ijfatigue.2018.01.012.

AFNOR, 2006. Matériaux métalliques - méthodes des essais applicables: Partie 001: Essais de traction à temperature ambiante. Norme européenne NF EN 2002-001.

AFNOR, 2012. Série aérospatiale matériaux métalliques méthodes d'essai — essai de fatigue à amplitude constante. Norme européenne NF EN 6072.

Aman, M., Tanaka, Y., Murakami, Y., Remes, H., Marquis, G., 2017. Fatigue strength evaluation of small defect at stress concentration. Procedia Structural Integrity 7, 351–358. doi:10.1016/j.prostr.2017.11.099.

Axinte, D., Andrews, P., Li, W., Gindy, N., Withers, P., Childs, T., 2006. Turning of advanced ni based alloys obtained via powder metallurgy route. CIRP Annals 55, 117 – 120. URL: http://www.sciencedirect.com/science/article/pii/S0007850607603795, doi:https://doi.org/10.1016/S0007-8506(07)60379-5.

Ayesta, I., Izquierdo, B., Flaño, O., Sánchez, J.A., Albizuri, J., Aviles, R., 2016. Influence of the wedm process on the fatigue behavior of inconel® 718. International Journal of Fatigue 92, 220 – 233. URL: doi:https://doi.org/10.1016/j.ijfatigue.2016.07.011.

Belan, J., 2015. High frequency fatigue test of in 718 alloy – microstructure and fractography evaluation. Metalurgija 54, 59–62.

Bonneric, M., Brugger, C., Saintier, N., 2020. Investigation of the sensitivity of the fatigue resistance to defect position in aluminium alloys obtained by selective laser melting using artificial defects. International Journal of Fatigue 134, 105505. URL: doi:https://doi.org/10.1016/j.ijfatigue.2020.105505.

Booysen, C., Heyns, P., Hindley, M., Scheepers, R., 2015. Fatigue life assessment of a low pressure steam turbine blade during transient resonant conditions using a probabilistic approach. International Journal of Fatigue 73, 17 – 26. URL: doi:https://doi.org/10.1016/j.ijfatigue.2014.11.007.

Chen, Q., Kawagoishi, N., Othubo, K., Kondo, E., Sakai, M., Kizaki, T., 2001. Ultrasonic fatigue strength in inconel 718 , 573–582.

Chen, Z., Moverare, J., Peng, R.L., Johansson, S., 2016. Surface integrity and fatigue performance of inconel 718 in wire electrical discharge machining. Procedia CIRP 45, 307–310. URL: 3rd CIRP Conference on Surface Integrity.

Davies, D., Jenkins, S., Legg, S., 2014. The effect machining processes can have on the fatigue life and surface integrity of critical helicopter components. Procedia CIRP 13, 25 – 30. URL: doi:https://doi.org/10.1016/j.procir.2014.04.005. 2nd CIRP Conference on Surface Integrity (CSI).

Dixon, W.J., Mood, A.M., 1948. A method for obtaining and analyzing sensitivity data. Journal of the American Statistical Association 43, 109–126. URL: doi:10.1080/01621459.1948.10483254.

El Khoukhi, D., Morel, F., Saintier, N., Bellett, D., Osmond, P., Le, V.D., Adrien, J., 2019. Experimental investigation of the size effect in high cycle fatigue: Role of the defect population in cast aluminium alloys. International Journal of Fatigue 129, 105222. URL: http://www.sciencedirect.com/science/article/pii/S0142112319303263, doi:https://doi.org/10.1016/j.ijfatigue.2019.105222.

Forsman, S., 2012. Fatigue Initiation Fail Mode Classification of a nickel base Superalloy. Master's thesis in applied physics. Chalmers University of Technology Gothenburg Sweden.

Gribbin, S., Ghorbanpour, S., Ferreri, N.C., Bicknell, J., Tsukrov, I., Knezevic, M., 2019. Role of grain structure, grain boundaries, crystallographic texture, precipitates, and porosity on fatigue behavior of inconel 718 at room and elevated temperatures. Materials Characterization 149, 184 – 197. URL: doi:https://doi.org/10.1016/j.matchar.2019.01.028.

Guo, Y., Schwach, D.W., 2005. An experimental investigation of white layer on rolling contact fatigue using acoustic emission technique. International Journal of Fatigue 27, 1051 – 1061. URL: doi:https://doi.org/10.1016/j.ijfatigue.2005.03.002.

Holmberg, J., Wretland, A., Hammersberg, P., Berglund, J., Suárez, A., Beno, T., 2021. Surface integrity investigations for prediction of fatigue properties after machining of alloy 718. International Journal of Fatigue 144, 106059. URL: doi:https://doi.org/10.1016/j.ijfatigue.2020.106059.

Imran, M., Mativenga, P., Gholinia, A., Withers, P., 2015. Assessment of surface integrity of ni superalloy after electrical-discharge, laser and mechanical micro-drilling processes. The International Journal of Advanced Manufacturing Technology 79. doi:10.1007/s00170-015-6909-5.

ISO12107, 2012. metallic materials – fatigue testing – statistical planning and analysis of data Norme européenne NF EN 6072.

Javadi, H., Jomaa, W., Dalgaard, E., Brochu, M., Bocher, P., 2018. Influence of surface residual stresses on the fatigue life and crack propagation behavior of turned inconel 718 super-alloy. MATEC Web of Conferences 165, 18004. doi:10.1051/matecconf/201816518004.

Li, W., Guo, Y., Barkey, M., Jordon, J., 2014. Effect tool wear during end milling on the surface integrity and fatigue life of inconel 718. Procedia CIRP 14, 546 – 551. URL: doi:https://doi.org/10.1016/j.procir.2014.03.056. 6th CIRP International Conference on High Performance Cutting, HPC2014.

Ma, X., Duan, Z., Shi, H.j., Murai, R., Yanagisawa, E., 2010. Fatigue and fracture behavior of nickel-based superalloy inconel 718 up to the very high cycle regime. Journal of Zhejiang University SCIENCE A 11, 727–737. doi:10.1631/jzus.A1000171.

Moussaoui, K., Mousseigne, M., Senatore, J., Chieragatti, R., Lamesle, P., 2015. Influence of Milling on the Fatigue Lifetime of a Ti6Al4V Titanium Alloy. Metals 5, 1148–1162. URL:

Novovic, D., Dewes, R., Aspinwall, D., Voice, W., Bowen, P., 2004. The effect of machined topography and integrity on fatigue life. International Journal of Machine Tools and Manufacture 44, 125 – 134. URL: doi:https://doi.org/10.1016/j.ijmachtools.2003.10.018.

Ono, Y., Yuri, T., Sumiyoshi, H., Takeuchi, E., Matsuoka, S., Ogata, T., 2004. High-cycle fatigue properties at cryogenic temperatures in inconel 718 nickel-based superalloy. Materials Transactions - MATER TRANS 45, 342–345. doi:10.2320/matertrans.45.342.

Pagliaro, P., Prime, M., Robinson, J., Clausen, B., Swenson, H., Steinzig, M., Zuccarello, B., 2011. Measuring inaccessible residual stresses using multiple methods and superposition. Experimental Mechanics 51, 1123–1134. doi:10.1007/s11340-010-9424-5.

Price, C., 1984. Observations on the faceted fatigue fracture of an "sel" superalloy turbine blade. Metallography 17, 359 – 370. URL: http://www.sciencedirect.com/science/article/pii/0026080084900739, doi:https://doi.org/10.1016/0026-0800(84)90073-9.

Price, C., Kunc, R., 1986. Occurrence of faceted fatigue fractures in nickel. Metallography 19, 317 – 326. URL: doi:https://doi.org/10.1016/0026-0800(86)90019-4.

Pusavec, F., Hamdi, H., Kopac, J., Jawahir, I., 2011. Surface integrity in cryogenic machining of nickel based alloy—inconel 718. Journal of Materials Processing Technology 211, 773 – 783. URL: doi:https://doi.org/10.1016/j.jmatprotec.2010.12.013.

Qian, G., Li, Y., Paolino, D., Tridello, A., Berto, F., Hong, Y., 2020. Very-high-cycle fatigue behavior of ti-6al-4v manufactured by selective laser melting: Effect of build orientation. International Journal of Fatigue 136, 105628. URL: doi:https://doi.org/10.1016/j.ijfatigue.2020.105628.

Saklakoglu, N., Bolouri, A., Gencalp Irizalp, S., Baris, F., Elmas, A., 2021. Effects of shot peening and artificial surface defects on fatigue properties of 50crv4 steel. The International Journal of Advanced Manufacturing Technology , 1–10doi:10.1007/s00170-020-06532-y.

Seco, 2020. Holemaking Catalog and Technical Guide 2020.

Sun, D., Keys, D., Jin, Y., Malinov, S., Zhao, Q., Qin, X., 2016. Hole-making and its impact on the fatigue response of ti-6al-4v alloy. Procedia CIRP 56, 289 – 292. URL: doi:https://doi.org/10.1016/j.procir.2016.10.085. the 9th International Conference on Digital Enterprise Technology – Intelligent Manufacturing in the Knowledge Economy Era.

Sun, D., Lemoine, P., Keys, D., Doyle, P., Malinov, S., Zhao, Q., Qin, X., Jin, Y., 2018a. Hole-making processes and their impacts on the microstructure and fatigue response of aircraft alloys. The International Journal of Advanced Manufacturing Technology 94. doi:10.1007/s00170-016-9850-3.

Sun, J., Wang, T., Su, A., Chen, W., 2018b. Surface integrity and its influence on fatigue life when turning nickel alloy gh4169. Procedia CIRP 71, 478 – 483. URL: doi:https://doi.org/10.1016/j.procir.2018.05.029. 4th CIRP Conference on Surface Integrity (CSI 2018).

Suárez, A., Veiga, F., Polvorosa, R., Artaza, T., Holmberg, J., de Lacalle, L.L., Wretland, A., 2019. Surface integrity and fatigue of non-conventional machined alloy 718. Journal of Manufacturing Processes 48, 44 – 50. URL: doi:https://doi.org/10.1016/j.jmapro.2019.09.041.

Thakur, A., Gangopadhyay, S., 2016. State-of-the-art in surface integrity in machining of nickel-based super alloys. International Journal of Machine Tools and Manufacture 100, 25 – 54. URL: doi:https://doi.org/10.1016/j.ijmachtools.2015.10.001.

Wang, X., Huang, C., Zou, B., Liu, G., Zhu, H., Wang, J., 2017. Experimental study of surface integrity and fatigue life in the face milling of inconel 718. Frontiers of Mechanical Engineering 13. doi:10.1007/s11465-018-0479-9.

Waqas Tofique, M., Bergström, J., Burman, C., 2016. Very high cycle fatigue crack initiation mechanisms in different engineering alloys. Procedia Structural Integrity 2, 1181 – 1190. URL: http://www.sciencedirect.com/science/article/pii/S2452321616301597, doi:https://doi.org/10.1016/j.prostr.2016.06.151. 21st European Conference on Fracture, ECF21, 20-24 June 2016, Catania, Italy.

Yin, Q., Zhanqiang, L., Wang, B., Song, Q., Cai, Y., 2020. Recent progress of machinability and surface integrity for mechanical machining inconel 718: a review. The International Journal of Advanced Manufacturing Technology 109. doi:10.1007/s00170-020-05665-4.

Zhong, L., Hu, H., Liang, Y., Huang, C., 2018. High cycle fatigue performance of inconel 718 alloys with different strengths at room temperature. Metals 9, 13. doi:10.3390/met9010013.

Zhong, L., Hu, H., Liang, Y., Huang, C., 2019. High cycle fatigue performance of inconel 718 alloys with different strengths at room temperature. Metals 9. doi:10.3390/met9010013.

Chapter VI

Conclusions and perspectives

1 Main conclusions 236
2 Perspectives 237

1 Main conclusions

The main objective of the PhD work was to evaluate the cryogenic approach performance using two different cryogenic fluids namely the liquid nitrogen "LN_2" and the carbon dioxide "LCO_2" in terms of machining performance as well as fatigue limit of cryogenic drilled specimens considering as a reference the conventional lubrication "wet". According to the results of the PhD work, the main conclusions that could be drawn depending on each workpackage are listed below :

Mechanical behavior

— A new experimental cryogenic set-up has been conceived allowing to provide a stable and homogeneous cryogenic temperature (-185°C) in compression tests;

— Cryogenic temperature induced the highest resistance behavior at all strain rate ranges: higher mechanical properties namely the yield stress and the peak stress in comparison with the room temperature configuration. The yield stress at -188°C and at the strain rate of 10 s^{-1} indicating an increase around 19 % compared to room temperature. The peak stress R_m showed a rise of 351 MPa under cryogenic condition at 10 s^{-1} in comparison with room temperature;

— Concerning microstructure alterations, cryogenic temperature did not probably show any change compared to the room temperature testing condition in spite of the strain rate value according the analyses conducted in this study.

Machining performance

— Conventional lubrication provided the lowest tool flank wear (within 15 min) and the lowest cutting forces whereas both cryogenic coolants induced much higher cutting forces. Regard the tool flank wear, LCO_2 showed similar results compared to the conventional condition revealing 15 min of tool life. However, LN_2 cryogenic configuration lead to the highest tool flank wear and thereby shorter tool life holding 13 min;

— Cutting forces components (F_c, F_f and F_p) indicated higher values under both cryogenic conditions compared to conventional lubrication revealing that the flow stress of the work material increased due to cryogenic temperature. Additionally, it was noticed that the passive forces are the most sensitive component to tool flank wear rise;

— Concerning the residual stresses distribution, results pointed out that when cutting using new tools, wet condition disclosed the highest tensile value near the surface (483 MPa) and produced the lowest compressive peak (-200 MPa) along the cutting direction. In both cryogenic conditions, near the surface, the hoop residual stresses showed approximately similar values (180 MPa and 102 MPa obtained respctively in LCO_2 and LN_2). Nevertheless, LCO_2 condition induced

the highest maximum compressive value holding around -300 MPa when cutting with new tools;

— Overall, when comparing the three tested cooling conditions, LCO_2 cooling strategy is the most appropriate since it is able to withstand 15 min with acceptable tool wear and to produce a better surface integrity than conventional and LN_2 conditions. It could be concluded that LCO_2 cooling strategy is a good alternative to replace the conventional lubrication owing to the ecological advantage as well.

Fatigue resistance

— LN_2 drilled specimens showed the lowest fatigue limit compared to LCO_2 and wet cooling methods holding respectively 102 MPa, 133 MPa and 148 MPa at high-cycle fatigue regime (2.10^6);

— Fracture surface analyses have shown that the fatigue cracks nucleated from facets structure in the majority of investigated cases of drilled specimens in wet and LCO_2 cooling conditions. However, most of the LN_2 fatigue fracture surfaces exhibited coarse defects at the vicinity of the surface regardless of the applied stress and the fatigue lives. These defects are likely the main sources of crack initiation.

General conclusion

Overall speaking, the LCO_2 revealed a promoting approach since it has shown a very good performance not only during the turning experiments but also with respect to the fatigue limit compared to the LN_2 condition. So that, extensive investigations could be conducted in order to optimize the efficiency of this cryogenic method.

2 Perspectives

The present dissertation has suggested a comparative study between two cryogenic coolants efficiency either with respect to machining performances or the fatigue limit considering the wet condition as a reference. However, more works may still be carried out in the future targeting to perfect our current results and to try other techniques. Therefore, the estimated perspectives as a continuity for the present work are listed below:

— Recently, researchers have focused on more efficient cooling strategies when machining steels and titanium alloys. They have proved that the combination between Minimum Quantity of Lubricant (MQL) and the LCO_2 enhanced the machining performance of these materials in terms of tool life as well as the surface integrity. For this reason, the MQL+LCO_2 could be examined in the case of Inconel 718;

— Besides, it could be interesting to carry out cryogenic drilling campaigns under the three considered strategies employed in the current PhD work in order to estimate the industrial requirements related to the tool life and the surface integrity;

— Finally, it is well known that the access to very local zone is hardly possible through experimentally approaches or techniques such as local deformation, local stresses and cutting temperature. The perfect complementary method consists of the numerical modeling allowing to understand better the local phenomena and the damage mechanisms occurring during the cutting process under cryogenic conditions.

Scientific Contributions

Published papers

— An article was published,"Comparison between cryogenic coolants effect on tool wear and surface integrity in finishing turning of Inconel 718", S. Chaabani, P.J. Arrazola, Y. Ayed, A. Madariaga, A. Tidu and G. Germain. Journal of Materials Processing and Technology, Volume 285, 2020, 116780, https://doi.org/10.1016/j.jmatprotec.2020.116780.

Contributions to Conferences

— Oral contribution to a national conference Manuf21 at Metz in France, in January 2018, Cryogenic assisted machining of aeronautic alloy: Inconel 718;

— Oral contribution to a national conference Manuf21 at Toulon in France, in January 2019, Cryogenic assisted machining of aeronautic alloy: Inconel 718;

— Oral contribution to an international conference ESAFORM in Spain, in May 2019, Tool wear and cutting forces when machining Inconel 718 under cryogenic conditions: Liquid nitrogen and carbon dioxide;

— Oral contribution to an international conference ESAFORM in Germany (Virtual conference), in May 2020, Surface Integrity When Machining Inconel 718 Using Conventional Lubrication and Carbon Dioxide Coolant.

Sana CHAABANI

Cryogenic machining of the aeronautic alloy: Inconel 718

Résumé

Les alliages à base de nickel sont largement utilisés dans le secteur aéronautique vu leurs excellentes propriétés mécaniques à haute température et leur résistance à la corrosion. Cependant, l'usinage de ces matériaux est particulièrement difficile. Ceci est dû principalement à leurs grandes propriétés mécaniques, leur très haute réactivité chimique avec la plupart des matériaux coupants et à un dégagement de chaleur important au niveau de la zone de coupe. Dans ce cadre, s'inscrivent les procédés d'usinage avec assistance visant à améliorer la productivité de certains matériaux qui sont difficiles à couper. Dans notre cas, on s'intéresse à l'assistance cryogénique. Elle consiste à injecter l'azote liquide (LN2) ou le dioxyde de carbone liquide (LCO2) dans la zone de coupe permettant de faire chuter la température. Par conséquent, certains mécanismes d'usure sont décélérés et la durée de vie de l'outil est augmentée. En revanche, l'application de cette approche lors de l'usinage de l'Inconel 718 a démontré certaines limites en termes de durée de vie de l'outil et l'intégrité de surface de la pièce usinée contrairement à l'alliage de titane Ti64. C'est pourquoi, il s'avère très intéressant de discerner les mécanismes de dégradation de la productivité de l'Inconel 718 sous assistance cryogénique et d'améliorer au mieux les conditions opératoires. En plus, le comportement dynamique de l'Inconel 718 à des températures cryogéniques a été établi dans le but de caractériser les changements métallurgiques de l'Inconel 718 qui peuvent avoir lieu. Finalement, la prédiction de la tenue en fatigue est réalisée pour des éprouvettes percées sous conditions cryogéniques.

Mots clés: Comportement dynamique, Inconel 718, Usinage cryogénique, Tenue en fatigue.

Abstract

Nickel-based alloys are widely used in the manufacture of aerospace engine components due to their excellent high-temperature thermo-mechanical properties and good corrosion resistance. However, machining these materials poses a number of challenges, mainly because they maintain their properties at high temperatures. Additional difficulties result from their high chemical reactivity with most cutting tool materials and their low thermal conductivity, which leads to wear due to the high temperatures reached at the cutting edge. In this context, the use of cooling/lubrication systems are very relevant in order to improve productivity in machining. Thus, this research work focuses on cryogenic machining, which consists of projecting liquid nitrogen (LN2) or liquid carbon dioxide (LCO2) into the cutting zone to reduce the temperature. The aim is to reduce some wear mechanisms and increase tool life. However, the application of this lubrication system machining Inconel 718 has to date shown limitations in terms of tool life and surface integrity of the machined part, as opposed to Ti64 titanium alloy. It is therefore considered of great interest to discern the mechanisms responsible for the poor machinability of Inconel 718 in cryogenic machining in order to propose a suitable process window. To this end, the dynamic behavior of Inconel 718 at cryogenic temperatures is characterized to determine the metallurgical alterations that may occur in the machined part. The surface integrity condition obtained is also analyzed and a study is made of the fatigue behavior of drilled specimens under cryogenic conditions.

Keywords: Cryogenic machining, Dynamic behavior, Fatigue resistance, Inconel 718.